



University
of Glasgow

Gallagher, Jamie Brian (2015) Synthesis of nanostructured materials with potential renewable energy generation applications. PhD thesis, University of Glasgow.

<http://theses.gla.ac.uk/7040/>

Copyright and moral rights for this thesis are retained by the author

A copy can be downloaded for personal non-commercial research or study, without prior permission or charge

This thesis cannot be reproduced or quoted extensively from without first obtaining permission in writing from the Author

The content must not be changed in any way or sold commercially in any format or medium without the formal permission of the Author

When referring to this work, full bibliographic details including the author, title, awarding institution and date of the thesis must be given

Synthesis of Nanostructured Materials with Potential Renewable
Energy Generation Applications

By

Jamie Brian Gallagher



University
of Glasgow

Submitted in fulfilment of the requirements for the degree of
Doctor of Philosophy

School of Chemistry

College of Science and Engineering

University of Glasgow

September 2015

Abstract

The work in this thesis is concerned with growth of low dimensional materials in a variety of morphologies which have potential renewable energy generation applications. The work described within demonstrates synthesis methods for the production of materials with thermoelectric applications and materials for photovoltaic purposes. Products are characterised using a range of techniques including: scanning and transmission electron microscopy; energy dispersive X-ray spectroscopy and powder X-ray diffraction.

Presented here is an investigation into the growth of bismuth telluride on silicon surfaces *via* chemical vapour deposition (CVD). Resultant particle morphology is reported in relation to experimental conditions such as surface conditions (silicon, gold/palladium on silicon and disordered silicon surfaces), temperature and reagent concentration. Successful synthesis of Bi_2Te_3 plates is presented starting from elemental precursors *via* a closed vessel CVD process. Plates with sub-micron thickness (but up to 40 μm diameter) are produced template free on a silicon surface and without the need for transport gases or expensive precursors. Using modification of silicon surfaces the growth of 2-4 μm tetragonal pyramids of Bi_2Te_3 are demonstrated. CVD is also used to produce bismuth rich nanowires up to 40 μm but <100 nm in diameter, these were produced by increasing the bismuth concentration in comparison to other methods.

This thesis also details an investigation into the suitability of a range of substrates for CVD. Alumina is demonstrated to be a suitable surface for Bi_2Te_3 CVD with nanostructured Bi_2Te_3 spheres of 5-20 μm diameter presented. Additionally vertically aligned arrays of copper telluride are presented using a single step CVD process. Arrays consist of hexagonal plates <500 nm in thickness but up to 25 μm in diameter. Due to preferential reaction with tellurium GaAs is demonstrated to be a poor facilitator for Bi_2Te_3 growth as is cobalt.

The production of nanostructured sphere of TiO_2 is also presented. Spheres with tuneable diameter are produced in <60 s in multi-mode microwave reactors using a hydrothermal process. The spheres are comprised of radially aligned nanorods producing spheres of 1-3 μm . Spheres are demonstrated to be a single rutile TiO_2 phase. Spheres are characterised with phase, band gap and morphology presented and influence of experimental parameters such as time and reagent concentration is discussed.

Finally this work investigates the doping and conversion of TiO_2 structures to TiN and $\text{TiO}_{2-x}\text{N}_x$ structures. Using ammonolysis TiO_2 is converted to a TiN structure while retaining its original spherical morphology. Using the same ammonolysis process TiO_2 is doped and the demonstrational shift in band gap to the visible region is presented.

Abbreviations and definitions

Abbreviation	Definition
BET	Brunaur-Emmett-Teller
CVD	Chemical vapour deposition
CVT	Chemical vapour transport
DI	Deionised
EDX	Energy dispersive X-ray
EELS	Electron energy loss spectroscopy
emf	Electromotive force
IPA	Iso-propanol
MOCVD	Metal-organic chemical vapour deposition
RTG	Radioisotope thermoelectric generator
SNAP	Systems for nuclear auxiliary power
SEM	Scanning electron microscope
TEM	Transmission electron microscope
UV/Vis	Ultraviolet/Visual
VLS	Vapour liquid solid
XRD	X-ray diffraction
ZT	Thermoelectric figure of merit

Table of contents

Acknowledgements	9
1 Introduction	10
1.1 Scope of work	10
1.2 Energy materials	10
1.3 Thermoelectrics	10
1.3.1 History	11
1.3.2 The Thermoelectric effect	11
1.3.3 Figure of Merit	14
1.3.4 Improving thermoelectrics	17
1.3.5 Thermoelectric materials	19
1.3.6 Bismuth telluride	21
1.3.7 Applications	23
1.3.8 Device design	24
1.3.9 Thermoelectrics in solar cells	26
1.4 Titanium dioxide	26
1.4.1 Current uses	27
1.4.2 Structure	29
1.4.3 Crystalline structure	29
1.4.4 Structural characterisation	30
1.4.5 Doping of structure	30
1.5 Titanium nitride	31
1.5.1 Current uses	32
1.5.2 Structure	32
1.6 Aims	32
2 Experimental	34
2.1 Synthesis techniques	35
2.1.1 Chemical vapour deposition	35
2.1.2 Heating profiles	39
2.1.3 Microwave hydrothermal synthesis	43
2.1.4 Ammonolysis	43
2.2 Characterisation techniques	44
2.2.1 Crystallography	44

2.2.2	XRD	47
2.2.3	Electron interactions with matter	48
2.2.4	Scanning electron microscopy	50
2.2.5	Transmission electron microscopy.....	55
2.2.6	Raman Spectroscopy	61
2.2.7	Brunauer–Emmett–Teller surface area analysis.....	63
2.2.8	Diffuse reflectance UV/Vis spectroscopy	63
3	Silicon based material growth.....	65
3.1	Gold-palladium reactions	67
3.1.1	Reaction set up	67
3.1.2	Results	67
3.1.3	Excess gold/palladium	71
3.1.4	Conclusions	73
3.2	Disrupted surface reactions	74
3.2.1	Reaction set up	75
3.2.2	Results	75
3.2.3	Conclusions	78
3.3	Vertically oriented reactions	79
3.3.1	Reaction set up	79
3.3.2	Results	81
3.3.3	Conclusions	83
3.4	Temperature difference reactions	83
3.4.1	Reaction Set Up.....	84
3.4.2	Results	85
3.4.3	Conclusions	93
3.5	Transport agent reactions	94
3.5.1	Reaction set up	94
3.5.2	Results	95
3.5.3	Conclusions	97
3.6	Bismuth reactions	97
3.6.1	Reaction set up	98
3.6.2	Results	98
3.6.3	Conclusions	99
3.7	Equimolar bismuth/tellurium reactions	99
3.7.1	Reaction set up	100

3.7.2	Results	100
3.7.3	Conclusions	103
3.8	Test structure	104
3.9	Conclusions	111
4	Non silicon based growth of telluride structures	113
4.1	Bismuth telluride growth on aluminium oxide wafers	115
4.1.1	Reaction set up	115
4.1.2	Results	115
4.1.3	Conclusions	119
4.2	Single element transport onto aluminium oxide substrate reactions	119
4.2.1	Tellurium.....	119
4.2.2	Single bismuth reactions	121
4.3	Bismuth telluride growth on gallium arsenide	124
4.3.1	Reaction set up	124
4.3.2	Results	125
4.3.3	Conclusions	128
4.4	Cobalt surface reactions	128
4.4.1	Reaction set up	128
4.4.2	Results	128
4.4.3	Conclusions	135
4.5	Copper foil reactions	136
4.5.1	Reaction set up	137
4.5.2	Results, 700 °C.....	137
4.5.3	Conclusions, high temperature	142
4.5.4	Results 450 °C.....	142
4.5.5	Conclusions, 450 °C reactions	149
4.5.6	Bismuth transport on copper	150
4.5.7	Elemental analysis.....	153
4.5.8	Conclusions	153
4.6	Solvothermal synthesis of Bi ₂ Te ₃	154
4.6.1	Reaction set up	154
4.6.2	Results	155
4.6.3	Comparison to previous work	158
4.6.4	Conclusions	159

4.7	Conclusions	160
5	Nanostructured spheres of titanium dioxide by microwave hydrothermal reactions.	162
5.1	Experimental technique	163
5.2	Results and discussion multi-mode cavity synthesis.....	164
5.2.1	Crystalline phase identification.....	165
5.2.2	Morphology.....	167
5.2.3	TEM analysis	168
5.2.4	Phase characterisation	171
5.3	Experimental parameters effect on morphology	173
5.3.1	Effect of irradiation time.....	173
5.3.2	Effect of titanium tetrachloride concentration	174
5.3.3	Effect of hydrochloric acid concentration.....	178
5.3.4	Conclusion of morphology control	182
5.3.5	Band gap measurements.....	182
5.3.6	Thermogravimetric analysis.....	184
5.3.7	Surface area measurements	185
5.4	Single-mode microwave reactions	186
5.4.1	Results.....	188
5.4.2	Crystalline phase identification.....	189
5.4.3	Phase characterisation	190
5.4.4	Morphology.....	191
5.4.5	Band gap measurement	193
5.4.6	Energy effect.....	194
5.5	Conclusions	195
6	Doping of titanium dioxide spheres to nitride and oxynitride structures.....	197
6.1	Full Conversion to TiN structure.....	198
6.1.1	Reaction set up	198
6.1.2	Results.....	198
6.1.3	UV/Vis spectroscopy	208
6.1.4	Elemental analysis.....	210
6.1.5	Reconversion to TiO ₂	211
6.1.6	Crystalline phase identification.....	211
6.1.7	Morphology.....	212
6.1.8	Surface area measurement.....	213

6.1.9	Band gap measurement	214
6.1.10	Conclusions	215
6.2	Doping of TiO ₂	216
6.2.1	Post-reaction appearance.....	216
6.2.2	Crystalline phase identification.....	217
6.2.3	Morphology.....	218
6.2.4	TEM	219
6.2.5	Surface area measurement.....	222
6.2.6	CHN elemental analysis	222
6.2.7	Band gap measurement	222
6.2.8	Conclusions	223
6.3	Conclusions	224
7	Conclusions	226
8	References	230
9	Appendix	237
9.1	Appendix A	237
9.2	Appendix B.....	241
9.3	Appendix C.....	249

Acknowledgements

I would like to thank my supervisors Prof Duncan Gregory, Prof Douglas Paul and Prof Andrew Knox. I'd also like to thank the University of Glasgow for supporting this research through a Lord Kelvin Adam Smith Scholarship.

I'd also like to thank many in the research group past and present for their help, support and company over the years, from Dr Bob Hughes helping me find my feet in the early days through to swapping SEM and EDX knowledge for Raman Spectroscopy information with Dr Hazel Reardon and Dr Jennifer Kennedy. Gracias to Dr Nuria Tapia for her help. Thanks go to the technicians Andy Monaghan and Kim Wilson for always being happy to help. Yann Romani was also of great assistance and a pleasure to work with during his summer placement.

I'm very grateful to Prof Graeme Cooke and Dr Justin Hargreaves for all the help, support and advice with my thesis, their time and effort is very much appreciated.

Without the love, support and encouragement from my family none of what I've achieved would have been possible. Mum, Gran, Grandad, Ellenor, Bobo, Papa – everyone who set me off on my journey – thank you.

I also want to thank my friends, I won't name them all or articulate the innumerable ways they help and have always helped. But I will say this: yes Gass, Neil does get a mention. Neil Boyd has been a great friend for most of my life and I'm grateful he was able to add his drawing skills to this thesis.

Finally I want to thank Patrick for making me happy every single day; for always inspiring, supporting and encouraging me. Patrick, you are my happiness.

And thanks Star Trek, this is all your fault....

1 Introduction

1.1 Scope of work

The research described in this thesis investigates the syntheses of low dimensional morphologies of materials with potential renewable energy generation applications. The aim of this work was to find suitable synthetic routes to grow low dimensional structures of thermoelectric and photocatalytic materials. The synthetic routes employed to create these structures were chemical vapour deposition (CVD), to create telluride structures with potential thermoelectric applications, and rapid microwave synthesis of the photocatalytic compound TiO_2 . The objective was to create the low dimensional structures in a reproducible and controllable manner while applying routes comprising the minimal number of steps.

Reported in the four results chapters of this thesis include telluride structures grown on silicon surface, telluride structures on non-silicon surfaces, and TiO_2 growth *via* microwave hydrothermal synthesis. These chapters detail the methodology used to create interesting particle morphology including sheets, plates and wires, and rods of bismuth telluride, and nanorods of TiO_2 aligned spherically. The final results chapter also details and investigation into the pseudomorphic conversion and doping of the TiO_2 spheres into nitride and oxynitrides. Synthesis conditions are reported and the products characterised.

1.2 Energy materials

Energy materials are capable of storing or transforming energy. This area has grown spectacularly in recent decades and spans the fields of chemistry, engineering and physics. Increasing importance is given to these materials due to concerns about the impact current energy production methods have on the environment. Energy materials include photovoltaics, thermoelectrics, battery technology and piezoelectrics. This thesis deals with materials used in photovoltaic and thermoelectric applications.

1.3 Thermoelectrics

Thermoelectric devices are modules capable of producing an electrical current from a temperature difference (the Seebeck effect). They are gaining importance in today's energy climate as a promising avenue for renewable energy these devices can be used to scavenge waste heat from inefficient systems and convert it into electricity. This could improve the efficiency of current energy processes as well as providing an easily retrofittable device to

numerous systems. Working devices or modules are also now being adapted to allow devices to run simply body heat¹.

1.3.1 History

The discovery of thermoelectrics occurred in the early 1800s when a compass needle was deflected when placed next to a circuit of two dissimilar metals which were held at different temperatures. It was regarded by the scientific community as somewhat of a novelty, a curious yet useless quirk of science. The investigation of thermoelectrics lay largely dormant for over 100 years, until the 1950s when the topic was more heavily invested in and put into practical use by the Soviet Union and the American military². At this time the technology had very few areas in which it could be employed. It was not yet suitable for a commercial market due to high cost and low efficiency. Therefore it could only be used when the cost was not prohibitive with respect to the reliability leading to the use of thermoelectric generators in niche military and medical applications.

1.3.2 The Thermoelectric effect

The thermoelectric effect is governed predominantly by three phenomena. These effects deal with the production of voltage from a temperature difference, the creation of a temperature difference when provided with a voltage, and the third representing the heat produced when current flows along a conductor with a non-uniform temperature. These three effects are described below.

1.3.2.1 The Seebeck effect

The Seebeck effect is the process by which a voltage is produced due to a temperature difference across a material. The Seebeck effect was discovered, though erroneously explained, by Thomas Johann Seebeck in 1821^{3,4}. Seebeck discovered that a compass needle could be deflected when placed in the centre of a loop made of two dissimilar metals in which the junctions were held at different temperatures.

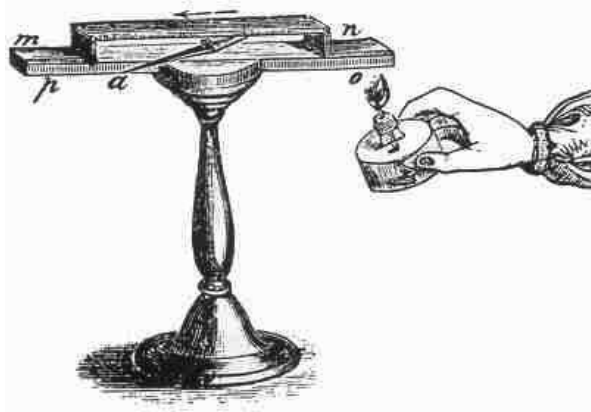


Figure 1-1: Diagram of Seebeck's original apparatus ⁵

It was initially believed that this was a thermomagnetic effect. Seebeck hypothesised that the temperature difference was inducing a magnetic field. While in a manner he was correct, he made no initial connection to the magnetic field itself being induced not directly by a temperature difference but by a current flowing through the material following Ampere's circuital law. The effect can be demonstrated by the simple schematic shown in Figure 1-2.

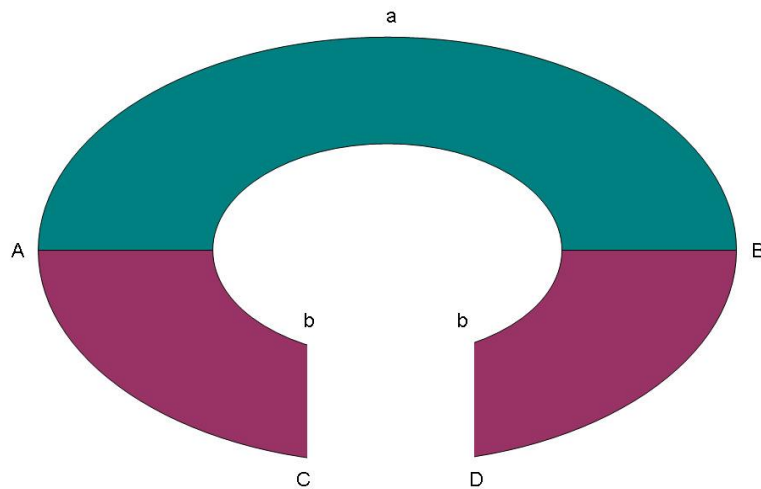


Figure 1-2: Seebeck model. Green (a) and purple (b) represent dissimilar conductors. A and B represent the junctions of the conductors. C and D are the points where an external circuit would be joined

Here, two dissimilar conductors, green (a) and purple (b) are connected in series with each other. If they are held thermally in parallel - so that junctions A and B held at different temperatures, T_1 and T_2 . Taking A to be the warmer junction and with the temperature at B

cooler then we have $T_1 > T_2$. An open circuit electromotive force (emf), V , is developed between C and D. This relationship is expressed in the following equation:

$$V = \alpha (T_1 - T_2) \quad (1)$$

Here α represents the Seebeck coefficient. Occasionally it is given the symbol S . The Seebeck coefficient is normally referred to in units of $\mu\text{V/K}$ as it is a measure of the voltage induced by the temperature difference, $\alpha = V/\Delta T$.

1.3.2.2 Peltier effect

The Peltier effect can be thought of as the opposite to the Seebeck effect as an electrical source is applied in order to create a temperature difference⁶. The effect was discovered by Jean Charles Athanase Peltier in 1834⁶. Four years later, Heinrich Friedrich Emil Lenz added to this discovery noting the direction of the current dictated whether the material would heat or cool, and used the same experimental set up to freeze and melt ice subject to a reversal of current.

The Peltier effect is the observed temperature difference resulting from an external emf applied to two dissimilar conductors. The effect can be enhanced, as is the case in commercial applications, by use of semiconductors. Defining a circuit as shown in Figure 1-2 and applying a current flowing in an A to B direction then there would be a resulting temperature difference created at the junctions (points A and B) of materials. Defining the rate of heating as q (and corresponding cooling of the second conductor as $-q$) then the Peltier coefficient, Π , becomes the relationship linking the current I with q and is represented by equation 2.

$$\Pi = \frac{I}{q} \quad (2)$$

Connecting two dissimilar conductors of Peltier coefficient Π_a and Π_b , and applying a current I , there is a resultant Peltier heating of \dot{Q} described as:

$$\dot{Q} = (\Pi_a - \Pi_b)I \quad (3)$$

It should be noted that the above description ignores heat produced from Joule heating. The Peltier effect leads to the common use of thermoelectric materials as heat pumps.

1.3.2.3 *The Thomson Effect*

The third effect which underlies the thermoelectric effect was discovered in 1851 by William Thomson (later Lord Kelvin) and is known as the Thomson Effect ⁷. This effect takes into account a temperature difference across the conductor and the heat absorbed or produced from a flowing current along the temperature gradient. Where a small temperature difference is recorded, ΔT , the Thomson coefficient (β) is given by:

$$\beta = \frac{q}{I\Delta T} \quad (4)$$

In the above equation, β is the Thomson coefficient, q the heat, and I the current.

1.3.2.4 *The Kelvin Relationships*

The Seebeck, Peltier and Thomson coefficients can be related using thermodynamics and are represented by the Kelvin relationships.

$$\alpha_{ab} = \frac{\Pi_{ab}}{T} \quad (5)$$

and

$$\frac{d\alpha_{ab}}{dT} = \frac{\beta_a - \beta_b}{T} \quad (6)$$

1.3.3 *Figure of Merit*

The comparison of thermoelectric materials is made through the dimensionless figure of merit, ZT , which determines the fraction of Carnot efficiency that can be theoretically attained as a thermoelectric. Each material type has a particular range at which ZT is maximised as shown in Figure 1-3⁸.

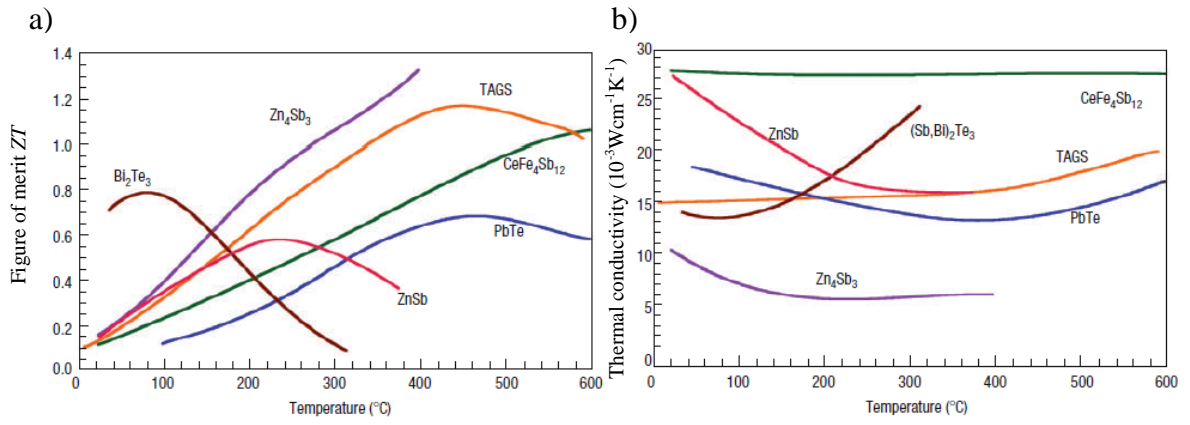


Figure 1-3: (a) Figure of merit (ZT) vs temperature; (b) thermal conductivity vs temperature ⁸

For temperatures circa 100 °C, bismuth telluride has the highest ZT value. The most common form in which the ZT is expressed is the following:

$$ZT = \frac{\alpha^2 \sigma T}{\kappa} \quad (7)$$

Here, σ is the electrical conductivity, T is the temperature, κ is the lattice thermal conductivity, and α is the Seebeck coefficient. It is this value that is used as a measure of the thermoelectric efficiency. Current research aims to maximise ZT . Refinement of materials has thus far lead to a plateau of $ZT \sim 1$ for commercial applications. Various modifications to existing materials were trialled leading to some success but the scaling up of highly efficient materials to bulk quantities is proving problematic. Other routes were developed which proved promising in developing materials further. The first wave of thermoelectric devices available to the market place had a ZT of around 0.8-1.0. This translates to an effectiveness of 5-6% when functioning as a Carnot engine. Second generation devices available commercially have ZT s in the range 1.3-1.7 and an efficiency of 11-15%. The long term current goal is a ZT value of three. Theoretically this is an attainable goal, but the route to synthesising a material with this high a value in a reproducible and commercially viable way is unclear. Superlattices have the highest ZT to date- but these are not suitable for large scale production or long term usage⁹⁻¹¹. Increasing ZT made slow progress in the early days of this technology. In the first 50 years spent attempting to improve bulk materials, only incremental gains were made, raising the figure from around 0.6 to 1¹². Research has failed to make notable increases to this value in bulk materials. Other routes were suggested as a means to increase the ZT and the leading

method currently is the decrease of dimensions (producing materials which have a fine nanostructure opposed to bulk material). It has been shown from proof of principle studies¹³ that low dimensional structures show an increased ability to tailor ZT . The greatest hardship that must be overcome is the direct relationship between thermal conductivity and electrical conductivity. When the scale of the material is small enough to allow quantum confinement effects, α , σ and κ can be controlled quasi-independently. Nanoscaled materials also have a secondary advantage over their bulk counterparts as they contain additional crystal boundaries. The fine grain boundaries found in nanoscale material play a significant part in disrupting phonons; this uses classical effects making use of scattering from boundaries and interfaces. This leads to a poorer thermal conductivity through the material while not hampering electrical conductivity. The positive effect of these boundaries has been clearly demonstrated by the improved performance of nanocomposite materials. Simple ball milling of a standard ingot of Bi_2Te_3 can have a significant effect on the thermal conductivity. Ren *et al.*¹⁴ and Zhao *et al.*¹⁵ showed that grinding followed by hot pressing gave a material that had reduced thermal conductivity but with no significant reduction in electronic conduction. Increases of 25% compared to bulk have been observed.

A good thermoelectric material inherently must have a poor thermal conductivity to retard an equilibrium being set up between the hot and cold sides of the device. This presents a significant problem when it is also necessary for the material to be a good electrical conductor. The thermal conductivity is one of the key parameters for the development of higher ZT materials. The lattice thermal conductivity arises from two sources in semiconducting materials- electrons (κ_e) and phonon (κ_p).

$$\kappa_{\text{lattice}} = \kappa_e + \kappa_p \quad (8)$$

The thermal conductivity of electrons cannot be reduced without having an adverse effect on the conductivity, therefore attention must be focused on reducing the contribution made by the phonons. This can be achieved by trapping the phonons as in skutterudites^{16, 17} (*vide infra*) or by stopping thermal transport with quantum confinement or grain boundary placement.

The ultimate goal in the development of thermoelectronic materials is the design of “Phonon Glass Electron Crystals”. This phrase, commonly found in the literature, refers to a material with poor thermal conductivity akin to that of an amorphous glass material but that still retains the ability for good electrical conductivity.

1.3.4 Improving thermoelectrics

One of the current leading methods to improve the efficiency of thermoelectric devices, both theoretically and experimentally, is decreased dimensions. Hicks *et al.*¹⁸ showed theoretically that by reducing thermoelectronic materials to the nanoscale, the efficiency of these devices can be multiplied many times. This increased ZT is represented in Figure 1-4. The rise in efficiency is due to the combination of many effects such as phonon scattering at the crystal grain boundaries leading to poor thermal conductivity and quantum confinement effects.

Figure of Merit (ZT) of 1D, 2D and 3D Systems

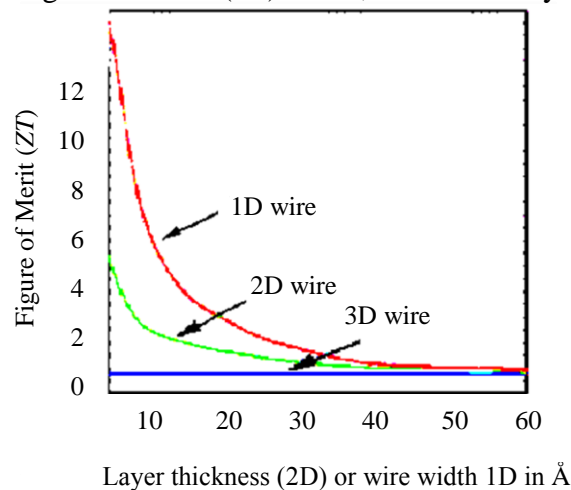


Figure 1-4: Reduced dimensions improving ZT ¹⁸

Increased efficiency is predominantly due to the decrease in thermal conductivity opposed to the increased powerfactor. The drive is towards a material which is a “phonon glass electron crystal” with the thermal conduction of an amorphous material but the electron conduction of a good conductor.

There are numerous routes to improving ZT such as the creation of nanocomposites. Here the thermoelectric is made of predominantly one material with the addition of a similar but different material in the form of a nanodot. These nanodot particles are dispersed

throughout the material in low enough quantity so that there is no significant disruption to the electrical conductivity. However the quantity is enough to significantly disrupt phonon transport. The mid to long range phonons are disrupted by Rayleigh scattering¹⁹ following interaction with the nanodots and this leads to a reduced thermal conductivity and correspondingly to an increase in the overall thermoelectric efficiency. There have also been improvements in thermoelectric performance by inclusion of “inert” organic molecules such as fullerenes²⁰.

Improvements have been seen by simply ball milling the bulk sample²¹ and hot pressing the resulting product back together. It is assumed in this case that there is creation of grain boundaries which hamper thermal transport but continue to allow for electrical transport, a key property in a high functioning thermoelectric material. There has also been research into the modification of structures by selective etching of samples, allowing for growth of desired and controllable patterns¹.

One of the leading methods in disrupting thermal transport has been to create a bulk material from nanocomposites. This involves the production of nanoparticles that are subsequently hot pressed to create a useable bulk material. The nanoparticles used in this method have been created in numerous ways such as wet chemical and ball milling²¹. Taking these nanoparticles and pressing back to bulk introduces countless nanoparticle interfaces. Nanocomposites lead to decreased thermal conductivity due to the introduction of these grain boundaries. The crystal boundaries scatter phonons but allow for relatively unhindered electron transport. There can be an additional, though smaller, increase in the thermoelectric power factor caused due to electron filtering at grain boundaries. There has been widespread success using the nanocomposite method. Indeed the ZT of materials can be improved by simply grinding and repressing the original bulk material. The nanocomposite method does face challenges, where wet chemical and ball milling methods risk the introduction of contaminants which can negatively affect the efficiency. The repressing of the nanoparticles to a comparable density of bulk material is a significant challenge. If samples are not sufficiently pressed and result in a low density material the conducting properties of the material will be drastically reduced resulting in a severely affected thermoelectric power factor.

New methods of production are also cited as leading to higher ZT . Producing bulk matter *via* the Bridgeman method ²², for example, where reagents are reacted as a movable furnace travels along a reaction chamber has shown to be a route of producing high quality bulk material.

The leading experimental production method currently used is metal-organic chemical vapour deposition (MOCVD). This method is similar to that carried out in this thesis but the reagents have organic components. Commonly used materials are the gases trimethylbismuth, dimethyltellurium or diethyltellurium. The gases flow over the desired surface which is placed in a furnace. The organometallic compounds crack as they enter the hot zone, leaving the bismuth and tellurium free to react with each other ²³⁻²⁶.

The production of nanomaterials is one part of the significant problems faced in creating the next generation of thermoelectric materials. Testing properties such as thermal conductivity is nontrivial at such low dimensions. Currently the Three Omega is the leading method. One interesting adaptation of this was shown by Zhang *et al.* ²⁷ which showed a way of simultaneously measuring both thermal conductivity and Seebeck coefficient of thin films.

1.3.5 Thermoelectric materials

There are many materials which are considered to be good thermoelectric materials or to have good potential as thermoelectric materials. Some of the leading structure types are described below.

1.3.5.1 Clathrates

Clathrates are a relatively new area of study compared to conventional thermoelectrics ²⁸. ²⁹. Their interesting thermoelectric properties arise from a unique structure leading to a potentially tuneable thermal conductivity. The structure consists of a framework of Group 13 or 14 atoms into the voids of which additional atoms can be trapped. Clathrates come in two types with the first having the general formula $X_2Y_6E_{46}$ and with cubic crystal structure $Pm\bar{3}n$ ²⁸ the rarer type-II having a formula of $X_8Y_{16}E_{136}$. In this formula X and Y represent the atoms held within the structure of E which denotes the Group 13 or 14 atoms (most commonly silicon or germanium) ³⁰.

In type-I, each E atom is coordinate with four other E atoms creating a Zintl phase semiconductor, with the guest atoms donating their outer electrons to the host cage. The creating of a high size ratio between the host structure and its contained atoms can cause a “rattling” effect, which theoretically can lead to a reduction in thermal conductivity³¹. This type of system is investigated as a route for the creation of a phonon-glass electron-crystal model which is the idealised version of a thermoelectric material. The vibration of the caged atoms helps to minimise thermal transport while the covalent sp^3 hybridized orbitals in the framework led to crystal-like electrical conductivity³².

1.3.5.2 Filled Skutterudites

Skutterudites take their name from the mineral of the same name discovered by Wilhelm Karl von Haidinger in the mining town of Skutterud in Norway³³. The research into filled skutterudites as thermoelectric materials was once again driven by the quest to find a “phonon glass electron crystal”. Skutterudites have an open crystal framework with good electrical conductivity. The open structure allows additional ions to be added for the purpose of disrupting thermal transport.

Skutterudites have the formula MX_3 where M is Co, Rh or Ir and X is a Group 15 element. The structure takes the form of body centred cubic with a space group $Im\bar{3}$. The result is a very open structure where the M atoms are too far apart to form bonds with each other and are instead connected through X octahedra³⁴. As the structure stands, it is a poor thermoelectric material despite having high electrical conductivity, there is a correspondingly high thermal conductivity. This problem can be overcome by “filling” some of the open structure with cations^{16, 17, 35}.

The skutterudite structure has been filled with rare earth elements. These atoms are loosely held in place and have freedom of movement and are described as “rattlers”. Phonons induce oscillations in the filler atoms thereby hampering transport and lowering thermal conductivity. Promising results have been obtained by Shi *et al.*, who reported a ZT of 1.7 at 850 °C³³.

1.3.6 Bismuth telluride

The crystal structure of bismuth telluride is rhombohedral with the space group $R-3m$ ³⁶. Part of the reason why bismuth telluride is an effective thermoelectric is due to the structure it forms. Certain aspects of the crystal structure appear to conform to that of a primitive cubic structure. Bismuth atoms are six-coordinate, as are one third of the tellurium atoms, $Te_{(1)}$ Figure 1-5. The remaining tellurium ($Te_{(2)}$) is three coordinate³⁷. From this structure there is a larger slab structure formed. The crystal is arranged in a layered structure along the c -axis³⁸, this follows the pattern of Te-Bi-Te-Bi-Te—Te. After every five atomic layers there are two layers of tellurium held together with van der Waals forces¹⁵. This structure is advantageous to the material as it promotes good in-plane electrical conductivity while transmittance of phonons between layers is inhibited³⁸.

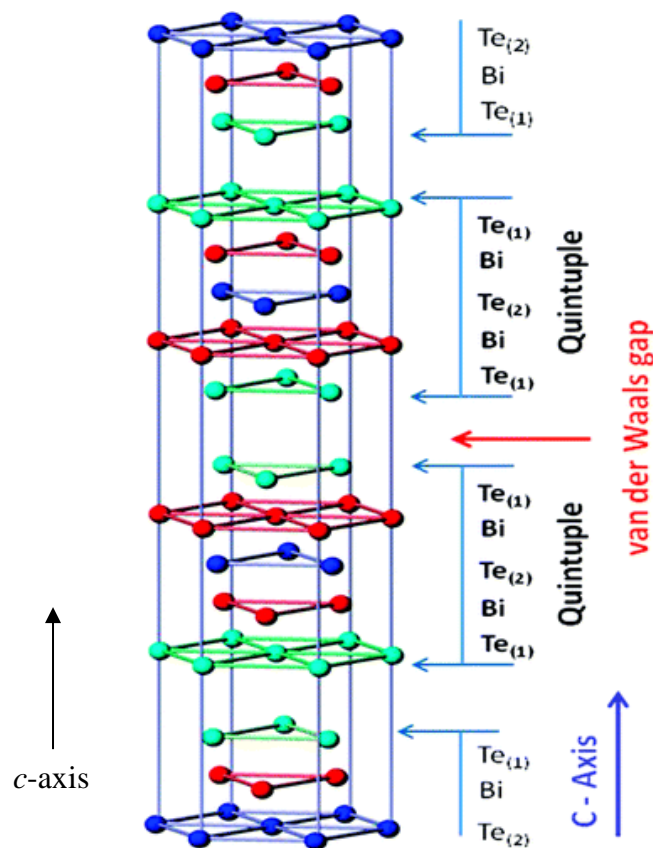


Figure 1-5: Bi₂Te₃ structure³⁹

The structure of Bi₂Te₃ is similar to that seen for TiS₂³⁸. This is encouraging as it has been shown that nanomaterials, including wires of TiS₂, can be easily produced and it is hoped that under the correct conditions that Bi₂Te₃ could follow a similar growth process. Within the structure each atom has three neighbours in an upper plane and three neighbours in the

lower plane. The structure is represented by a hexagonal cell (comprising three quintets) which can be considered as being comprised of stacking of deformed cubes.

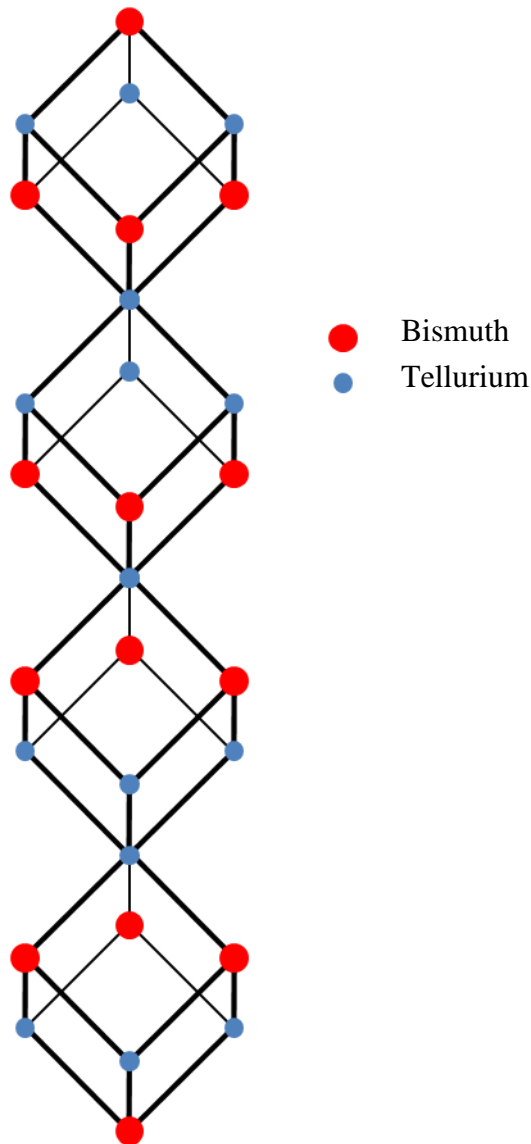


Figure 1-6: Cubic stacking schematic of Bi₂Te₃⁴⁰

The above schematic diagram shows the bismuth telluride structure is comprised of stacking of cubes along the (111) direction. A concentration of charge carriers can be obtained by either doping with other elements or commonly by the creation of vacancies caused by deviation from stoichiometry^{41,42}. The *ZT* of bismuth telluride has been successfully improved by the methods described in Section 1.4.4. There have been significant improvements in *ZT* achieved by methods such as nanostructuring through ball milling and the imbedding of nanoparticles in a bulk matrix.

Another interesting feature of bismuth telluride is that it is a topological insulator with conduction states across the surface; as such ultra-thin layer sutures have interesting conduction properties ³⁹.

1.3.7 Applications

The application of thermoelectrics on a wide scale in the commercial sector is a goal of most research. These devices can be integrated easily into existing technology - the only current drawback to the technology is the low efficiency of these devices. Since the 1960s small fridges have used thermoelectric modules in (reverse) producing a temperature difference using electricity. As electrical generators, they have some unrivalled properties. The devices are totally solid state, with no moving parts and this lends itself to long life stability. Modules can be connected and left to run and do not require regular maintenance, additionally they can operate over large temperature differences. In car engines, devices have to cope with a very rapid change in temperature. For example, braking causes a very sharp spike in temperature. Some machinery and materials may have difficulty in coping with such situations, but many thermoelectrics do not. The main drawbacks of thermoelectrics are the supporting equipment; deficiencies in solder or water crystallising within the module can cause malfunction. It can be difficult to obtain a constant voltage from a generator as the voltage produced is of course entirely temperature dependent – this can be resolved with the inclusion of a transformer along with the module.

Some applications include wearable devices for energy generation ^{43, 44} to power devices such as medical sensors. These have a high dependence on the stability and low maintenance advantages of thermoelectrics.

1.3.7.1 Radioisotope thermoelectric generators

One of the greatest indications of the strength of thermoelectric generators is the space exploration projects using radioisotope thermoelectric generators (RTGs). For deep space exploration, power sources must be reliable, long-lasting and self-sufficient. Combustion engines would not be suitable nor battery packs as both would soon find their reserves spent. Solar panels become ineffective as the distance from the sun increases. Thermoelectric generators provide the perfect energy solution. The basis of these generators is a radioactive source which is typically an alpha emitter such as ²³⁸Pu which

will cause a significant amount of radioactive heat which can then be absorbed by thermoelectric modules.

The first use of such a device was in 1961 and was used to produce less than 3 W of power. This mission's use of a System for Nuclear Auxiliary Power (SNAP) led the way for future missions and now thermoelectronic devices have been used on the surface of the moon and of Mars, as well as being an essential component of the furthest exploratory missions from earth - the Voyager space probes. Several thermoelectric devices have also been placed on the moon by successive missions and they continue to function. The Voyager space probes were launched in the 1970s with the mission to explore the furthest reaches of our solar system and beyond. The sole power source is the heat converted from ^{238}Pu . The main disadvantage to the RTGs is that the sources continually decay. The plutonium source of Voyager has a half-life of 87.7 years. This results in Voyager having an ever decreasing supply of power. As of November 2013, Voyager 1 was continuing to produce 254.9 W ⁴⁵ which is 54% its original launch value of 470 W ⁴⁶. Voyager 1 still has sufficient power to continue to report, despite having now left the solar system and travelled over 25.7 billion km ⁴⁷. The Mars Curiosity Rover project is also powered by a RTG.

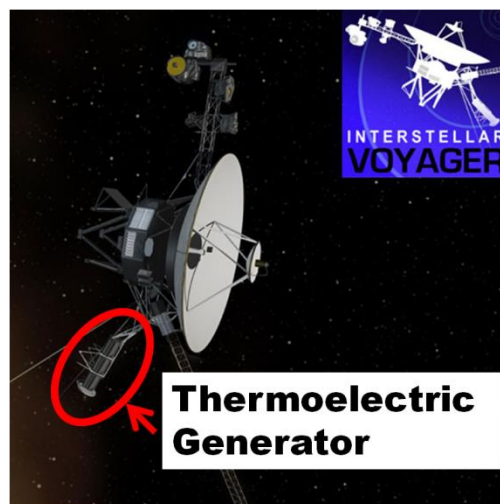


Figure 1-7: Voyager 1 with thermoelectric generator leg highlighted ⁴⁸

1.3.8 Device design

Thermoelectric devices have a simple and repetitive design. Devices can be made of any size and are typically created as thin square arrays on the centimetre scale. These arrays

consist of semiconductor millimetre dimensioned cubes, each part of a pair - one is an n-type semiconductor the other a p-type. These cubes are connected to their neighbour (electrically in series and thermally in parallel).

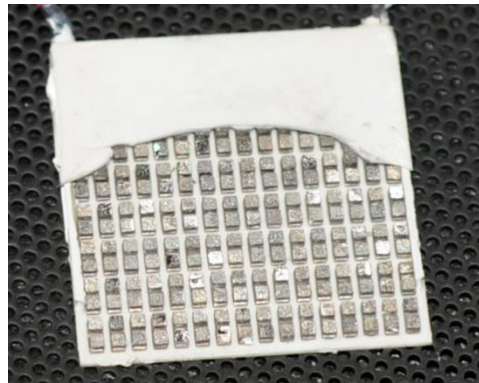


Figure 1-8: Thermoelectric module

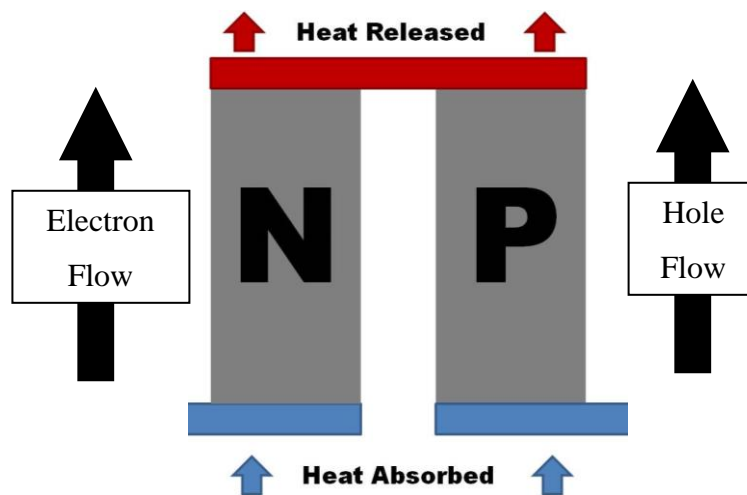


Figure 1-9: Thermoelectric junction pairing schematic

Figure 1-8 shows an actual thermoelectric module with one of the ceramic plates partially removed exposing the small cubes of semiconductors - in this case bismuth telluride based. Figure 1-9 shows a schematic of an individual pairing. In this case the negative end of the power source (electron flow) would be connected to the left hand side and the positive to the right (hole flow). This creates a temperature difference. From the above diagram it is clear how the blocks are held electrically in series but thermally in parallel.

The semiconducting material is connected with conducting solder and is held between two non-conducting ceramic plates. One advantage of the thermoelectric design is the scalability of the device; smaller or larger devices can be created in order to have the most

appropriate size. Devices can also be stacked together or full devices held in series to cover larger areas.

One of the leading producers of thermoelectric modules is MicroPelt®. The fabrication of these devices generally involves creating an array of n-type semiconductors on a single substrate then creating a corresponding array of p-type on a second substrate. The single substrates are then sandwiched together to create the important n-p pairings and a working device.

1.3.9 Thermoelectrics in solar cells

Until recent years solar cells were produced for one energy conversion process alone – the conversion from light to electricity.

It is possible to insert functional thermoelectric layers underneath the photovoltaic panels⁴⁹ designed to harvest heat and thus generate power from both the solar panel and the thermoelectric layer, and therefore produce a higher output than either device would have been capable of individually⁵⁰. Most of the heat energy arises from sunlight heating the panel through infrared radiation. However there is also a contribution from by the photovoltaic process as a degree of thermal energy is released upon charge recombination.

Another method employed by Chen *et al.*⁵¹ was to include Bi₂Te₃ directly into the photoanode by incorporating nanoparticles with TiO₂. This benefitted the device in two ways: the nanoparticles of bismuth telluride led to enhanced electron mobility due to the thermoelectric effect and the efficiency of the TiO₂ anode was increased by acting as a charge transfer catalyst which increases the overall efficiency.

1.4 Titanium dioxide

Titanium(IV) dioxide, the most common oxide of titanium, is an extremely diverse and useful compound with numerous applications. The compound plays a significant role in many scientific fields as well as being a huge commercial resource. Titanium dioxide is to be found on a daily basis in many different formats, its brilliant white and high opaqueness lend it to being an ideal pigment.

1.4.1 *Current uses*

Titanium dioxide has many exciting properties that allow it to be exploited in numerous areas. Perhaps the most common use of TiO₂ is as a pigment. Since its first commercial production in 1918⁵², TiO₂ has risen to dominate the white pigment industry, accounting for over 70% of the market. The compound has a brilliant whiteness and an unrivalled refractive index. The refractive index of the rutile structure is 3.87, with anatase having the slightly lower value of 2.5-3.0⁵³. These values are high, exceeding that of diamond. These high values give the compound a high opacity; very thin layers appear brilliantly white and allow very little light to be transmitted. These properties combined with the material's relative chemical and biological inertness have led not only to TiO₂ almost entirely replacing the dangerous lead based pigments which were commonly used until the 1960s, but to the compound also being commonly found in food products and cosmetics. Registered with the European Union as safe for human consumption, and classed as colouring agent E171, this additive can be found in many consumables. Most TiO₂ will pass through the body intact, although certain areas in the body do appear to retain small quantities. Titanium dioxide can also be found in almost every sunscreen available. The ability to absorb the harmful UV radiation makes the compound ideally suited to this task. There are also potential biomedical applications: encouraging results have been obtained in the destruction of cancerous cells⁵³ and in using TiO₂ as a dental or bone implant⁵⁴.

The scientific community has a high interest in TiO₂. Some of the reasons are briefly mentioned above - the refractive index, ability to absorb UV light and chemical inertness. In recent years the research into this chemical in its various forms has risen almost exponentially. In 1995 alone around 700 papers were published concerning TiO₂. This has risen each year subsequently and had almost tripled by 2003 to 2,000 papers⁵⁵. The number of papers published demonstrates the ever growing scientific fascination of the compound and the quest for innovation as new commercial avenues exploit its unique properties. Titanium dioxide is a semiconducting material with a relatively large band gap. The band gap of the material corresponds to wavelengths found in natural sunlight, albeit in the UV region.

In 1972 a sceptical scientific community was introduced to the water-splitting ability of semiconducting TiO₂. Fujishima and Honda shattered the common perception that water splitting could not be achieved by light with their report in *Nature*⁵⁶. Since this technology

was discovered, it has been further investigated, and now the photosplitting of water is well established and has attracted much attention as a potential source of hydrogen fuel ⁵⁷⁻⁶¹.

Much attention has been focused on the photocatalytic properties of TiO₂, or perhaps more correctly the “semiconductor-assisted photoreaction properties”, as the term photocatalyst is misused in many circumstances ⁵³. One of the most active areas of interest is the photodegradation of organic molecules and pollutants within water supplies or in gaseous form. Titanium dioxide has proven capable of photodegrading over 200 different molecules ⁶². When exposed to an organic pollutant in an atmosphere containing oxygen and exposed to a wavelength of light greater than the band gap, TiO₂ can destroy the harmful material. Titanium dioxide is capable of breaking down the harmful pollutant into non-toxic compounds. This is achieved when electrons which have been promoted to the conduction band leave holes in the valence band which form radicals with surrounding water or oxygen. These OH and O₂ are capable of destroying contaminants ⁶³. This is the basis of the self cleaning properties of certain TiO₂ coated products. For a compound to be capable of this kind of reaction certain requirements must be met ⁵³:

- Photoactive
- Capable of utilizing visible or near UV wavelengths of light
- Biologically and chemically inert
- Photostable (i.e. not liable to photoanodic corrosion)
- Inexpensive

Titanium dioxide meets these requirements and is indeed one of the best compounds capable of doing so.

Another area based on the photochemical abilities of TiO₂ is that of solar cells. Again this technique has a high importance due to its application in the renewable energy field. Titanium dioxide has proved a promising material to be included in solar cells ⁶⁴.

Lou *et al.* ⁶⁴, in a comprehensive review of hollow nanostructures highlight the use of TiO₂ as an anode material in high powered lithium batteries. Titanium dioxide has exceptionally fast lithium insertion-extraction kinetics. These properties, as with the ones mentioned above, depend heavily on the shape of the particles. In this case, hollow spheres appear to be best tailored to these reactions as they can cause multiple internal reflections of light.

1.4.2 Structure

The above properties depend heavily on several controllable aspects of TiO₂ as a material. Parameters that control properties include: phase of crystal, morphology of particle, nanostructure and purity of the sample (or, doping level).

1.4.3 Crystalline structure

Titanium dioxide is a versatile material capable of existing in different crystalline phases. Multiple crystal structures have been identified⁶⁵ with 3 phases being identified as being stable at standard atmospheric and temperature conditions. These are the only phases to be found in nature⁶⁶: rutile, anatase and brookite. The most thermodynamically stable is rutile, with the two other phases being meta-stable and convert to rutile upon heating at temperatures >700 °C⁶⁷. Rutile and anatase are the most commercially useful phases of TiO₂. The structures of these phases are shown in Figure 1-10.

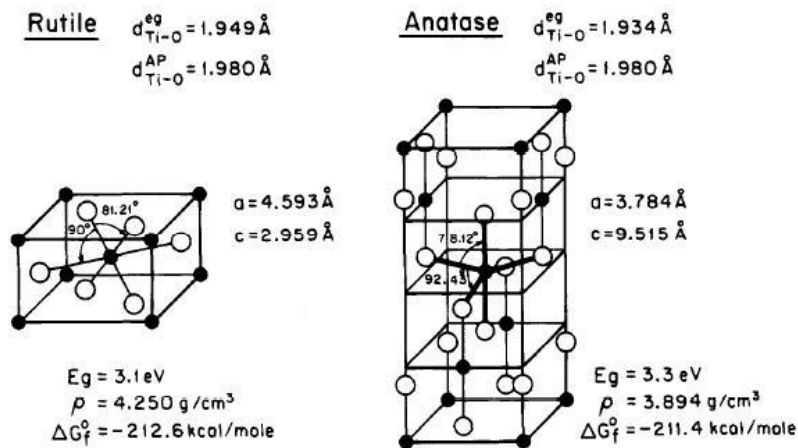


Figure 1-10: Crystal structure of rutile and anatase⁶⁸

Rutile has the space group number 136: P_{42}/mnm ⁶⁹. The structure is described in terms of each titanium atom being surrounded by a slightly distorted octahedron of oxygen atoms with titanium atoms forming the points of an almost equilateral triangle around each oxygen atom. The structure has a coordination of 6:3³⁷. Commonly the structure is described as a distorted hexagonal array of anionic oxygen with half of the octahedral holes occupied by titanium⁷⁰. The distortion of these structures can be understood as the octahedral holes lie in a line parallel to the *c* axis of the lattice. When occupied by highly charged ions such as titanium(IV), there is a repulsive force between the ions destabilising the structure. The structure of rutile is not uncommon for metal dioxides and difluorides.

Manganese dioxide, SnO₂ and PbO₂ are but a few of the compounds which display the rutile structure⁷¹. Occasionally the antirutile structure is also observed in some materials, where the metal and non-metal have exchanged positions relative to the normal rutile structure⁷²⁻⁷⁴.

The structure and valency of the elements cause TiO₂ to be an intrinsic semiconductor with a band gap of around 3.2 eV for rutile and around 3.0 eV for anatase³⁷. This corresponds to a wavelength of 387 nm, in the near UV region for rutile and 413 nm for anatase. When light of correct energy is incident on the surface of the material electrons can be promoted into the empty conduction band which allows for conduction within the valance band⁵⁵.

1.4.4 Structural characterisation

Over recent years there has been a development in the number of particle morphologies which can be formed from TiO₂, with particular focus on nanostructures. For example, wires, belts, sheets and rods have all been created on the nanoscale⁷⁵⁻⁸⁰. Each structure shows different characteristic properties. High surface area is extremely desirable in many reactions and catalytic processes and producing nanostructures is an effective way to accomplish this⁵⁵. When the scale is small enough that the particles can effectively be described as one-dimensional (below 50 nm), quantum confinement effects further influence the properties. It has been shown that if crystals can be reduced to the nanoscale, quantum effects can alter the wavelength necessary for electrons to be promoted using the optical band gap^{75, 81-83}. Potential uses for some of these structures include gas sensors⁷⁸, electrochemical detection and as photocatalysts.

This thesis concentrates on the synthesis of spherical particles. One advantage to spherical particles is the potential for multiple internal reflections of photons. Especially noted with hollow spheres, light can be reflected internally leading to an increase in the absorption of appropriate wavelengths.

1.4.5 Doping of structure

The properties mentioned above are dependent on the material absorbing light which is greater than or equal to the band gap of the material. Although with the pure form, this can be achieved by direct sunlight, the majority of the energy is of a form too low to be of use.

Only around 4% of the light from the sun is capable of inducing semiconductor activity in TiO_2 . The radiative energy of the sun can be represented to a good approximation as the energy given off by a black body. At the temperature of the sun, the maximum output wavelengths correspond to the visible spectrum. Plotting this as a cumulative function it can be seen that a red shift in the energy band gap would produce an exponential increase in the percentage of sunlight capable of inducing activity. Therefore, modification of the band gap is required to increase efficiency. As with other commonplace semiconductors doping is a viable means to increase activity.

Many potential dopants have been investigated. Initially research focused on doping with other transition metals such as iron⁸⁴. Research continues in these areas but to a lesser extent as current methods concentrate on incorporating non metals in place of oxygen. Doping the structure with carbon⁸⁵ and sulfur⁸⁶ have had some success in reducing the band gap. This thesis will concentrate solely on nitrogen doping. Nitrogen is perhaps the most useful element to incorporate into the structure.

By doping with nitrogen, it is anticipated that the material would retain many of its properties which allow TiO_2 to be as versatile as it is. The presence of nitrogen allows the compound to remain inert and safe for use in everyday environments. Small quantities of nitrogen can allow the 2p orbitals of both the oxygen and the nitrogen to combine which lowers the band gap. It has been shown that $\text{TiO}_{2-x}\text{N}_x$ exhibits a photoactivity not associated with pure TiO_2 and that this activity can only be as a result of nitrogen being present within the structure⁸⁵.

1.5 Titanium nitride

Recent years have seen the desire for new non-oxide compounds. Titanium nitride has demanded some the greatest interest from the nitrides of transition metals. This compound has many interesting properties. Titanium nitride can be described as displaying advantageous qualities of both its inherent covalency, combined with properties more commonly seen in metals. Titanium nitride has a high conduction, comparable to that of metals⁸⁷, but with increased stability and a lower reactivity⁸⁸. The compound also has a high melting point, 2950 °C^{87,89}, extreme hardness, $\approx 2000 \text{ kg mm}^{-2}$ and a resistivity reported as $20 \mu\Omega \text{ cm}^{90}$.

1.5.1 Current uses

Titanium nitride has been useful commercially for many years. Properties such as extreme hardness and gold colouring make it extremely desirable to create attractive wear-resistant coatings on various implements such as drill bits and knives. Great investment has gone in to developing ways to deposit thin coatings of TiN on various surfaces to extend their durability.

Potential applications in the electronic industry have recently been investigated. Due to TiN's ability to withstand extreme conditions such as heat and pressure, it has the potential to be used in electronics which must withstand extreme environments. There have been positive reports of photovoltaic effects observed in TiN/Si junctions where the material proved "ultra-fast" with a "high sensitivity". Wu *et al.*⁹¹ evaluated the compound's potential for use within lithium batteries. It was discovered that the inclusion of this material could enhance battery efficiency. In the current climate of miniaturisation, Wu *et al.* also reported that TiN could be used to reduce the potentially destructive volume changes which are associated with silicon on the nanoscale. Properties specific to the nanoscale have also been recorded such as improved sintering and catalytic effects.

1.5.2 Structure

The structure of TiN is superficially simpler than the rutile TiO₂. The crystal structure is described by the space group number 225, *Fm3-m*, the face centred cubic structure of common salt. The structure forces the nitrogen to adopt an octahedral environment which is unusual to find in first row elements. The structure also suggests a Coulombic interaction between atoms as this is a structure more commonly seen in ionic materials. Although the material is conducting, this property cannot be attributed to metal-metal bonds as the conductivity is effected by the stoichiometric ratio of Ti and N⁸⁸.

1.6 Aims

The research presented in this thesis investigates the growth of nanostructured materials with potential renewable energy applications. The aim of the work was to produce new low dimensional and reproducible morphologies of crystal through new or improved synthesis processes using minimal steps and precursors. It has been established that the morphologies of materials can lead to different functionality and that new simple synthesis

routes directed to low dimensional growth are required. In particular the work explores the growth of low dimensional Bi_2Te_3 and TiO_2 .

Bismuth telluride is one of the best performing thermoelectric materials but there is room for improvement. This work concentrates on CVD using elemental precursors on a range of surfaces. The work targets the growth of material using closed spaced CVD with structures being characterised by SEM imaging, EDX analysis and powder XRD. The work looks at producing nanostructured materials without the need for MOCVD which requires expensive and volatile precursors yet is the method currently favoured in the literature.

The TiO_2 work attempts to give rise to a reproducible production and characterisation of nanostructured single phase TiO_2 using a microwave hydrothermal process. Additionally the work attempts to give rise to the pseudomorphic doping and conversion of TiO_2 to nitride and oxynitride structures.

2 Experimental

This chapter sets out the experimental procedures used during this project and the techniques employed to characterise the reaction products.

The primary technique used for the telluride synthesis in this work was chemical vapour deposition (CVD) using elemental reagents. The reagents were sealed under vacuum and reacted at elevated temperatures and the resulting growth analysed. This has proven to be a powerful technique in chalcogenide growth and has created many interesting low dimensional morphologies. This method is advantageous as it can be readily scaled for commercial processes; indeed many semiconductor manufacturers use CVD as their primary growth technique.

Also reported in this work are oxide structures synthesised through microwave hydrothermal reactions. These reactions can lead to rapid reaction times of the order of seconds compared to conventional hydrothermal processes which take hours to complete. This leads to a reduction in the energy cost in synthesising products. As will be discussed later, the rapid microwave synthesis is also able to unlock morphologies and phases not normally accessible through conventional heating.

The final chapter in this work looks at the ammonolysis of oxide structures for conversion and doping of TiO_2 . This was carried out at elevated temperatures under a flow of ammonia in an oxygen free environment.

The products resulting from the procedures mentioned above were subject to a number of characterisation techniques. Particle morphology was analysed by electron microscopy with further information obtained from complementary techniques such as energy dispersive X-ray (EDX) spectroscopy and electron energy loss spectroscopy (EELS). All samples were examined by powder X-ray diffraction (XRD) to determine the crystalline phases present. Where appropriate, samples were additionally analysed with UV/ Visible and Raman spectroscopies.

This chapter details the experimental and characterisation techniques which were applied over the course of the research.

2.1 Synthesis techniques

2.1.1 Chemical vapour deposition

2.1.1.1 Ampoule preparation

Chemical vapor deposition (CVD) reactions were carried out in sealed quartz ampoules. Substrates were used as surfaces for growth. The schematic below shows a quartz vessel sealed under vacuum with powdered reagents at one end and a substrate (held in place by a narrowing of the vessel walls to create a neck) several centimetres away. The usual length of a sealed ampoule was 20-30 cm.

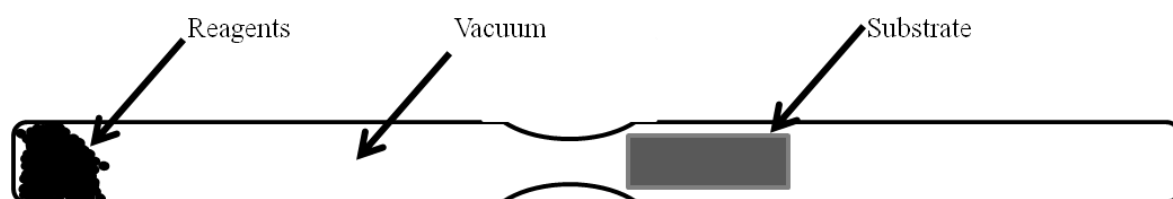


Figure 2-1: Schematic of a sealed ampoule

The quartz was acquired in 2 m lengths with a outer diameter of 12 mm and a wall thickness of 1 mm. Tubes were split sealing at one end to create the required length (10-60 cm).

If a substrate was to be used, a 'neck' was created to separate the substrate from the powdered reagents. This was achieved by heating the tube with an oxygen/natural gas flame and pulling gently along the length of the tube to collapse the quartz partially inwards.

The required reagents were added to the ampoule before sealing by means of a long necked filter funnel. This was used to avoid any reagent coming into contact with the walls of the vessel. If powdered reagent coats the walls of the quartz this can cause problems on sealing as the reagents will be heated and can adhere to the wall of the vessel, potentially causing fractures in the glass.

Ensuring that the ampoule containing elemental powder stays in a vertical position with one end sealed, a substrate was then introduced. The relevant substrate was dropped into the reaction vessel and is secured 5-20 cm away from the powdered reagents by the 'neck'.

The ampoule was then connected to a rotary vacuum pump (Edwards Pump BC: 2212 oil pump); an electronic pressure monitor to indicate the vacuum reached; a glass trap to collect any debris and to prevent pump oil entering the reaction ampoule, and a length of rubber tubing (Figure 2-2). The end of the rubber tubing was connected to a short length of the same diameter quartz tube (12 mm). The ampoule to be sealed was then connected to the glass tube attached to the pump through the use of a Swagelok fitting, thus allowing the reaction vessel to be evacuated.

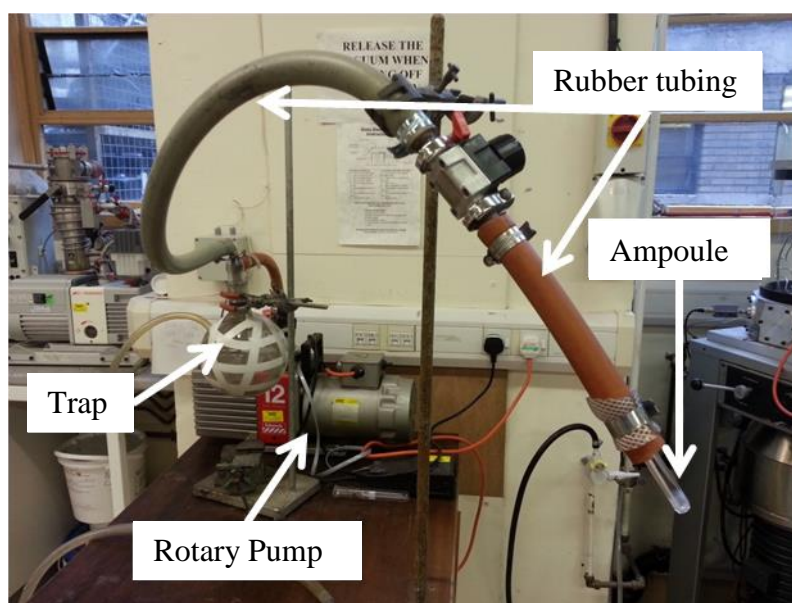


Figure 2-2: Ampoule sealing apparatus

Once attached to the pump system the ampoule atmosphere was evacuated. The tube was left for over 10 minutes or until the pressure registered below 3×10^{-3} mbar. When this level was reached, the tube was heated using an oxygen/natural gas flame to form a heated band 5-10 cm below the Swagelok fitting. When the quartz glowed white three equally spaced dimples were created around the diameter, taking advantage of the internal vacuum and collapsing the tube. The uniform heating was resumed and the ampoule detached. This created a sealed vacuum for CVD (Figure2-3).

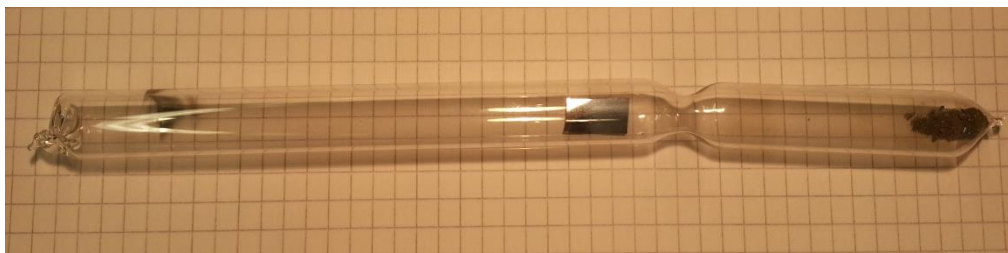


Figure 2-3: Sealed ampoule

One by-product of preparing reaction tubes in this manner was a band of metal deposited in a ring 2 cm below the sealing point (Figure 2-4). The ring was present in all reactions using powdered reagents. This did not seem to play any significant role in any subsequent reaction and was simply due to small metal particles within the tube depositing on the vessel after exposure to the blowtorch.

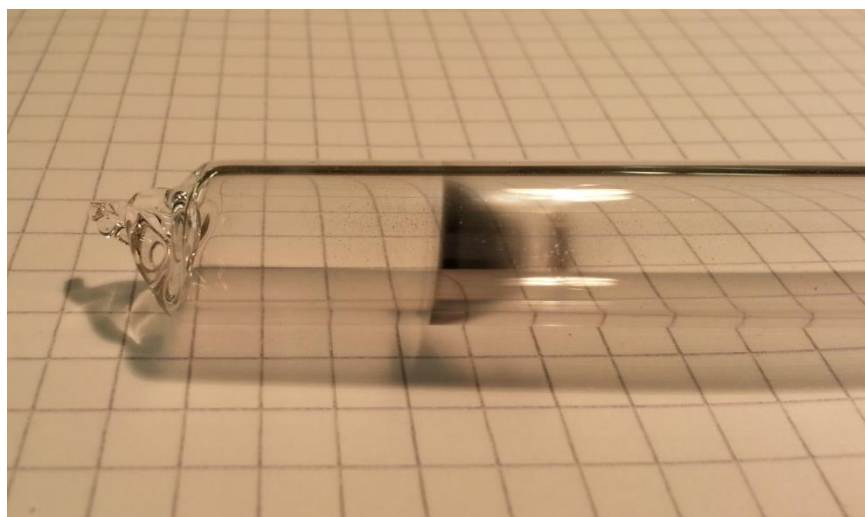


Figure 2-4: Silver coloured deposition caused by flame heating the tube

2.1.1.2 Substrate

Elemental silicon, gallium arsenide and alumina were purchased as 3 inch diameter wafers that were cleaved before use. Substrates were not handled directly to avoid contamination of the surface; 1 cm x 2 cm substrates were used.

2.1.1.2.1 Oxidised silicon substrates

Oxidised substrates are silicon wafers which retain their native oxide layer. These substrates were prepared with a non-etching process. Wafers were cleaved into segments \leq 1 cm wide due to the 10 mm diameter of the quartz tube being a limiting factor. The length of ampoule was dependent on reaction methodology.

Cleaved wafer pieces were submerged in 20 mL of deionised water and sonicated for 90 s. Following the first sonication the deionised water was mostly, but not entirely, drained and 20 mL of acetone added. The reason for the small quantity of water being allowed to remain is to allow the substrate to remain wet throughout the cleaning process and to avoid drying marks which can appear due to solvent evaporation. This partial emptying of the beaker containing the acetone and water was then repeated, with liquid being decanted off and replenished with acetone to ensure water removal.

Following the addition of the acetone, the substrate is sonicated for a further 90 s and the acetone drained off and replenished with iso-propanol - a solvent less likely to leave drying marks on the surface of the wafer. This draining process was carried out twice to ensure no acetone remains.

When the substrate was immersed in the 20 mL of iso-propanol, the third and final sonication was begun (again running for 90 seconds). When complete, the substrate was removed from the beaker with carbon-tipped or plastic tweezers (metal has the potential to scratch the surface). A stream of nitrogen gas was used to dry the substrate. This rapid and thorough drying is used to make sure all solvent has been removed from the surface before experimental usage or further cleaning is carried out.

2.1.1.2.2 Oxide free silicon substrate

The native oxide on silicon wafers can be removed to allow surface structures to form a better contact with the underlying material. This also forms a more reactive surface for growth.

In order to remove the oxide layer from the silicon, hydrofluoric acid was used. Great care was taken since HF is such a reactive compound. In preparation for acid etching of the surface layer, the aforementioned cleaning procedure was followed to remove surface debris and prepare the surface to be etched.

The clean substrate was then taken to an HF suitable working area and all full personal protection equipment worn, including double gloving and a plastic apron.

The HF solution was a standard premixed buffered solution with hydrofluoric acid (49%) and ammonium fluoride (40%) in a 1:10 ratio. At this concentration, etching occurs at > 1 nm per second at room temperature.

The HF solution was added to an HF-ware plastic beaker, using the minimal volume (less than 15 mL). The clean substrate was added to this solution with fluoroware tweezers. The solution was continually swirled gently to facilitate the homogeneous etching of the surface. Following 30 s of exposure, the substrate was removed from the acid etch and immersed in 500 mL of deionised water.

Care was taken to dispose of all acid solution in a correct and safe manner. To guarantee no exposure or cross contamination, the beaker of deionised water was flushed with deionised water several times.

The substrate was then removed from the deionised water and dried under a flow of nitrogen gas. To prevent regrowth of the oxide layer on the surface of the silicon wafer, pieces were transported in a portable nitrogen box to the site of next reaction.

2.1.2 Heating profiles

2.1.2.1 Complex temperature profile

The research group at the University of Glasgow have an established history in the investigation of the growth of low dimensional materials. This section of the thesis sets out the standard procedures used for low dimensional growth through CVD. Reactions used elemental reagents in sealed ampoules and were then placed in a box furnace with a pre-programmed variable temperature profile.

These reactions were carried out in a Vecstar box furnace or a Vecstar four tube furnace. These were fitted with temperature controllers that allowed for the programming of ramping, dwelling and cycling options. Initial reactions used 5 dwell steps.

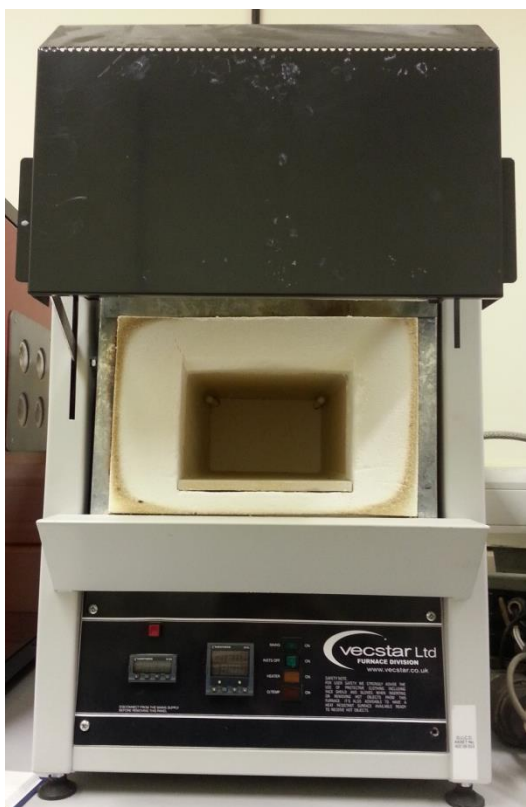


Figure 2-5: Vecstar box furnace

Ampoules were placed in the furnace at room temperature and then the temperature set to ramp up to 450 °C at a rate of 250 °C per hour. When the desired temperature was reached the furnace was held there for 12 h before being left to cool (slowly and effected by turning heating elements off) to a temperature of 250 °C, and here was held for a period of 2 hours. This process of heating to 450 °C then cooling naturally was repeated three times. The temperature profile is shown below:

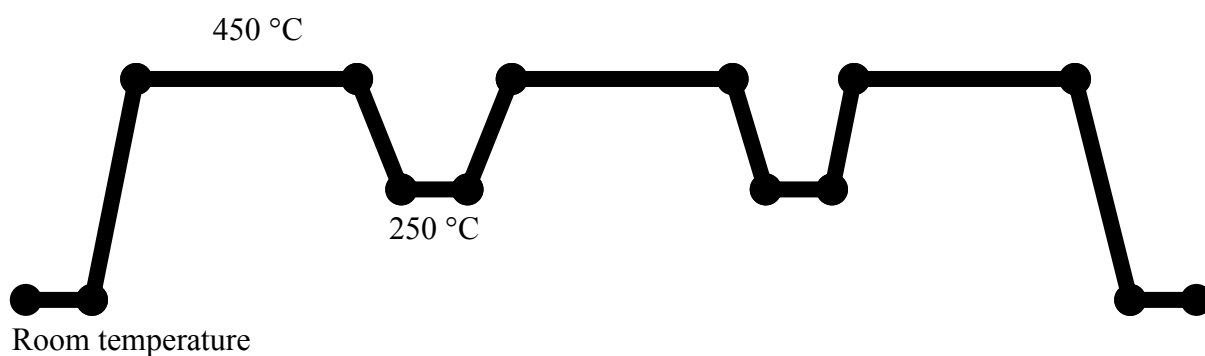


Figure 2-6: Complex temperature profile

The premise of these reactions was to allow waves of deposition to form. Having chemical vapour settle on the surface of the wafer during the cooler phases allowed further seeded growth to form later in the reactions.

2.1.2.2 *Constant temperature*

Constant temperature reactions were once again carried out in quartz ampoules sealed under vacuum. These were then placed in a box furnace either horizontally or vertically. One of two furnaces was used for these reactions: the programmable Vecstar (Figure 2-5), or a Carbolite furnace (Figure 2-7).



Figure 2-7: Carbolite box furnace

The furnace was programmed to heat at 250 °C per hour and to reach a temperature of 450, 750 or 1200 °C as appropriate. Cooling to room temperature was carried out by switching off the heating elements and allowing the furnace to cool over 6-8 h with the door of the furnace closed.

The reactions were held in the centre of the furnace on a notched heat brick. A standard temperature profile is shown below.

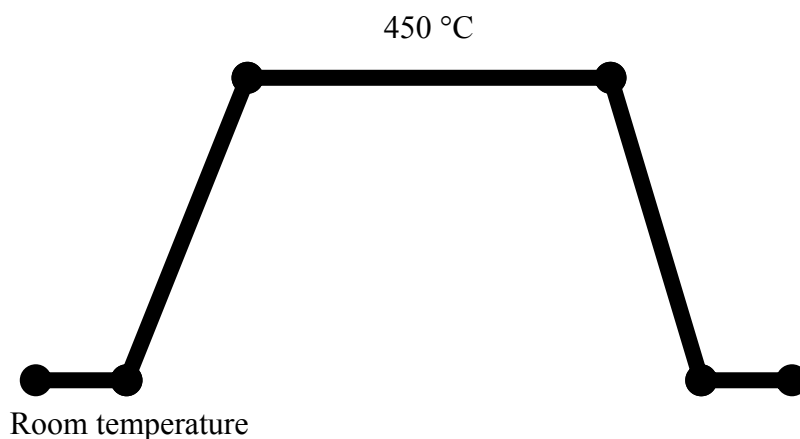


Figure 2-8: Constant temperature profile

2.1.2.3 *Temperature difference reactions*

Temperature difference reactions were carried out in a Carbolite horizontal three-zone tube furnace. The furnace was equipped with three heater regions and as such was capable of producing distinct regions of different temperature over the metre length of furnace.



Figure 2-9: Three zone Carbolite tube furnace

The central zone (in which the reactant end of a sealed evacuated quartz ampoule was always placed) was controlled by the main thermostat and the regions on either side could be set above, below or to match this central temperature.

2.1.3 Microwave hydrothermal synthesis

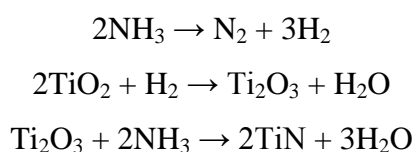
The application of temperature and pressure to aqueous solutions to perform synthesis, otherwise known as ‘hydrothermal synthesis’, has been a well-established technique for a wide range of reactions since the mid-1800s⁹². Conventionally the reaction is performed in a steel autoclave, which is heated in an oven for the required length of time. This reaction methodology is still widely used today but in more recent times a subset of these reactions, microwave hydrothermal synthesis, has been developed. Using autoclaves made of plastic and heated under microwave radiation this process has the advantage of being extremely fast. Microwave heating is based on electromagnetic radiation interacting with the dipoles of the molecules opposed to simple conduction of thermal energy⁹³. The sample can be heated from the centre to reach high temperatures rapidly. Reaction time can be reduced from several hours to a matter of minutes.

Microwave hydrothermal synthesis could be an extremely advantageous technique for the production of nanoscale materials: these reactions can be performed at relatively low temperatures and have a very short time scale which is often important in the formation of nanomaterials. Excessive heat or long reaction times can lead to severe agglomeration of particles⁹³. Microwave hydrothermal reactions have produced many forms of 1D materials such as rods, wires and tubes.

2.1.4 Ammonolysis

The oxide particles produced in this work (Chapter 5) were subsequently investigated to examine a possible route to pseudomorphic conversion into nitrides and oxy-nitrides following ammonolysis.

For complete conversion to nitride, the starting material for these reactions was the TiO₂ produced by the microwave hydrothermal process described in Chapter 5. The pathway for the reaction is as follows:



When a doped structures were desired, the same experimental process was used but at the lower temperature of 450 °C.

In both cases the flow of ammonia was maintained until the furnace had cooled to room temperature.

2.2 Characterisation techniques

2.2.1 Crystallography

Crystallography is an important area in many scientific disciplines. Many characterisation techniques applied to crystalline materials are based on the long range order of their structures. Each position in the lattice can be described by its own lattice point given by the position vector:

$$\mathbf{r}_{123} = n_1\mathbf{a} + n_2\mathbf{b} + n_3\mathbf{c} \quad (2-1)$$

In Equation 2-1 n represents an integer, and a , b and c represent the translational symmetry axes. When we come to consider the three dimensional symmetries of the crystal we define repeating units as unit cells. The bulk material is comprised of unit cells translated symmetrically along the a , b and c axes. There are only 14 ways of arranging equivalent lattice points in 3D space and these are called the Bravais lattices. These lattices are sub divided into seven crystal systems: cubic, tetragonal, trigonal, orthorhombic, hexagonal, monoclinic and triclinic as shown in Figure 2-10.

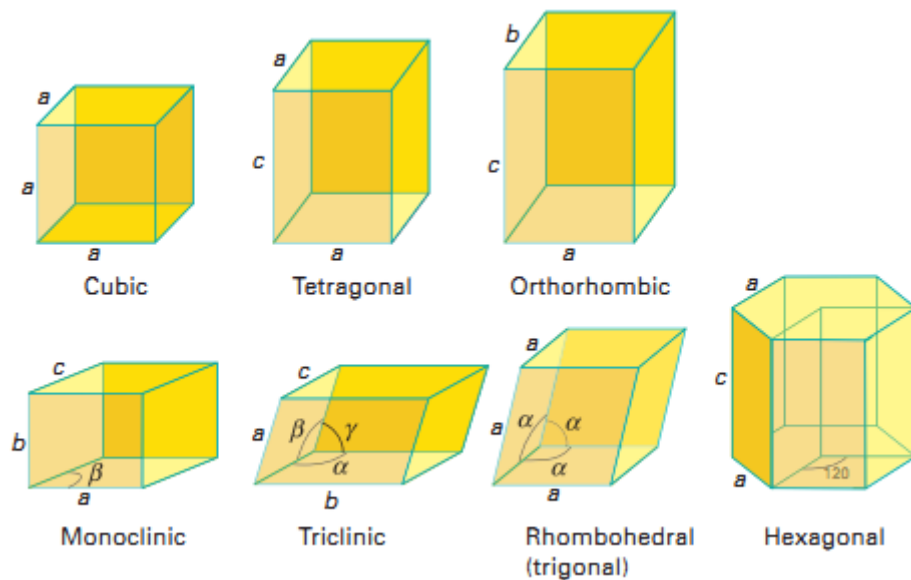


Figure 2-10: Schematic of the seven crystal systems

The seven crystal systems are shown above in Figure 2-10. The crystal systems can be further described in terms of the 14 Bravais lattice system which takes into account the lattice points within a crystal system. Bravais lattices can be translated by applying many symmetry operations such as reflection, rotation and screw axes. There are 32 possible symmetry operations and these are called the point groups. When these point groups are taken in conjunction with the 14 Bravais lattices, the result is 230 possible space groups. The space groups therefore contain information not only on the lattice type but the symmetry operations which can be performed on it.

2.2.1.1 Crystal planes

Instead of considering the Bravais lattices as a series of connected points they can be viewed as a series of intersecting two dimensional planes. These planes are particularly important when considering the anisotropic nature of crystals as many properties such as conductivity can be directionally dependent. Planes in a crystal can be defined using Miller index notation. Miller indices define planes in the notation (hkl) where the Miller index is a plane orthogonal to h , k and l .

To identify the Miller index of a plane in a three dimensional crystal (which has Cartesian axes x , y , z) the planes coordinates of intercept with the axes are recorded. If these are set to a hypothetical $(\frac{1}{2}, \frac{1}{2}, \frac{1}{2})$ then the Miller index is defined as:

$$(hkl) = \left(\frac{1}{1/2} \frac{1}{1/2} \frac{1}{1/2} \right) \quad (2-2)$$

$$(hkl) = (2 \ 2 \ 2)$$

The plane (2 2 2) can be represented by the diagram below:

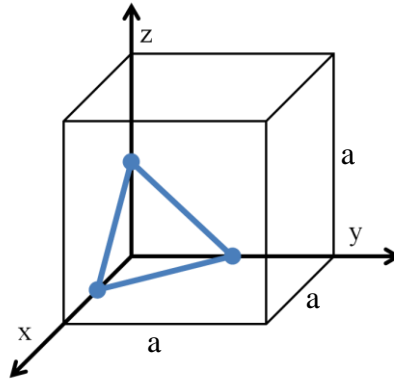


Figure2-11: Cubic cell with length “a” showing a (2 2 2) Miller index plane due to intercepts occurring at $\frac{1}{2}a$ on each axis

The interplanar spacing is given by d_{hkl} .

2.2.1.2 Bragg diffraction

One of the most powerful characterisation techniques in crystallography is in the use of diffraction from crystal planes. The basis of diffraction techniques is Bragg’s law. Starting with the crystal planes shown below in Figure 2-12 and with monochromatic radiation incident on these planes Bragg’s law can be defined.

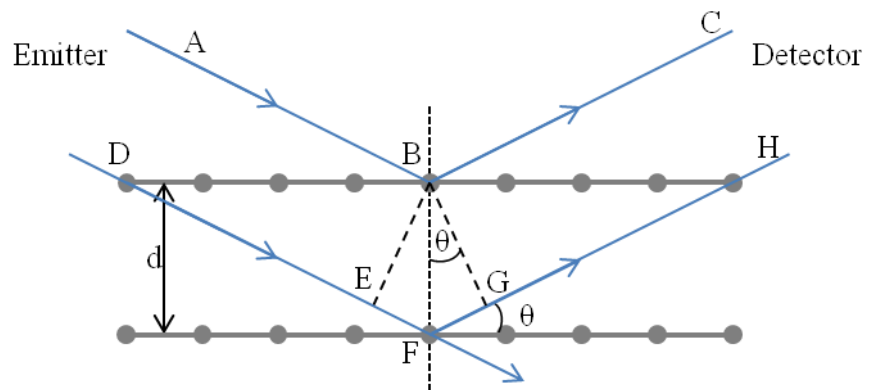


Figure 2-12: Bragg diffraction

If monochromatic radiation in Figure 2-12 follows path A it is diffracted at point B then follows the path C. A second beam follows path D to E, interacts at F before emerging to follow the path from F to G, and finally H. It can be seen that the second beam follows the additional distance EF and FG in comparison to the first.

Defining the marked angles as θ we can then define the following:

$$EF = FG = d_{hkl} \sin \theta \quad (2-3)$$

Therefore the total path difference between beam following ABC and the second beam following the path DEFGH can be given as:

$$\text{path difference} = EF + FG = 2d_{hkl} \sin \theta \quad (2-4)$$

For the monochromatic light travelling in phase then this additional distance must be an integer number (n) of X-ray wavelengths (λ). This is represented by Bragg's Law:

$$n\lambda = 2d_{hkl} \sin \theta \quad (2-5)$$

2.2.2 XRD

For this study powder X-ray diffraction was used. In this technique X-rays are diffracted off numerous crystals held in a random orientation. By measuring the beams diffracted following Bragg's law, crystal structural information can be deduced.

For X-ray diffraction, the most common X-ray source used is copper. In the diffractometers used for this thesis high energy electrons bombard copper metal causing Bremsstrahlung X-rays as well as, in the case of copper, three characteristic wavelength peaks. The three distinctive X-ray peaks produced by copper are the $K_{\alpha 1}$, $K_{\alpha 2}$ and K_{β} wavelengths. These wavelengths are produced when an electron is ejected from the K shell and a higher energy electron from the M or L shell fills the vacancy.

In the case of $K_{\alpha 1}$ and $K_{\alpha 2}$ the electron filling the vacancy originates from the L shell. Which K_{α} peak is produced is dependent on the spin orbit interaction energy. The $K_{\alpha 1}$ is

the one most frequently used for powder X-ray analysis. The K_{β} emission arises from an electron in the M shell falling to replace the vacancy in the K shell.

The radiation used in diffractometry must be monochromatic and therefore a monochromator is used. For copper, a nickel filter is used. For this investigation a PanAlytical Xpert instrument was used with a copper $K_{\alpha 1}$, ($\lambda = 1.54056 \text{ \AA}$) X-ray source.

Samples to be analysed were held on a glass plate or an aluminium holder which was placed at the centre of the diffractometer. The X-ray source and the detector were then rotated around the sample to investigate various angles. Intensity peaks were produced when the Bragg condition was fulfilled. The angles investigated in this experiment ran from 5-85 2θ (deg.). XRD patterns obtained were then matched to standard patterns.

2.2.3 Electron interactions with matter

As electron microscopy formed a large part of this investigation, an understanding of the basic interactions that electrons have with matter is essential for understanding the results from this technique. Figure 2-13 shows the basic interactions.

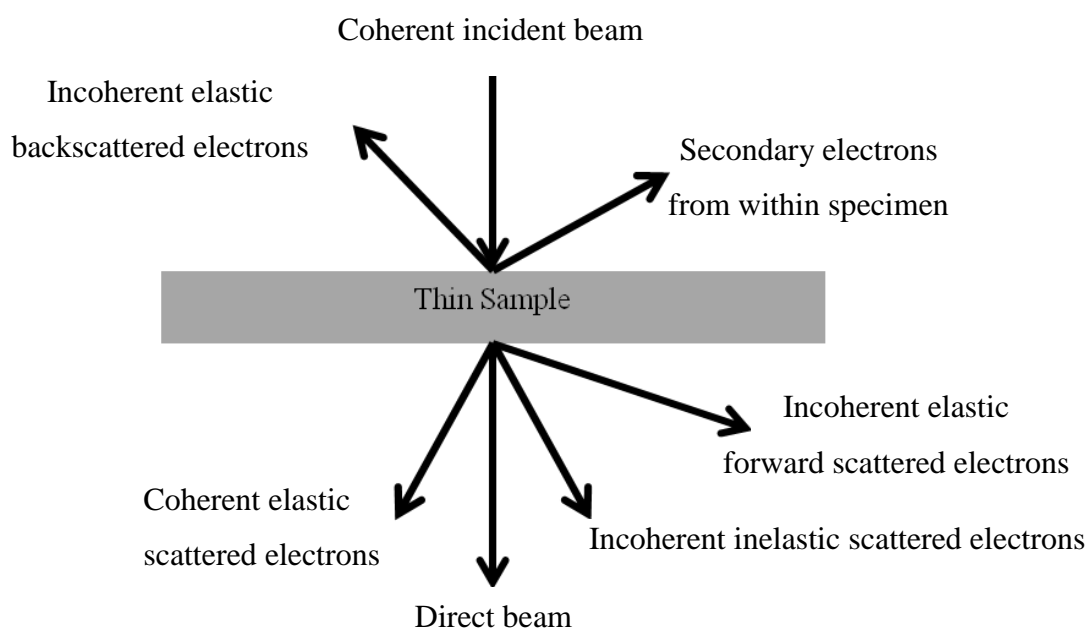


Figure 2-13: Electron interactions with matter

Primary interactions can either be an effect of electrons scattering from the surface or from transmittance through the sample.

Elastic interactions are those where the energy transfer from incident electron to the sample can be considered to be zero and therefore the incident electron emerges with the same energy as before the interaction. The simplest of the elastic interactions is that of the direct beam. The direct beam which passes through the sample is composed of electrons which are undeflected from their initial trajectory and have no discernible energy loss.

Incoherent elastic electrons are the result of Coulombic interactions. The negatively charged electrons can penetrate into the electron cloud of the sample's atoms. Once within the atom the electron is attracted to the positive nucleus. The Coulomb force is described by the following relation:

$$F = \frac{Q_1 Q_2}{4\pi\epsilon_0 r^2} \quad (2-6)$$

Equation 2-4 shows Coulomb's law where F is the resultant force, Q_1 and Q_2 the charges of the particles, ϵ_0 the dielectric constant, and r the distance between the charges. The opposite charges result in a deflection from the original trajectory that scatters the electron. As Coulomb's law is strongly dependent on the distance between charges the closer the proximity to the nucleus that the electron reaches the further it will be scattered. If the electron is scattered at an angle less than 90° and the electron is transmitted through the sample in the direction of the beam the electron is said to be incoherent elastic forward scattered. It is possible when the electron is in close proximity the nucleus it can be scattered at an angle greater than 90° and, such electrons are known as incoherent elastic backscattered electrons.

When a sample has a crystalline structure it is possible for Bragg diffraction to occur from crystal planes. The atoms of the crystal planes form regular scattering centres. These are called coherent electric scattered electrons and can be used for crystal structure determination.

The second type of interaction for the incident electrons are inelastic interactions. In this case, the electrons targeted at the sample emerge with less energy than originally incident. This can be due to many factors such as energy transfer to the sample or in the emission of braking radiation. Some examples of inelastic interactions are mentioned below. These

electrons play a very important part in electron microscopy as their interactions are the basis of complementary techniques such as EDX and EELS.

As mentioned above, an electron entering the electron cloud of an atom becomes strongly influenced according to Coulomb's law. It is possible that when an electron enters the atom the Coulombic force will cause the electron to slow, and as the electron loses kinetic energy that energy is released in the form of X-rays. The emitted radiation is known as "braking radiation".

A second route for loss of energy is the ionisation of inner shell electrons. In this scenario the incident electron is able to eject an inner shell electron. Assuming enough energy is transferred, there is potential for ionisation of the atom if the electron is ejected to the continuum. Again this process is described in the production of the distinctive K_{α} X-rays used in XRD. This process is the basis for EDX analysis described below.

A third example of an inelastic interaction is the ejection of slow secondary electrons. In this process the electrons in the conduction or valence band (which require less energy to ionise) are ejected. This process is particularly important for scanning electron microscopy (SEM) where secondary electrons are detected and used to form the images.

2.2.4 *Scanning electron microscopy*

Scanning electron microscopy (SEM) is primarily an imaging tool. It is analogous to an optical microscope with electrons instead of photons and electromagnetic lenses opposed to a physically refracting lens. SEM is capable of imaging over huge ranges, up to six orders of magnitude. The technique uses a highly focused beam of electrons to scan across the surface of a sample. These electrons penetrate the surface of the sample and interact with the atoms of the material. Secondary electrons and backscattered electrons are then detected and these are used to form an image. The first SEM was developed in 1935⁹⁴.

The primary SEM used in this work was an Hitachi S-4700 at an accelerating voltage of 10 keV. The Hitachi S-4700 is a cold field emission SEM, wherein the electron beam is not produced by the thermal stimulation of a metal source but uses a negative potential applied to a narrow tip to cause electrons to tunnel from the source. The filament producing

electrons in the Hitachi S-4700 is a thin monocrystalline tungsten wire tapered to a point of less than 100 nm. When a negative potential is applied to this tip, a narrow cone of electrons is produced which is focused to a point using a magnetic condenser lens, of which the Hitachi S-4700 has two. A schematic of the SEM used in this work is shown below in Figure 2-14.

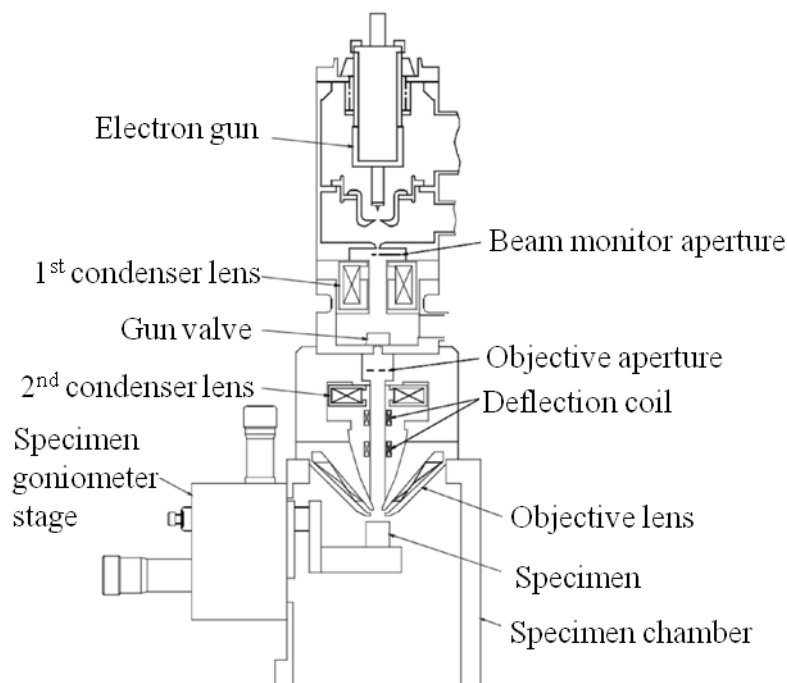


Figure 2-14: Schematic of the Hitachi S-4700 SEM used in this work

As the field emission gun uses a cold field technique the filament wire must be regularly cleaned to ensure good current. Therefore the filament was regularly “flashed”; this involves heating the wire to 2500 K to remove any gas molecules which might affect the emission of electrons. Repeated flashing leads to eventual blunting of the tip but the Hitachi S-4700 has a filament lifetime >1000 hours, significantly higher than techniques emitting electrons through heating of the wire.

Samples to be analysed by SEM were fixed to an aluminium holder with an adhesive carbon tab. In the case of large substrates, which may charge under the beam of electrons, additional copper tape was placed on corners the sample to ground the surface to the aluminium holder. The holder and sample were then loaded in to the specimen chamber (Figure 2-14).

2.2.4.1 Particle size distribution

SEM can be used to record the dimensions of particles. Markers are added to particles and the displacement between these markers recorded. On all samples multiple readings are taken from several areas. Where large sets of similarly dimensioned particles are recorded the average particle size is quoted along with the calculated sample standard deviation. Equation 2-7 is used to calculate the sample standard deviation.

$$s = \sqrt{\frac{1}{n-1} \sum_{i=1}^n (x_i - \bar{x})^2} \quad (2-7)$$

In Equation 2-7 above: s is the sample standard deviation, n the sample size, x_i an individual reading and \bar{x} the sample mean.

2.2.4.2 Energy dispersive X-ray spectroscopy

Energy dispersive X-ray (EDX) spectroscopy is a tool for quantifying elemental composition in conjunction with SEM. The technique is based on the energy released by the relaxation of an electron from one shell to an inner more shell.

EDX analysis is based strongly on the shell structure of the atom (Figure 2-15).

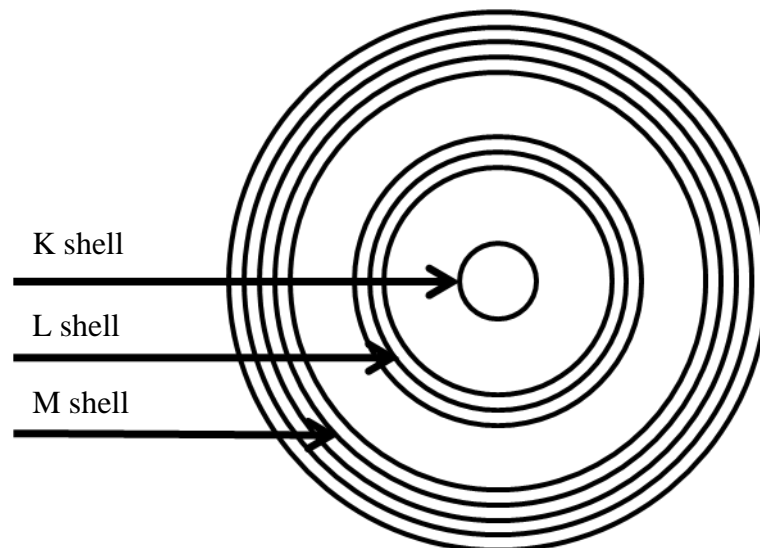


Figure 2-15: Electron orbital schematic showing the K, L and M shells and subshells

EDX is primarily concerned with the inner-most shells - K, L and M - and the electronic transitions between them. Figure 2-15 above shows the K shell (quantum number $n = 1$) is

capable of hosting 2 electrons. Further from the centre is the L shell ($n = 2$) which is comprised of three sub-shells each in a different quantum state. The L shell can accommodate 8 electrons. The outermost shell shown in the diagram is the M shell ($n = 3$) which has 5 sub-shells and can accommodate 18 electrons.

During EDX spectroscopy, the material is bombarded with a high energy beam of electrons that can, having enough energy, eject an inner shell electron. When the inner electron is ejected the atom is left in a higher energy configuration until an outer shell electron relaxes down to fill the vacancy.

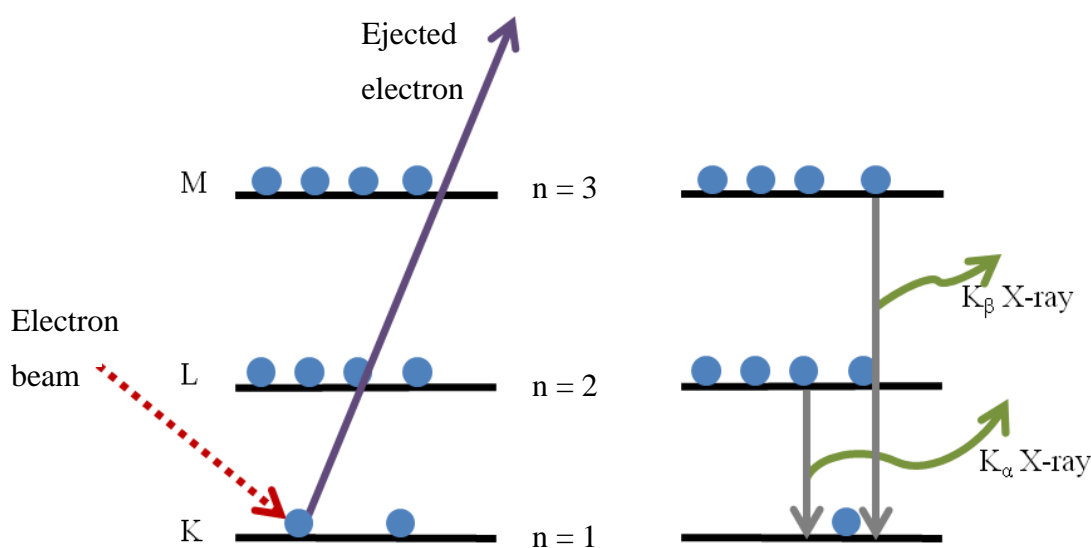


Figure 2-16: Electron ejection and relaxation schematic

Figure 2-16 shows a high energy electron beam incident on a sample. The electron beam ejects an electron from the K shell. This vacancy is filled by an electron dropping from a higher shell. When an electron falls from a higher shell to a lower there is an associated emission in the form of an X-ray. As each energy level is discrete there is a unique wavelength associated with it. Detection of these X-rays can identify the element being examined. Quantification of these X-rays along with comparison to a calibration standard gives elemental quantification.

If an electron undergoes an L-to-K transition, the X-ray is labelled K_{α} emission, an M-to-K transition labelled K_{β} . As there are sub-levels, these X-rays are given the additional label of 1, 2, 3, etc.

In samples where the atomic number is greater than 35 the K shell may require too high an energy to cause electron ejection, and in this case the L_{α} signals (an M-to-L transition) are recorded.

In addition to the characteristic K and L X-ray signals there is also Bremsstrahlung radiation which is filtered as a background.

The detection of the produced X-rays is carried out by a semiconductor detector, most commonly a silicon-lithium material that causes ionisation and therefore a charge when exposed to the radiation. The idealised charge creation is proportional to the energy of incident photon. The detector is kept at cryogenic temperature to minimise electrical interference. The detector is protected from the sample and electron beam by a beryllium window.

One of the limitations of EDX is the inability to resolve peaks accurately. Some elements have overlapping emissions and because of this it may be difficult, or impossible to quantify or differentiate elements with similar spectrum.

Figure 2-17 shows an example of an EDX spectrum of bismuth telluride on silicon showing distinct peaks associated with the unique energy transitions within elements.

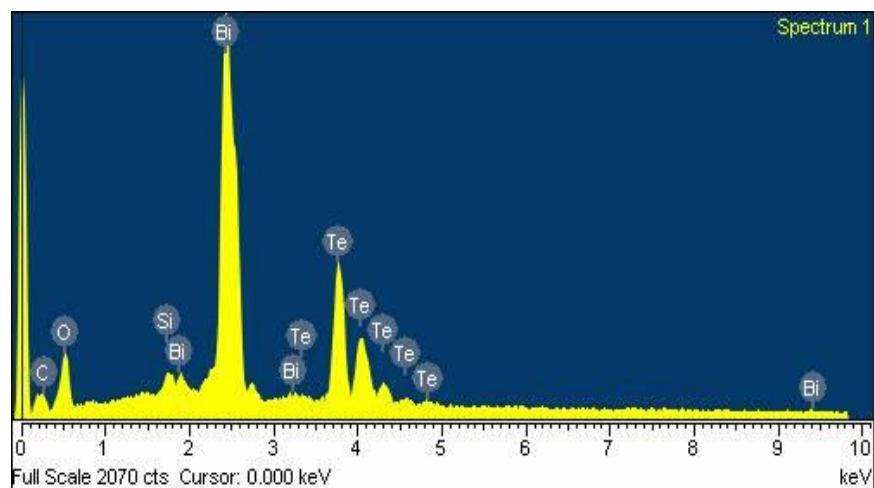


Figure 2-17: Example of an EDX spectrum showing bismuth telluride on silicon

2.2.5 Transmission electron microscopy

TEM is an extremely important method for characterising materials. The apparatus is capable of many forms of analysis with high precision. For this investigation a FEI Tecnai T20 was used. This uses electrons accelerated to 200 keV, corresponding to a de Broglie wavelength of 2.51 pm (including relativistic corrections). This wavelength is capable of extreme magnification and single crystal diffraction. Images were acquired using a SIS Megaview III CCD camera.

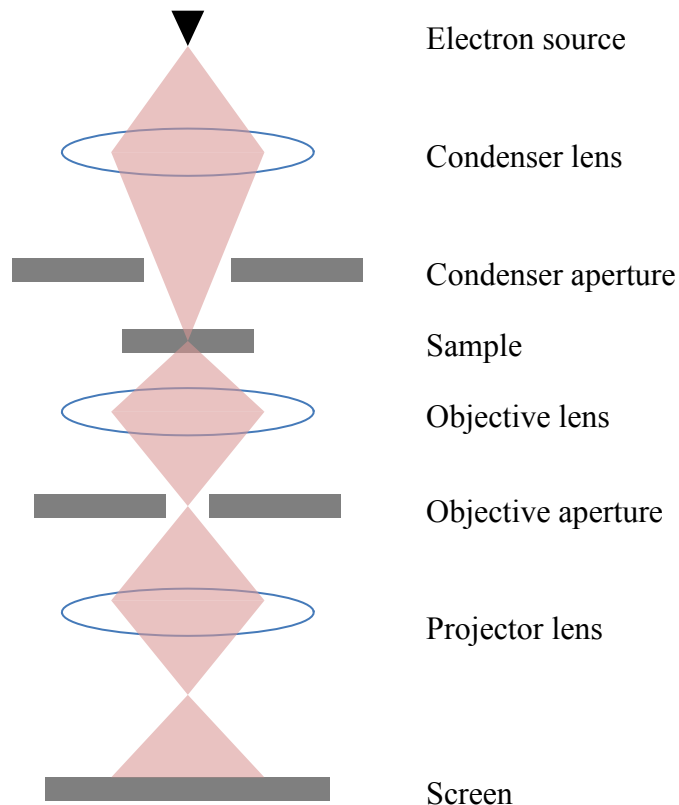


Figure 2-18: TEM schematic

Figure 2-18 shows a schematic diagram of a TEM. Once again the beam of electrons is focused by magnetic lenses.

Samples must be <100 nm thick to allow sufficient transmission of electrons. Samples were mounted on a porous carbon film suspended over a copper framework. This disc was then inserted using a double tilt rod above the objective lens (Figure 2-18).

2.2.5.1 Preparation of samples

As the spherical particles are of micron dimensions they were unsuitable for immediate TEM analysis. To reduce the thickness of the particles to be analysed to be less than 100 nm and therefore electron transparent, larger particles had to be destroyed.

A small amount (around 5 mg) of the product was suspended in a minimal amount of isopropanol and then lightly ground with an agate mortar and pestle for 20-30 seconds. Three drops of the resulting solution were applied to the carbon grid.

2.2.5.2 Imaging

Imaging is perhaps the most basic function of a TEM. Resolutions unattainable with SEM can be achieved. The most important aperture for imaging is the objective aperture (Figure 2-18).

2.2.5.2.1 Bright field imaging

In bright field imaging only the direct beam is used to form an image. An 'objective aperture' is inserted into the TEM which blocks all electrons except the direct beam that passes the small central hole of the aperture. All scattered electrons are blocked by the objective aperture and the image is formed as a function of areas which has led to weakening of the direct beam. The change in the local intensity of the direct beam can be caused by a number of factors. Differences in sample depth will be apparent in bright fields imaging with thicker areas showing darker than thinner areas where less electrons have been successfully transmitted without scattering. Similarly differences in crystallinity can often be observed, though not quantitatively. Areas with high crystallinity are likely to lead to a high degree of scattering due to diffraction and therefore crystalline areas often appear darker on bright field imaging. Thirdly, as different atomic masses will scatter electrons to different degrees, changes in elemental composition can often be visualised with bright field imaging.

2.2.5.2.2 Dark field imaging

In contrast to bright field imaging, dark field imaging uses only scattered electrons to form an image. All unscattered electrons are excluded, leading to a dark image unless scattering is present, scattered electrons will show as bright areas on the dark background. Dark field

imaging has significant lower intensity than that of bright field imaging but is also capable of obtaining higher contrast. Dark field imaging can be used to highlight similarly oriented crystal planes within a material. If the sample is rotated the Bragg condition is fulfilled and subsequently unfulfilled as different angles are examined and correspondingly the sample will show bright then dark dependent on angle.

2.2.5.3 *Electron diffraction*

The principle of electron diffraction is the same of that for X-ray diffraction. A specific advantage to diffraction on a TEM is the ability to acquire patterns from selected areas. By inserting a selected area aperture into the column an area of nanometre dimension can produce a diffraction pattern. Electron diffraction patterns taken from single crystals produce distinctive spots with regular repeating patterns inherent to the crystal structure being investigated.

Spot patterns produced from single crystals can be clearly labelled to identify specific lattice vectors. The samples presented in this report are in most cases polycrystalline, giving rise to circular diffraction rings. These too can be labelled, the structure identified and the lattice parameters calculated. These spots represent Miller indices and correspond to the planes causing the diffraction. The spacing of these spots is inversely proportional to the d_{hkl} spacing between the planes. For polycrystalline samples where many orientations are present, the spot pattern is replaced by a ring pattern with each ring related to the d_{hkl} spacing.

Single crystal and polycrystalline patterns can be indexed to deduce the structure. A schematic of the diffraction is shown in Figure 2-19 with key features labelled.

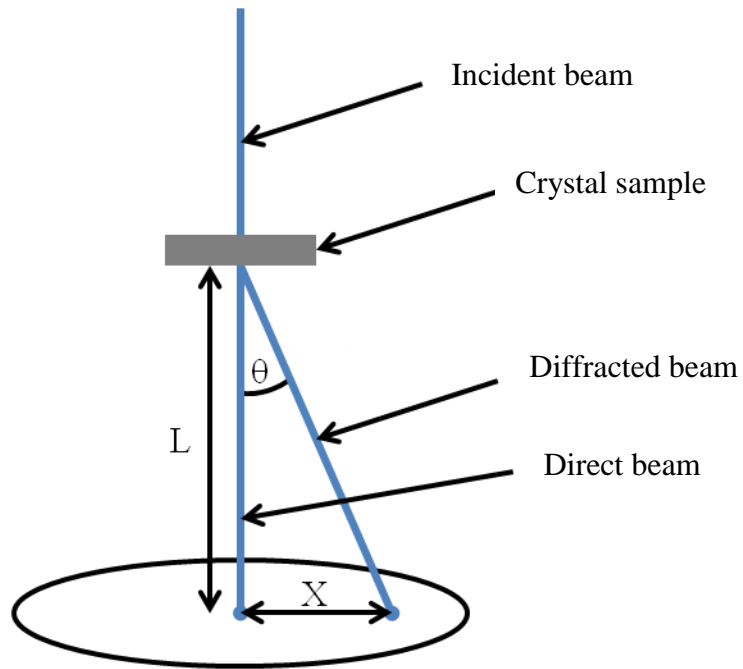


Figure 2-19: Schematic of electron diffraction in TEM with labels

From Figure 2-19 it follows that,

$$\tan 2\theta = \frac{X}{L} \quad (2-8)$$

where θ is the angle between the direct beam and diffracted beam, X is the distance from the direct beam to the diffraction spot and L is the camera length. For small displacements, the approximation seen in equation 2-9 can be made.

$$\tan 2\theta \approx \sin 2\theta \approx 2\theta \quad (2-9)$$

Combining this with Bragg's law, (equation 2-5), the following can be expressed,

$$\frac{X}{L} = 2\theta = \frac{2\lambda}{2d_{hkl}} \quad (2-10)$$

where λ is the wavelength of the electrons. Finally the d_{hkl} spacing can be expressed by:

$$d_{hkl} = \frac{L\lambda}{X} \quad (2-11)$$

$L\lambda$ is known as the camera constant.

Using the above relations, the d_{hkl} spacing can be calculated using the camera constant along with the diffraction spacing. In this work, d_{hkl} spacings were compared to standards for the investigated materials and hkl values assigned. Knowing both the d_{hkl} spacing and hkl values, the cell parameters can be calculated. For cubic structures, such as titanium nitride the relation follows;

$$d_{hkl} = \frac{a}{\sqrt{h^2 + k^2 + l^2}} \quad (2-12)$$

where a is the cubic cell length. The above relation becomes increasingly complex as the degree of structure symmetry decreases.

2.2.5.4 *Electron energy loss spectroscopy*

Electron energy loss spectroscopy (EELS) is an elemental analysis technique, capable of identifying and quantifying the elemental composition of a material. It is a technique discovered in the 1940s but rose to prominence in the 1990s with advances in microscope technology. The technique is capable of extreme accuracy and had been reported capable of identifying single atoms in a matrix⁹⁵.

EELS is concerned with electrons which have undergone inelastic scattering. The monoenergetic electron column of the TEM was targeted at the sample and the energy loss of electrons which have undergone inelastic scattering was recorded. There are numerous routes to the loss of energy in the scattering process but this work is primarily concerned with inner shell ionisation.

As discussed with EDX, a high energy electron is capable of ejecting an inner shell electron from an atom. When an incident electron collides and ejects an electron, the original incident is scattered and travels with a new energy which is equal to that of the initial energy minus the ionisation energy for the ejected electron. When spectra are analysed (recorded by an electron spectrometer) there are distinct peaks that are specific ionization edges. These peaks show numerous electrons having a common energy loss, ascribed to the ionisation energy of an element. As the ionisation potential of an electron is

an element specific quantity the successful elemental composition determination can be made.

The electron spectrometer which is located below the TEM is capable of detecting a wide range of energies.

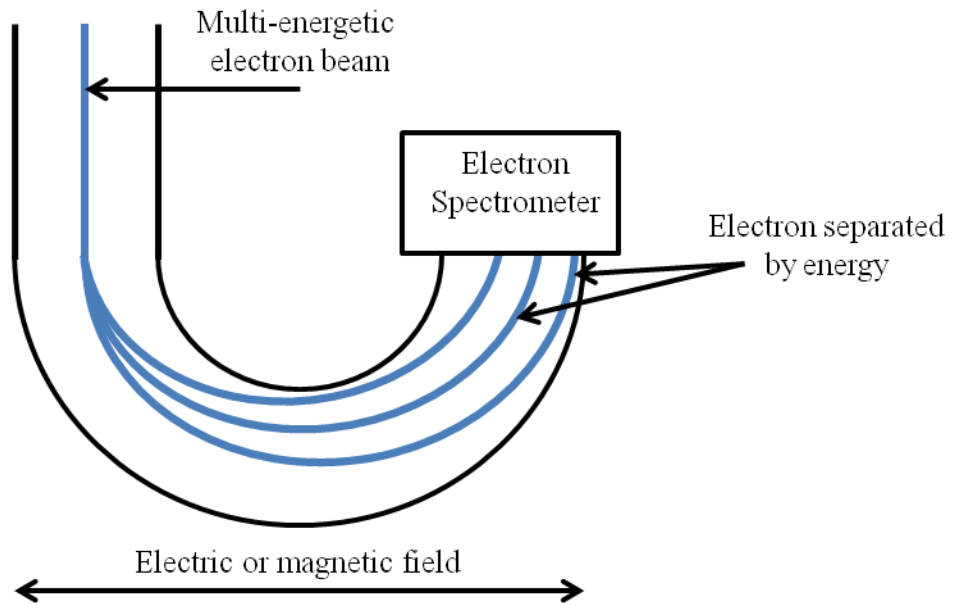


Figure 2-20: Diagram of electron spectrometer

The electrons following interaction with the subject material are emitted into the spectrometer. These are exposed to an electric or a magnetic field which will deflect the path of electrons. Higher energy electrons are deflected less. By far the most intense is the zero loss peak pertaining to electrons which have not undergone inelastic scattering. The various energies are collected into a spectrum where specific elemental ionisation energy edges can be identified. An example of an EEL spectrum is shown in Figure 2-21 showing the number of electrons against energy loss. Peaks can be resolved due to specific energy values associated with inner shell electron ejection.

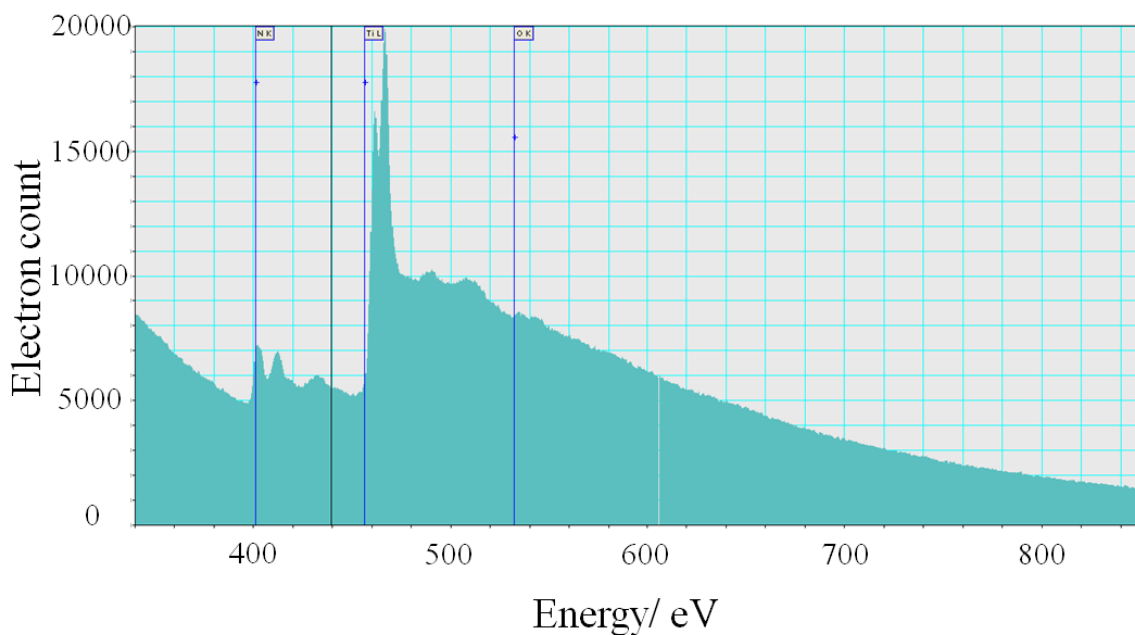


Figure 2-21: Example of EEL spectrum of TiN showing distinct elemental peaks caused by inner electron ejection

2.2.6 Raman Spectroscopy

Raman spectroscopy is a powerful technique offering information about structure and composition of a material. In some cases Raman spectroscopy can also be used to obtain information on particle size. When light is incident on a surface there are many possible outcomes: reflection, absorption, transmittance and scattering. Raman spectroscopy is concerned with the scattering of monochromatic light from substances. Light scattering from molecules is dominated by Rayleigh scattering, where the light that is scattered has the same wavelength as the original photon. Scattered light which has a higher or lower wavelength is the basis of Raman Spectroscopy.

Light incident on a molecule can interact with the electron cloud and the bonds of that molecule. The photon can be absorbed and raise the energy of the molecule to a virtual excited state. Relaxation to a lower state generates a photon. If the resultant photon is the same wavelength as the original (> 99% of the photons) this is Rayleigh scattering and is excluded from Raman analysis. If the wavelength of the resultant photon has increased, then this loss of energy is referred to as a Stokes shift in energy. A decrease in wavelength is referred to as an anti-Stokes shift. There is disparity in the frequency of Stokes and anti-Stokes emissions, because the initial photon must be incident on a system which is already in an excited state in order for an anti-Stokes shift to occur. The probability of a system to

be in an excited state opposed to a ground state at room temperature is generally lower and therefore there is a higher intensity of Stokes shifted emissions. The scattering can be visualised through a simple energy diagram, (Figure 2-22).

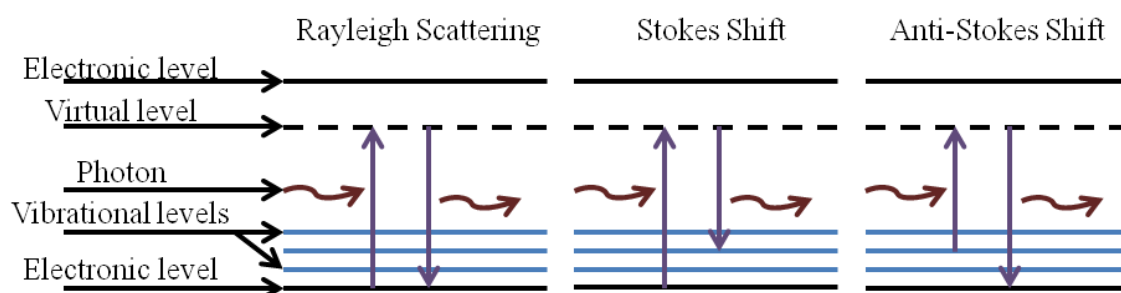


Figure 2-22: Energy diagram showing scatter effects

The diagram above details the energy level transition responsible for Rayleigh, Stokes and anti-Stokes scattering. The change in energy found in the Stokes and anti-Stokes shifts is indicative of the energy spacing in the ground level and it is through this change in wavelength that structural information is obtained.

The Rayleigh scattering is filtered out as is the anti-Stokes shifted wavelengths. Anti-Stokes contains the same structural information as the Stokes lines but has a much lower intensity. Raman spectra can be complicated with numerous peaks it is therefore common practice to compare spectra with known literature standards. Raman spectroscopy was used in this study for phase and structure determination as well as highlighting differences between bulk and nanomaterials.

Samples were analysed in bulk form loaded on a glass substrate. Experiments were carried out at room temperature on a Horiba LabRam with HR confocal microscope using a 325 nm UV laser, 100 μm aperture, 600 groove/mm grating and Synapse CCD.

2.2.7 Brunauer–Emmett–Teller surface area analysis

Brunauer–Emmett–Teller (BET) surface area analysis was carried out to obtain surface area measurements of samples as well as average pore volume. BET is an isothermal adsorption technique where gas molecules are physically adsorbed on the surface of the material. The isothermal adsorption techniques are based on Langmuir or BET theory. In Langmuir theory a single monolayer of gas molecules is adsorbed onto the surface whereas BET theory considers multiple layers.

For this work, nitrogen was used as the gas to adsorb on the surface as it has a strong interaction with many solids. Initially the samples were “degassed” – a recorded mass of the sample was held under flow of nitrogen overnight at room temperature. This degassing procedure removed surface adsorbed contaminants. Following degassing the samples were held under vacuum and cooled to 77 K. Known quantities of high purity nitrogen gas were then introduced into the vessel and the variation in pressure was recorded. This procedure is repeated until saturation occurs.

No further layers of gas were adsorbed when the molecules on the surface reached an equilibrium with the introduced gas. Analysis of the BET isotherm yields the volume of gas required to produce a monolayer on the surface of the sample and from this the surface area was determined.

Isotherms were recorded on a Micromeritics Flow Prep 060 and Gemini BET machine by Mr Andrew Monaghan of the University of Glasgow’s School of Chemistry.

2.2.8 Diffuse reflectance UV/Vis spectroscopy

Diffuse reflectance UV/Vis spectroscopy was used to record the photons scattered from the surface of TiO₂ powders and related materials. These samples were all opaque; in the case of TiO₂, the samples were a brilliant white suggesting 100% visual light reflectance.

In diffuse reflectance spectroscopy, the sample is exposed to a range of wavelengths and the resultant reflectance recorded. The sample is held in a metallic holder providing a surface area of 1 cm². The photon beam was focussed onto this sample and the apparatus covered with 2 hemispherical mirrors. When the sample is irradiated, some of the photons will be absorbed and others will be reflected, therein scattered to the surroundings. The two

mirrors focus this reflected light to a detector point. Using this procedure a reading of incident radiation and subsequently reflected radiation is obtained. This is plotted as reflectance as a function of wavelength.

The majority of the difference between the incident and reflected beams is caused by absorbance. In the case of the materials being examined most visible light will be reflected, however there is a set point where the photons will have sufficient energy to promote an electron from the valence band to an empty conduction band. A photon with sufficient energy can be absorbed producing a sharp decrease in the reflectance. The energy associated with these photons corresponds to the energy required to promote the electron and is therefore a measure of the band gap.

UV/Vis spectra were recorded between 200-800 nm on a Cary 500 spectrophotometer.

3 Silicon based material growth

This chapter details an investigation into the CVD of bismuth telluride starting from elemental reagents. It explores a range of silicon-based surfaces and characterise the growth morphology. The aim was to obtain a variety of reproducible morphologies of bismuth telluride structures using an elemental reagent CVD process to develop growth on a range of silicon-based surfaces. This chapter describes the production of sub-micron thickness plates and regular octahedra of bismuth telluride, bismuth rich nanowires, and sets out a method for detailed low dimensional characterisation of electrical and thermal properties. There is a drive to discover methodologies that produce novel morphologies of bismuth telluride materials for thermoelectric applications. There are numerous synthetic routes to produce particles of bismuth telluride, each with their own advantages and drawbacks. An increasingly successful experimental method is metal-organic chemical vapour deposition (MOCVD)⁹⁶⁻⁹⁸. MOCVD and CVD are advantageous due to their scalability and ability to produce low dimensional materials. CVD is already widely used in semiconductor manufacturing. MOCVD however has significant drawbacks. The methods reported in the literature require expensive, specially prepared reagent gases such as trimethyl-bismuth⁹⁷ and diethyl-tellurium⁹⁸ which are unsuitable for commercial production. The work reported here requires only elemental reagents in a single step CVD process.

There are reports of bismuth telluride being deposited *via* a chemical vapour process but none employing a single step process from elemental reagents. Kujomana and Mathai⁹⁹ grew millimetre length hollow wires of bismuth telluride using bulk Bi₂Te₃ as a starting material *via* chemical vapour transport. Gothard¹⁰⁰ demonstrated deposition using commercial thermoelectric material which was transported along a quartz ampoule under argon flow. Although an interesting spherical particle morphology was obtained, it proved difficult to control the composition of the product and spherical particles of up to 95% tellurium were obtained. Similarly John reported the transport of pre-prepared Bi₂Se₃¹⁰¹ Most recently, in February 2014, Benjamin *et al.*¹⁰², reported that “no single source precursors for the CVD of Bi₂Te₃ are currently known”, and while there are two reagents utilised in the work, it demonstrates precursor innovation.

Samples described in this chapter are tabulated in Table 3-1. All samples used silicon substrates reacted with elemental bismuth and tellurium.

Table 3-1: Samples described in Chapter 3

Identifier	Cleaning process	Etching process	T/ °C	Modification	Section
G1	DI water/ Acetone/ IPA	None	700	10 s Au/Pd sputtering	3.1
G1(repeat)	DI water/ Acetone/ IPA	None	700	10 s Au/Pd sputtering	3.1
G3	DI water/ Acetone/ IPA	None	700	60 s Au/Pd sputtering	3.1
D1	None	None	700	Surface scratched with glass paper	3.2
V1	DI water/ Acetone/ IPA	None	700	Vertical orientation	3.3
L1	DI water/ Acetone/ IPA	None	700	Temperature gradient applied	3.4
L1(repeat)	DI water/ Acetone/ IPA	None	700	Temperature gradient applied	3.4
T1	DI water/ Acetone/IPA	Buffered HF	500	Transport gas reactions including I ₂	3.5
B1	DI water/ Acetone/IPA	Buffered HF	700	Te free reaction	3.6
B1(repeat)	DI water/ Acetone/IPA	Buffered HF	700	Te free reaction	3.6
EB1	DI water/ Acetone/IPA	Buffered HF	700	1:1 ratio of reagents	3.7
EB1(repeat)	DI water/ Acetone/IPA	Buffered HF	700	1:1 ratio of reagents	3.7

3.1 Gold-palladium reactions

It is well established that the presence of metal nanoparticles can seed the growth of low dimensional structures *via* the vapour-liquid-solid method (VLS) ¹⁰³⁻¹⁰⁵. Following this growth methodology, gold and palladium nanoparticles were deposited on a silicon surface to seed low dimensional growth.

3.1.1 Reaction set up

Silicon wafers were cleaved into 1 x 1 or 1 x 2 cm² pieces and then cleaned using sonication in deionised water, followed by acetone then iso-propanol treatment. Clean substrates were then sputtered with gold and palladium using an Agar automatic sputter coater calibrated to 9 nm deposition over 60 s and fitted with a gold-palladium disc.

Sputter-coated wafer pieces were sealed in a quartz ampoule under vacuum following the standard process previously described. The reagents for these reactions were: bismuth (2 mmol, 99% pure, 100 mesh, Sigma Aldrich) and tellurium (3 mmol, 99.8% pure, 200 mesh, Sigma Aldrich). Sealed tubes were heated in a box furnace at 700 °C for 48 h.

3.1.2 Results

Samples G1, G1(repeat) and G3 from Table 3-1 are described in this section as example systems.

3.1.2.1 Sample Morphology

SEM was used to examine the morphology of the particles on the surface. Distinct morphologies were produced dependent on sputter quantity used. Where short sputter times were used (< 30 s), a hexagonal or triangular morphology was observed.

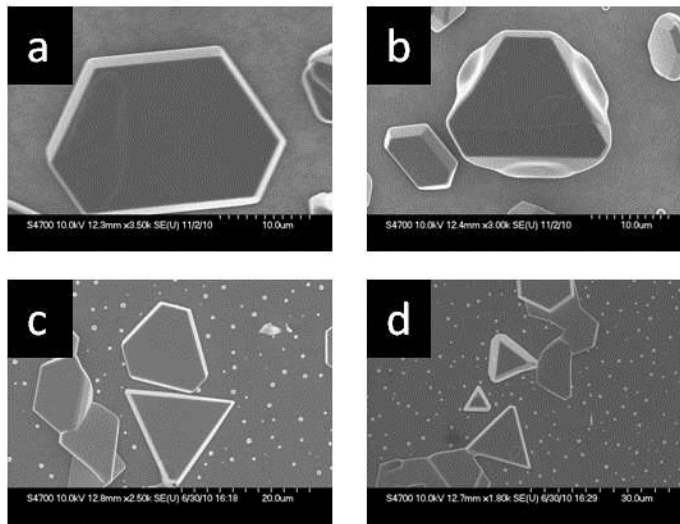


Figure 3-1: SEM micrographs showing Bi₂Te₃ plates and dots of tellurium grown on silicon: (a-b) G1, (c-d) G1(repeat)

Shown above are images of the plates grown on the silicon surface. These substrates had been sputtered for 10 s with a minimal amount of Au/Pd. The plates were 5-10 μm in diameter, however there were a small number with a much greater surface area, 40 μm being the largest diameter observed. The plates exhibit a large aspect ratio in regard to their thickness and diameter, with the plates below 1 μm in height.

While the plates were found consistently across the surface, most samples had an excess of tellurium which was seen to form irregular spherical particles as depicted in Figure 3-1 c and d.

3.1.2.1.1 Sheet

Sample G1(repeat) exhibited, a unique sheet approximately 50 x 40 μm² in width and height but less than 50 nm in thickness (Figure 3-2).

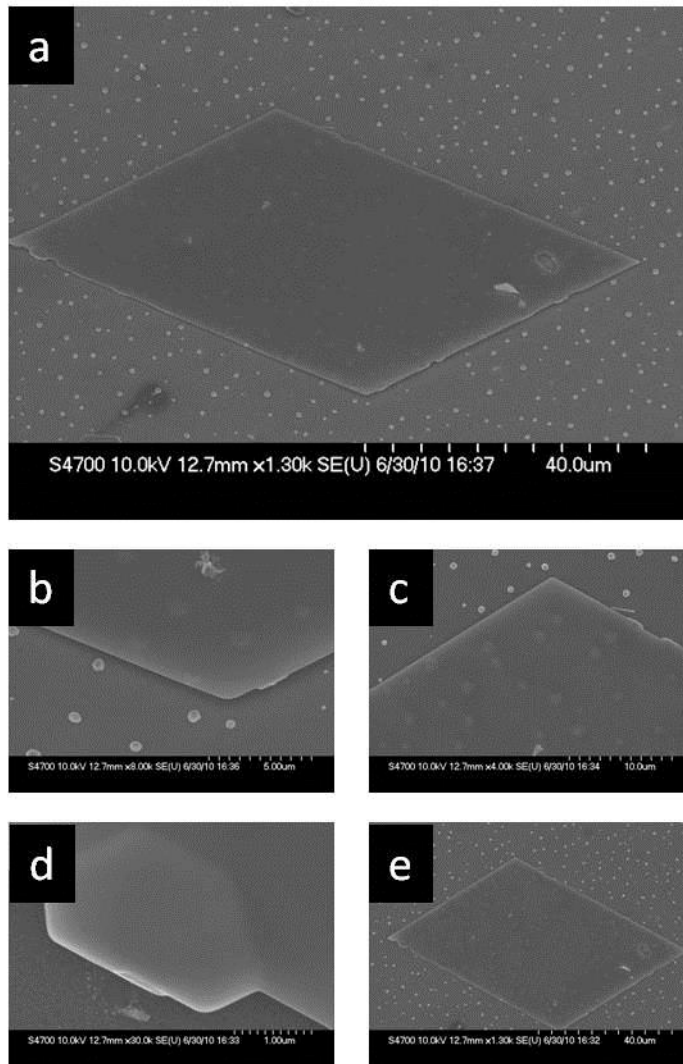


Figure 3-2: SEM micrographs showing ultra-thin sheet on the surface of G1(repeat)

The sheet was partially transparent to electrons with the excess tellurium visible beneath the sheet. It is possible that many sheet type morphologies exist but due to the thin and almost electron transparent nature of the growth they may be difficult to image by SEM.

There is precedent for the discovery of these sheets. Similar findings were reported by Zhao *et al.*,¹⁰⁶ who produced thin sheets of bismuth telluride grown on the surface of silicon and were evidenced to be 6 nm thick and show a match to Bi_2Te_3 by XRD and TEM electron diffraction.

3.1.2.2 Elemental analysis

EDX was used to confirm the elemental composition of the plates (Figure 3-3). The plates showed a match to stoichiometric Bi_2Te_3 .

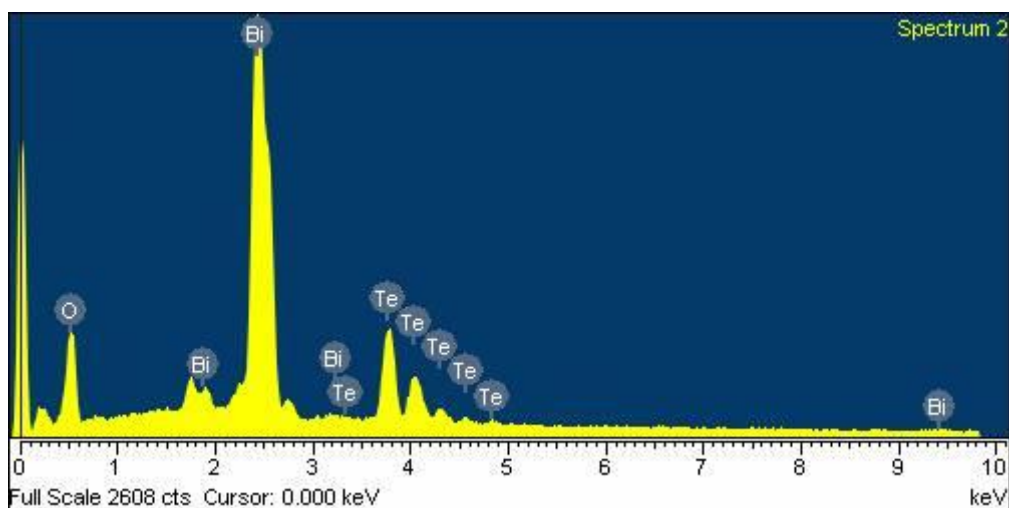


Figure 3-3: EDX spectrum of plate from G1(repeat)

Silicon, oxygen and carbon were also detected but these are also detected when a blank silicon surface is examined in this method. G1 can be seen in Appendix A (Figure 9-1).

3.1.2.3 Crystalline phase identification

Powder X-ray diffraction was used to identify the crystal phase of surface growth. The only peaks identified (excluding the silicon substrate) matched to Bi_2Te_3 . These reactions sputtered with Au/Pd for only 10 s are expected to have less than 2 nm of Au/Pd on the surface and this low concentration was not detected by XRD. Figure 3-4 below shows an example XRD pattern obtained from sample number G1(repeat). The XRD pattern obtained can be found in Appendix A (Figure 9-2) and the pattern obtained from G1 matching to Bi_2Te_3 can be seen in Figure 9-3.

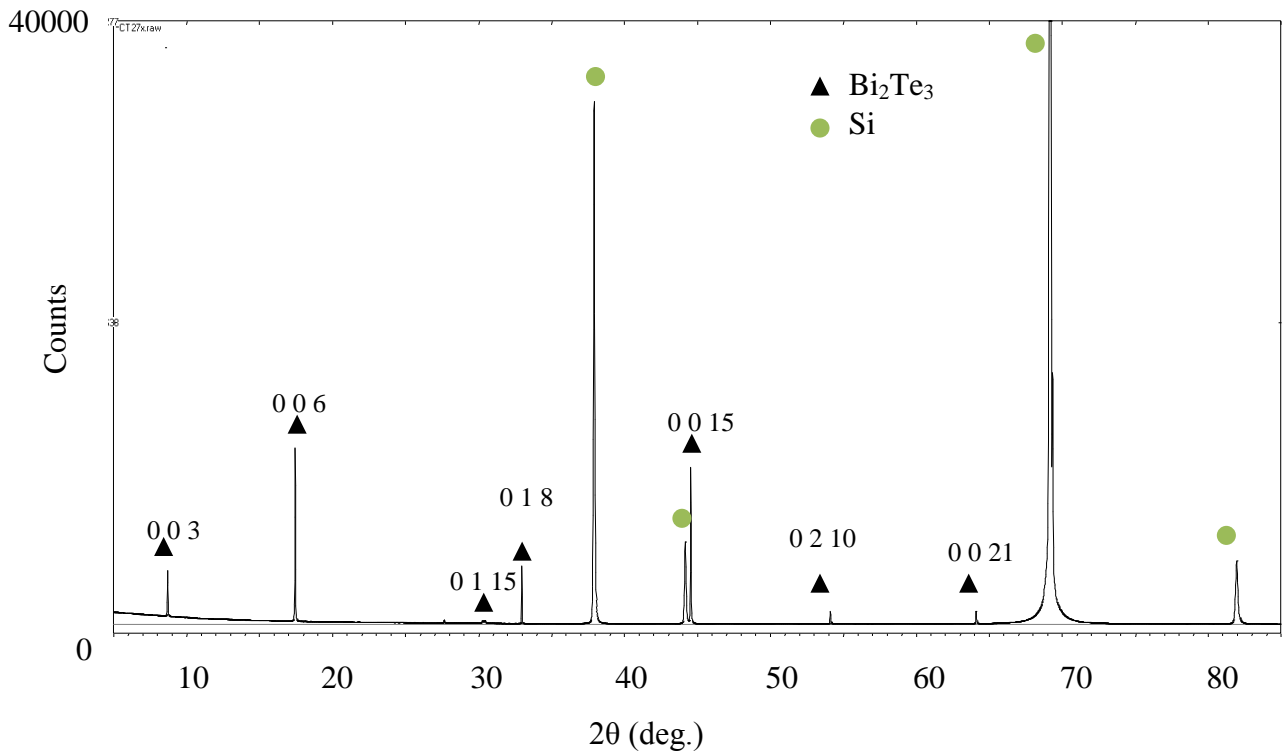


Figure 3-4: XRD pattern obtained from sample G1(repeat) showing only the presence of Bi₂Te₃ and silicon

3.1.3 Excess gold/palladium

The above reaction used a minimal coating of gold as the goal was to initiate growth as opposed to growth incorporating gold or palladium through the structures. To observe the effect of excess Au/Pd, several reactions were carried out looking at substrates which had 9 nm (or greater) of Au/Pd deposited.

3.1.3.1 Morphology

Samples with an extended sputter time (30-60 s) had a vastly different appearance from the plate like morphology shown above.

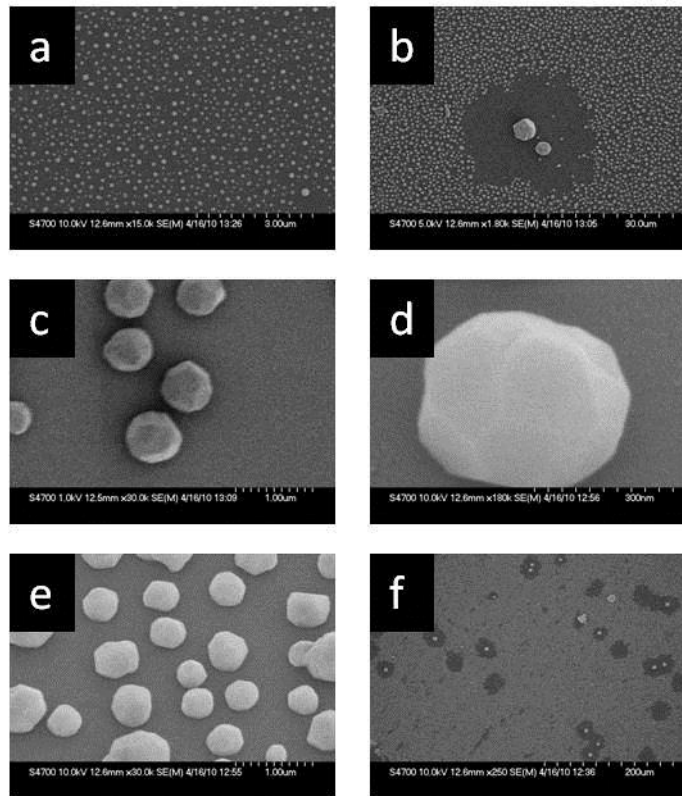


Figure 3-5: SEM micrographs showing nanodots of Au/Pt, sample G3

The surface was covered in nanodots of gold and palladium. The metals had aggregated to form droplets akin to water on a hydrophobic surface. The nanodots were generally 100-300 nm in diameter. Some particles with micron scale dimensions were observed, these were found in the centre of areas otherwise free from deposition. This suggests that the larger particles are agglomerates formed by fusing of smaller particles; this is noticeably evident in Figure 3-5 b and f.

3.1.3.2 Elemental Analysis

EDX (Figure 3-6) confirmed that no deposition of bismuth or tellurium was present on the surface. Elemental analysis revealed only the presence of silicon, gold and palladium.

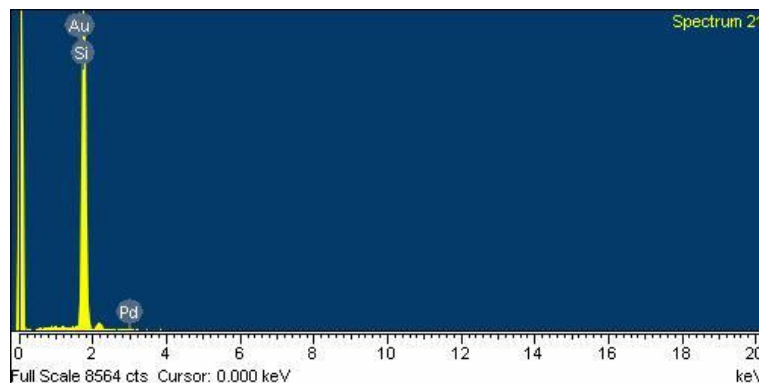


Figure 3-6: EDX spectrum of surface of G3

A large surface-wide EDX spectrum showed 96% silicon, 2% gold and 2% palladium.

3.1.3.3 Crystalline phase identification

The XRD pattern of extended sputter reactions showed very few peaks, all of which had very low of intensities (excluding the silicon) and no matching phases were able to be identified. The pattern of sample G3 can be seen in Appendix A (Figure 9-4).

3.1.4 Conclusions

Using a minimal quantity of gold on the surface of silicon, bismuth telluride plates were grown across the surface using chemical vapour transport at 700 °C from elemental reagents. The short sputter time proved an effective growth route for reproducible micron diameter plates of bismuth telluride with nanoscale thickness. These plates have sub-micron thickness and on average 5-10 μm across.

The plate morphology can be understood by considering plate growth being along the a and b axes as this is where the dangling bonds of the crystal lattice are. These dangling bonds are capable of forming the ionic-covalent Te-Bi bonds required for growth. The c axis growth is normal to the silicon surface, as evidenced by the $(0\ 0\ l)$ peaks in Figure 3-4. The upper surface is capable of van der Waals bonding⁹⁶, leading to a high aspect ratio. The majority of plate particles are hexagonal but there were also triangles and distorted hexagons. Hoa *et al.*¹⁰⁷ rationalised the mixed appearance by describing the hexagonal plates and triangular structures being related and dependent on preferential growth. Under ideal conditions the plate is free to grow along directions 60 ° to one another. There can be deviation from the normal uniform growth leading to some directions showing preferential

growth. In extreme cases when only 3 directions are preferred, triangular particles are formed.

Where growth preference is less extreme, non-uniform hexagons can be produced. Growth of this form is indicative of a preference in the (110) plane. It has been proven that growth in this direction is linked to the highest-performing Bi_2Te_3 thermoelectric materials¹⁰². Growth patterns seen in MOCVD systems have been shown to produce dominant growth along the less desirable (001) direction²⁴.

Also observed *via* this synthesis method was a nanoscale sheet with a high aspect ratio. Although only one of these sheets was observed by SEM, it is deemed of interest due to its stark similarities to the sheets reported by Zhao and co-workers¹⁰⁶. These sheets have great potential due to the topographic insulator properties of bismuth telluride.

Long sputter times with greater than 9 nm of deposition were ineffective with the proposed catalyst material aggregating into regular spherical nanoparticles on the surface devoid of bismuth and tellurium.

3.2 Disrupted surface reactions

Other reactions described in this work feature growth on surfaces with nanoscale smoothness. It has been shown that plates are grown on the surface of the silicon with the *c* axis normal to the substrate (*vide supra*). The smoothness of the surface was destroyed to observe the effect on particle morphology. A further motivation is the lack of nucleation sites found on clean silicon surfaces. It was hoped that using rough silicon surfaces would produce additional growth sites. Reactions then proceeded as previously described for comparison to the smooth surface reactions (Section 3.1.1).

It should also be acknowledged that although the deposition morphology is of interest, the initial disruption of the surface would make the surface itself unsuitable for any electronic applications. The scratching of the surface introduces a disordered surface which may be undesirable in device production. For productive use of the growth demonstrated here the particles may need to be removed from the disordered surface and adhered to substrates with more regular and predictable surfaces.

3.2.1 Reaction set up

As the silicon was deliberately scratched, there was no wet chemical cleaning process. Wafers were cleaved into 1 x 1 or 1 x 2 cm² pieces and then rubbed with glass paper several times visibly scratching the surface. These were sealed in a quartz ampoule under vacuum - following the standard process previously described in Section 2.1.1.1. The reagents for these reactions were bismuth (2 mmol, 99% pure, 100 mesh, Sigma Aldrich) and tellurium (3 mmol, 99.8% pure, 200 mesh, Sigma Aldrich). Sealed tubes were heated in a box furnace at 700 °C for 48 h.

3.2.2 Results

Sample D1 from Table 3-1 is described here as an example system. The samples was analysed by XRD, SEM and EDX.

3.2.2.1 Post- reaction appearance

Most of the reagent powder had formed a single ingot at the base of the tube. The quartz tube became cloudy in the area around the reagents for a length of 2-3 cm in each reaction; this is a common occurrence in transport reactions of this type. Samples were iridescent. The direction of substrate scratching is apparent on sample D1 Figure 3-7.

It should be noted that in the images below, sample D1 has copper tape at either end. This played no part in the reaction, and was added for the sole function of reducing any surface charge on (such a large substrate) when analysed by SEM.

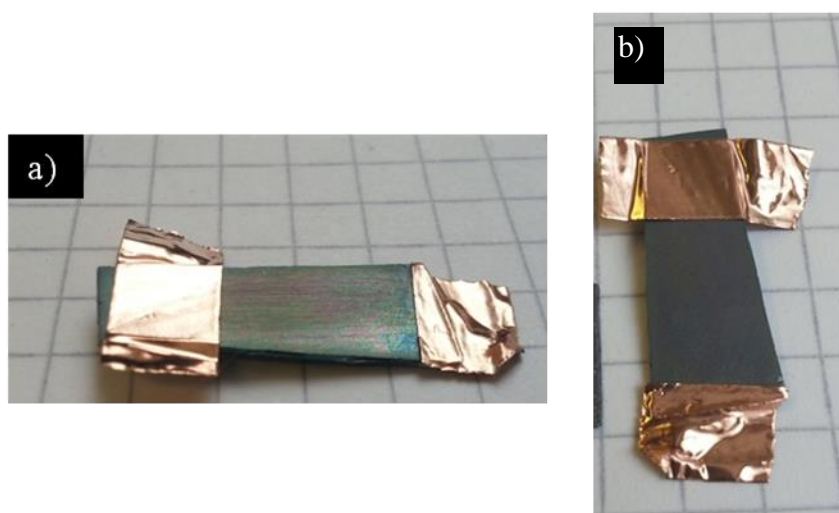


Figure 3-7: Post-reaction surface appearance sample D1

3.2.2.2 Morphology

SEM revealed the morphology of the particles on the substrate surface.

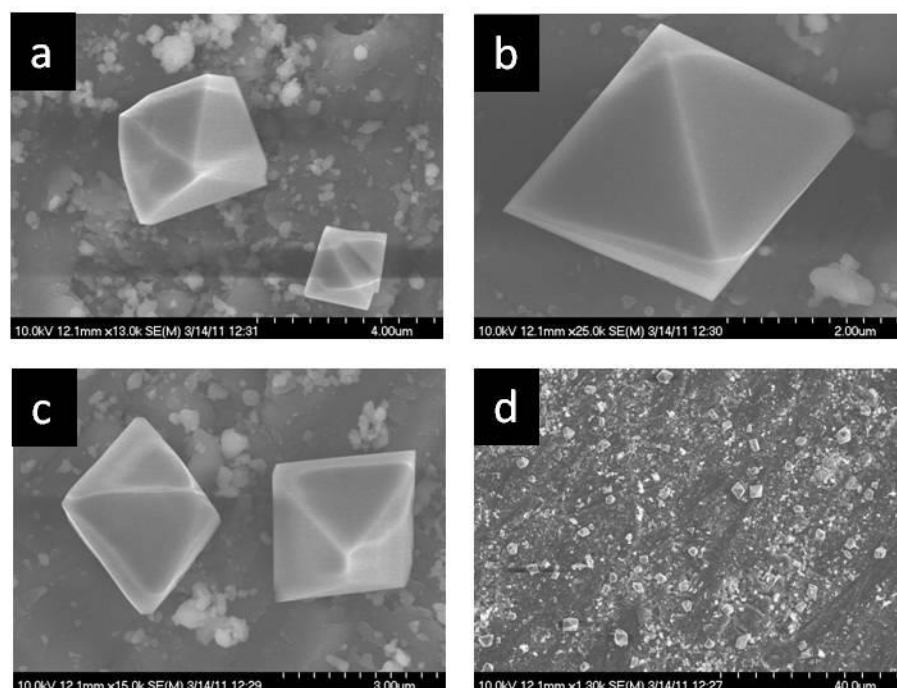


Figure 3-8: SEM micrographs showing regular isolated octahedra on scratched Si surface, sample D1

The surface of the substrate was decorated with octahedra of Bi_2Te_3 with side length of 2-3 μm and 3-4 μm along the longest axis. Beneath the octahedral particles were smaller nanoparticles of variable size and shape, these can be seen clearly relative to the larger octahedron in Figure 3-8 c. Particles were dispersed across the entire surface of the substrate.

3.2.2.3 Elemental Analysis

EDX was used to measure the elemental composition of the particles. The octahedra were identified as being composed of a 2:3 bismuth/tellurium stoichiometric ratio. An example spectrum is shown below.

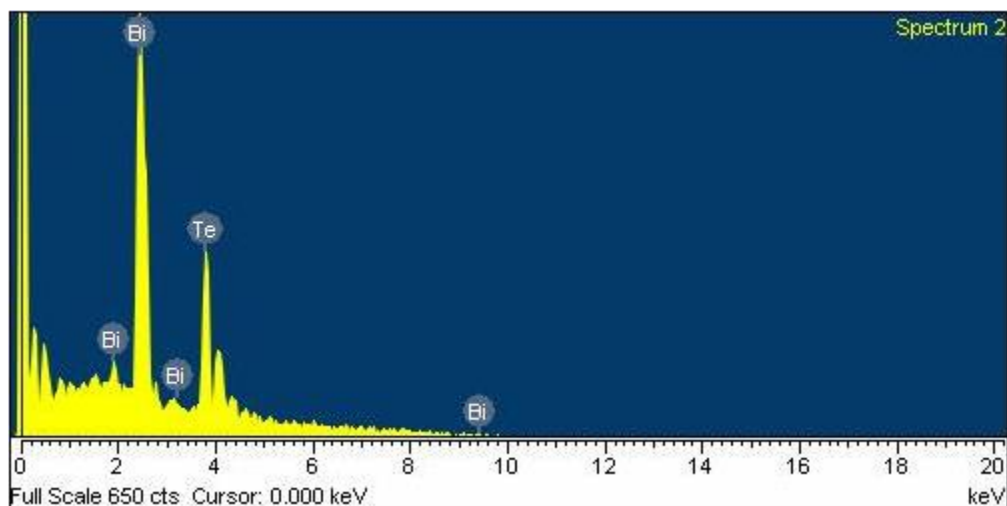


Figure 3-9: EDX spectrum showing the elemental composition of Bi_2Te_3 from sample D1

EDX spectroscopy point size was not small enough to examine the smaller surface particles in isolation. As the silicon was scratched, it is possible that much of this is damaged silicon substrate.

3.2.2.4 Crystalline phase identification

Powder XRD confirmed the presence of bismuth telluride. Figure 3-10 shows the pattern obtained for D1 with a clear match to bismuth telluride. Unique to the scratched surface reactions, additional peaks for silicon were revealed. The usual dominant peaks at 37 and 69 2θ (deg.) were present along with characteristic silicon peaks at 45, 53 and 55 $^\circ 2\theta$.

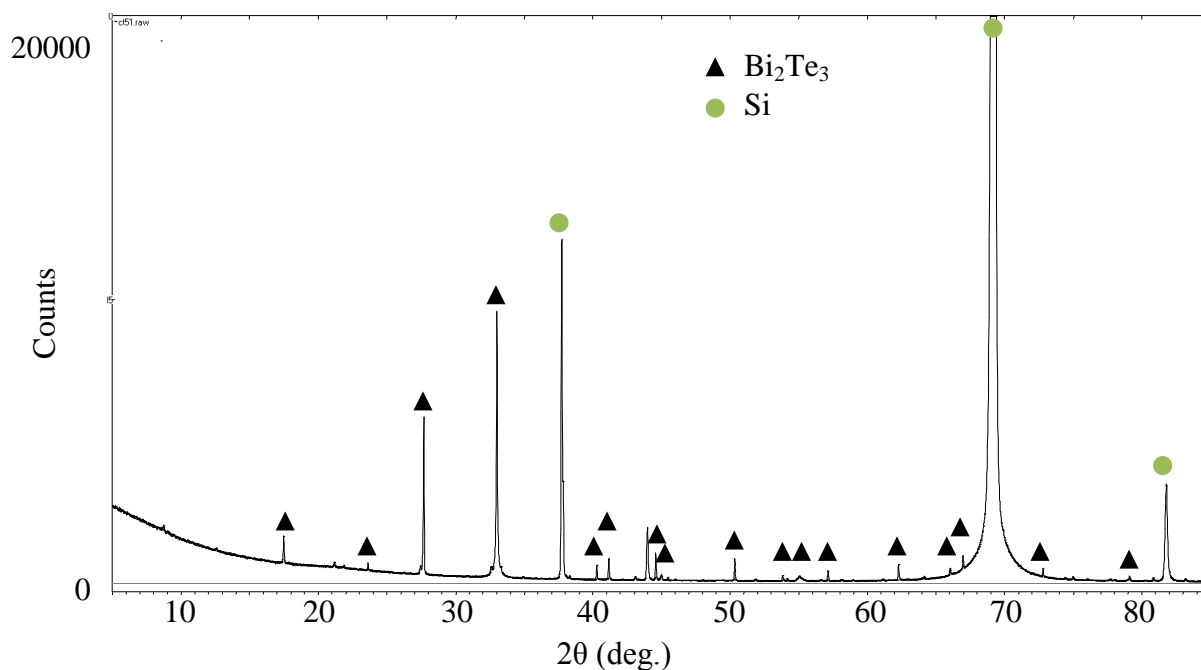


Figure 3-10: XRD pattern showing bismuth telluride on silicon surface (D1)

3.2.3 Conclusions

The reaction here shows a method to create octahedra of bismuth telluride by CVD on a non-smooth silicon surface. These structures have not been reported elsewhere in the literature. There is precedent for the formation of the octahedral morphology; Francombe found that sputtering of Bi_2Te_3 in an argon atmosphere lead to the formation of hexagonal growth interspersed by regular octahedra ¹⁰⁸.

Previous reactions with a smooth silicon surface showed a tendency towards two dimensional (plates) structures with growth along the a and b axes but here with a disrupted surface the particles from regular octahedra. The disrupted surface reactions were conducted following the same procedure as the smooth surface reactions but as the growth is dramatically different it is clear that surface disruption alters particle morphology, leading to three dimensional growth. There is a significant amount of surface debris caused by the scratching process which is of the form of irregularly shaped particles. However the regular and crystalline octahedra result from the growth process and can be characterised using XRD and EDX spectroscopy as Bi_2Te_3 .

It can be seen that using a disrupted surface a different particle morphology to that of a smooth surface was obtained. Regular hexagons have previously been identified in this chapter (Section 3.1) and the octahedron - a trigonal antiprism- is related to the hexagonal dihedral symmetry family. It is logical that, under the correct conditions, the three dimensional structures may be preferred. Further evidence of the relation between crystal growth variation between plates and octahedra can be seen in the growth of hexagonal plates and regular octahedra of cobalt oxide ¹⁰⁹. Purkayastha *et al.* rationalised the formation of bismuth telluride octahedra as a $(5\bar{5}1)$ projection of the rhombohedral crystal structure ¹¹⁰. The octahedral morphology is desirable, as it has been shown that in some examples tetrahedral and octahedral particles can exhibit a lower κ_{lattice} leading to improved thermoelectric performance¹¹⁰.

Particles were not tightly adhered to the substrate and showed movement under the electron beam during SEM analysis and in contact with tweezers. This makes the particles suitable for transferral onto alternate substrates. This method therefore is a potential route to produce additives which can be integrated into bulk material to increase grain boundaries and disrupt thermal transport.

Further work should concentrate on increasing the quantity of particles on the surface and control of particle size. This should be investigated by looking at a range of temperature and reaction times. Particles should also be individually tested for thermoelectric properties and bulk measurements made if sufficient quantities are produced.

3.3 Vertically oriented reactions

The aim of these reactions was to expose the silicon surface to bismuth and tellurium vapour in an alternative orientation to the horizontal set up used above to observe the possible effect on particle growth morphology.

The vast majority of reactions carried out in this area target growth of particles on the surface of a wafer or metal foil. As a comparative experiment, vertical reactions were carried out using similar conditions to the horizontal reactions with the substrate being held directly above the reagents.

3.3.1 Reaction set up

Reactions were prepared according to the method set out in Section 2.1.1.1, using bismuth (2 mmol, 99% pure, 100 mesh, Sigma Aldrich) and tellurium (3 mmol, 99.8% pure, 200 mesh, Sigma Aldrich). A small square piece of silicon less than 10 mm on the diagonal was held above the reagents. The substrate was inserted into the tube by attaching it to a thin tube of soda glass using Kapton tape (Figure 3-11). The substrates in these cases were not chemically etched and only treated *via* a more gentle acetone/water/iso-propanol sonication process (Section 2.1.1.2.1)

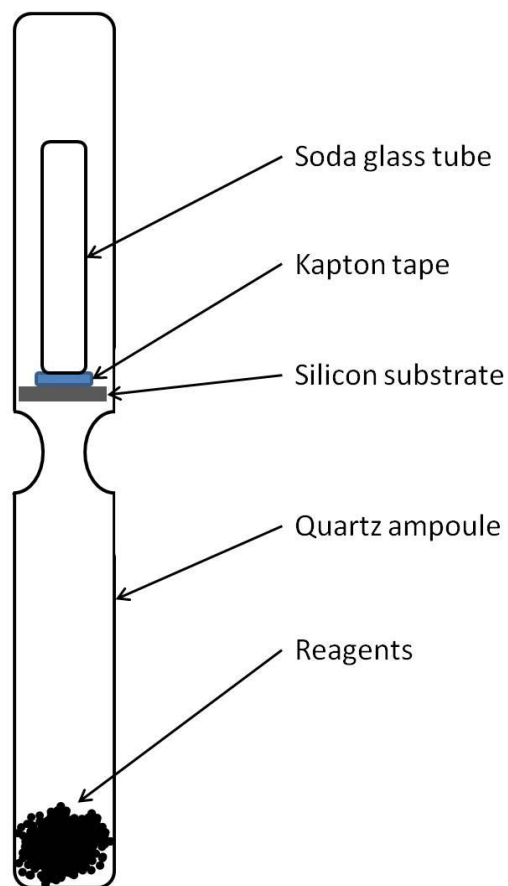


Figure 3-11: Schematic of vertical reactions showing ampoule in upright position with powder at the base and substrate held directly above

Sample tubes were held in the upright position by placing them inside ceramic cylinders inside the Vecstar furnace (Figure 2-5). The reactions were run at 700 °C for 48 h. The temperature of the sample was ramped (250 °C per hour) to the reaction temperature and subsequently allowed to cool slowly in the furnace.

3.3.2 Results

Sample V1 from Table 3-1 is described here as an example system.

3.3.2.1 Post-reaction appearance

The Kapton tape (used as an adhesive only) had charred, blackened and crumbled, and the soda glass holding the substrate in place had deformed in all cases.

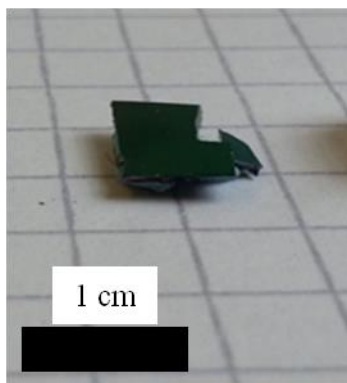


Figure 3-12: Post-reaction appearance of V1

Substrates had taken on a slight purple sheen. The damage to V1 shown in Figure 3-12 was caused during analysis and was not a result of the reaction process.

3.3.2.2 Morphology

Shown below is a representative selection of SEM micrographs gathered from sample V1.

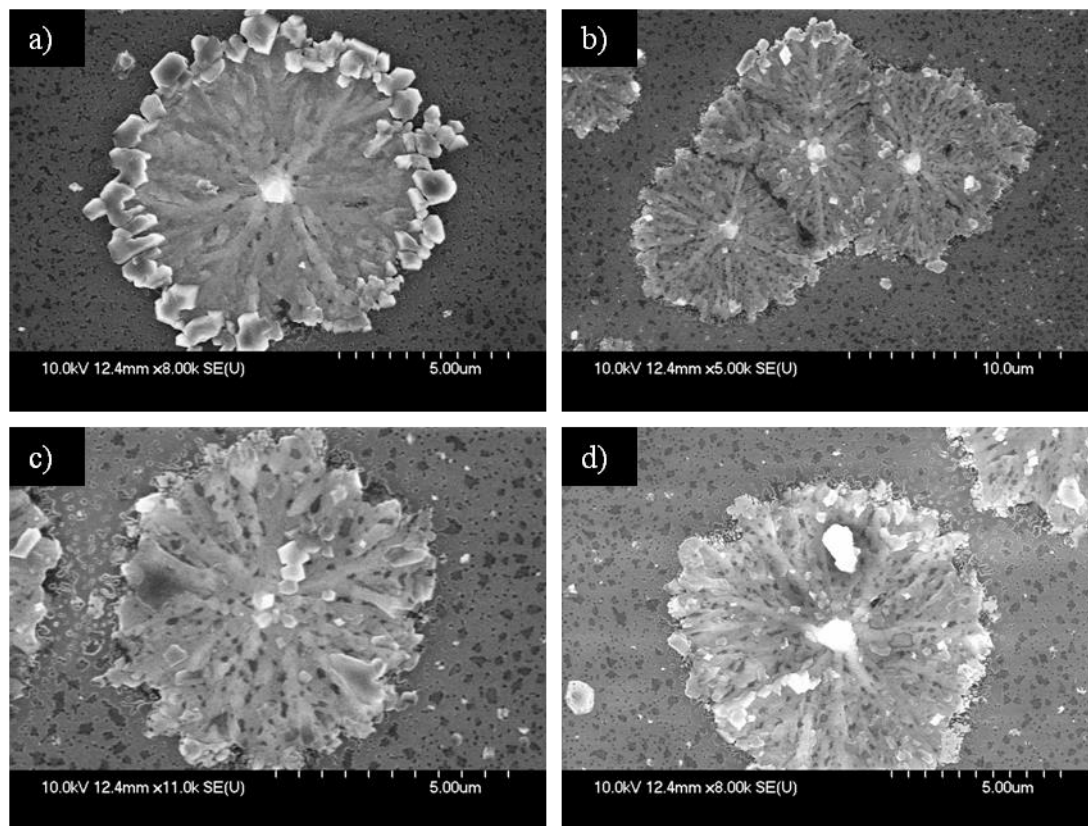


Figure 3-13: SEM micrographs showing substrate surface from vertical reaction (V1)

Samples showed circular islands of growth typically 5-10 μm in diameter. There was also an abundance of irregular shaped particles distributed across the surface. These reactions proved to be less predictable than the standard horizontal reactions described in Sections 3.2 and 3.3.

3.3.2.3 Crystalline phase identification

The metallic ingots formed in the bottom of the quartz tube were identified as consisting of Bi_2Te_3 . An example of this is shown in Figure 3-14.

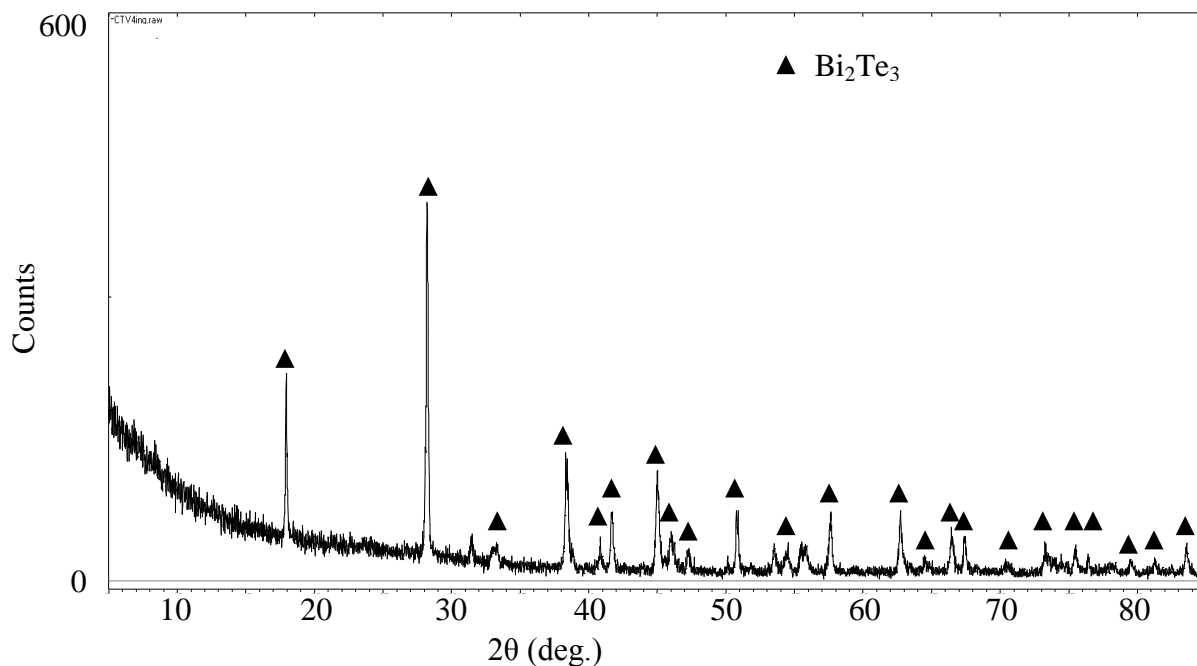


Figure 3-14: XRD pattern of ingots formed at the base of ampoule showing bismuth telluride (V1)

Figure 3-14 shows the presence of all major bismuth telluride peaks in the diffractogram. Two peaks (31 and 56 °2θ) can be attributed to a small excess of bismuth.

The XRD patterns from the substrates in this investigation showed little comparability to each other. This confirmed very little crystalline material had been deposited on the surface and that there was little consistency between depositions.

3.3.3 Conclusions

The variability of results with vertical reactions can be attributed to the reaction set up. The Kapton tape will have introduced an impurity not found in the horizontal reactions. Additionally the soda glass proved to be unsuitable for holding the substrate in position at an elevated temperature. After numerous vertical reactions, in addition to those reported here with poor and inconclusive results, vertical reactions were abandoned.

3.4 Temperature difference reactions

Described here is the CVD of bismuth and tellurium to induce surface growth of bismuth telluride on silicon substrates. This was achieved by application of a temperature gradient across a vacuum-sealed ampoule using the furnace seen in Figure 2-9. As mentioned in the introduction, there is very little information in the literature about the CVD of bismuth telluride from non-organic sources and no examples of using elemental reagents under

vacuum to deposit Bi_2Te_3 *via* a temperature gradient. This section targeted the production of a higher quantity of deposition material in comparison to the reactions conducted with the ampoule at a uniform temperature along its length. This was undertaken with a view to the optimisation of the deposition conditions.

3.4.1 *Reaction Set Up*

Reactions were carried out in a large tube furnace as shown in Chapter 2 (Figure 2-9). Initial reactions took place in standard CVD reaction vessels consisting of sealed ampoules ~ 30 cm in length. These reactions produced similar results to those reported previously in this chapter in the constant temperature reactions (Section 3.1). Further investigation revealed that no temperature difference was being created over the 10-15 cm gap between substrate and reagents. For the reactions reported here, the length of reaction vessel was extended to half the total length of the furnace tube (120 cm). Hence, 60 cm quartz ampoules were used. One end of which was placed at the hottest central point, and the other at the edge of the furnace tube at room temperature.

The temperature difference generated within the tube furnace was investigated by temperature mapping the length of the tube while the furnace was running at 700 °C. Temperatures were mapped to an accuracy of ± 0.5 °C. A long thermocouple was inserted into the tube furnace and the temperature at each centimetre along the length recorded. The results are plotted in Figure 3-15.

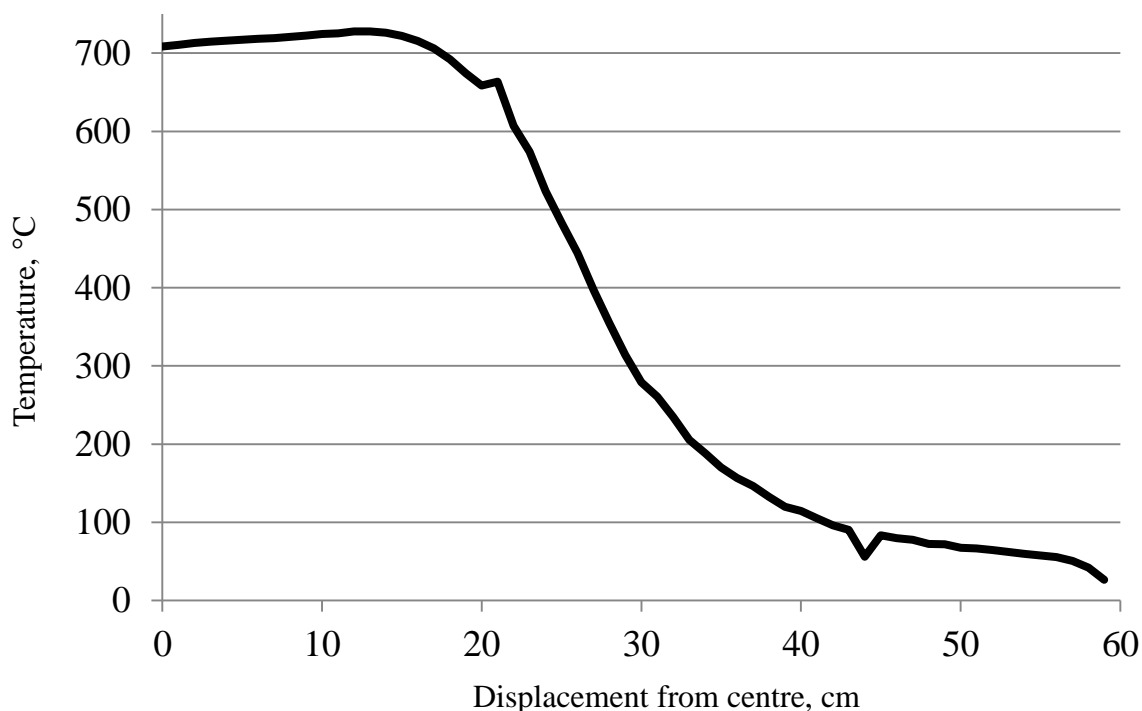


Figure 3-15: Temperature map of tube furnace. The small but sharp peaks at 20 and 42 cm are due to the edge of the heating element and the edge of furnace zone respectively.

In preparation for the experiments described in this section the likely areas of deposition were investigated. The ampoule was charged with, bismuth (8 mmol, 99% pure, 100 mesh, Sigma Aldrich) and tellurium (12 mmol, 99.8% pure, 200 mesh, Sigma Aldrich) and sealed under vacuum, and placed in the tube furnace at 700 °C (i.e. with the centre of the furnace held at this temperature). The end of the ampoule with the reagents was placed in the centre of the tube furnace with the opposite end placed at the end of the work tube of the furnace. The furnace was held at 700 °C for 48 h then allowed to cool. Areas of deposition were identified and silicon wafers were deployed in these regions. Silicon wafers (washed in acetone, deionised water and iso-propanol) were sealed in a quartz ampoule under vacuum.

3.4.2 Results

Samples L1 and L1(repeat) from Table 3-1 are described here as example systems.

The majority of powdered reagents had formed a single ingot at the hot end of the ampoule. Additionally there was a small ingot (with silver-metallic appearance) deposited at the cool end of the tube. Noticeably, there were two distinct rings of deposition, as shiny

metallic silver areas on the quartz. The areas of deposition along with the temperature map are shown in Figure 3-16.

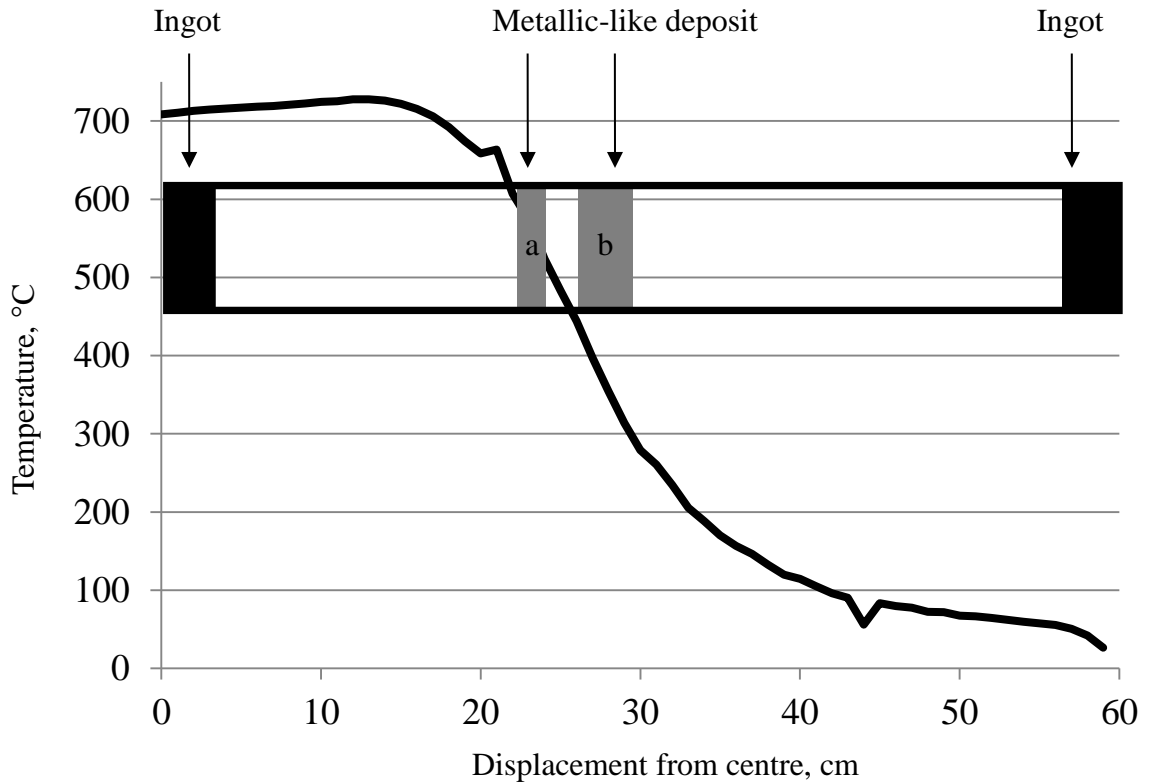


Figure 3-16: Temperature profile overlaid with scaled ampoule schematic showing grey and black bands indicating deposition regions. Region “a” represented the band of deposition in the hotter region and “b” the second band in the cooler region.

The areas of deposition along with correlating temperatures are shown in Table 3-5 below. Deposition bands a and b correspond to the areas of deposition in the hotter and cooler regions respectively.

Table 3-2: Deposition areas and temperatures

Name	Deposition band	Deposition areas from centre, cm	Temperature region, °C
L1	a	23.5-25.5	549-464
L1	b	27.0-30.0	397-279
L1(repeat)	a	22.0-24.4	607-506
L1(repeat)	b	26.0-30.0	444-279

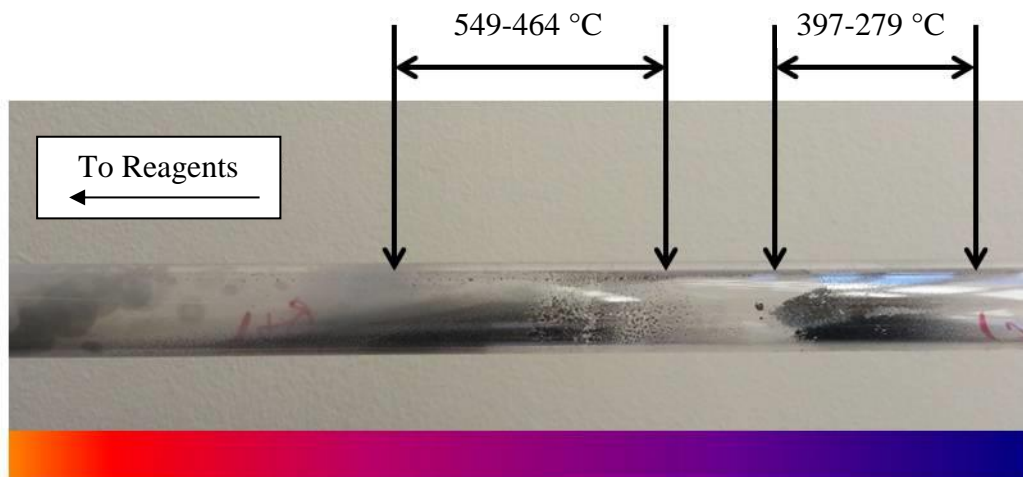


Figure 3-17: Reaction L1 showing distinct areas of deposition

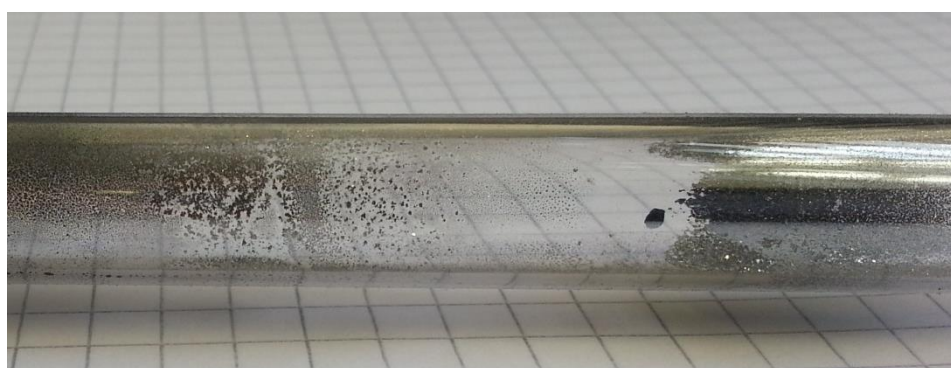


Figure 3-18: Area free from deposition (L1)

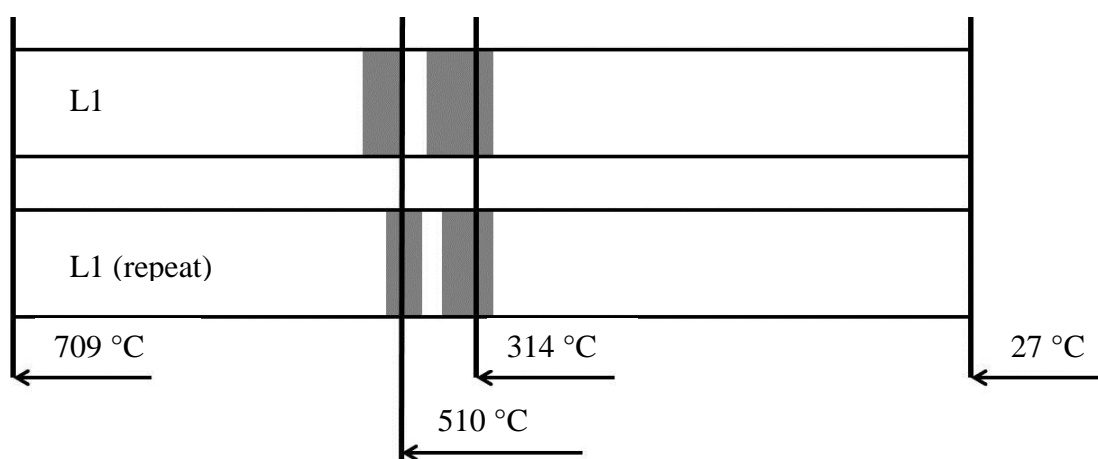


Figure 3-19: Schematic of deposition areas with temperature guides showing hottest area, coolest area and average deposition area temperature

The deposit on the walls of the tube was removed by scraping the walls of the vessel with a spatula. The area of deposition found at the hotter point was slightly darker in colour to

that of the cooler areas of the tube. The darker deposition was a fine powder with a grey appearance (Figure 2-20) and the cooler deposition had a shiny silver appearance (Figure 3-21). The cooler deposition tended to flake away from the surface of the quartz producing both a fine glittery powder and larger flakes (Figure 3-21).

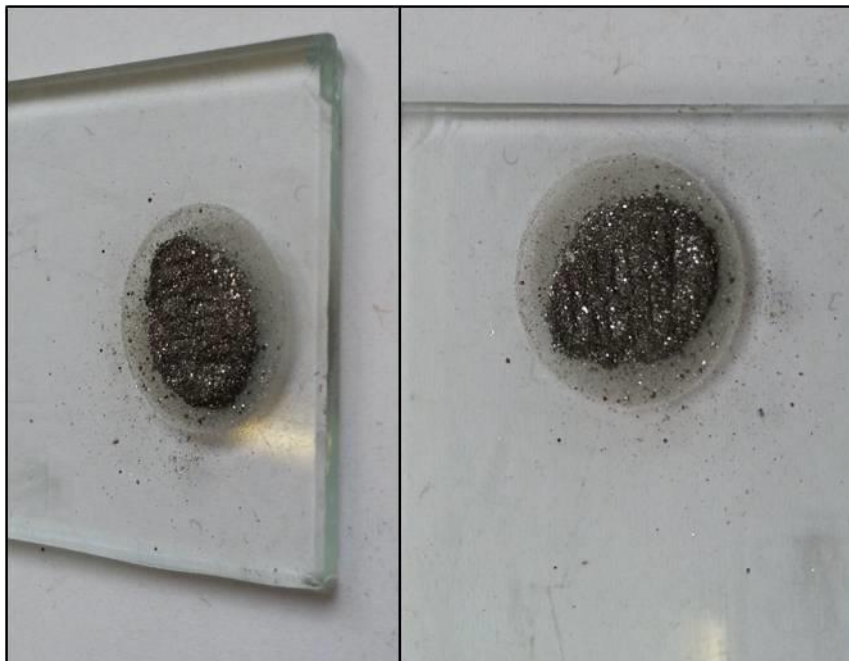


Figure 3-20: Darker material deposited at ~510 °C (sample L1)

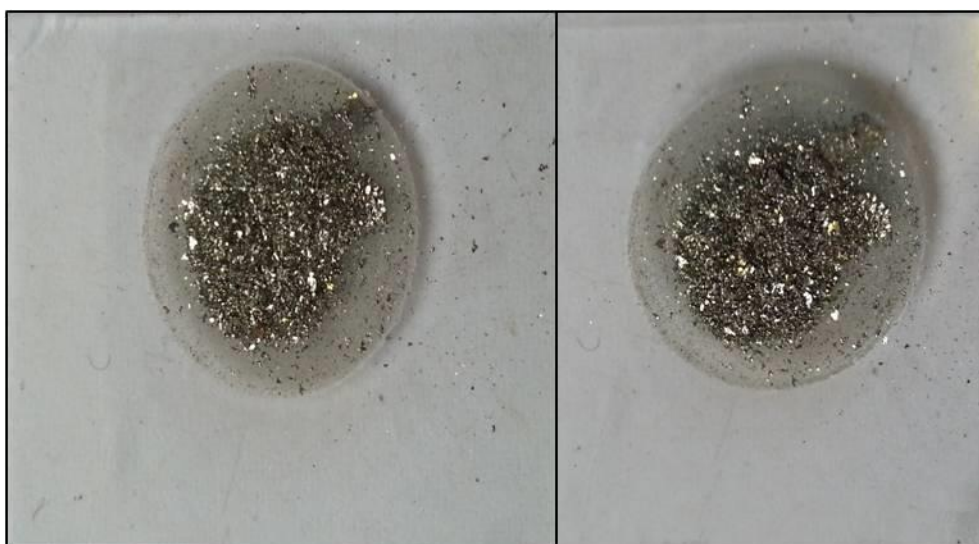


Figure 3-21: Lighter material deposited at ~314 °C (sample L1)

3.4.2.1 Crystalline phase identification

Powder XRD revealed the crystal phase of the deposition areas to be very different. The material in the hotter region of 464-549 °C was matched to single phase bismuth telluride.

The XRD pattern from sample L1 is shown below, L1(repeat) can be found in Appendix A (Figure 9-5).

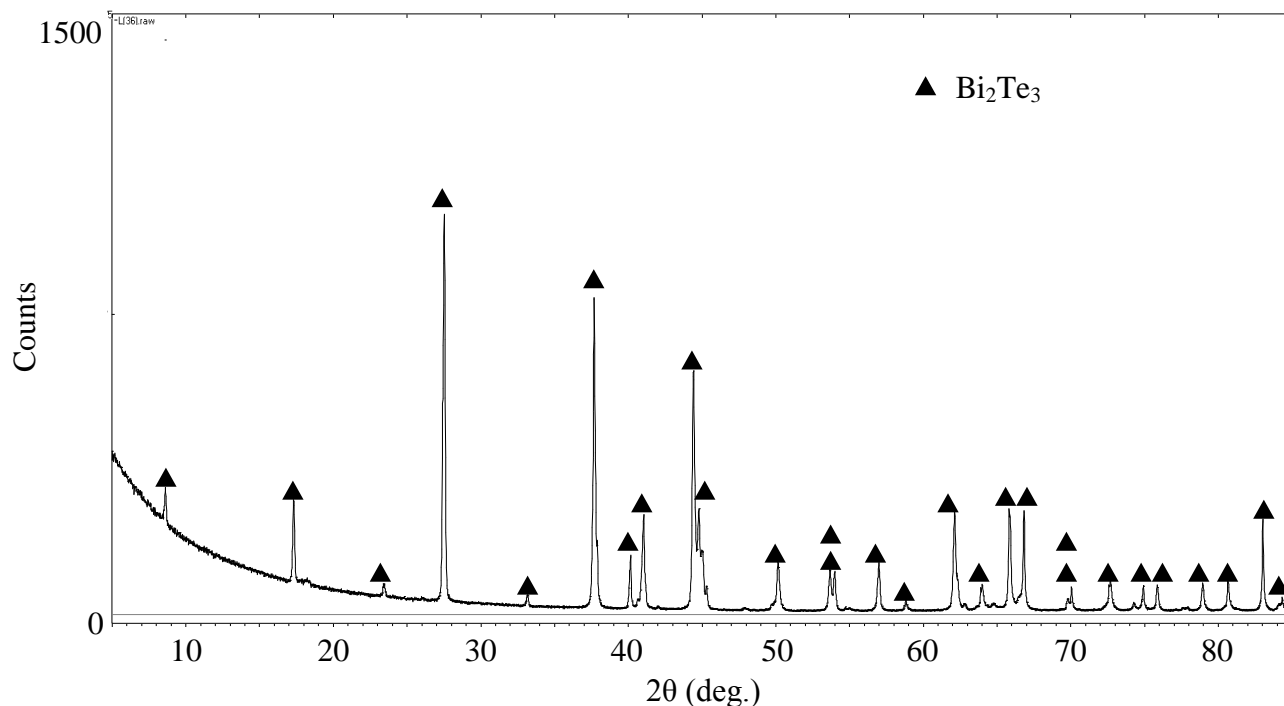


Figure 3-22: XRD pattern obtained from material found in hotter region of deposition showing single phase Bi₂Te₃ (sample L1)

The material recovered from the cooler regions (279-397°C) was matched to tellurium with a small quantity of bismuth telluride. Using the diffractometer's refinement tool, the deposit was identified as >90% tellurium. This was consistent across the range of samples produced with bismuth telluride present only in small (<10%) quantities.

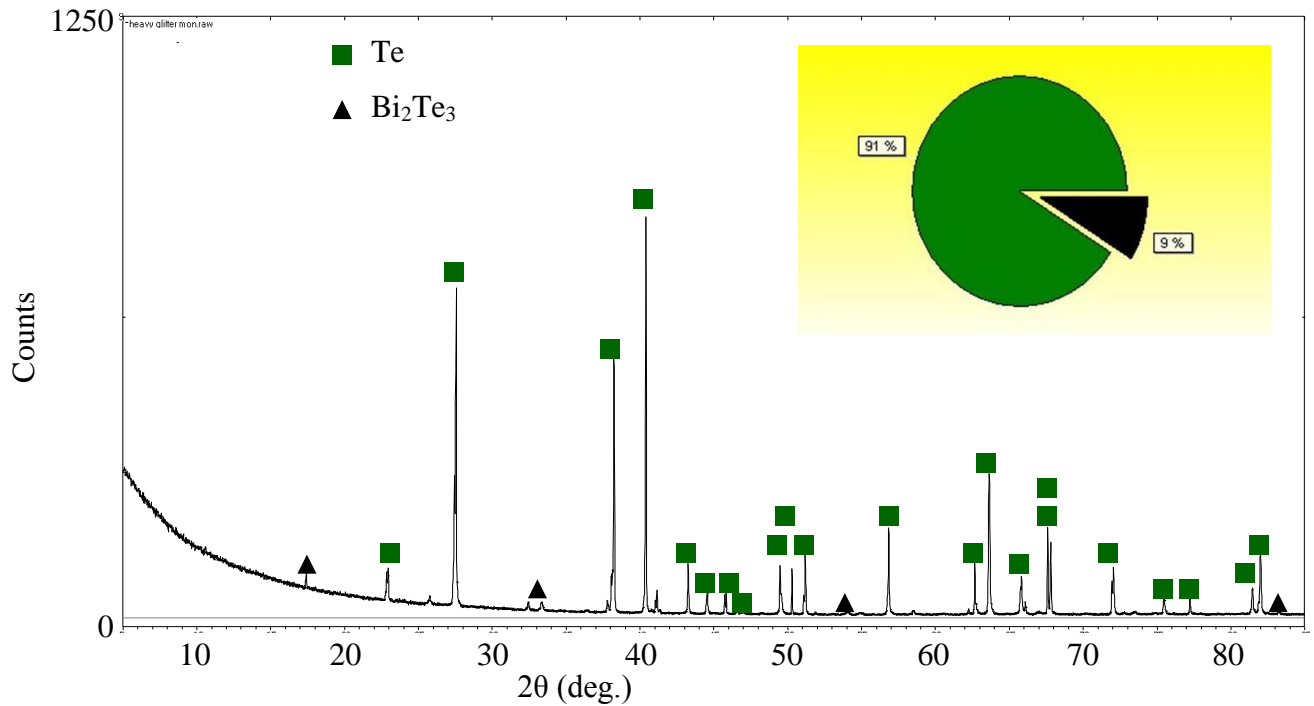


Figure 3-23: XRD pattern of material discovered in the cooler regions showing the transport and deposition of tellurium (sample L1). Inset shows percentage composition based on peak and profile fitting calculated by the Highscore programme from Panalytica

3.4.2.2 Morphology

SEM was used to observe the morphology of the particles from both areas. The bismuth telluride sample was composed of irregular micron-scale blocks of material. On closer inspection, these large blocks showed a layered appearance consistent with the crystal structure of bismuth telluride with its characteristic terminating layers. The layers were between 100 and 200 nm in thickness and 20-250 μm wide. In some areas the sheets had self-separated leaving the surfaces visible. A layer of 100 nm in thickness would represent 33 unit cells along the *c*-axis. These particles may make promising candidates for a mechanical exfoliation process to separate the individual layers.

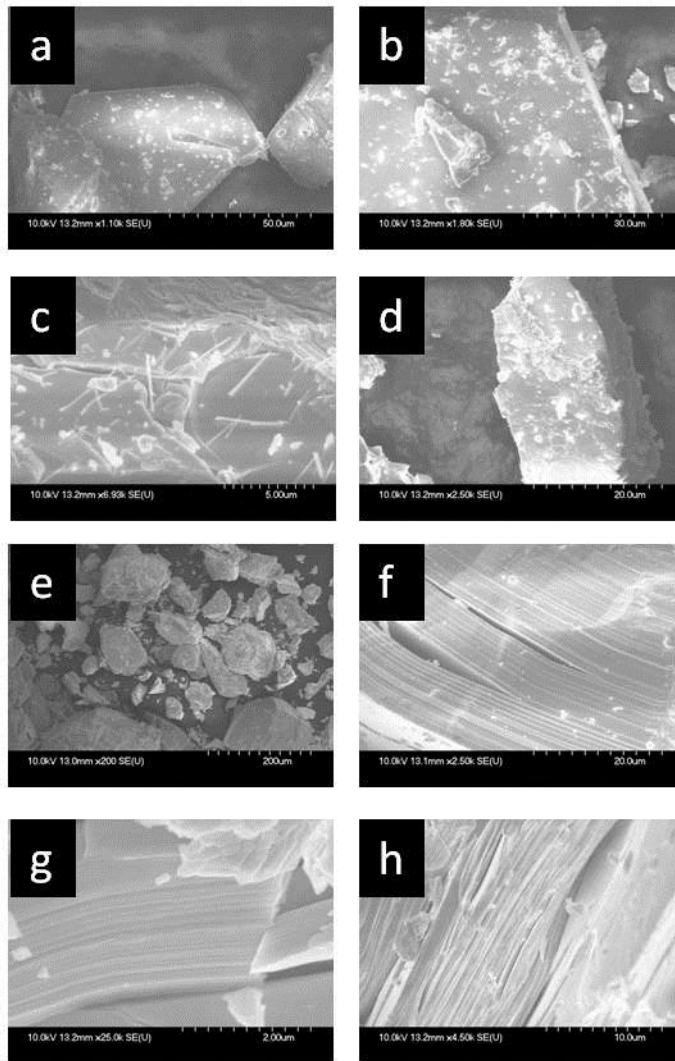


Figure 3-24: SEM micrographs of deposited bismuth telluride: (a-d) sample L1(repeat), (e-h) sample L1

The second area of growth, identified as tellurium by XRD, also showed a different particle morphology to the bismuth telluride particles. Selected samples and areas are shown in Figure 3-25.

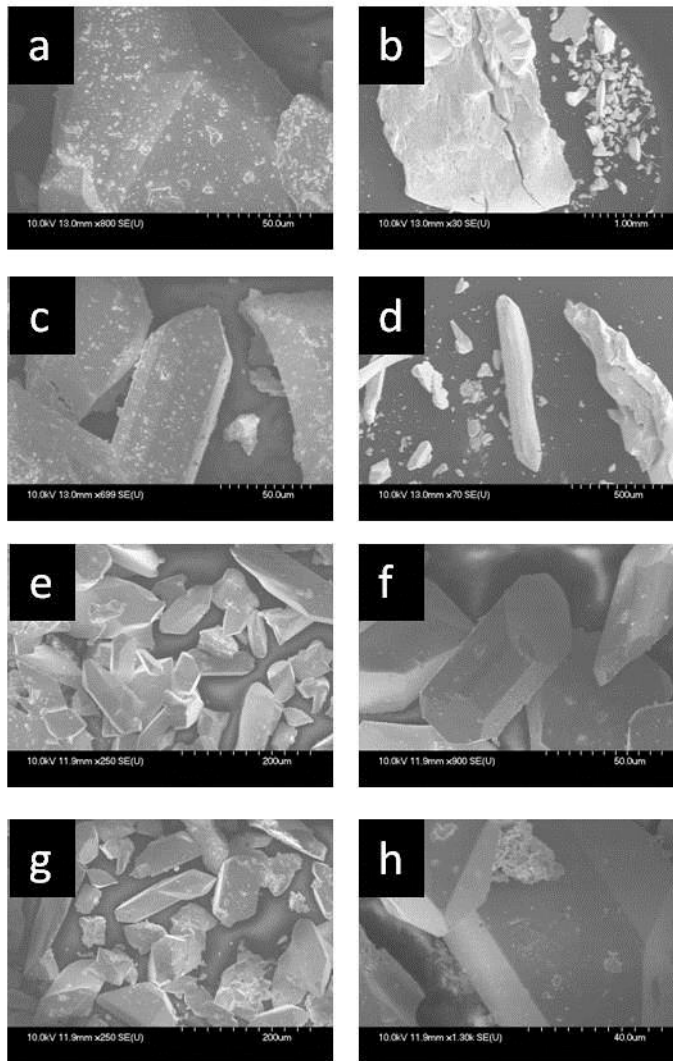


Figure 3-25: SEM micrographs of tellurium particles deposited in cooler region: (a-d) sample L1(repeat), (e-h) sample L1

The tellurium deposited in the cooler region showed prismatic or needle-like morphology. The needles were 200-600 μm in length and 40-100 μm in width with tapered ends.

3.4.2.3 Elemental Analysis

EDX was used to obtain information about elemental composition. The growth in the hotter region of the ampoules was identified to be Bi_2Te_3 . An example spectrum is shown in Figure 3-26. This spectrum was taken from the particle shown in Figure 3-24 f (sample L1). An EDX spectrum from the hotter region of sample L1 (repeat) matching to Bi_2Te_3 can be found in Appendix A (Figure 9-6).

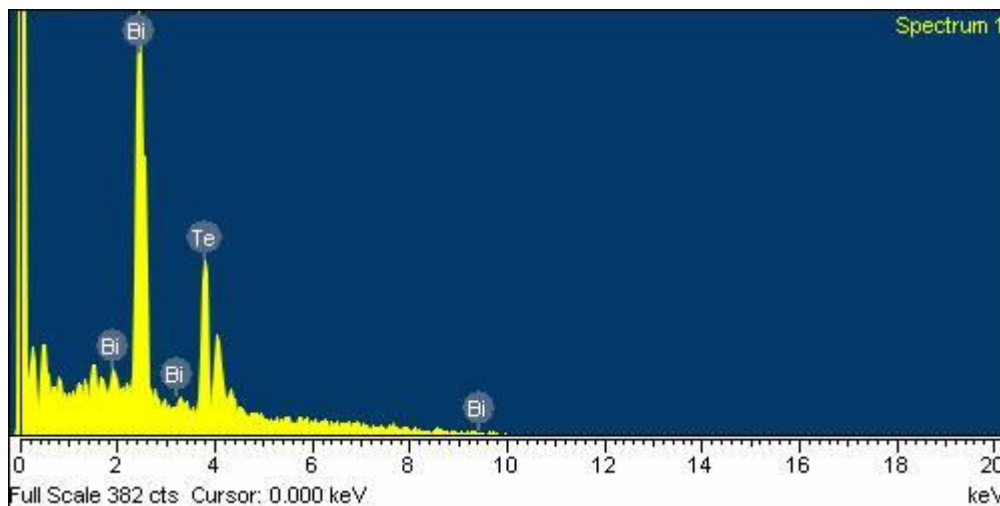


Figure 3-26: EDX spectrum taken from hotter region growth of L1 matching Bi_2Te_3

The EDX spectra obtained from the cooler region showed the presence of tellurium exclusively. Figure 3-27 is an example spectrum taken from the cooler region of L1. The small quantity of carbon identified is attributed to the carbon tab on which the sample was held and the sample is therefore elemental tellurium. An EXD spectrum of L1 (repeat) matched to tellurium can be seen in Appendix A (Figure 9-7).

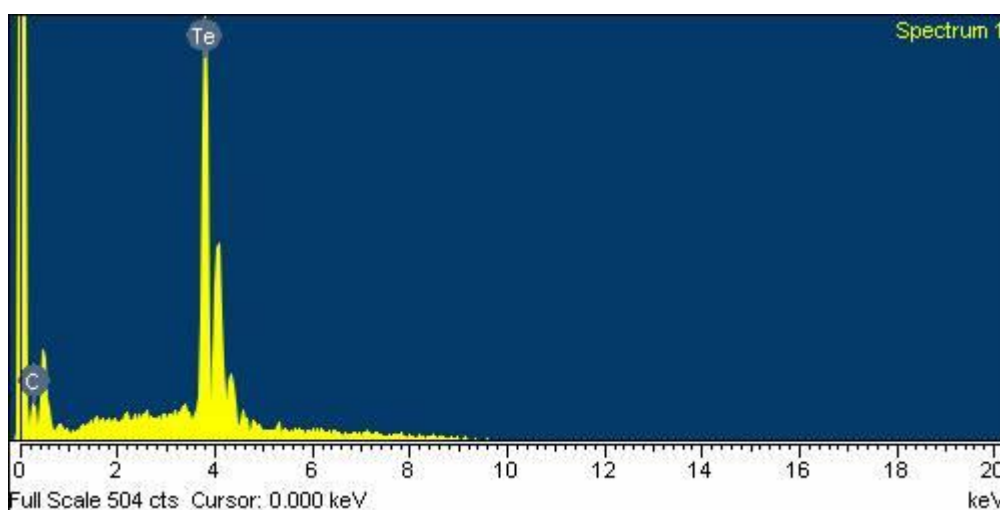


Figure 3-27: EDX spectrum of sample L1 showing elemental tellurium (carbon peak caused due to the carbon tab holding the sample)

3.4.3 Conclusions

Presented here is the growth of bismuth telluride and tellurium particles by use of CVD. Two distinct growth regions were produced by applying a temperature gradient. In the hotter region of 549- 464 °C bismuth telluride was grown and at 397- 279 °C tellurium was deposited. Deposited materials were analysed by use of powder XRD for phase

identification, SEM to determine particle morphology, and EDX for elemental composition. It was shown that bismuth telluride was deposited with irregular morphology with a nanoscale layered structure (visible on high magnification). The tellurium was found to have a micron-dimensioned prismatic-like morphology.

The hotter deposition region 549- 464 °C is comparable to that reported by Kong *et al.*,¹¹¹ where they used an argon flow to deposit layers of Bi₂Te₃ from a preformed starting material. With the method described here, it is possible to grow material using elemental reagents without the need for a transport gas.

The unique layered structure of the bismuth telluride deposition is extremely interesting as some gaps between layers are visible and it may be possible to separate the layers into thinner sheets. There are reports of bismuth telluride being either chemically or mechanically exfoliated to create ultra-thin sheets¹¹²⁻¹¹⁴. The particles synthesised in this work may be suitable for such applications. It would also be interesting to measure the electrical and thermal properties of these particles to quantify the effect nanostructuring has on the thermoelectrical properties. As this bulk material is composed entirely of nanostructured sheets, stacked to be 10-50 µm thick with a high aspect ratio, they represent promising nanostructured bulk materials.

3.5 Transport agent reactions

Often in CVD an additional agent is introduced to facilitate the transport of desired reagents. Iodine has proven useful as a transport agent in growing chalcogen materials such as molybdenum disulfide¹¹⁵, and in the growth of other semiconducting materials such as GeAs¹¹⁶. Feutelais *et al.* successfully used iodine as a transport gas to synthesis plates of bismuth telluride on the millimetre scale¹¹⁷. Here iodine was used alongside elemental reagents in an effort to improve surface coverage across the substrate.

3.5.1 Reaction set up

Reactions were set up as previously described (Section 2.1). Square centimetre Si pieces were sonicated in deionised water followed by acetone then iso-propanol. After this cleaning process, the oxide layer was removed with a 5:1 NH₄F/HF buffered solution.

Clean wafer pieces were sealed in a quartz ampoule under vacuum. The reagents for these reactions were: bismuth (2 mmol, 99% pure, 100 mesh, Sigma Aldrich), tellurium (3 mmol, 99.8% pure, 200 mesh, Sigma Aldrich) and iodine (0.4 mmol, granular, Sigma Aldrich).

Sealed tubes were heated in a tube furnace set at 500 °C for 48 h. The 500 °C temperature was selected for safety reasons as introducing iodine to the reaction leads to increased pressure inside the ampoule. A temperature difference was applied across the tube with the substrate at the cooler end (457-459 °C). The reagents were positioned several centimetres away and exposed to a temperature of 499-503 °C while the substrate was held at 457-459 °C

3.5.2 Results

Sample T1 from Table 3-1 is described here as an example system.

3.5.2.1 Post-reaction appearance

Following heating and cooling, the iodine had moved from the reagent end of the quartz tube across the substrate to the opposite end of the tube. The iodine had formed a single crystal at the furthest end of the ampoule having moved past the substrate.

In reactions without a transport agent, it is usual for reagents to form an ingot at the hot region of the tube, however with reactions involving iodine, the elemental reagents had remained as a powder. The only change in appearance over the course of reaction was a darkening of the reagents from grey to black.



Figure 3-28: Black powder obtained from reaction T1

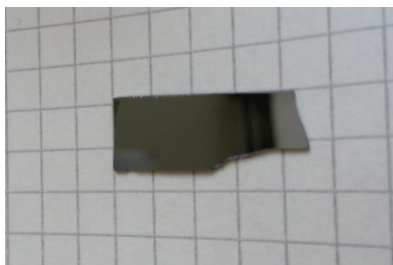


Figure 3-29: Substrate (T1) post reaction

There was no evidence of deposition on the surface of the substrate.

When sealed in a sample vial it became evident that the substrate had become infused or coated in iodine as there was distinctive discolouration of the storage vial's plastic lid (Figure 3-30).

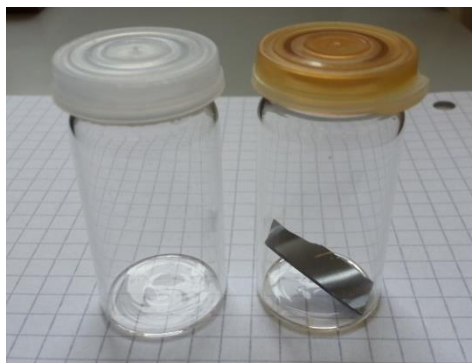


Figure 3-30: Discolouration of sample vial lid due to iodine T1 substrate on the right

3.5.2.2 Crystalline phase identification

Powder XRD did not identify any deposition on the substrate and the standard pattern for silicon was obtained.

X-ray analysis of the powder remaining at the reagent end of the tube revealed that the bismuth and tellurium had not reacted with each other (Figure 3-31).

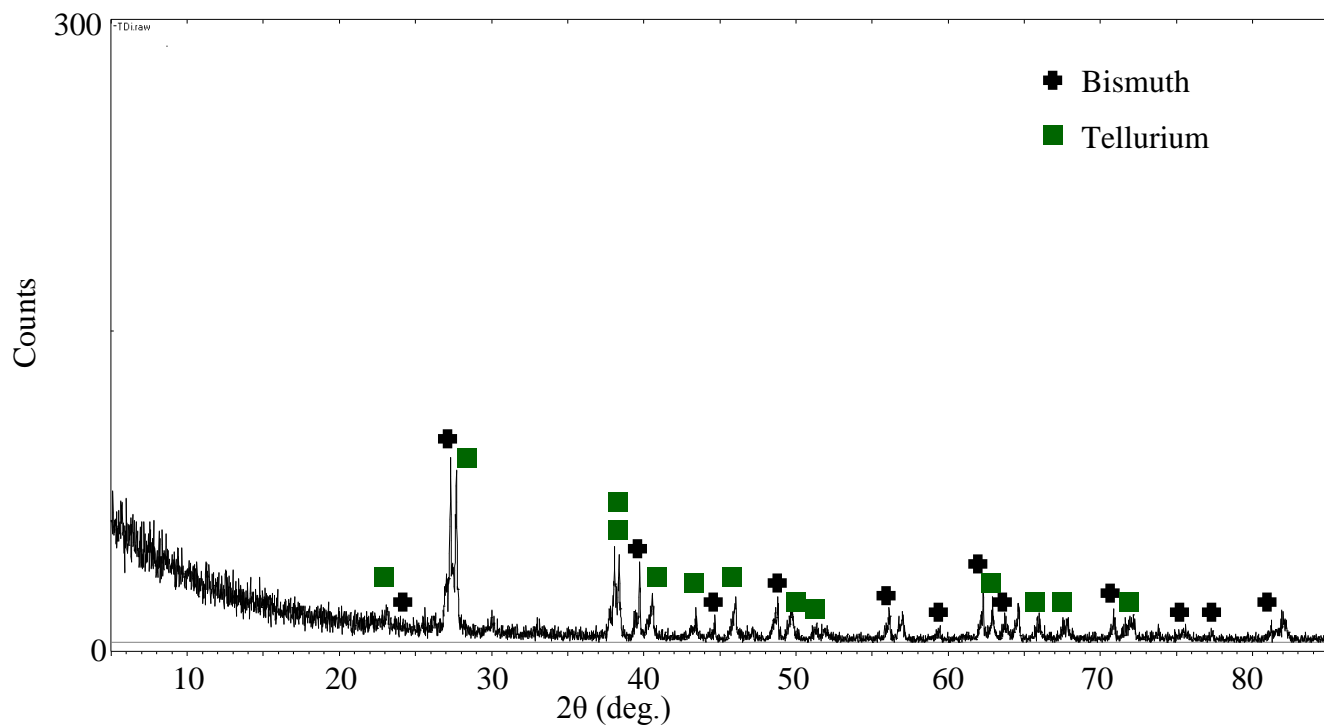


Figure 3-31: XRD pattern of sample T1

3.5.3 Conclusions

It is clear from the above reactions that iodine was hindering, rather than assisting, the transport and reaction of materials. The iodine had vaporised and had been transported to the opposite end of the vessel, and in the process of doing so had actively stopped bismuth and tellurium from reacting or reacting or migrating. Reactions of the type above were the only reactions carried out at elevated temperatures in which the elemental reagents remained powdered and unreacted.

3.6 Bismuth reactions

Reported here are attempts to grow low dimensional structures of bismuth on the surface of silicon *via* chemical vapour transport from the elemental powder. It has been shown that tellurium can be incorporated into bismuth structures to produce (2:3 stoichiometric or otherwise) bismuth telluride. As such the aim was to grow structures on the surface which could later be reacted with tellurium to produce new particle morphologies of bismuth telluride.

3.6.1 Reaction set up

Reactions were set up as described previously. Square centimetre Si wafer pieces were sonicated in deionised water followed by acetone then iso-propanol. After this cleaning process, the oxide layer was removed with a 5:1 $\text{NH}_4\text{F}/\text{HF}$ buffered solution. Clean wafer pieces were sealed in a quartz ampoule under vacuum following the standard process previously described. The reagent for these reactions was bismuth (2 mmol, 99% pure, 100 mesh, Sigma Aldrich). Sealed tubes were heated in a box furnace at 700 °C for 48 h.

3.6.2 Results

Samples B1 and B1(repeat) from Table 3-1 are described here as example systems.

3.6.2.1 Post-reaction appearance

Quartz tubes showed clear transport of the bismuth. Most of the reagent had formed a single shiny metallic like ingot while some material had transported and condensed at the far end of the tube forming numerous droplets approximately 1-2 mm in diameter.

The substrates appeared clean to the naked eye. Shown below are samples B1 and B1(repeat) following reaction, which retain the mirror-like appearance of the silicon wafer.

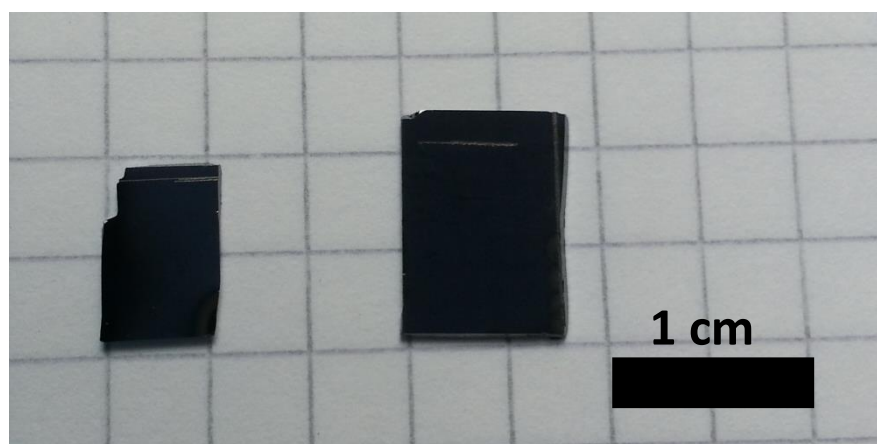


Figure 3-32: Si pieces post-reaction (B1 and B1(repeat))

3.6.2.2 Morphology

SEM showed no discernible structures on the surface of the wafers.

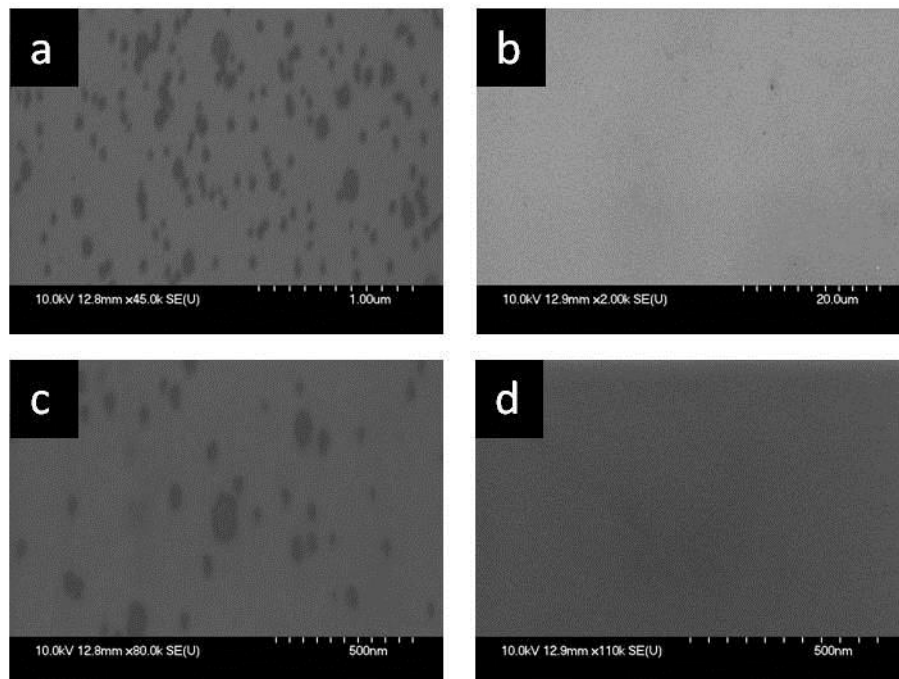


Figure 3-33: SEM micrographs of B1 (a and c) and B1(repeat) (b and d)

There was some speckled discolouration on the surface of B1. The contrast difference observed in SEM imaging suggests there may have been an interaction on the surface with the bismuth but insufficient for particle growth. It is not expected for bismuth to penetrate the silicon surface in a similar manner to that of gold ¹¹⁸.

3.6.2.3 Crystalline phase identification

Powder XRD did not detect any deposition peaks (showing only silicon).

3.6.3 Conclusions

The attempted growth of bismuth structures on clean silicon using CVT was not successful. While the bismuth was transported, as evidenced by the formation of ingots at the opposite end of the reaction vessel, there was no growth of structures at the silicon substrate surface observed on any samples.

3.7 Equimolar bismuth/tellurium reactions

Previous work indicated that an excess of tellurium was deposited on the surface of the silicon during CVD of bismuth and tellurium and while stoichiometric bismuth telluride could be successfully grown, there were cases where additional structures of tellurium

were identified. To create a phase pure system, reactions were carried out using a non-stoichiometric ratio of bismuth and tellurium.

3.7.1 *Reaction set up*

Reactions were set up as described previously. Square centimetre Si wafer pieces were sonicated in deionised water followed by acetone then iso-propanol. After this cleaning process the oxide layer was removed with a 5:1 $\text{NH}_4\text{F}/\text{HF}$ buffered solution. Clean wafer pieces were sealed in a quartz ampoule under vacuum. The reagents for these reactions were bismuth (6 mmol, 99% pure, 100 mesh, Sigma Aldrich) and tellurium (9 mmol, 99.8% pure, 200 mesh, Sigma Aldrich). Sealed tubes were heated in a Carbolite box furnace at 700 °C for 48 h.

3.7.2 *Results*

Samples EB1 and EB1(repeat) from Table 3-1 are described here as example systems.

3.7.2.1 *Post-reaction appearance*

In all cases the reagents had formed into one or two ingots at the reagent end of the tube. Metallic-like droplets formed on the lower internal surface of the quartz tube (the lower side rests on a furnace brick within the furnace). These droplets were each <2 mm in diameter.

The surface of each of the substrates was speckled with a white deposit (Figure 3-34). The deposited material was scattered irregularly across the surface of the silicon.

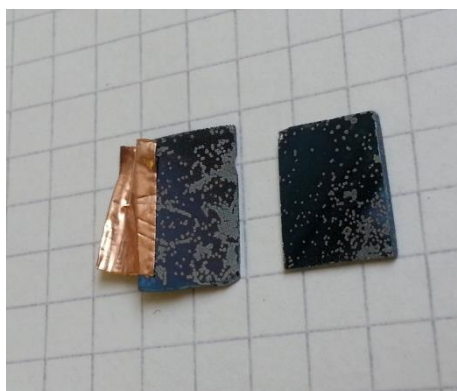


Figure 3-34: Si pieces post-reaction (EB1 and EB1(repeat))

3.7.2.2 Morphology

SEM images showed extremely interesting particle growth and the presence of nanowires growing from larger particles (Figures 3-35 d-f).

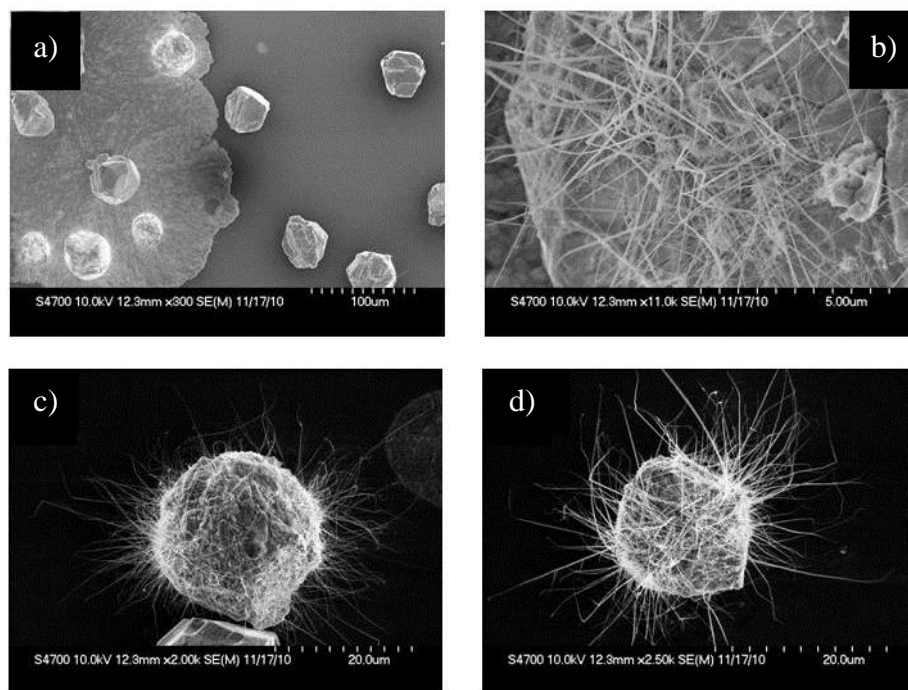


Figure 3-35: SEM micrographs of EB1 (a and b), EB1(repeat) (c and d) showing nanowire growth

These wires were not found in any CVD reaction involving a 2:3 ratio of bismuth and tellurium, respectively, but were found in every reaction involving a 1:1 ratio. In all cases the wires were seeded from larger particles (Figure 3-35 c and d). No wires were found detached from a larger structure or growing directly from the surface. Wires were around 100 nm thick and up to 40 μm in length. While many of the base particles had an irregular shape, all were approximately 30 μm in diameter. Almost all larger particles had wire growth on the surface but in varying amounts. Figure 3-35 (a) shows a particle with a low concentration of wires, whereas Figure 3-38 shows a particle entirely encased in wires.

The growth seen on the left hand side of Figure 3-35 (a) above should be noted. This structure was seen on each of the substrates and is responsible for their white colour. This is believed to be an oxide phase, as EDX showed higher than background oxygen levels. This distinctive pattern of growth was seen on each of the substrates, it can be seen in the top corner of Figure 3-35 (b) above. The particle distribution and wire growth seemed to bear no relation to the presence of the oxide phase in each reaction. Similar areas were also

seen on substrates, where a 2:3 stoichiometry was used (Section 3.4). These areas are attributed to an oxide contaminant.

Figure 3-36 below shows an SEM micrograph of a single wire from sample EB1(repeat). This wire was 60 nm thick and 20 μm long.

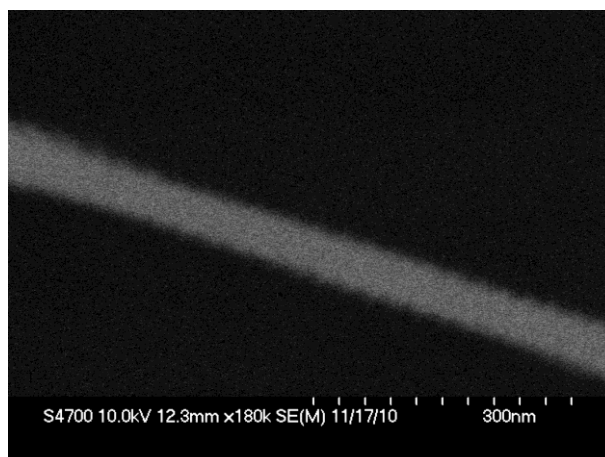


Figure 3-36: SEM micrograph of a wire from sample EB1(repeat)

This wire is typical of those found in all reactions. Wires were <100 nm in diameter and 10's of microns in length. They also showed a uniform diameter throughout the length with a slight tapering off at the end.

3.7.2.3 *Elemental Analysis*

EDX showed a higher concentration of bismuth in the wire covered areas. Areas of particle growth absent of wires showed a 2:3 stoichiometry for the bismuth/tellurium ratio. However wire areas showed an average Bi content of 50-55%.

As all wires grow from larger particles, it is impossible to take readings of the wires exclusively due to the underlying particle from which the growth was seeded. Wires which grew away from the particle were too narrow and in too low a concentration to obtain a conclusive reading of the elemental composition of the wires.

3.7.2.4 *Crystalline phase identification*

Powder XRD confirmed the presence of bismuth telluride and also showed the presence of $\text{Bi}_4\text{Si}_3\text{O}_{12}$. Shown below is the XRD pattern of EB1 (Figure 3-37). Sample EB1 shows

characteristic silicon peaks as well as those of Bi_2Te_3 and bismuth silicon oxide. The XRD pattern in Figure 3-37 is presented using an expanded scale to show the low intensity peaks of the oxide phase. The pattern obtained for EB1(repeat) can be found in Appendix A (Figure 9-8).

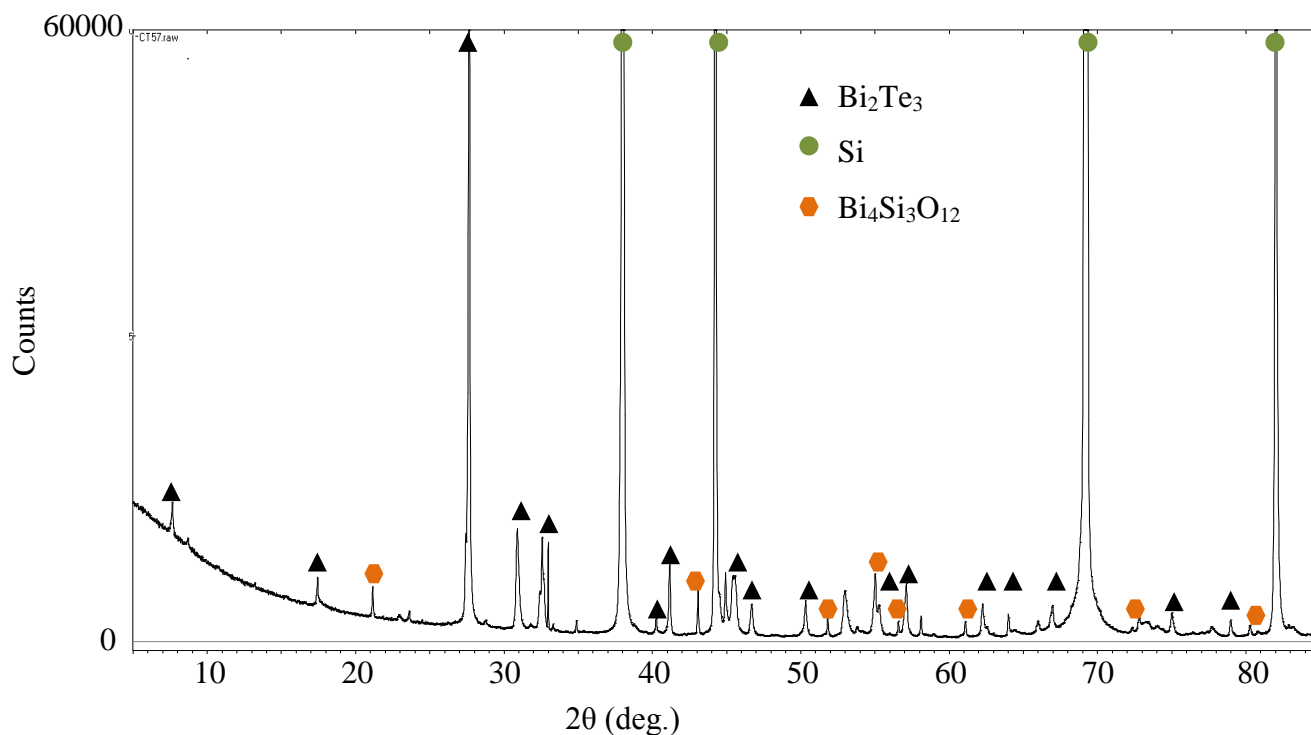


Figure 3-37: XRD pattern of sample EB1 showing presence of bismuth telluride

3.7.3 Conclusions

Bismuth-rich nanowires were discovered to grow having been seeded from the surface of bismuth telluride particles. Wires were discovered to grow in all cases when bismuth and tellurium were used in a molar ratio of 1:1. Wires were up to 40 μm long (though most were of 20-30 μm length) and had an average diameter of 100 nm. The wires did not deposit on the silicon substrate.

Larger particles were distributed across the entire surface of the substrate and almost all particles displayed wires, although in differing concentrations. Particles with 20-50 wires were observed, as in Figure 3-35 (a), as well as particles with more numerous wires to the point of covering the entire underlying particle, e.g. Figure 3-38.

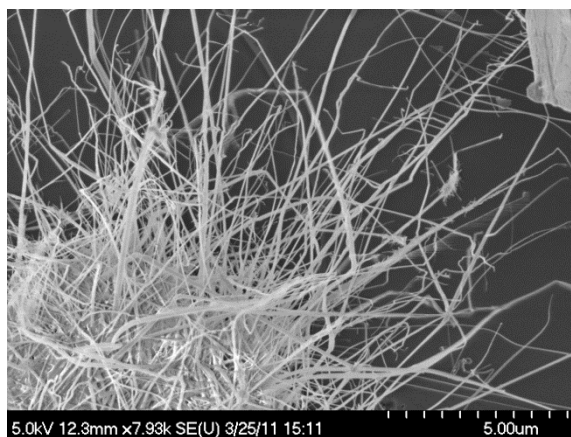


Figure 3-38: SEM micrograph showing particle which is fully encased in nanowires EB1 (repeat)

EDX confirmed these wires as 50-55% bismuth but due to the underlying material, exact determination of the stoichiometry is difficult. For XRD, the wires are in such low concentrations, in comparison to bismuth telluride and silicon, that no peaks were discovered or assigned to them.

Future work would involve removing the wires from their base particles. The wires are thin and well suited for TEM and EELS analysis to determine composition and growth mechanism. As with the octahedral particles described earlier in this chapter, there was some degree of movement of the wires and particles by the electron beam during SEM analysis, suggesting that particles could be easily and gently removed from the silicon.

3.8 Test structure

This chapter has detailed routes to materials of varying morphologies with potential thermoelectric properties. The next step is to obtain measurements of the electrical and thermal properties of these materials. This project concentrated on the synthesis of morphologies rather than the measurement of material properties, however reported in this section is a test structure designed during this work as a means to obtain further information about low dimensioned particles. There was not scope during the project for this device to be fabricated but dimensions and functionality are described here that the structure may be produced subsequently.

The testing of new materials for thermoelectric applications has proved problematic. Often, as in the case with this work, experimental materials are not prepared in the multi-gram quantities required for standard measurements of thermal and electrical properties. The

second problem is that of density, once sufficient quantities of low dimensional material is obtained. Low dimensional materials can be pellet pressed and these used for electrical and thermal testing, however if these pellets are not pressed to sufficient density then the thermoelectric properties recorded may not be a true reflection of the material properties. Thermoelectric materials require good electrical conductivity with a comparatively low thermal conductivity. If materials are not sufficiently dense this will greatly affect the electrical conductivity of the sample. A material which is insufficiently dense will have significantly poorer electrical conductivity due to the electrons being unable to transfer through any small gaps in material contact. The normal method to avoid density issues is pressing of materials at elevated temperature and pressure. The proposed method removes density problems by detailing testing of individual particles as opposed to pressed bulk material.

To obtain good property measurements certain conditions must be fulfilled. Good electrical contacts must be made; this should be done with 4 electrical contacts so that the 'contact resistance' between sample and metal can be calibrated. The particle must be exposed to a well calibrated thermal gradient, where one side of the particle is a different temperature to the other.

The device shown below is a metallic circuit deposited on either a silicon nitride wafer or a silicon nitride topped silicon wafer (Figure 3-39). A gap is chemically etched down creating a hole in the centre. On either side, electrical circuits are printed consisting of three parts. The three parts of the circuits are: a copper conductor designed to make electrical contact to the particle, a platinum strip which will serve as a thermometer, and a nickel-chromium heater.

Testing of individual particles also has difficulties. One significant problem which must be overcome is the challenge of creating a temperature difference over small areas.

The device described below uses a vacuum to isolate thermal elements to minimise thermal radiation and ensure that the main source of thermal transport is through the particle. The structure is shown in Figure 3-39. The device is designed so that the particle will cross the gap in the middle creating a bridge between the two identical sides.

Each colour in the diagram represents a different material with a specific purpose. The key and role of material is shown in Table 3-3.

Table 3-3: Key showing representations and properties of materials for use in the test structure

Colour	Material	Role	Rational for chosen material
Cyan	Silicon nitride	Provides the support structure	Low thermal conductivity
Orange	Copper	Electrical contacts, resistance measurements	Good electrical conductivity, stable, cheap
Green	Nickel-chromium alloy	Heater	High resistance therefore high capacity for joule heating
Grey	Platinum	Thermometer	Strong correlation between temperature and conduction

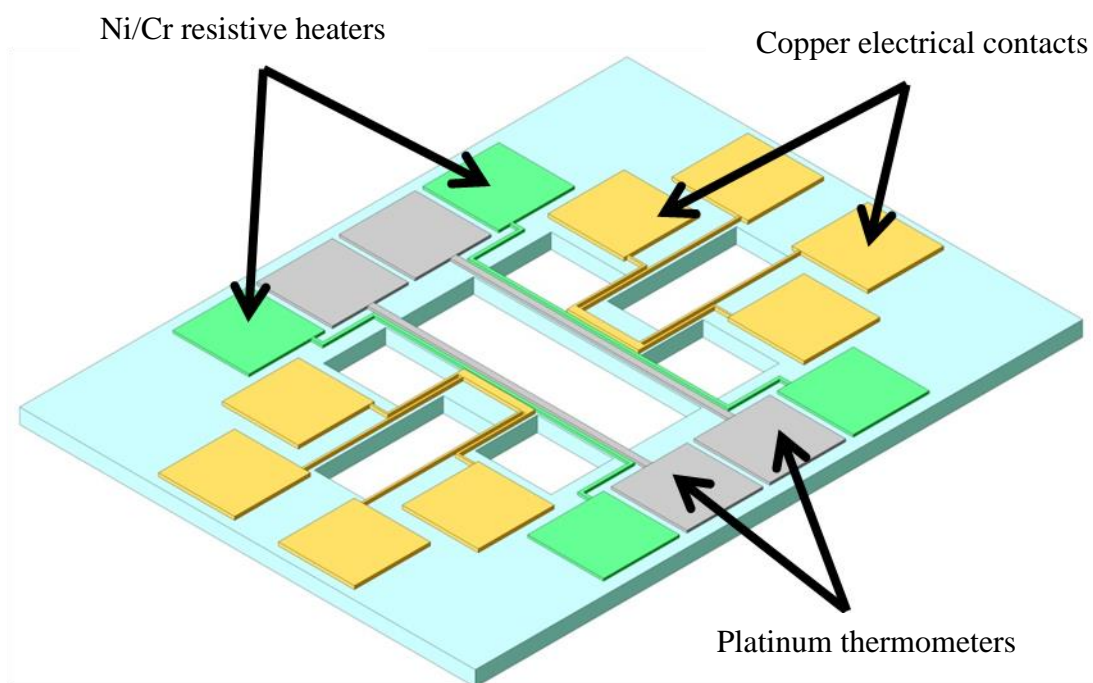


Figure 3-39: Isometric view of the test structure. The base is silicon nitride with deposited copper, nickel-chromium and platinum. The large squares of deposit are bond pads suitable for connecting the device to external electrical contacts

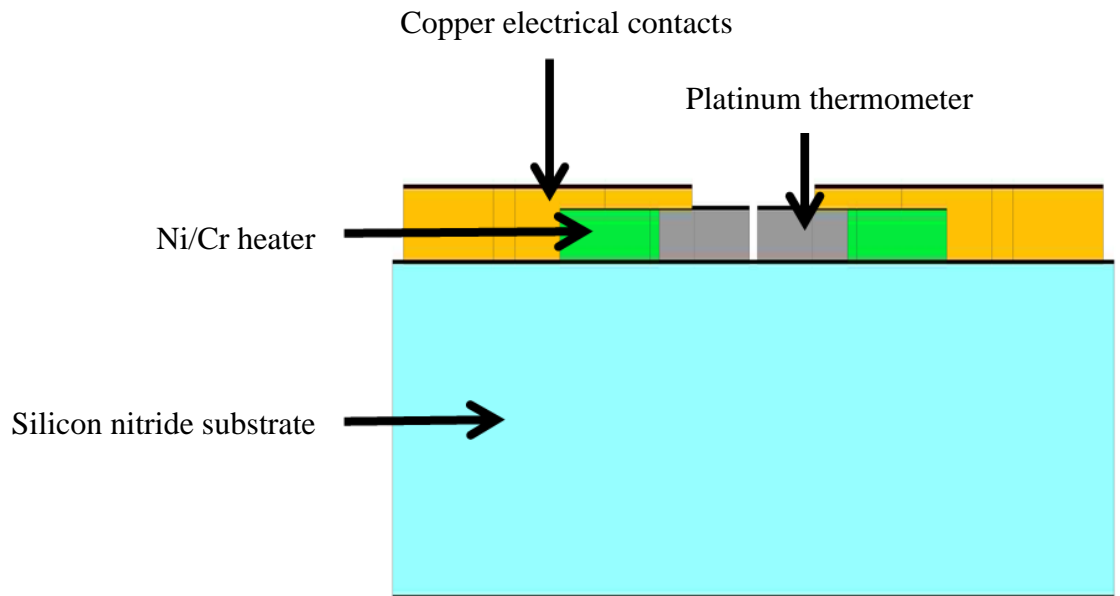


Figure 3-40: Truncated side elevation of test structure showing the silicon nitride base with deposited material on the surface

The base structure, shown in cyan above is composed of silicon nitride. This is grown to a minimum height of 2 μm on a silicon wafer (not shown). Silicon has a thermal conductivity almost 5 times that of silicon nitride, therefore the latter is more suitable for thermal isolation of particles. When this insulating nitride layer is deposited, it can then be etched to create the holes over which particles can be suspended, further ensuring thermal isolation. Photoresist (a light sensitive material which can be used for surface patterning) can be deposited on selected areas of the surface of the silicon nitride using photolithography and when fully developed, can be used as a protective barrier. The photoresist protects covered areas while the seven holes required can be etched out in areas not covered by the photoresist.

The second phase in production is the deposition of the metals. The copper will be used to obtain electrical conductivity of the particles. Copper is one of the most common metals used for low dimensional circuits, having good electrical conductivity. A nickel-chromium alloy will act as a resistor and heater. When a current is passed along the Ni/Cr alloy wire, the resistivity will create Joule heating for temperature gradients. Finally, platinum will be used as a thermometer. Platinum has a resistance highly dependent on temperature and by monitoring the resistance of this wire the temperature can be recorded. The large squares

are to be used as bonding pads to form electrical contacts with fine electrical probes placed directly on to the pads, or wire-bonded on.

Photoresist is used to selectively mask areas while different metals are deposited. The resistance of the metal is important when considering the heating of the device. Resistance is related to the dimensions of the wire by the following relationship where R is resistance, ρ the resistivity of the material, l the length of the wire and A the cross section area of the wire:

$$R = \frac{\rho l}{A} \quad (3-1)$$

It is also essential that only copper metal be in contact with a particle suspended over both sides of the circuit so all electrical conduction will flow along the copper as the path of least resistance and an accurate measurement of the electrical conductivity obtained. To ensure copper is the only metal surface exposed it is deposited significantly thicker than the other metals. Finally the entire structure except the copper is covered in an insulating layer of silicon nitride. Proposed metal thicknesses are shown below in Table 3-4.

Table 3-4: Material deposition thickness

Colour	Material	Thickness (nm)
Cyan	Silicon nitride	2000
Orange	Copper	450
Green	Nickel chromium alloy	318
Grey	Platinum	318

The key dimensions of the structures are shown in Figure 3-42.

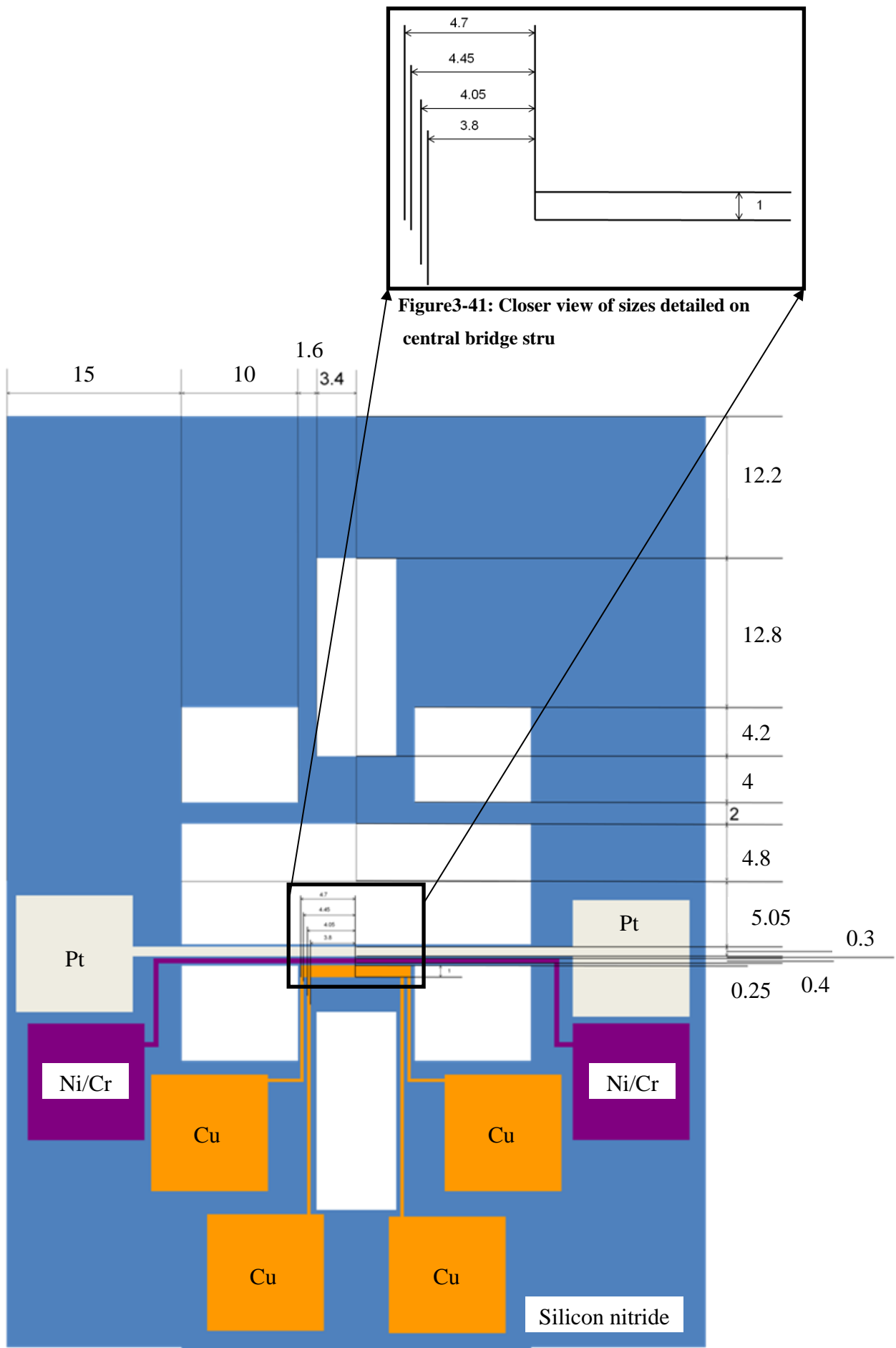


Figure3-41: Closer view of sizes detailed on central bridge stru

Figure 3-42: Schematic of test structure showing dimensions, (sizes in μm) for clarity the metals are only shown on the lower half of the circuit

Using the above design, the resistance of the Ni/Cr heater was calculated to be 432.4Ω ($\rho=1 \times 10^{-6} \Omega \text{ m}$). This is sufficient to create a measurable temperature change and is two orders of magnitude higher than the resistance of the copper.

When the structure is fully deposited and the necessary areas isolated with an insulating layer, the device must be calibrated. The first step in calibration is achieved by passing a current through the Ni/Cr wire which will heat up. The conductivity of the platinum wire can then be recorded and used to calculate the temperature at a single side. The same process can be performed on the second side to ensure calibration.

The next stage is to measure the temperature of both sides without heating again to calibrate both sides. One side only is heated by passing a current through the Ni/Cr wire and recording the temperature by measuring the conductivity of the platinum. Across the bridge the temperature of the second platinum wire is recorded. Any increase in temperature in the second wire is due to the radiative heat given off by the first side. Recording the temperature at both the side being heated and on the thermometer on the opposite side will allow for a calibration curve to be produced. This curve will show the temperature increase to be expected when the Ni/Cr heater is used.

The third stage of the measurement is the introduction of a particle across the central hole (Figure 3-40) to create a bridge. This can be achieved by sonicating substrates with particle growth in iso-propanol to dislodge them from the surface, and to then add them dropwise to an array of test circuits. When dry, micromanipulators can be used to position particles correctly across the central hole touching the copper pads on either side. Again one side of the structure is heated and the temperature of that side recorded using the platinum thermometer. The temperature can then be recorded at the opposing side, and by comparison to previously established calibration curves the increase in temperature caused by the thermal conduction across the particle can thus be obtained.

The copper circuits on either side of the central hole are used to measure the electrical resistance (Figure 3-39). These have 4 bond pads each to remove any contact resistance reading due to contact between the probe and the copper, giving a more accurate reading of

electrical resistance. The centre gap of the structure can be tailored to the size of the particles to be investigated.

The method described above would be suitable for property testing a range of low dimensional materials. It sets out a method for isolating a particle thermally by applying and recording a temperature difference as a means to calculate thermal conductivity and so obtaining an accurate electrical conductivity measurement.

3.9 Conclusions

This chapter details CVD of bismuth telluride on silicon surfaces. Materials are grown from elemental reagents sealed in ampoules under vacuum. There are very few examples of CVD compared with MOCVD routes to bismuth telluride in the literature^{38,99}. CVD has many advantages over MOCVD, such as the use of elemental reagents over that of complex metal-organics, a change that reduces cost both financially and in terms of energy required. The CVD processes described in the chapter do not require specially synthesised reagents. This chapter presents the conditions of growth for a range of particular morphologies by altering experimental parameters such as reagent concentration and surface condition of the silicon substrate.

Section 3.1 details the production of Bi_2Te_3 hexagonal plates using less than 2 nm of gold to seed growth on smooth silicon surfaces. These plates have a high aspect ratio being up to 40 μm across and a sub-micron thickness. The plate-like morphology is typical of Bi_2Te_3 when growth is directed along the a and b axes. The plates were confirmed as Bi_2Te_3 by powder XRD and EDX, and morphology was obtained by SEM. It is reported that increasing the covering of gold/palladium on the surface deters growth. Growth of Bi_2Te_3 will not occur if more than a minimal quantity is gold/palladium is sputtered. This highlights the sensitivity of the reaction and the influence surface condition has on particle growth.

Control over the morphology of the particles was demonstrated by surface modifications in Section 3.2. Here reactions analogous to those in Section 3.1 were carried out with a Si surface which had been scratched creating grooves and a rough surface for growth. In the

absence of a smooth surface Bi_2Te_3 grew into octahedra. These were up to 3 μm in length and were confirmed by XRD and EDX.

Section 3.4 described the use of a temperature gradient to produce higher quantities of material. Use of a temperature gradient produced two distinct areas of growth. It was shown that the optimum temperature for Bi_2Te_3 deposition was around 510 $^\circ\text{C}$ while elemental tellurium was discovered at the cooler region around 314 $^\circ\text{C}$. The Bi_2Te_3 material grown was in the form of large particles up to 100 μm in each dimension but showed a distinct nanostructure of large particles built from nanosheets less than 100 nm thick.

The use of iodine as a transport agent was investigated in Section 3.5. It proved detrimental to the reaction and to the transport of material. When iodine was introduced to the reaction vessel no growth took place. The I_2 hampered not only the transport of the material but also its reaction. Bi and Te remained a mix of elemental powders following the closed space CVD with I_2 .

In Sections 3.6 and 3.7, growth dependence on reagent quantities was examined. Bismuth alone showed no ability to transport and grow on the surface of silicon requiring the presence of tellurium for growth to occur on the desired sites. An equimolar ratio of bismuth and tellurium produced nanowires which were less than 100 nm in diameter, but up to 40 μm in length. These nanowires were seeded from larger particles and were present on every sample with a 1:1 ratio of Bi and Te, but were not found on any reactions where a 2:3 ratio was used.

The final section in this chapter sets out a proposed means for testing the properties of the particles produced here. Particles would be dropped onto a wafer with holes etched in it. The particle (with correct placement) would then form a bridge structure with the majority of the particle being suspended above the hole. Applying a temperature gradient to one side and monitoring the temperature transport at the other, whilst the particle is suspended, could provide a method of quantifying the thermal properties of a single particle. Testing this proposed device was beyond the scope of this project.

4 Non silicon based growth of telluride structures

The previous chapter concentrated on the growth of telluride structures on the surface of silicon. It was demonstrated that the surface composition and texture played an important role in the surface growth. This chapter expands on this work and investigates the growth of telluride structures without the use of a silicon surface. Reported here are results for the growth on copper and cobalt foil; aluminium oxide (substrates); gallium arsenide (substrates) and also the results for a substrate-free solvothermal method.

There has been very little investigation into the chemical vapour deposition of bismuth telluride (excluding metal-organic deposition techniques). The few studies that exist tend to concentrate on silicon surfaces, however it has been reported that silicon, in comparison to other surfaces, can hinder particle migration across the surface and therefore lead to a lower surface growth potential^{98, 119}. It is therefore of interest to investigate growth on to other surfaces.

There have been studies that show the successful growth or deposition of Bi_2Te_3 on surfaces such as gallium arsenide^{24, 120}, aluminium oxide⁹⁶ and the research group at the University of Glasgow has successfully deposited material on copper foils. These materials, aside from providing different growth environments, also have differing intrinsic properties making them of interest for further applications.

This chapter aims to further examine the growth of telluride structures which have potential uses in renewable energy generation applications. Products are characterised using powder X-ray diffraction (XRD), scanning electron microscopy (SEM) and where appropriate through energy dispersive X-ray (EDX) spectroscopy and Raman spectroscopy.

Samples described in this chapter are listed below:

4-1: List of samples described within Chapter 4

Sample identifier	Substrate	Cleaning process	Reagents	T /°C	Section
A1	Al ₂ O ₃	Acetone/ DI water/ IPA	Bi + Te	700	4.1
AT1	Al ₂ O ₃	Acetone/ DI water/ IPA	Te	700	4.2
AB1	Al ₂ O ₃	Acetone/ DI water/ IPA	Bi	700	4.2
G1	GaAs	Acetone/ DI water/ IPA/HCl	Bi + Te	450	4.3
C1	Co	Acetone/ DI water/ IPA	Bi + Te	450	4.4
Cu1	Cu	Acetone/ DI water/ IPA	Bi + Te	700	4.5
Cu2	Cu	Acetone/ DI water/ IPA	Bi + Te	450	4.5
Cu3	Cu	Acetone/ DI water/ IPA	Bi + Te	450	4.5
Cu4	Cu	Acetone/ DI water/ IPA	Bi	450	4.5
Cu4B	Cu + Bi	None	Te	450	4.5
S1	none	N.A.	See section 4.6.1	160	4.6

4.1 Bismuth telluride growth on aluminium oxide wafers

Aluminium oxide substrates are attractive for a number of applications. These substrates are electrically insulating unlike semi-conducting silicon they are able to withstand harsh environments with regards to high temperature and exposure to reagents unlike gallium arsenide. Aluminium oxide substrates have been successfully used for templated low dimensional growth of bismuth telluride previously^{96, 121, 122} however no study could be found involving chemical vapour deposition of elemental reagents in an evacuated ampoule. Here, demonstrated for the first time, is described a method of producing micron-dimensioned particles of bismuth telluride with a fine nanoplate structure.

4.1.1 Reaction set up

Large wafers of α -Al₂O₃ were cleaved into 1 x 2 cm pieces. There was no oxide or corrosive etch used to clean the wafers. Acetone, deionised water and iso-propanol were used in series and were sonicated for 60 seconds for each.

Clean wafer pieces composed of 99.996 %, α -Al₂O₃ were sealed in a quartz ampoule under vacuum, following the standard process previously described. The reagents for these reactions were bismuth (2 mmol, 99% pure, 100 mesh, Sigma Aldrich) and tellurium (3 mmol, 99.8% pure, mesh, Sigma Aldrich) Sealed tubes were reacted in a box furnace at 700 °C for 48 h.

4.1.2 Results

Sample A1 from Table 4-1 is described in this section as an example system.

4.1.2.1 Post-reaction appearance

Following the reaction the wafers showed no visible sign of deposition to the eye or any indication of damage to the surface of the substrate. An exemplar sample is shown below.

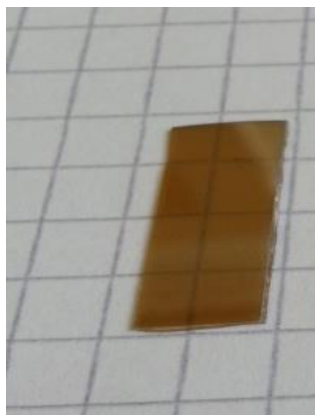


Figure 4-1: Post-reaction appearance of sample A1

As can be seen from Figure 4-1 the wafer remained in its original transparent state with its natural orange colour.

4.1.2.2 SEM

SEM revealed surface deposition on all samples. Surface coverage was lower than that of any silicon or metal substrate reaction. Surface coverage was estimated from SEM imaging to be less than 2.5%. Surface coverage is estimated using multiple areas over several samples. The growth detected was however very interesting and showed low dimensional growth patterns.

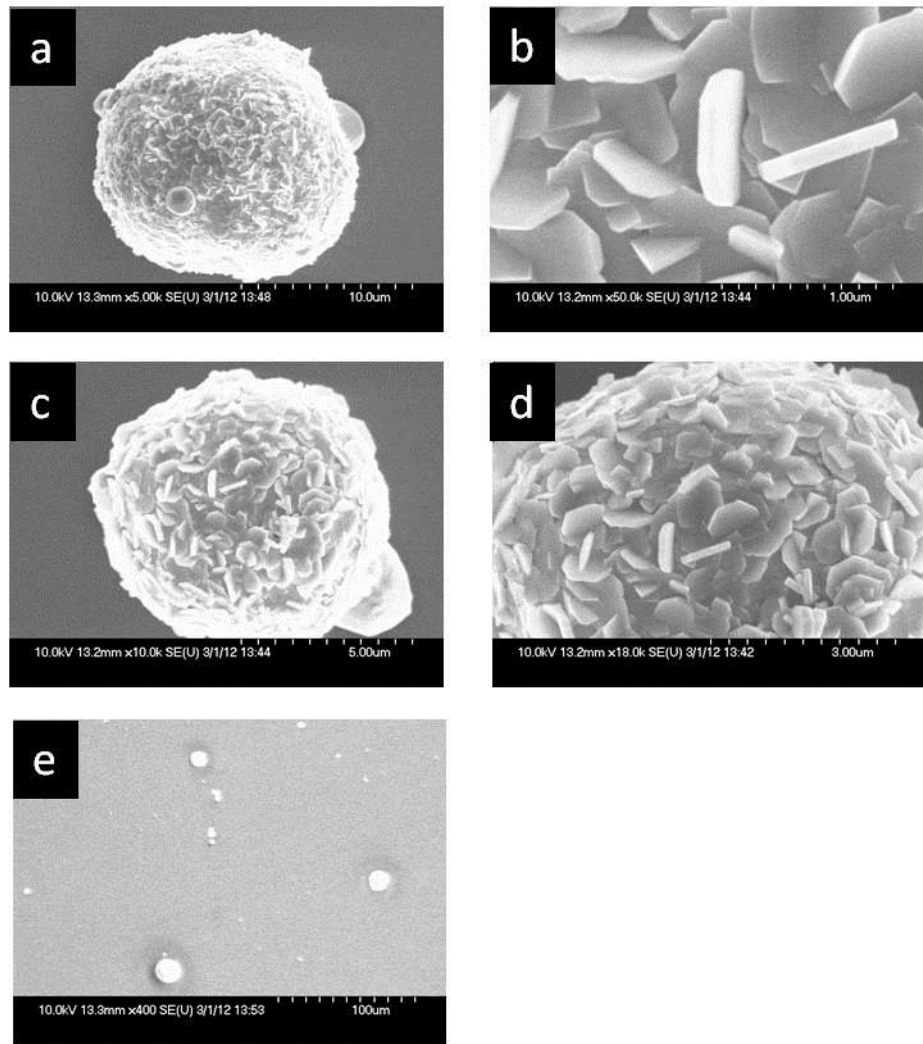


Figure 4-2: SEM micrographs of Al1 showing surface deposition

The lower magnification in Figure 4-2 e gives an indication of the low growth coverage. Most of the substrates appeared blank but there were distinct and, in most cases, spherical areas of growth. It appears that clean Al_2O_3 substrates provide poor surface adhesion for surface growth possibly due to the lack of nucleation sites on the smooth surface. Where growth had occurred it self-seeded allowing the formation of large, micron-dimensioned structures.

The magnified images showing the islands of growth shown in Figures 4-2 a and c were on the micron scale lying between 5 and 20 μm in diameter and composed of agglomerated nanoplatelets. The plates were mainly hexagonal, however, due to agglomeration and fusion of plates the exact morphology and dimensions are difficult to determine on many of the particles. The plates were all sub-micron in diameter being a maximum of 850 nm

across (thickness lay between 50- 200 nm). There was a variation in the thickness of the plates being between 20 and 200 nm.

The spherical nature of the growth lends further evidence to the argument that the bismuth telluride does not adhere well to the surface and creates islands of growth minimising the surface contact with the substrates.

4.1.2.3 Crystalline phase identification

Shown below is a standard powder X-ray diffraction pattern of a bismuth and tellurium reaction on the surface of Al_2O_3 .

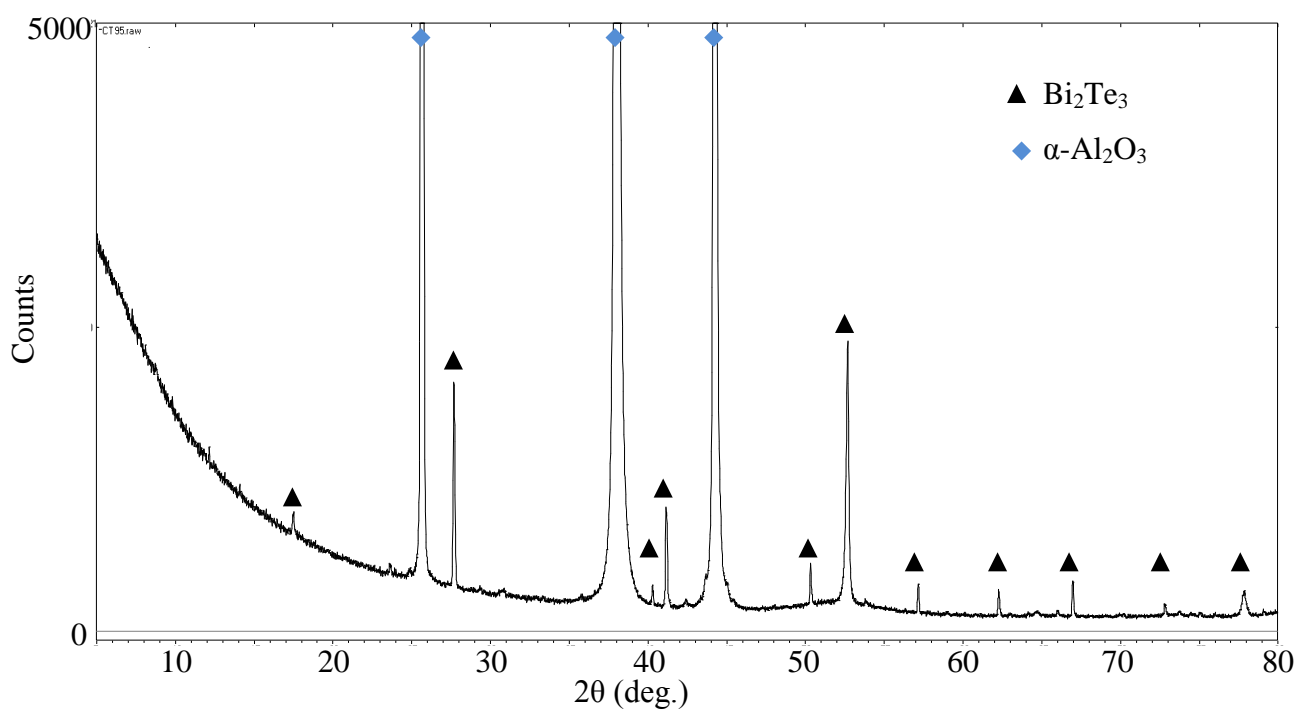


Figure 4-3: XRD pattern of sample A1 showing bismuth telluride deposition

From XRD the surface deposition can be identified as stoichiometric Bi_2Te_3 . No other phases or unidentified peaks were observed in any of the 13 h scans. The high intensity peaks at 25.7, 38.0 and 44.2 $^\circ 2\theta$ are the characteristic peaks of the Al_2O_3 substrate.

4.1.3 Conclusions

Alumina substrates are known for their non-conducting nature and their durability under extreme reaction conditions. Shown here is the growth of low dimensional bismuth telluride particles on the surface. The deposition surface coverage is low, this combined with the spherical agglomerates seen on the surface indicate that bismuth telluride does not have a natural affinity for surface growth on this particular substrate. It was however useful to note the growth of nanoscale plates from these reactions.

The plates self-assembled into agglomerates becoming particles 2-20 μm in diameter composed of a fine nanostructure. The nanostructure of these plates was characterised as being 55-850 nm in diameter and predominantly hexagonal. The thickness of the plates was not seen to exceed 200 nm and plates <20 nm in thickness were observed. XRD confirmed the surface coverage to be composed of a crystalline phase matching to Bi_2Te_3 .

4.2 Single element transport onto aluminium oxide substrate reactions

Alumina is a robust substrate with great potential for low dimensional growth. The main drawback of the method described above was the low level of surface coverage on the substrate. With the aim of improving surface coverage reactions were carried out to investigate the deposition using single reagents.

4.2.1 Tellurium

Reactions were carried out in the same procedure as A1 described above but using Te as the sole reagent. The sole reagent for these reactions was tellurium (6 mmol, 99.8% pure, 200 mesh, Sigma Aldrich). Reaction time, temperature and preparation procedure remained the same.

4.2.1.1 Results

Sample AT1 from Table 4-1 is described here as an example system.

4.2.1.1.1 Post-reaction Appearance

Substrate showed no significant differences following the reaction.

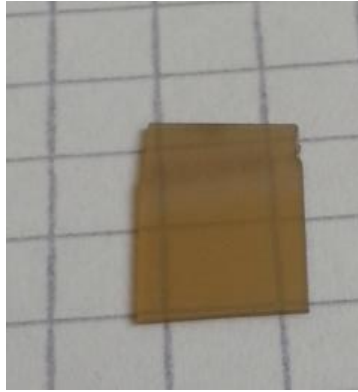


Figure 4-4: Sample AT1 following reaction at 700 °C

4.2.1.1.2 SEM

Surface area was slightly higher than in combined bismuth and tellurium reactions but was still less than 5% surface coverage. Additionally the particle deposition was on the micron scale and showed little uniformity across the surface appearing as irregular particles or agglomerates.

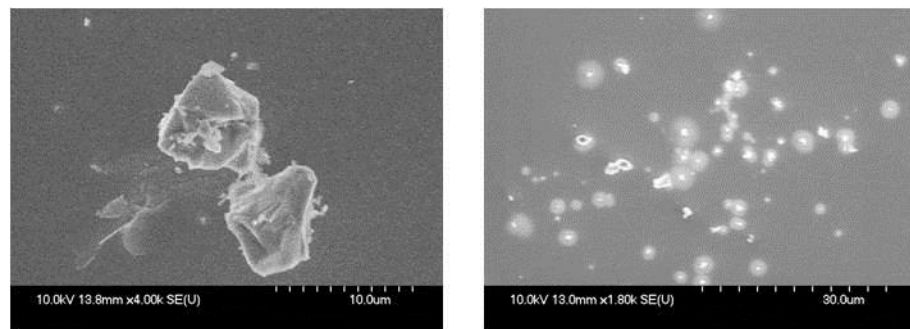


Figure 4-5: SEM micrographs showing tellurium particles on surface (AT1)

The surface was scattered irregularly with particles of 2-10 μm . There was no uniformity or trends in growth on any sample analysed.

4.2.1.2 Conclusion

Tellurium as a single reagent did not appear to be advantageous to the growth of surface material on Al_2O_3 substrates. The use of tellurium alone had not resulted in a higher surface coverage and as such samples were not suitable for a secondary reaction with bismuth. Assuming complete reaction with bismuth to form Bi_2Te_3 the surface coverage would be unacceptably low due to the sparse deposition of tellurium in the first step.

4.2.2 Single bismuth reactions

In a similar vein to the reactions directly above, bismuth transport and growth on Al_2O_3 wafers were investigated. Reactions were configured and prepared in the same process as described above, the only difference being that the sole reagent used for these reactions was bismuth (4 mmol, 99% pure, 100 mesh, Sigma Aldrich).

4.2.2.1 Results

Sample AB1 from Table 4-1 is described here as an example system.

4.2.2.1.1 Post-reaction Appearance

There were no visible changes to the surface of the substrate.

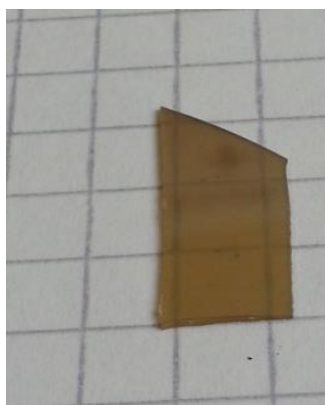


Figure 4-6: Substrate following reaction with bismuth (AB1)

4.2.2.1.2 SEM

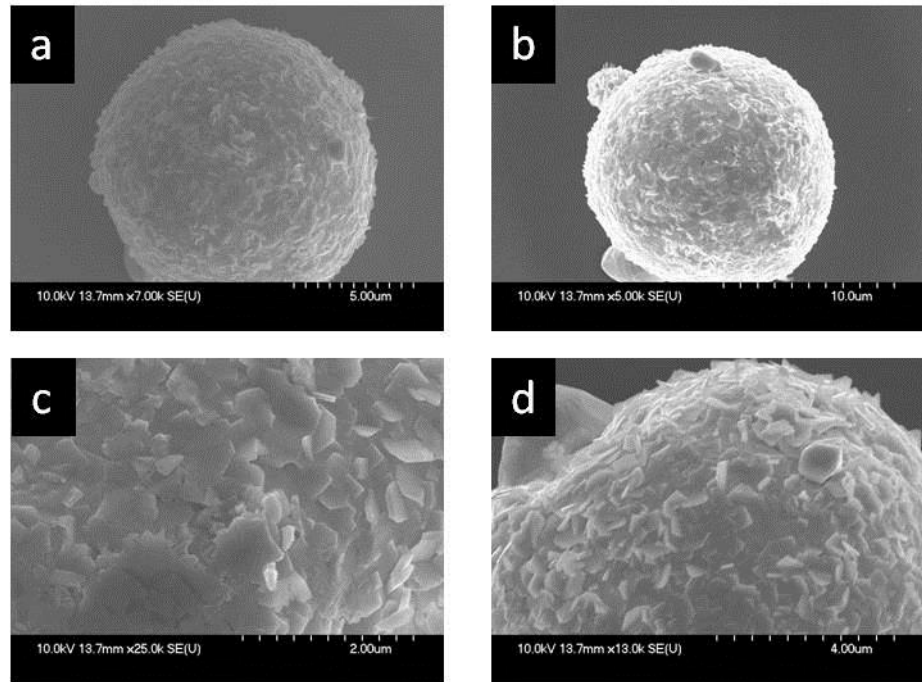


Figure 4-7: SEM micrographs of bismuth reaction on Al_2O_3 (AB1)

The SEM micrographs shown above in Figure 4-7 are analogous to the bismuth telluride reactions described earlier in Section 4.1. Growth resulted in spherical micron dimensioned particles with a fine nanoplake structure.

Al_2O_3 reactions involving a mixture of bismuth and tellurium produced spherical particles comprised of nanoplates with XRD confirming the sole presence of Bi_2Te_3 on the surface. Reactions using only bismuth only produced structures similar to those observed for the growth of Bi_2Te_3 but comprised bismuth alone.

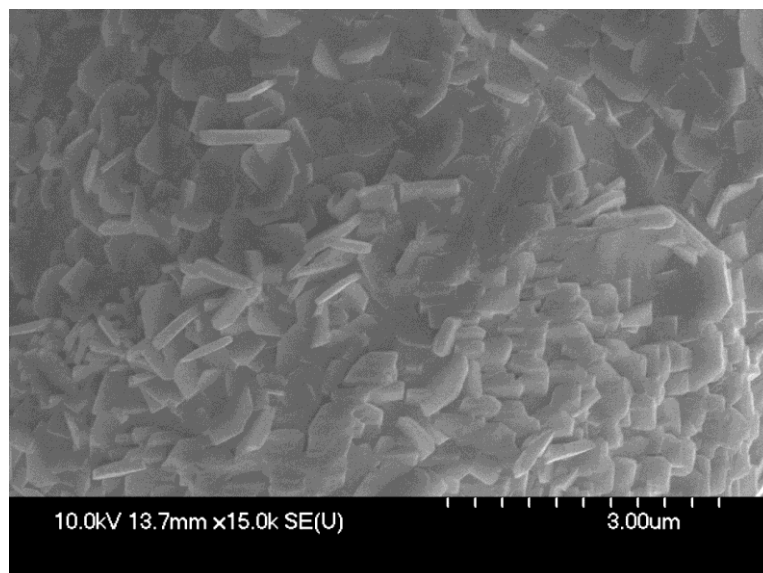


Figure 4-8: SEM micrograph showing bismuth plates grown on Al_2O_3 (AB1)

The plates seen on the surface of the bismuth reactions are consistently less than 150 nm in width and are 10-40 nm in thickness. Once again the surface coverage was extremely low, less than 1%.

4.2.2.2 Conclusions

The growth of bismuth on the surface is directly comparable to the growth of bismuth telluride however similarities were found with the irregular growth pattern displayed by tellurium. It can therefore be assumed that it is the presence of bismuth that is driving the morphology in the bismuth telluride reactions on the surface of Al_2O_3 . It is possible that the bismuth particles are forming and that during this process the distinctly smaller atoms of tellurium are being incorporated into the structure, leading to the similarity of structures in the two conditions.

The persistent problem with all the Al_2O_3 substrate reactions is the issue of low surface coverage. In its natural state Al_2O_3 does not facilitate the surface growth of the materials mentioned above. It is possible that, with the correct surface modifications, the coverage on this non conducting substrate could be improved.

4.3 Bismuth telluride growth on gallium arsenide

Literature shows that bismuth telluride can be successfully grown on (001) gallium arsenide surface by van der Waals epitaxy¹²³ and through the use of metal-organic chemical vapour deposition²⁴. The epitaxy method allows materials with lattice parameters to be held together allowing for surface growth of 2D or 3D structures¹²⁴.

As gallium arsenide has a naturally high resistance it makes an excellent electronically insulating substrate and is often used for electronic applications. Suitability for use as a substrate for the growth of bismuth telluride *via* chemical vapour transport was investigated.

4.3.1 Reaction set up

Experiments were set up following the standard reaction process described previously. Substrates were cleaned using a process suitable to the GaAs material described below. One cm² substrate pieces were sealed in quartz ampoule along with bismuth (2 mmol, 99% pure, 100 mesh, Sigma Aldrich) and tellurium (3 mmol, 99.8% pure, 200 mesh, Sigma Aldrich). Tubes were placed in a box furnace and held at 700 °C for 48 h. On cooling substrates were removed and examined by SEM.

4.3.1.1 Substrate preparation

An appropriate cleaning regime was followed to remove surface debris and the protective oxide surface layer. Deionised water followed by acetone (Chapter 2) was used initially then immediately followed by GaAs “De-Ox”. De-Ox consisted of an aqueous solution of hydrochloric acid, one part 37% concentrated HCl to 4 parts water. The wafer piece was sonicated in this solution for 30 s. Any longer than 30 s can caused damage to the surface of the wafer producing distinctive etch marks. Below in Figure 4-9 is an SEM image of a GaAs wafer piece etched for 60 s.

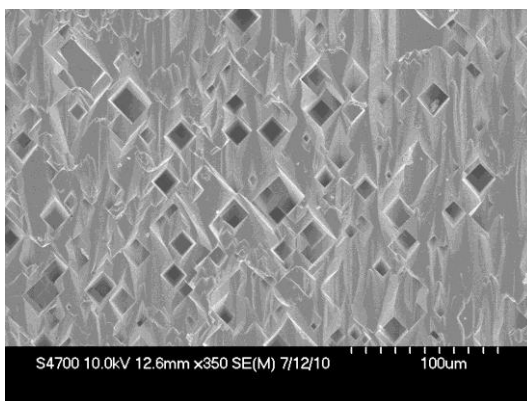


Figure 4-9: SEM micrograph showing damage (square holes etched into the surface) of GaAs caused by HCl

4.3.2 Results

Two reactions were carried out following the procedure above. These were designed as suitability tests. Sample G1 from Table 4-1 is described here as an example system. The appearance of both substrates following reaction was poor. The substrates had partially fragmented and showed distinct layers. The substrates appeared coated in ash which would flake off if disturbed. The upward face of the substrates particularly showed degradation.

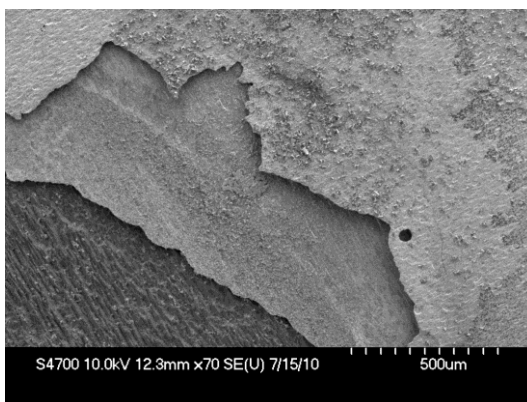


Figure 4-10: SEM micrograph showing sample G1 following reaction in tellurium atmosphere

The substrate had reacted with the tellurium. There is precedent for the interaction of tellurium with GaAs substrates as described by Dycus *et al.*¹²³. Closer examination shows the surface to have reacted in different ways depending on depth of layer. Larger particle growth took place on the uppermost layers of the flaked substrate as seen below in Figure 4-11.

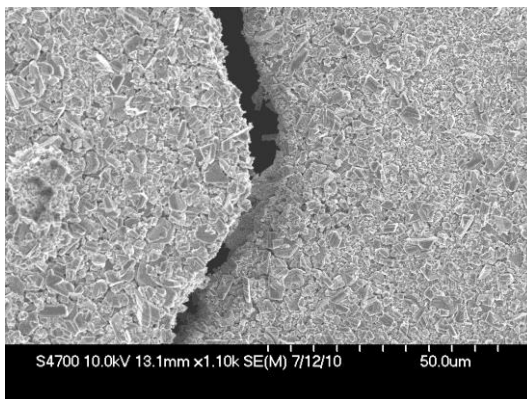


Figure 4-11: SEM micrograph showing large growth on surface of sample G1

Surface layer particles comprised of large irregular blocks of approximately single micron length. Below this layer was smaller particle growth as seen in the second layer growth image below.

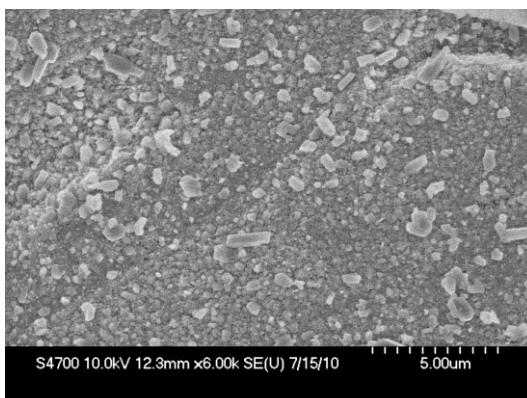


Figure 4-12: SEM micrograph showing sample G1 with surface layer removed

There were however some positive signs of potential Bi_2Te_3 growth on the surface layers. The hexagonal plates found on the surface of silicon based reactions were also found in low numbers across the surface of the uppermost layer on the GaAs wafers, shown in Figures 4-13 to 4-15.

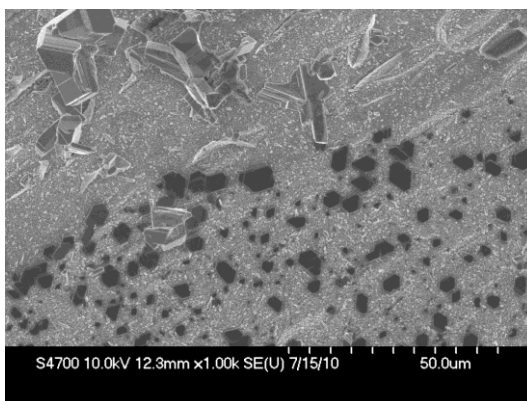


Figure 4-13: SEM micrograph showing hexagonal plates on surface of G1

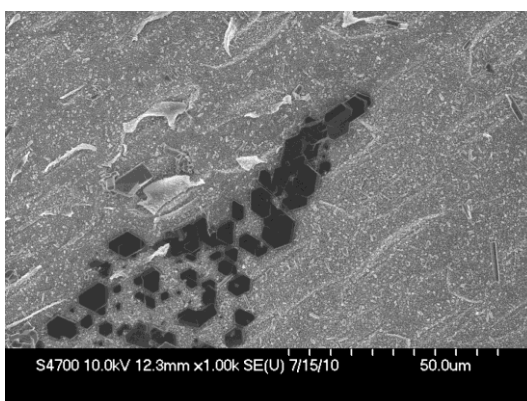


Figure 4-14: SEM micrograph showing hexagonal plates on surface of G1

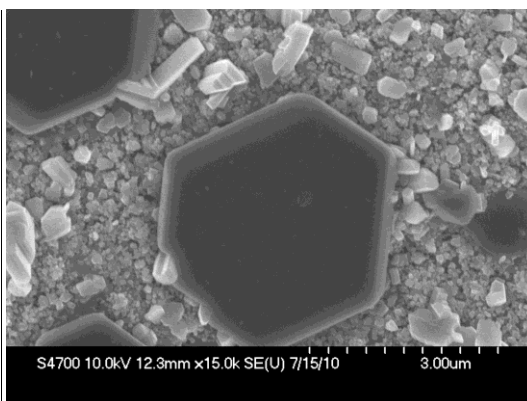


Figure 4-15: SEM micrograph showing single hexagonal plate on surface of G1

The hexagonal plates were gathered in groups of several dozen with these areas scattered across the surface layers of the particles. These plates match well with the ones grown on the silicon surfaces described earlier (section 3.1). The plates are hypothesised to be bismuth telluride owing to the similar growth pattern and also to the stark difference in conduction. There is an image contrast difference between the plates and the surface layer beneath. Areas where the electrons are more easily conducted appear darker whereas areas with lower conductance appear brighter in colour as more electrons are backscattered and detected.

Due to mixed phases and low product growth, XRD was not conclusive in identification of the plates.

4.3.3 *Conclusions*

From the test reactions carried out it can be assumed that gallium arsenide is unsuitable for the CVD. The elevated temperature and readiness to react with tellurium led to an unacceptable degree of damage to the substrate. It was decided not to pursue these reactions further as avoiding the surface damage would require a lower temperature which would have a negative effect on the growth of Bi_2Te_3 . Although particle growth is sparse the presence of the plates does suggest that GaAs may be a suitable substrate if less harsh conditions are used.

4.4 **Cobalt surface reactions**

Alongside nickel cobalt proves to be one of the most effective ohmic contacts available for bismuth telluride¹²⁵. Due to this excellent property and a melting point three times higher than either of the reagents (1495 °C compared to 450 °C for tellurium and 271 °C for bismuth) the potential for growth of structures of Bi_2Te_3 on the surface of cobalt *via* chemical vapour deposition was investigated.

4.4.1 *Reaction set up*

Reactions took place in a quartz ampoule sealed under vacuum with bismuth (2 mmol, 99% pure, 100 mesh, Sigma Aldrich) and tellurium (3 mmol, 99.8% pure, 200 mesh, Sigma Aldrich). The Bi and Te reagents were separated by a reduced diameter neck from a 2 x 1 x 0.1 cm³ cobalt metal sheet. No acid etch was used in these samples and the metal foil was only washed in a standard acetone, deionised water and iso-propanol routine. Sealed tubes were reacted for 48 hours at 450 °C.

4.4.2 *Results*

Sample C1 from Table 4-1 is described here as an example system.

4.4.2.1 Post-reaction appearance

The reagents had remained a dull grey powder while the foil had retained its shape and had become even brighter and shinier in appearance. Following the reaction the substrate surface was mottled, having a rougher texture and no longer retained the flat smooth appearance of the original unreacted foil. The substrate had also become brittle and was easily broken if pressure was applied.

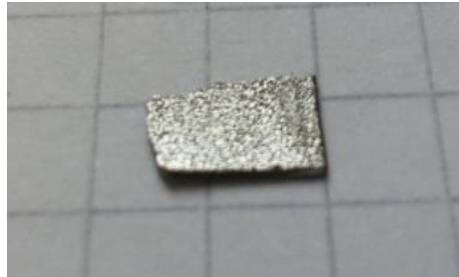


Figure 4-16: Cobalt foil after reaction at 450 °C (C1)

4.4.2.2 Morphology

On SEM inspection the foil pieces were discovered to have an unusual texture. The surface was disrupted by highly textured structures breaking through vertically.

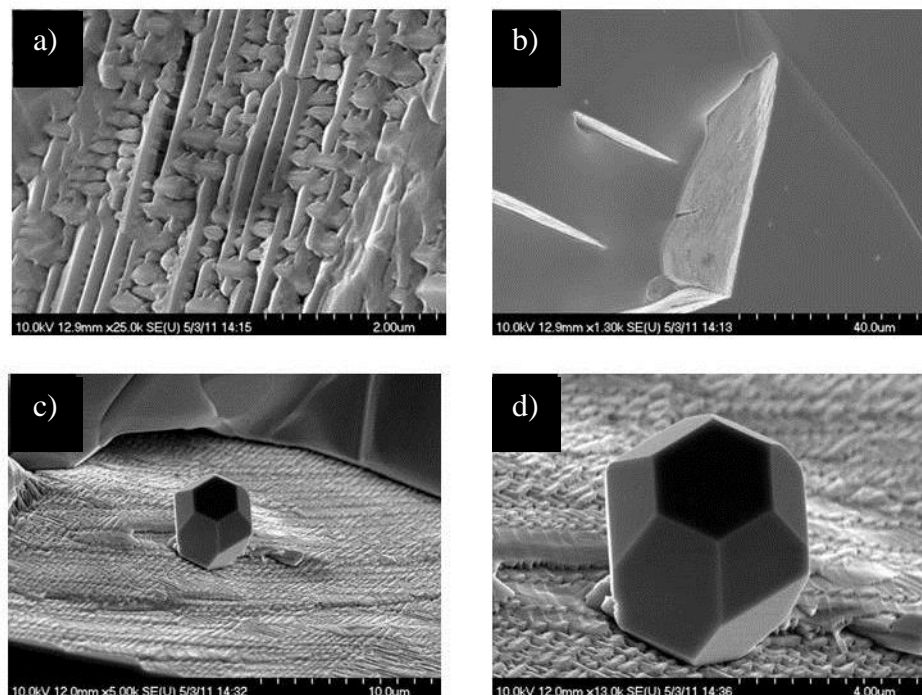


Figure 4-17: SEM micrographs showing growth on cobalt surface (C1)

The surface can be seen punctuated by the highly textured thin structures. Figure 4-17 (b) shows the standard appearance breaking through the surface and appearing to continue below the surface. It is believed that these structures continue into the depth of foil as they can be observed in Figure 4-17 b and c penetrating deeper into the surface.

The single crystal shown in Figure 4-17 c and d was a unique feature to sample C1. Of all cobalt foil samples produced only this single crystal was recorded. It is possible there were others but the small size and scarcity made them difficult to detect. It is included in this work due to its unique and interesting structure. The crystal appears to be a hexagonal bifrustum being composed of 2 hexagons and 12 trapezoids.

4.4.2.3 *Elemental analysis*

Here three distinct regions of the foil surface are reported- bulk surface, protruding textured surface and the singular hexagonal bifrustum particle.

4.4.2.3.1 *Surface*

The below EDX spectrum (Figure 4-19) was recorded from the highlighted area shown the SEM micrograph in Figure 4-18. It shows the presence of cobalt, tellurium and bismuth the quantification of which is shown in Table 4-2.

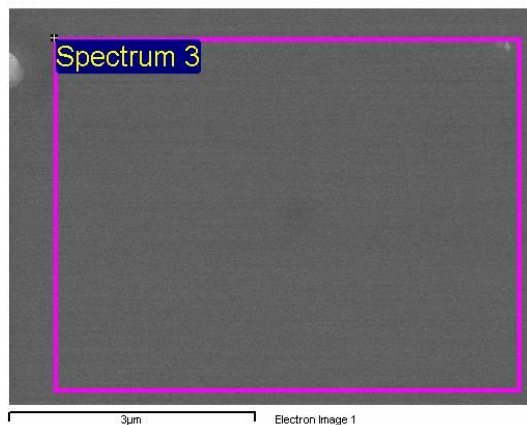


Figure 4-18: SEM micrograph of EDX area of foil surface (C2)

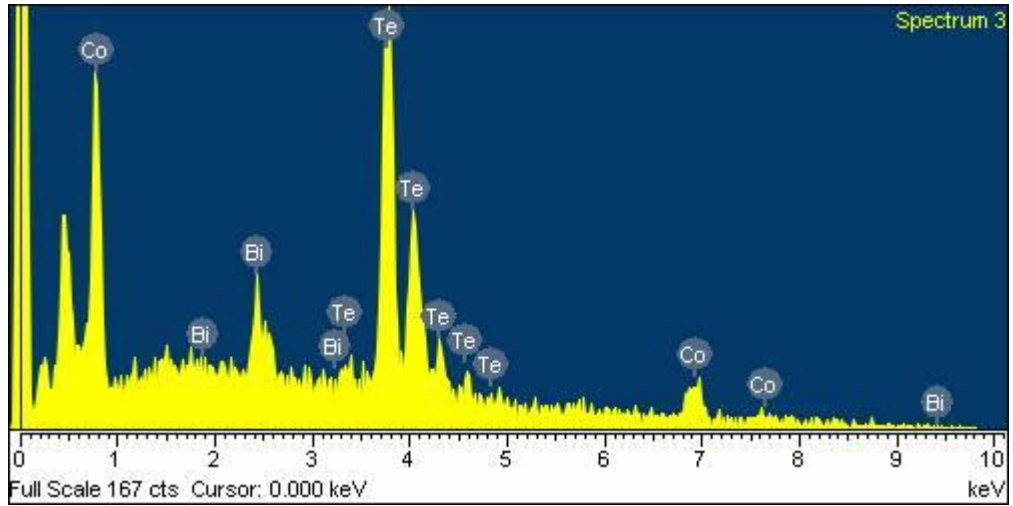


Figure 4-19: EDX spectrum of foil surface

Table 4-2: EDX of foil quantification

Element	Weight%	Atomic%
Co	25.88	43.88
Te	67.78	53.08
Bi	6.34	3.04
Total	100.00	100.00

The quantification of the EDX spectrum shows that the surface is almost entirely composed of cobalt and tellurium with bismuth present in very small quantities.

4.4.2.3.2 Cobalt oxide

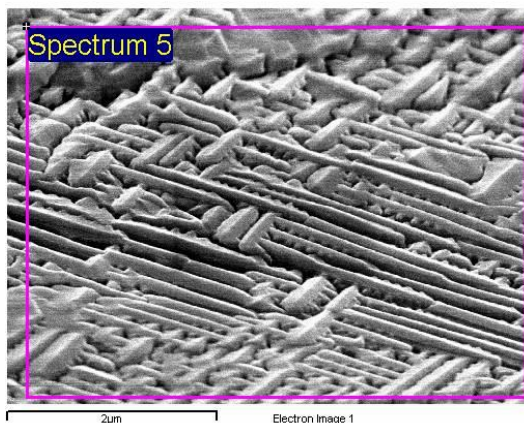


Figure 4-20: SEM micrograph of selected EDX area on highly textured surface structure (C1)

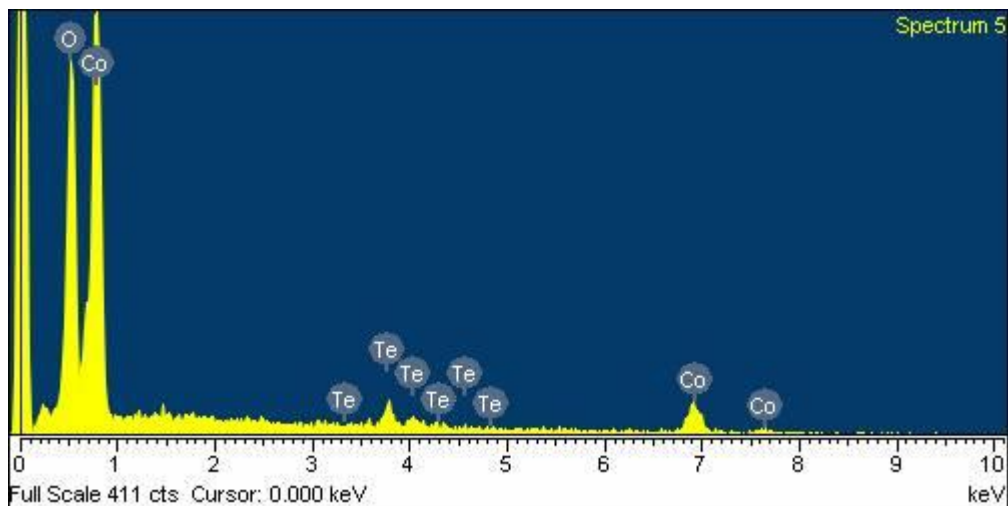


Figure 4-21: EDX spectrum from highly textured surface structure (C1)

Table 4-3: EDX of quantification highly textured surface structure (C1)

Element	Weight%	Atomic%
O	21.16	51.85
Co	66.80	44.45
Te	12.04	3.70
Total	100.00	100.00

The highly textured surface structures show very high levels of oxygen. It is possible that this is just due to the native oxide on the surface of the samples which was not acid etched off rather than any failure of the vacuum. It should be noted that it is normal for a certain level of oxygen to appear on samples as surfaces will naturally form an oxide layer when the seal of the reaction ampoule is broken. Oxygen levels here however are far beyond anything which can be explained by background surface oxygen. It is clear that the surface structures are composed of a cobalt oxide with a small quantity of tellurium.

4.4.2.3.3 Hexagonal bifrustum particle

Figures 4-22, 23 and Table 4-4 below show the area, spectrum and quantification taken from the single hexagonal bifrustum particle.

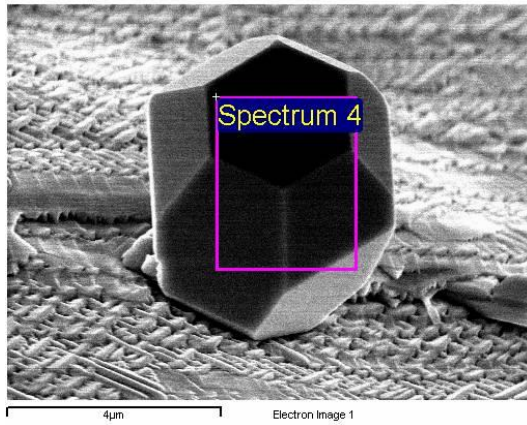


Figure 4-22: SEM micrograph showing EDX spectroscopy area from single hexagonal bifrustum particle (C1)

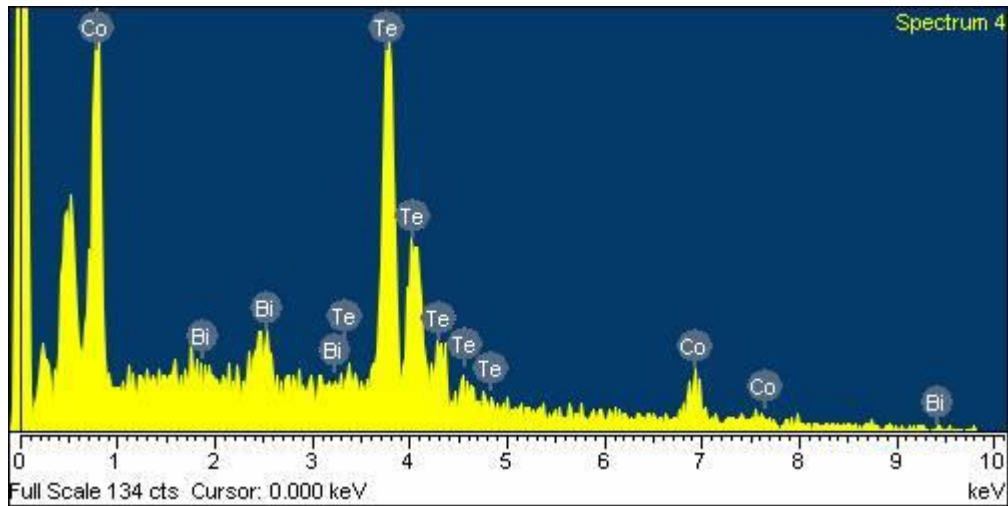


Figure 4-23: EDX spectrum from hexagonal bifrustum particle (C1)

Table 4-4: EDX quantification from hexagonal bifrustum particle (C1)

Element	Weight%	Atomic%
Co	29.94	48.78
Te	64.94	48.87
Bi	5.11	2.35
Total	100	100

The single hexagonal bifrustum particle is of a material closely comparable to the bulk surface being composed mainly of cobalt and tellurium with a small percentage of bismuth.

4.4.2.4 Crystalline phase identification

Firstly the composition of the ingot produced at end of the ampoule where the reagents were initially situated was investigated. In each case the bismuth and tellurium had reacted to form stoichiometric Bi_2Te_3 with peaks clearly matching to a standard bismuth telluride pattern. This is shown in Figure 4-24.

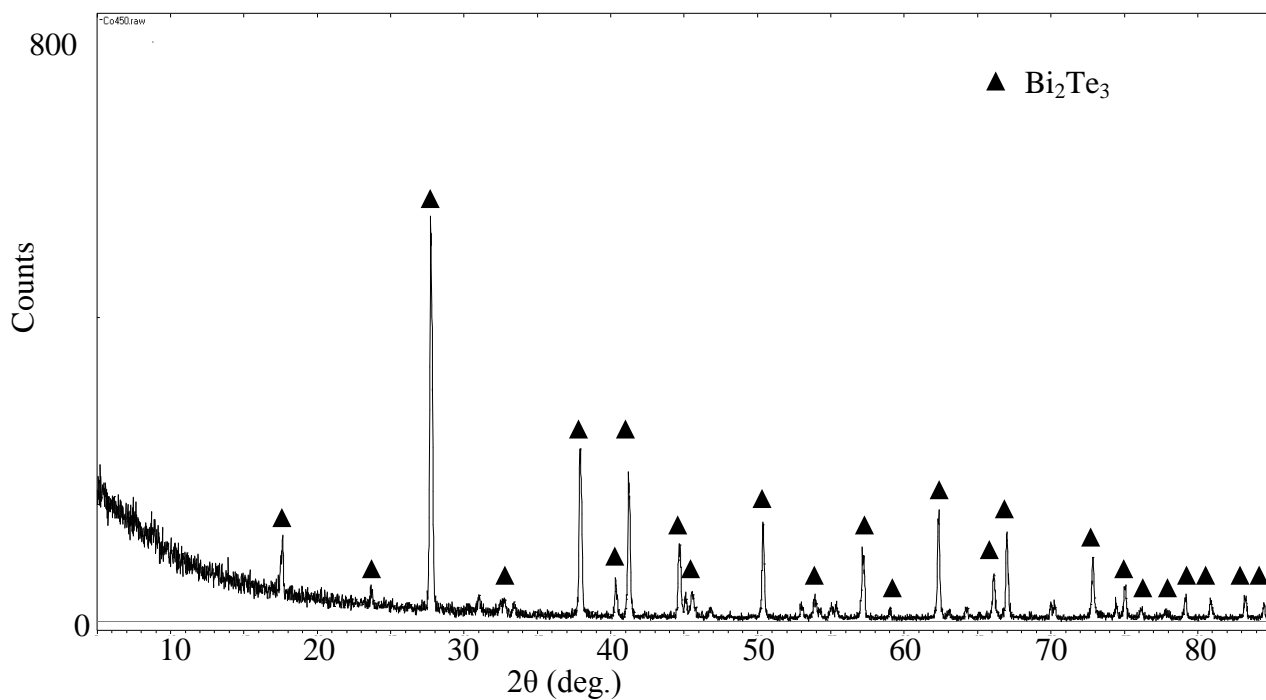


Figure 4-24: XRD pattern of reagents post-reaction (CT1)

4.4.2.4.1 Foil

The XRD of the foil, as to be expected from the SEM and EDX, showed a mixture of phases. The dominant phase appears to be a cobalt telluride matching to $\text{Co}_{0.63}\text{Te}$.

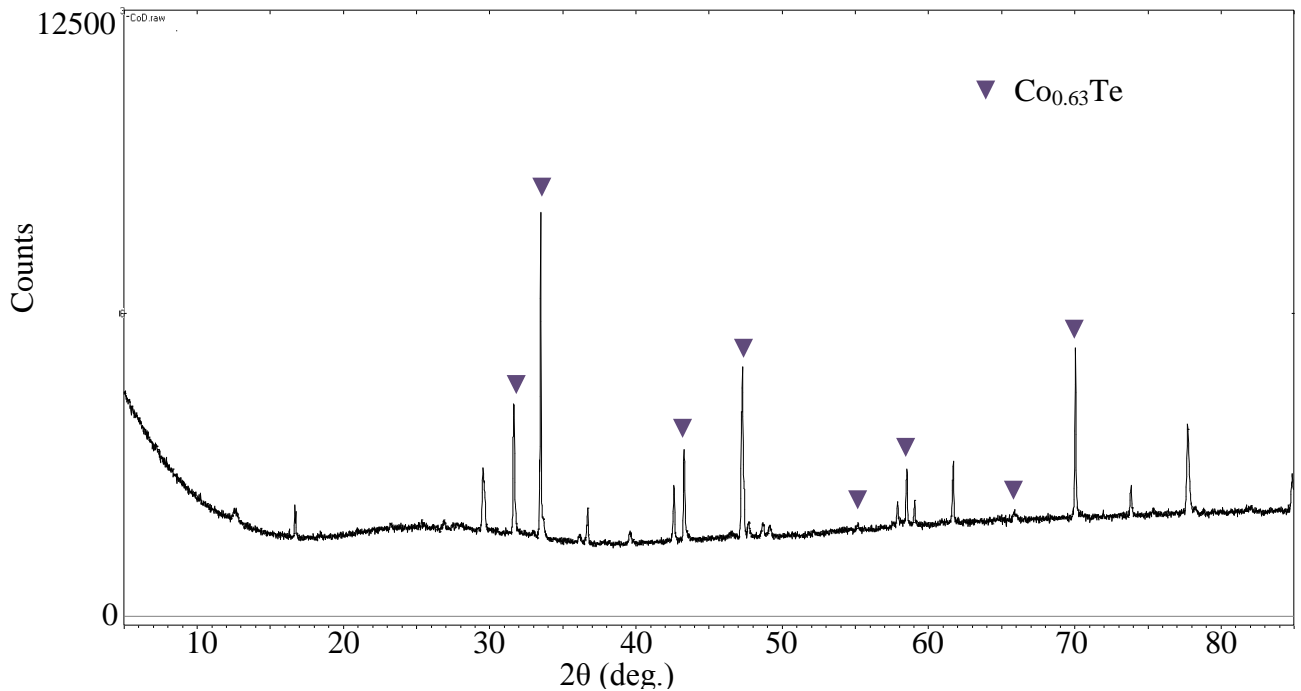


Figure 4-25: XRD pattern of foil (C1)

Although the dominant phase in this sample shown in Figure 4-25 (and all others analysed) was $\text{Co}_{0.63}\text{Te}$, there were other substances with peaks of lower intensity which were identified. Peaks were found for elemental tellurium, bismuth and CoTe . This is to be expected as there are distinct surface structures of vastly different elemental makeup to that of the surface.

XRD and EDX both confirmed a cobalt deficient cobalt telluride as the bulk material.

4.4.3 Conclusions

While cobalt proves an excellent ohmic contact material for bismuth telluride, its natural affinity to react preferentially with tellurium is detrimental in the chemical vapour transport reactions reported here. The tellurium readily reacts penetrating the wafer to form a bulk cobalt telluride while the native oxide is reacted to form cobalt telluride oxides.

Bismuth concentration was recorded to be very low- concentrations across the surface consistently below 5 atomic percent and averaged at 3 %. While the material located in the original reagent site had formed into a stoichiometric bismuth telluride it must be assumed that excess bismuth was deposited on the walls of the vessel explaining the higher concentration of tellurium on the substrate.

All reactions carried out proved absent of bismuth telluride growth on the cobalt surface making cobalt foil an unsuitable substrate for low dimensional bismuth telluride structures *via* chemical vapour transport but it did however prove an effective route for a simple production of bulk cobalt telluride. The structures of the oxide system may be of interest for other applications due to their interesting surface design combined with their dimensions. Furthermore, lattices, at least in one case, proved capable of supporting the growth of other particles on their surface.

4.5 Copper foil reactions

One of the most ubiquitously used contact metals for electrical applications is copper. With almost unrivalled electrical prosperities it finds a place in almost every electrical device used. Electrical properties combined with a melting point over 1000 °C led to an investigation of copper foiling being suitable for chemical vapour transport of bismuth telluride.

Copper foil had been successfully used as a substrate material for growth of antimony telluride structures using an argon gas transport reaction and the work in this section aimed to investigate the suitability of copper for ampoule-based chemical vapour deposition using elemental reagents.

Copper tellurides are of high interest themselves. Copper telluride compounds have been shown to be excellent ionic conductors^{126, 127}. Copper telluride compounds of various stoichiometry are used as back contacts in solar cells^{128, 129}, they have been shown to make the best electrical contacts to cadmium telluride¹²⁹, which is one of the most important compounds used in the harvesting of solar energy. Copper telluride has been synthesised *via* solvothermal methods¹²⁶ *via* pulsed laser deposition¹³⁰, sputtering techniques¹²⁹ and *via* extended vibrational heating¹²⁸.

This section explores the potential growth of bismuth telluride on a copper surface, the growth of copper telluride plates.

4.5.1 Reaction set up

Reactions took place in a quartz ampoule sealed under vacuum with bismuth (4 mmol, 99% pure, 100 mesh, Sigma Aldrich) and tellurium (6 mmol, 99.8% pure, 200 mesh, Sigma Aldrich). The Bi and Te were separated by a reduced diameter neck from a 2x1x0.2 cm³ copper metal sheet. No acid etch was used in these samples and the metal foil was used as obtained, newly purchased and packed under argon. Sealed tubes were reacted for 48 h at 700 °C and separate reactions were also investigated at 450 °C.

4.5.2 Results, 700 °C

Sample Cu1 from Table 4-1 is described here as an example system.

4.5.2.1 Post-reaction appearance

Reagents had formed a single ingot where they had been initially added to the ampoule. The foil (shown in Figure 4-26) showed a dramatic change in appearance. The original orangey pink sheen of the foil was lost and half the foil had become a mesh of black particles. This mesh while holding loosely to the original shape of the foil, had become brittle and easily crumbled to leave large black particles upon handling (Figure 4-27). The half which was further from the reagents stayed intact but was brittle and had taken on a charred appearance. A dark orange sheen could be observed under the darkened surface area. The foil had lost almost all malleability and could be broken in two when bent.

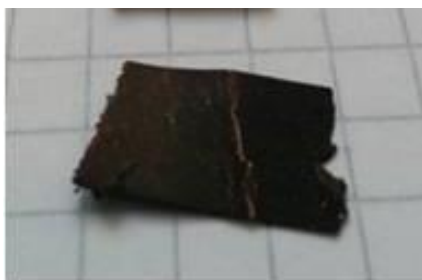


Figure 4-26: Post-reaction appearance of high temperature copper wafers (Cu1)

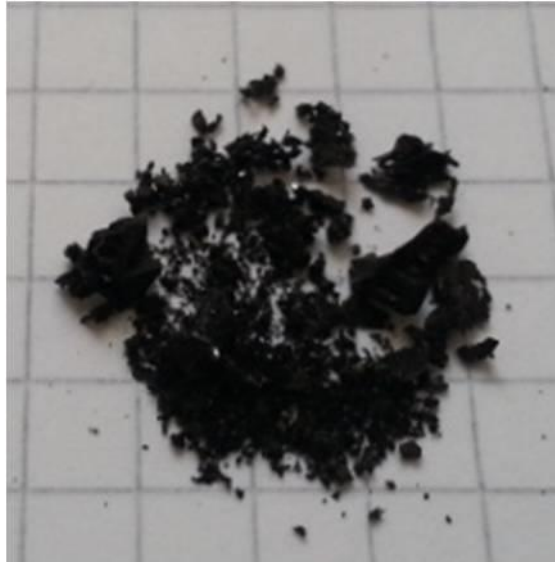


Figure 4-27: Degraded copper wafer following reaction with tellurium (Cu1)

4.5.2.2 *Crystalline phase identification*

The highest intensity reflections in all samples were attributed to Cu_2Te . The pattern shown below in Figure 4-28 shows a successful match to dicopper telluride.

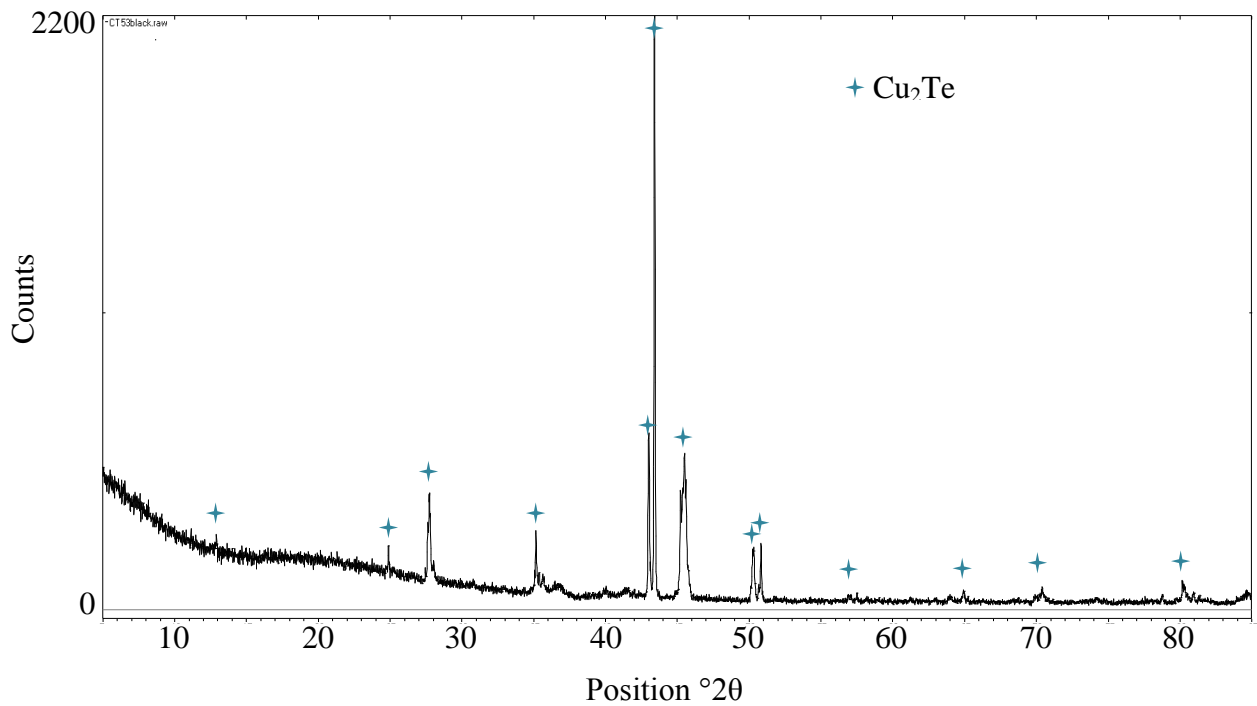


Figure 4-28: XRD pattern matching to Cu_2Te in sample Cu1

4.5.2.3 Morphology

The substrates and the black powder to which the substrate had degraded were examined by SEM. All samples showed a distinctive growth pattern showing a triangular morphology composed of layers.

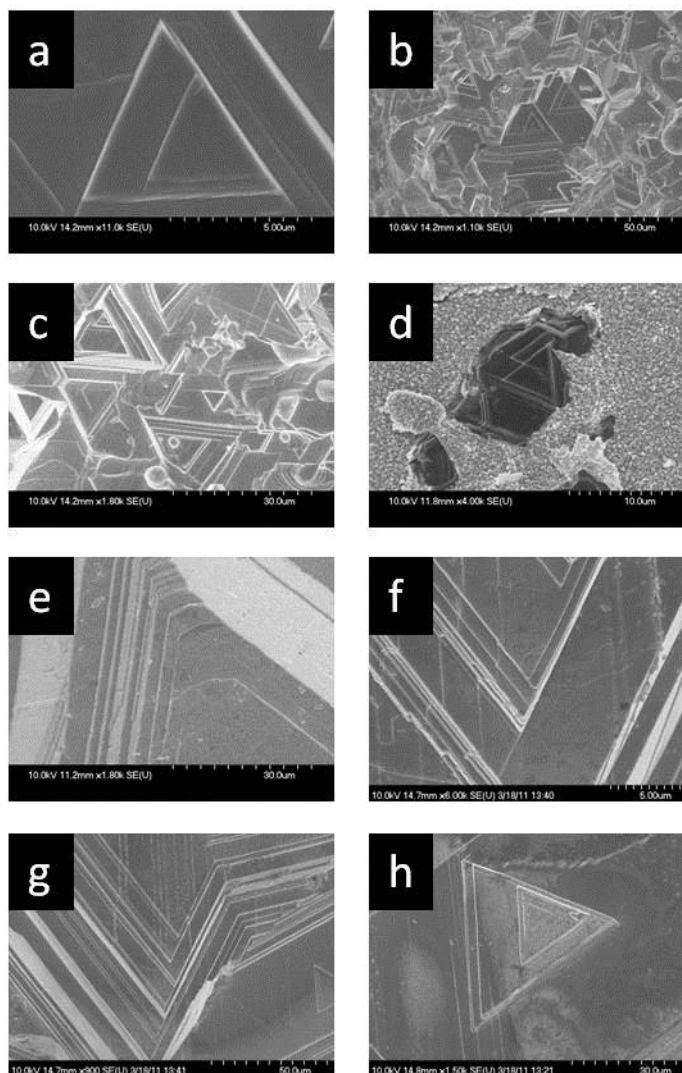


Figure 4-29: SEM micrographs of high temperature copper foil reactions (Cu1)

In areas where the substrate had disintegrated the particles displayed a triangular layered appearance but had fragmented into large blocks. Where the substrate remained intact, a consistent surface layer composed of the triangular layers was observed.

The edge of the substrate positioned furthest away from the powdered reagents did not display the consistent triangular stepped surface- this can be seen in Figure 4-29 d where areas of the distinctive growth appear to be emerging from the copper surface as evidenced by EDX (shown below).

4.5.2.4 Elemental analysis

EDX showed an elemental ratio of the triangular particle matching to a Cu_2Te stoichiometry.

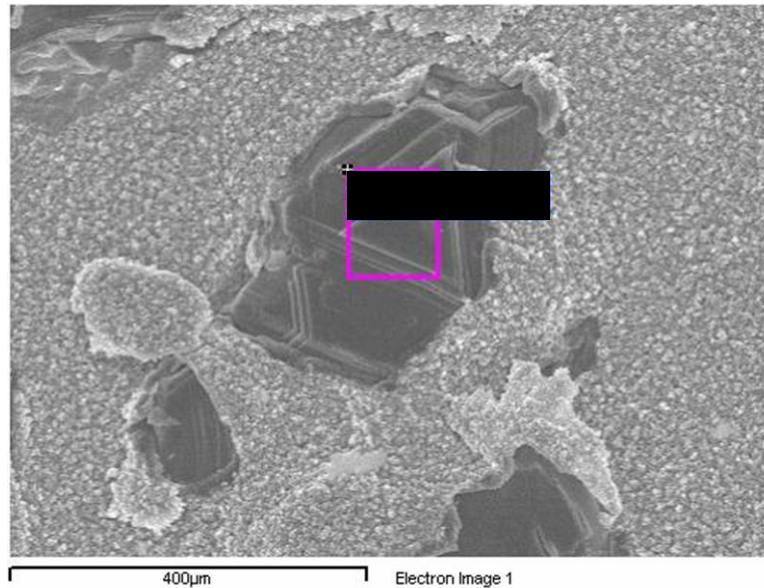


Figure 4-30: SEM micrograph showing selected area of EDX analysis on sample Cu1

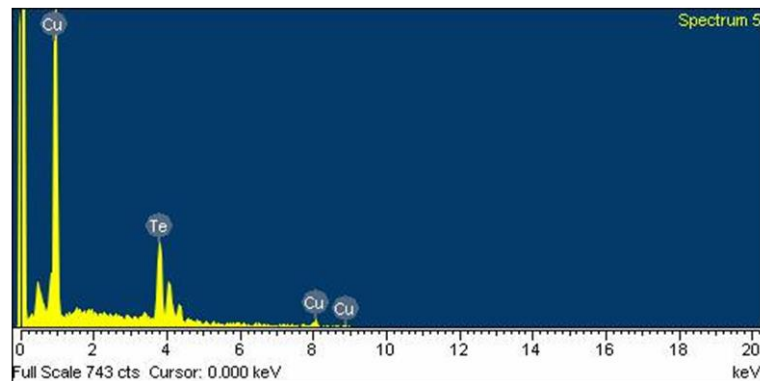


Figure 4-31: EDX spectrum showing copper telluride from sample Cu1

The image above (Figure 4-30) shows the selected area sampled for the above spectrum (Figure 4-31). The dark triangular structure emerging from the surface shows the presence of copper and tellurium only. These were quantified as copper and tellurium in an elemental ratio of 1.95: 1 respectively.

By contrast the few areas observed where the surface had not undergone conversion to the distinctive surface pattern remained as a match to copper alone. This is clearly apparent in

Figures 4-32 and 4-33 where a second spectrum was recorded adjacent to that in Figure 4-31 however in this second area, no tellurium is detected.

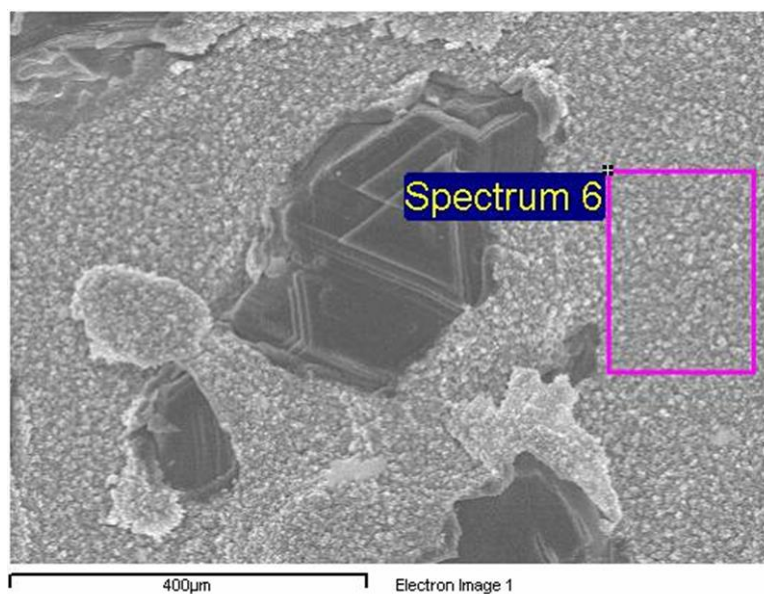


Figure 4-32: SEM micrograph showing selected area of EDX analysis on sample Cu1

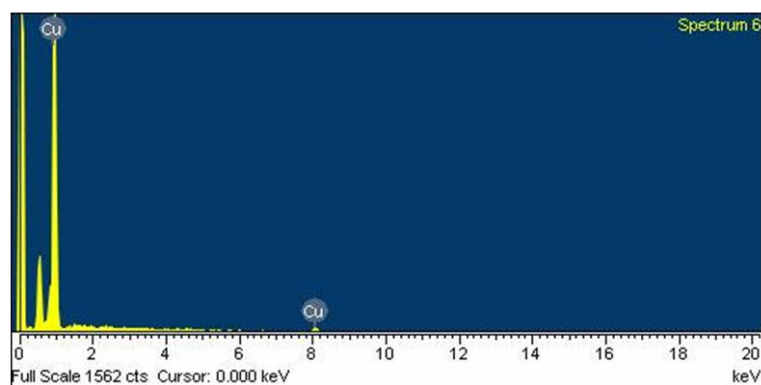


Figure 4-33: EDX spectrum showing copper only from sample Cu1

The EDX spectrum of Cu1 (Figure 4-43) shows that there are still some areas to be found that have remained free of tellurium but these areas are rare. The majority of the surface shows conversion to copper telluride. Although bismuth was present in the reaction vessel, bismuth was not found across the surface. The bismuth did not transport and deposit on the surface but remained in ingot and droplet forms inside the ampoule.

4.5.3 Conclusions, high temperature

The high temperature reactions did not produce bismuth telluride. Tellurium was seen to react with copper leading to transformation of the substrate. Substrates emerged brittle and at least 50% of all substrate had degraded into powder. The dark surface and black crystals that were obtained after reaction at 700 °C were identified as being composed of dicopper telluride. This is evidenced by its dark colouration, XRD pattern and elemental quantification through EDX spectroscopy.

This technique, while an effective route to producing quantities of Cu₂Te with a regular morphology failed to produce low dimensional structures desired in this work. Targeting the growth of low dimensional growth a lower temperature investigation was conducted.

4.5.4 Results 450 °C

Samples Cu2 and Cu3 from Table 4-1 are described here as example systems.

4.5.4.1 Post-reaction appearance

In contrast to the 700 °C copper foil reactions described above, there was no fragmentation of the substrate. The foil stayed intact and malleable but showed a change in colour. The bright orange-pink of copper had changed to a silver-grey. Some of the original colouration could still be seen at the far end of the substrate or on the underside seen as a slight colouration gradient across the surface with the darkest grey being at the end of the substrate closest to the reagents. Selected samples are shown below in Figure 4-34.



Figure 4-34: Post-reaction appearance of Cu2 (left) and Cu3 (right)

The black area seen below the substrate is a carbon tab (used using SEM imaging) and was not present during the reaction

4.5.4.2 Morphology

SEM revealed the substrates to have 3 distinct areas of surface reaction. The areas around the edge of the substrate had formed into platelets vertically aligned from the surface of the wafer. The second and most widespread area of reaction showed agglomerated platelets once again aligned perpendicular to the surface of the wafer. The third area observed showed little or no reaction; these were the smallest areas and were only found at the extremities of the foil.

4.5.4.2.1 Plates

The edge of the foil had formed into hexagonal plates which projected perpendicular from the surface. These ranged from 5 to 25 μm in diameter with the vast majority being 10 μm in diameter. The plates were all under 500 nm thick; Figure 4-35 shows these plates.

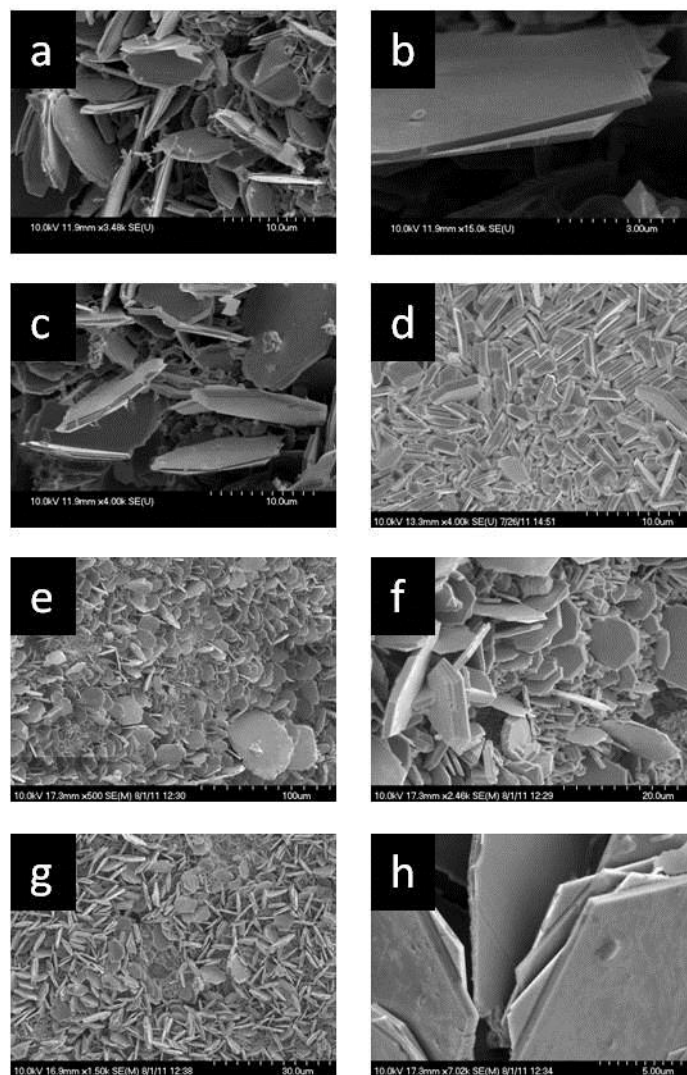


Figure 4-35: SEM micrographs showing plate structure (a-d) sample Cu2, (e-h) sample Cu3

The loose plates described above were found on all edges of the substrate. This suggests that this particular growth needs significant amount of space in order to develop. The centre of the substrate was also covered in plate like structures but these were not freestanding- these are described below

4.5.4.2.2 Elemental Analysis

The plates showed the presence of only tellurium and copper by EDX spectroscopy. A standard EDX spectrum is shown below in Figure 4-36.

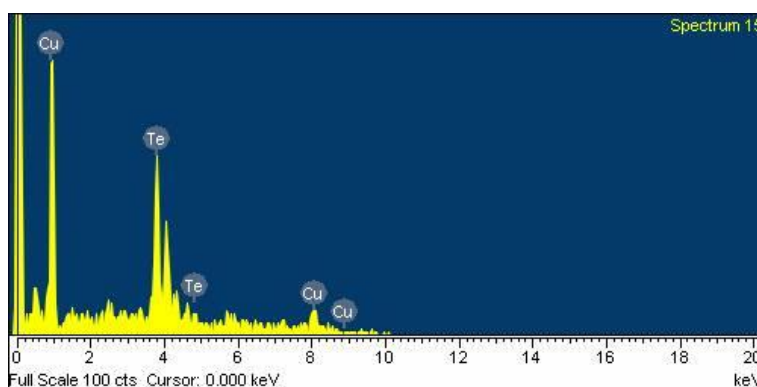


Figure 4-36: EDX spectrum of plates on copper substrate, sample Cu2

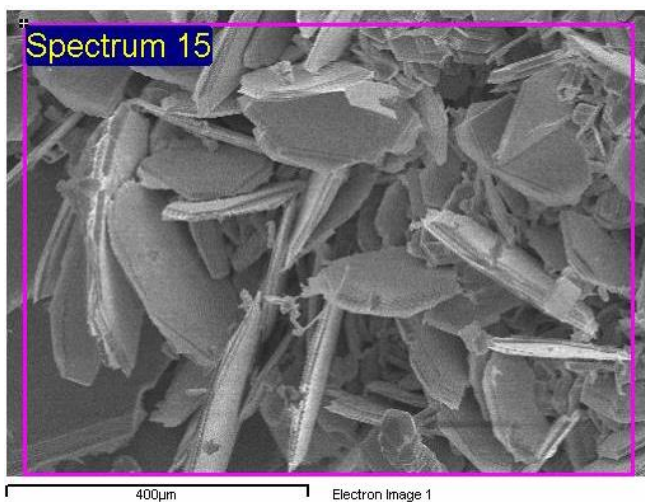


Figure 4-37: SEM micrograph of selected EDX area, sample Cu2

The elemental compositions of multiple areas on multiple samples were recorded and it was discovered that the plates had an average composition of $\text{CuTe}_{0.9}$.

4.5.4.2.3 Bound plates

Following reaction at 450 °C the majority of the copper substrates displayed a very distinctive growth pattern of perpendicularly grown plates with strong uniformity of direction. SEM micrographs of selected samples are show below in Figure 4-38.

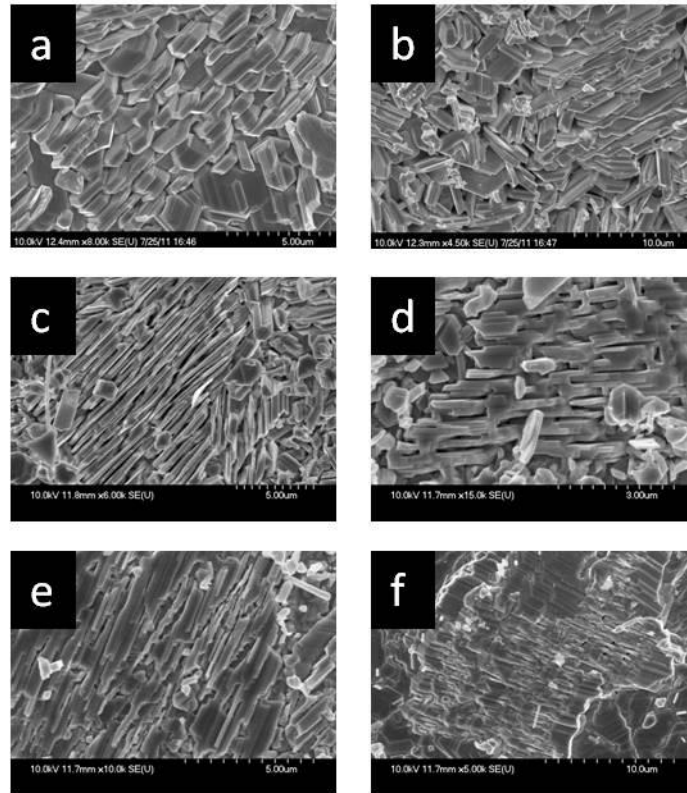


Figure 4-38: SEM micrographs showing bound plates on copper surface. (a-c) sample Cu3, (d-f) sample Cu2

The tightly packed plates shown in Figure 4-38 were typically 5 μm wide and 200-500 nm in thickness. There was strong directionality shown on a local scale however this long range order could be disrupted and a new direction established. Areas of aligned plates typically covered 50-400 μm^2 across the surface before a disruption would occur and a new direction of grown was established. The exact morphology of the plates is difficult to determine due to the close packed nature of the growth. It is assumed however that the individual plate morphology is likely to be closely comparable to that of the individual freestanding plates found at the edges of the substrate.

4.5.4.2.4 Elemental analysis

EDX spectroscopy was used to establish the elemental composition of the plates. A typical spectrum is shown below with the area from which it was obtained (Figures 4-39 and 4-40).

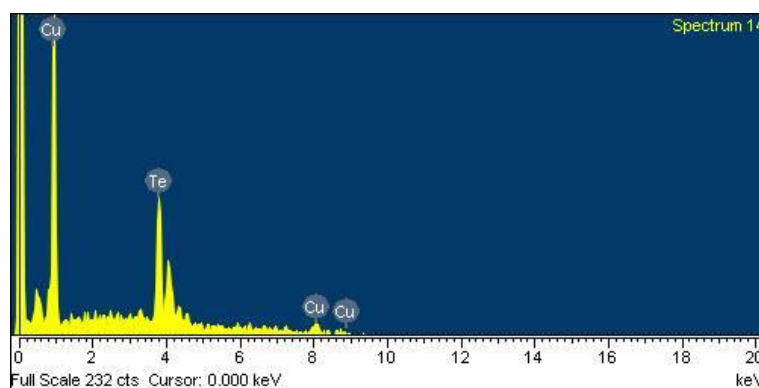


Figure 4-39: EDX spectrum from close plate structure on Cu2.

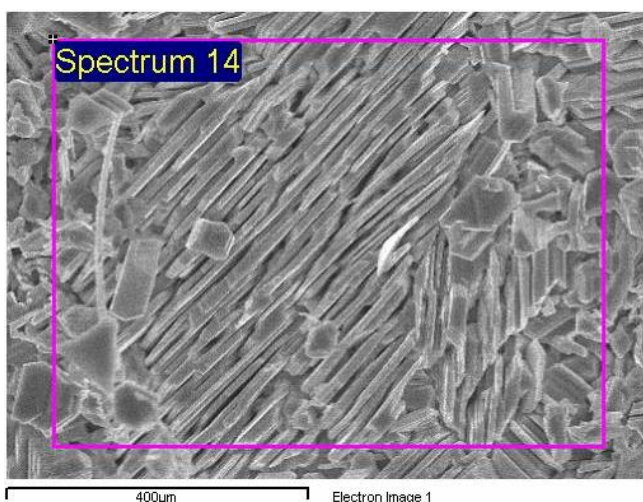


Figure 4-40: SEM micrograph of sample area (Cu2) analysed in Figure 4-39

EDX detected only tellurium and copper as being present. Elemental quantification was performed on multiple areas of each sample and the results averaged. The data showed the elemental composition of the closely bound plates to contain less tellurium than the free standing plates and was quantified as $\text{CuTe}_{0.6}$. On average the closely bound plates contained 25% less tellurium than the free standing plates.

4.5.4.2.5 *Unreacted surface*

The third surface type recorded on the lower temperature copper surface reactions showed small areas where no significant morphological changes had occurred from the originally

smooth surface. Unreacted areas, making up less than 10% of a substrate, were found at areas positioned furthest from the powdered reagents. Figure 4-41 shows one such unreacted area. There was no surface growth observed in these areas. SEM showed no plate structure but simply a roughened copper surface.

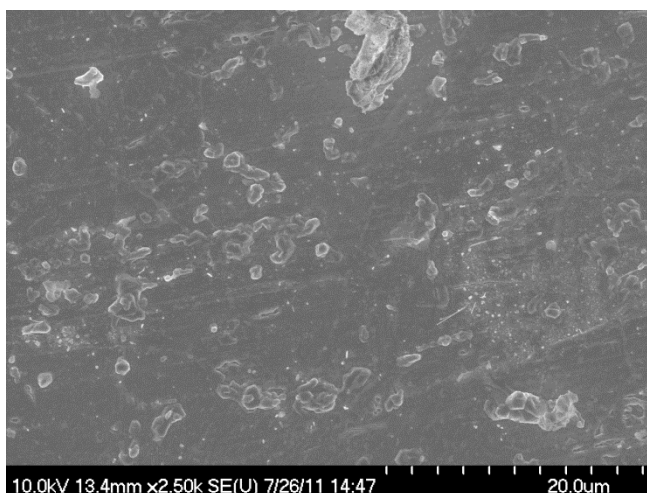


Figure 4-41: SEM micrograph showing unreacted area on Cu3

4.5.4.2.6 *Elemental analysis*

EDX of the few unreacted areas showed the surface to comprise almost entirely of copper. One significant contrast to the composition of the unreacted surfaces is the presence of bismuth albeit in very low quantities; this is shown in Figures 4-42 and 4-43. Quantification showed a copper composition of 86.66%, tellurium as 11.18% and bismuth as 2.16%.

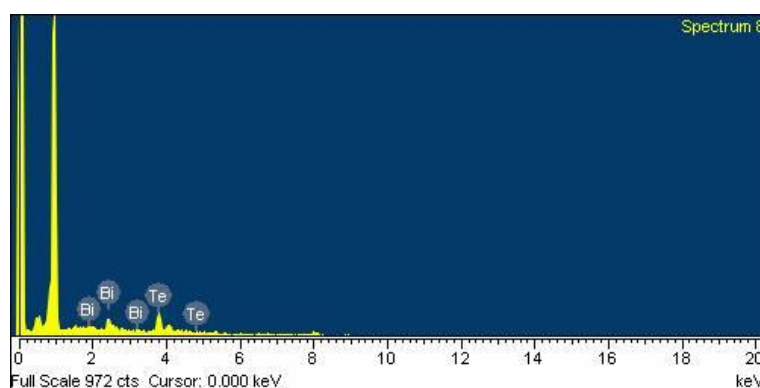


Figure 4-42: EDX spectrum showing over 85 % copper with small quantities of Te and Bi (sample Cu3)

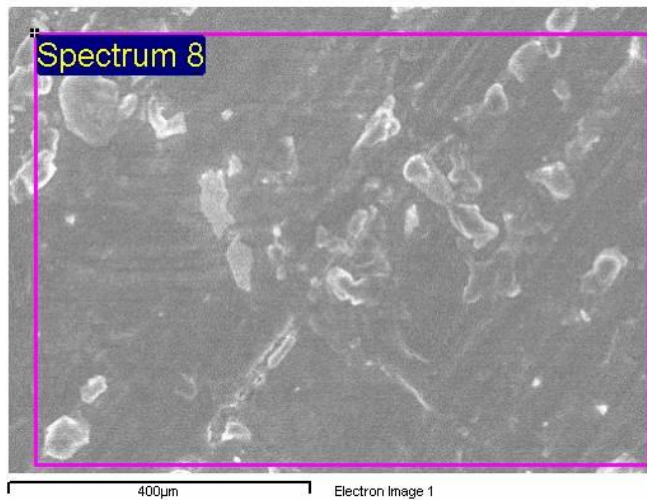


Figure 4-43: SEM micrograph showing selected area analysed in EDX spectrum above (sample Cu3)

4.5.4.3 Crystalline phase identification

As three distinct areas of growth were discovered, each with a different elemental composition, XRD did not prove to be particularly useful in these experiments as by its nature it examines the entire surface of the sample and is therefore exposed to a number of different phases. Shown below in Figure 4-44 is a standard pattern obtained from Cu₂.

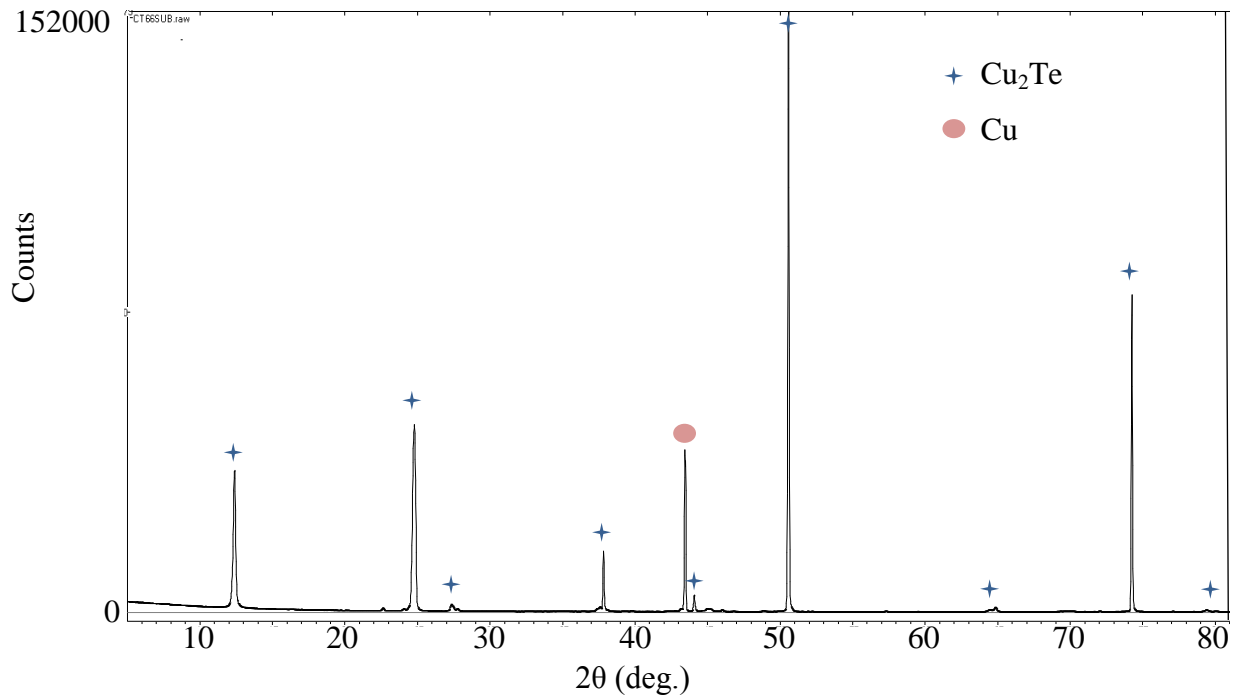


Figure 4-44: XRD pattern of sample Cu2 corresponding to Cu₂Te and Cu

The XRD data shown in Figure 4-44 correspond to a Cu₂Te phase. EDX spectroscopy revealed areas unlikely to match to a Cu₂Te phase however, it should be noted that EDX is a localised technique while XRD is sample wide.

In addition to the copper telluride phase identified, elemental copper is also evidenced. The Cu presence is expected assuming the penetration depth of the X-rays is sufficient to penetrate the surface growth, as unlike higher temperature reactions, the substrate had not entirely degraded and was instead only surface reacted.

4.5.5 Conclusions, 450 °C reactions

The initial reactions sought to grow structures of bismuth telluride on the surface of copper. It was discovered that under these conditions copper would be an unsuitable substrate to increase the surface growth of copper telluride. The copper reacted preferentially with the tellurium (as to be expected) but did not provide a suitable site for bismuth telluride growth.

Shown above is a simple route to a regular and interesting morphology of copper telluride. The tellurium reacts preferably with the copper meaning any exposed edges will seed growth of free-standing plates with nanoscale thickness and micron scale diameter. These plates align perpendicular to the copper edge and have a $\text{CuTe}_{0.9}$ stoichiometry.

If the edge of the copper is unavailable, the tellurium will still react with the copper but produce a slightly different morphology. When tellurium reacts with the central surface of the copper a tight packed plate structure is formed. Central plates are not freestanding and cause a textured pattern on the surface of the copper substrate. These closely packed plates have comparable nanoscale thickness to the freestanding edge plates but have a reduced diameter. The closely packed plates are evidenced by EDX to have a lower tellurium composition showing a ratio of 1:0.62 of copper and tellurium, respectively.

Small areas of the substrate were discovered on the far end of the sample which had produced no significant growth. These areas were shown to contain low levels of bismuth, <3%, these were the only areas where bismuth was identified.

In conclusion this synthetic route proves successful for the creation of a three dimensional array of nanostructured Cu_2Te particles but further work on the characterisation and properties of the particles is required.

4.5.6 Bismuth transport on copper

The above reactions had proved unsatisfactory in the growth of bismuth telluride structures due to copper's preferential ability to bond with the tellurium over the bismuth. To overcome this it was decided to react copper with bismuth alone. Subsequently these substrates were then reacted with tellurium.

Reactions were carried out by reacting copper substrates with bismuth (2 mmol, 99% pure, 100 mesh, Sigma Aldrich) at 450 °C for 48 h. Subsequently these substrates were reacted with tellurium (3 mmol, 99.8% pure, 200 mesh, Sigma Aldrich) at 450 °C for 48 h. Reactions took place in sealed ampoules in the same process as the previous section.

4.5.6.1 Results

Sample Cu4 from Table 4-1 is described here as an example system.

4.5.6.1.1 Post-reaction appearance

Following reaction with bismuth, the copper foil had retained its bright copper appearance, it could also be seen, by eye, that there were small silver droplets coating the surface of the copper.



Figure 4-45: Copper foil following reaction with bismuth Cu4

4.5.6.1.2 Morphology

SEM confirmed the bismuth surface deposition. The bismuth had transported and deposited in distinctive circular droplets.

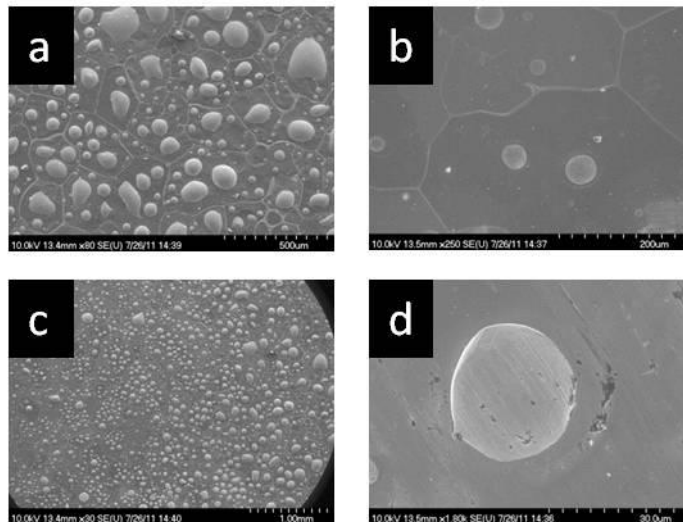


Figure 4-46: SEM micrographs of bismuth deposition on copper (Cu4)

As shown in Figure 4-46 the bismuth deposited on the surface as embedded circular droplets 10-20 µm in diameter. Also seen in Figure 4-46 b was the veining of bismuth through the surface of copper.

4.5.6.2 *Post-reaction with tellurium.*

Exemplar reaction described here was produced following a reaction between sample Cu4 and tellurium, following the reaction the sample is labelled Cu4B

4.5.6.2.1 *Post-reaction appearance*

Following reaction the samples emerged having lost their shiny metallic appearance replaced by a dark grey flaked appearance. There was significant damage to the surface of all substrates which underwent this second tellurium reaction; an example is shown in Figure 4-47.

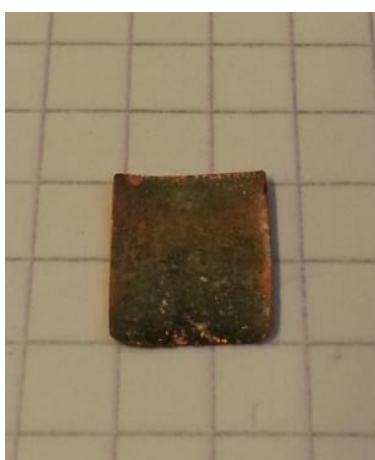


Figure 4-47: Cu4B following tellurium reaction.

4.5.6.2.2 *Morphology*

SEM micrographs (Figure 4-48) showed that substrate had undergone dramatic transformation as the copper reacted with the tellurium while bismuth had pooled separately. Islands of copper and tellurium were separated by intervening and connected areas of high bismuth concentrations (the following is evidence by EDX, shown below).

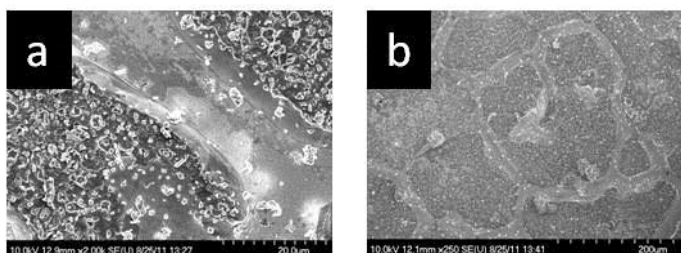


Figure 4-48: SEM micrographs following reaction with tellurium (Cu4B)

The bismuth has separated out leaving a distinctive veining pattern across the surface with the other areas showing irregular particle formation.

4.5.7 Elemental analysis

EDX mapping was used to show localisation of the 3 metals across the surface, this is shown in Figure 4-49.

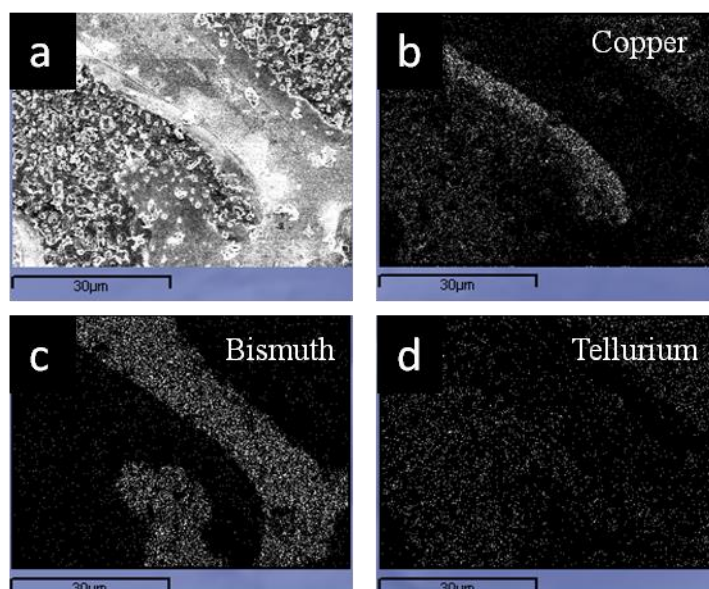


Figure 4-49: SEM micrographs showing elemental map of Cu4B

Figure 4-49 shows an EDX elemental map of the surface of the sample Cu4B. Figure 4-49 shows a) full image, b) the presence of copper highlighted, c) the presence of bismuth highlighted and d) the presence of tellurium highlighted. The mapping shows that the bismuth, previously found in isolated droplets or islands across the copper surfaces had now formed veins across the surface. Figure 4-49 c shows the presence of bismuth clearly corresponding to the distinctive smooth areas imaged by SEM. The EDX appears to show the tellurium preferentially reacting with the copper as despite tellurium being found in all areas of the substrate, the concentration is lower in areas with high bismuth content.

4.5.8 Conclusions

This section deals with the chemical vapour reactions involving bismuth and tellurium on copper foil surfaces. It was demonstrated that at high temperatures (700 °C) the tellurium reacts with the copper forming regular triangular layered crystals with a dicopper telluride structure, the composition of this was confirmed by XRD and EDX. This process is of interest as copper ditelluride has applications for use as fast ion conductors and ohmic

contacts for the cadmium telluride compounds found in commercial solar energy harvesters¹²⁶⁻¹²⁸.

When similar reactions were carried out at the lower temperature of 450 °C aligned copper telluride plates with nanoscale thickness could be grown. These plates had a high aspect ratio being 5-25 µm in width but less than 500 nm. The plates were hexagonal in appearance, a morphology which has been seen before when grown by pulsed laser deposition¹³⁰. The plates being a tellurium deficient CuTe phase may be of benefit as often non- stoichiometry phases prove to be the best conductors¹²⁹.

Also investigated in this section was the reaction with copper and bismuth and subsequent reaction with tellurium. The bismuth formed an alloy with the copper but did not show any evidence of new crystallographic structure. Post-reaction with tellurium led to the formation of copper telluride and the aggregation of bismuth into veins across the surface of the substrate.

4.6 Solvothermal synthesis of Bi₂Te₃

Reported here is a reproduction of the method used by Zhang *et al.*¹³¹ which consistently produced a different morphology of particle than that reported in the original work.

4.6.1 Reaction set up

The reaction followed a refluxing solvothermal process designed to create nanostructures of tellurium and then incorporate bismuth into these to produce Bi₂Te₃.

Reactions were conducted in a three necked round bottomed flask fixed with a water cooled reflux condenser in the central position. The right arm of the flask was connected to an argon supply to keep the reactions under an inert atmosphere. The left arm of the flask was sealed with a rubber septum and was used for injecting additional reagents mid-synthesis.

Before the septum was fixed to the flask, ethylene glycol (20 mL), polyvinylpyrrolidone (0.2 g), sodium hydroxide (0.6 g) and tellurium dioxide (3 mmol, powdered, Sigma Aldrich) were added and mixed using a magnetic stirrer bar. These were mixed to form a

milky solution. Once thoroughly mixed, heating using an oil bath brought the solution to 160 °C.

Upon heating and dissolving of the reagents the solution turned clear brown. To this mixture hydrazine hydrate (0.6 mL, Sigma Aldrich) was added *via* syringe through a rubber septum. This instantly created white vapour and bubbles within the solution. The hydrazine reduced the tellurium dioxide to form the basis of the final tellurium structure-Te nanowires. Within seconds of adding hydrazine, the solution turned a dark opaque brown/black suspension. This suspension is left stirring and at 160 °C for 1 h.

Following the method prescribed by Zhang *et al.*¹³¹, a bismuth solution was prepared in tandem with the tellurium reaction by dissolving $\text{Bi}(\text{NO}_3)_3 \cdot 5\text{H}_2\text{O}$ (2 mmol) in ethylene glycol (5 mL). Following 1 h heating of the tellurium containing suspension the bismuth solution is added, again this is injected using a syringe. The solution quickly turned black after the addition of the bismuth. The solution was left stirring at 160 °C for a further hour. After the 1 h had elapsed, the solution was removed from the oil bath and left to cool (maintaining the flow of argon throughout).

Under the process described by Zhang *et al.*, there was no post-reaction description or method for collecting samples¹³¹. It is unlikely that the difference in post-reaction treatment would have resulted in the different morphologies of particles obtained.

When cooled the solution was centrifuged, which separated an ethylene glycol layer from a black powder. The glycol layer was decanted off and the powder transferred into a sample vial and unsealed to dry overnight in an oven at 90 °C. The powders obtained were characterised by SEM, XRD and Raman Spectroscopy.

4.6.2 Results

Sample S1 from Table 4-1 is described here as an example system.

4.6.2.1 Crystalline phase identification

The powder XRD patterns of all samples matched well to Bi_2Te_3 . Shown below in Figure 4-50 is a pattern obtained from sample S1.

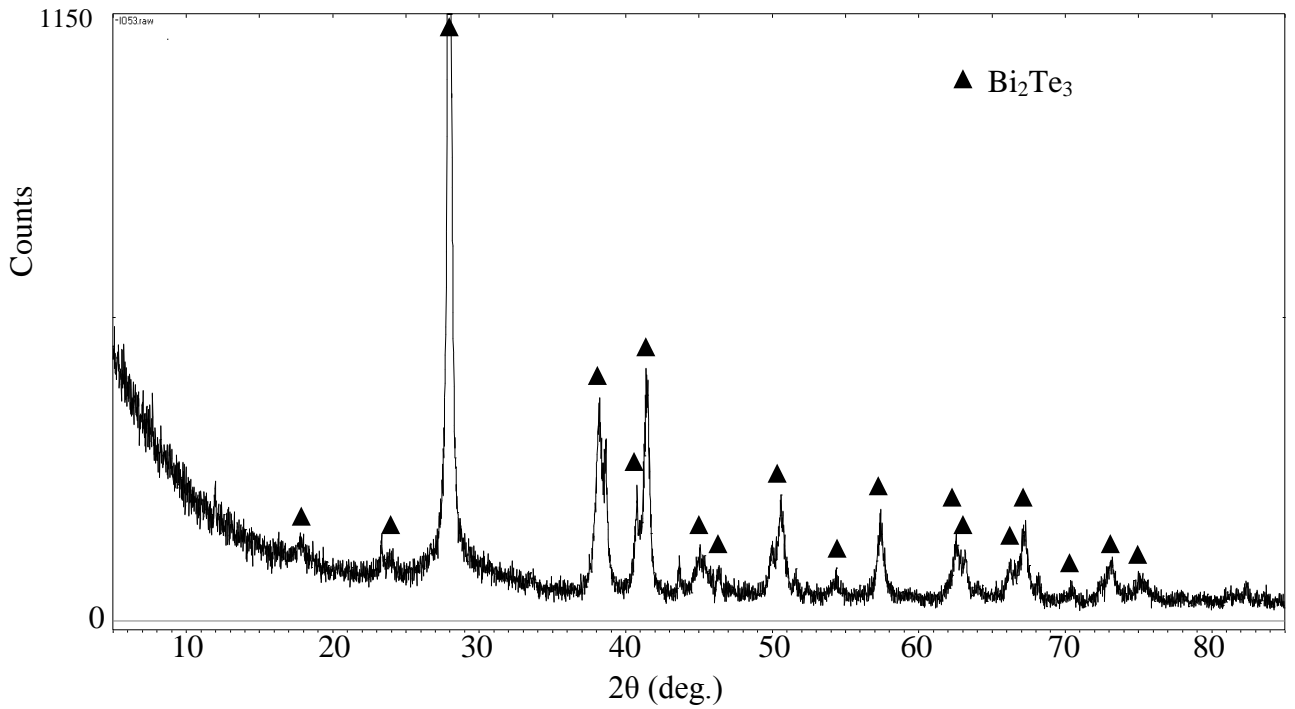


Figure 4-50: XRD pattern of S1 matching to Bi_2Te_3

4.6.2.2 Morphology

SEM showed the fine black powder to be composed of nanorods. The rods were 200- 500 nm in length and 40- 80 nm in diameter. Shown below in Figures 4-51 and 4-52 are a selection of SEM micrographs showing the rod structure. The rod structure can be clearly observed in Figure 4-52.

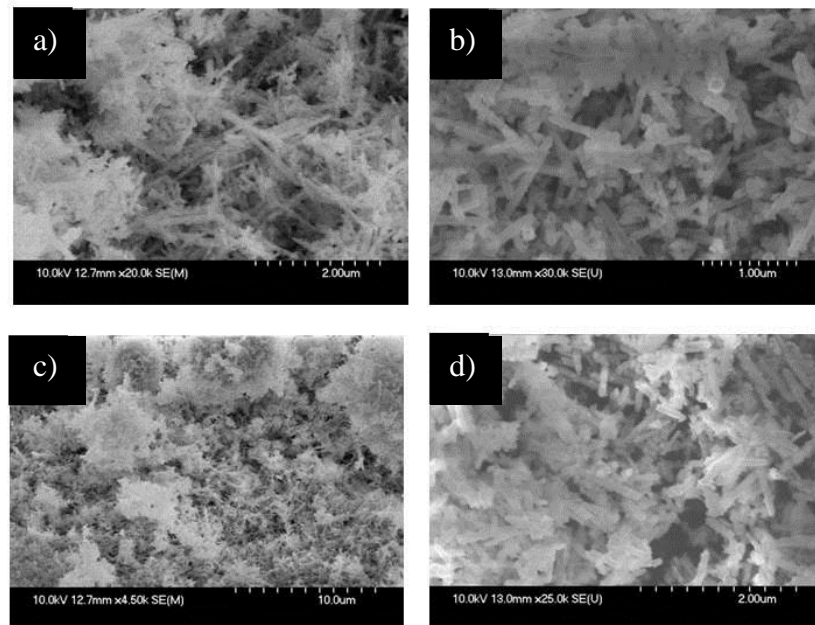


Figure 4-51: SEM micrographs of Bi_2Te_3 rods (S1)

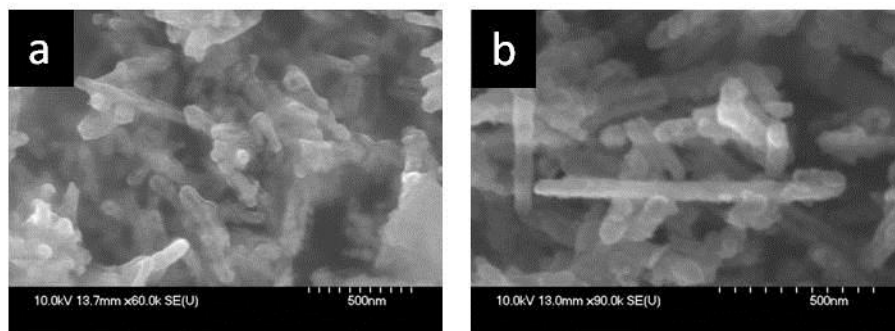


Figure 4-52: SEM micrographs showing high magnification of rods in S1

It is also of note that the contrast in the rods varies along their length. This may suggest that the rods are in fact hollow or partially electron transparent at points. It is clear from the images that the electron contrast is not uniform, and this suggests that some areas may be more transparent to the electrons than others. TEM would be useful to further investigate the rod composition.

4.6.2.3 Phase characterisation

Raman spectra for the samples were recorded. Spectra were recorded at various locations on each sample. The results of which are overlaid in Figure 4-60.

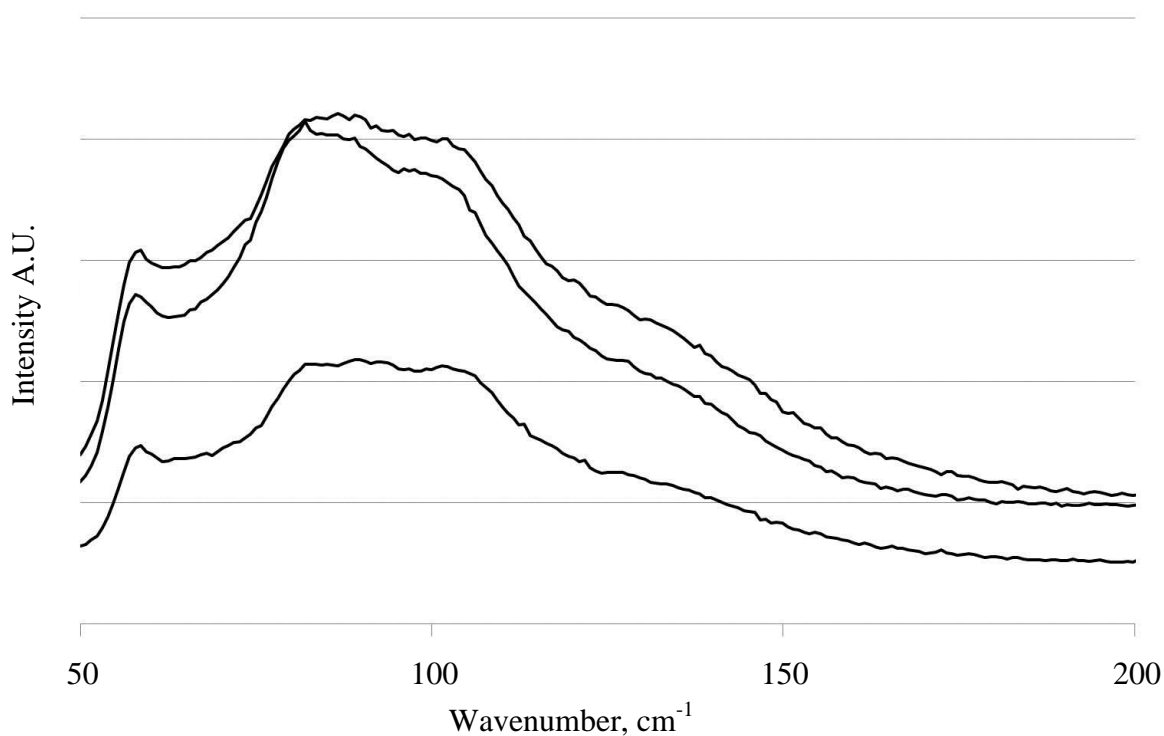


Figure 4-53: Raman spectra for sample S1

The wavenumber of the peaks and band assignments are shown in comparison to previously assigned literature values^{106, 113}.

Table 4-5: Raman spectroscopy peaks and assignments

	¹ E _g	¹ A _{1g}	¹ A _{1u}	² E _g	² A _{1u}	² A _{1g}
S1	46.3	63.0	90.3		112.9	138.0
Bulk ¹⁰⁶	40.2	60.2		100.8		133.2
Nanoscale ¹⁰⁶	40.1	59.1	87.8	100.8	115.2	137.2
bulk ¹¹³	34.4	62.1		101.7		134
Nanoscale ¹¹³	38.9	61.3		107.3	116.2	113

The samples display the ¹E_g, ¹A_{1g} and ²A_{1g} bands which are observed in bulk Bi₂Te₃. In addition to these bands, the ¹A_{1u} and ²A_{1u} bands are identified, which are associated with nanoscale bismuth telluride structures.

4.6.3 Comparison to previous work

Despite using the method set out by the previous work, the structures produced were noticeably different from those produced by Zhang *et al.*¹³¹. In the previous work, wires

of sub 10 nm length were demonstrated; rods produced here were considerably shorter and wider than those in previous work as shown in Figure 4-54.

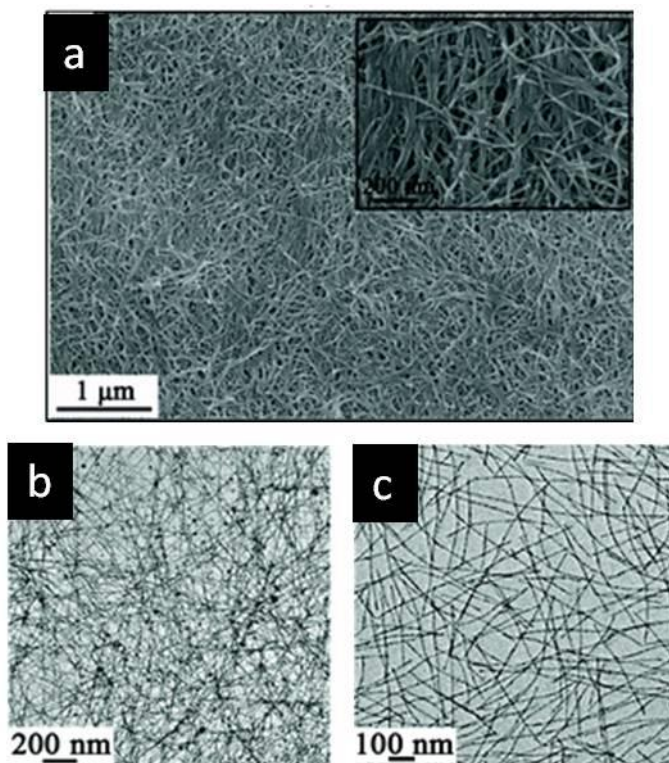


Figure 4-54: SEM micrographs showing thin wires reported by Zhang *et al.*¹³¹

4.6.4 Conclusions

Reported here is the synthesis of nanorods of 200-500 nm length and 40- 80 nm in diameter. These were produced by a solvothermal route previously described as producing wires of 8 nm width despite employing the same method. The only alterations to the previously described process were the use of Argon as a protective gas and the post-reaction filtering of the product.

The wires were identified as Bi_2Te_3 using XRD and Raman spectroscopy. All reflections identified by powder XRD matched to single phase Bi_2Te_3 , and Raman spectroscopy identified 5 bands attributed to bismuth telluride including 2 which are observed only in nanostructured Bi_2Te_3 .

4.7 Conclusions

This chapter investigated CVD reactions on a range of non silicon surfaces. This follows on from Chapter 3 which details the growth of Bi_2Te_3 on Si surfaces. Metal foils and commercial substrates were investigated.

The most promising alternative to Si was Al_2O_3 which is described in Section 4.1. Bi_2Te_3 was successfully grown on Al_2O_3 wafers. The particle morphology was distinct from the growth evidenced in similar reactions on a Si surface. The growth on Al_2O_3 had a spherical morphology which on closer inspection had a fine nanoplate structure. The 20 μm spheres were found at irregular intervals on the substrate surface following CVD using Bi and Te at 700 °C for 48 h. The spheres were comprised of nanoplates 50-850 nm wide. To further understand the growth of the particles, reactions were conducted with Te alone followed by Bi reactions. It was demonstrated by SEM that Te did not adhere well to the Al_2O_3 wafer but in contrast Bi growth was found on the surface which showed a nanostructured sphere pattern analogous to that of the Bi_2Te_3 growth. The single element reactions suggest that it is the growth of Bi on the surface which is driving the Bi_2Te_3 growth over that of Te.

Gallium arsenide wafers were also investigated for their suitability in closed space CVD reactions for growth of Bi_2Te_3 in Section 4.3. These wafers were shown to be unsuitable to cope with the high temperatures and reactive environments inherent in CVD reactions. No quantifiable Bi_2Te_3 growth was evidenced as the substrates had reacted with the tellurium and had fragmented. Some hexagonal plates indicative of Bi_2Te_3 were observed but could not be quantified.

Metal foils were investigated in Sections 4.4 and 4.5. Cobalt proved to be a poor facilitator of growth in a CVD environment. After 48 h reacting with Te and Bi, the foil had become fused with tellurium and was brittle with the surface showing very little growth by SEM. The foil was matched to a cobalt telluride structure by XRD. Copper foil was found to form a dicopper telluride structure following 48 h at 700 °C with Bi and Te. The substrate degraded and produced large triangular crystals of Cu_2Te as evidenced by XRD. Lowering the temperature to 450 °C provided a stark contrast with a vertically aligned nanoplate array being produced. The copper telluride plates were <500 nm thick but were up to 25 μm in diameter. At the edges of the substrate these plates were more free standing while in

the centre of the substrate they were tightly bound. Copper tellurides have potential as a contact material in solar cells.

The final section in this chapter (Section 4.6) looks at a reproduction of a literature synthesis of Bi_2Te_3 which repeatedly produced a different morphology to that reported. The samples were produced following the method described by Zhang *et al.*¹³¹ and a comparative study was carried out. This method produced nanorods of Bi_2Te_3 which were characterised by XRD, SEM and Raman spectroscopy.

5 Nanostructured spheres of titanium dioxide by microwave hydrothermal reactions.

This chapter details the rapid production of single-phase nanostructured TiO₂ spheres. The micron-dimensioned spheres are shown to have a fine hierarchical rod nanostructure. This chapter aims to investigate the growth of these spheres through hydrothermal microwave synthesis; to demonstrate the growth control of experimental parameters and to fully characterise the products.

Synthesis was carried out in a microwave hydrothermal reaction, both single and multi-mode microwave cavities are reported in this work. The products of these reactions were characterised with: powder X-ray diffraction (XRD); both scanning and transmission electron microscopy (SEM and TEM); elemental analytical techniques such as electron energy loss spectroscopy (EELS); and optical absorption properties by UV/Vis diffuse reflectance spectroscopy.

The synthetic route detailed in this work was developed by a previous group member¹³² and detailed here is the development and control of this synthetic technique.

Titanium dioxide is a ubiquitous compound found in thousands of products around the globe. While its functionality started primarily as a pigment by replacing harmful lead based pigments, it soon became one of the most interesting functional energy materials due to its photocatalytic, electrical and optical properties.

One issue faced in the commercial production of TiO₂ is the irregularity of particle size and morphology. Pigment grade TiO₂ can be produced from reacting the naturally occurring ilmenite (FeTiO₃) ore with sulfuric acid. While suitable for bulk pigment material there is little structure control. Similarly when titanium tetrachloride is reacted with oxygen directly there is little fine-control over morphology. Modern techniques look to create new and interesting morphologies in controllable manners. The goal of this control is tailoring functionality of the product as crystal structure and morphology play important roles in the overall properties of the material.

Spherical morphologies are of particular interest due to their surface to volume ratio and reflectance properties. Routes to spherical morphologies are fairly well established through traditional hydrothermal routes^{133, 134}, but in recent years microwave heating has unlocked new growth processes. The first report of the microwave technique being used to create particles of TiO₂ was published in 1992¹³⁵. Subsequent to that report, there has been very little interest taken until the early 2000s when the technique was revived.

Almost exclusively, microwave hydrothermal techniques lead to the anatase phase¹³⁶⁻¹⁴¹ of TiO₂ and production of pure rutile, the most thermodynamically stable of all TiO₂ phases, has been problematic.

One paper of particular interest by Baldassari *et al.*¹⁴² produced single rutile phased TiO₂ using microwave synthesis. Unlike the work described here Baldassari *et al.* were unable to produce a phase-pure product with short irradiation times. Baldassari *et al.* required two-hour exposure time to achieve fully crystalline products. This thesis will detail a successful synthesis requiring less than one minute. Ma *et al.* also successfully produced larger structures, roughly spherical, of single-phase TiO₂ by microwave hydrothermal growth¹⁴³.

Subsequently to the work reported in 2005, others have managed to reduce reaction time. In 2012 Yoon *et al.*¹⁴⁴ produced a range of TiO₂ phases in 30 min using titanium tetrachloride or titanium trichloride in various alcohols, although the process did require six hours of stirring before irradiation. In 2009 Li *et al.*¹⁴⁵ were able to produce anatase nanoparticles in 15 min (with >98% yield) using a rapid microwave-assisted esterification process.

Reported here for the first time is the synthesis of rutile-phase spheres with a hierarchical nanostructure produced in sub-minute reactions with control of sphere diameter. Further to this study the use of multi-mode and single-mode microwave reactors for synthesis is compared.

5.1 Experimental technique

The preparation of TiO₂ nanostructures followed a simple stepwise process: (i) create a stock solution of hydrochloric acid; (ii) add titanium tetrachloride to a small volume of

acid and (iii) transfer this to a Teflon autoclave for microwave irradiation followed by filtration and washing.

Initially a stock solution of hydrochloric acid (2 M) was prepared. Into a 10 mL volumetric flask 7 mL of the HCl stock solution was added and then it was packed in ice to cool. Using a needle and 1 mL syringe the required amount of TiCl_4 was quickly added to the volumetric flask and the vial of starting material resealed. A yellow precipitate of $\text{TiO}(\text{OH})_2$ was formed during addition, this was dissolved with the aqueous acid. Additional acid solution is added dropwise to fill to the 10 mL mark. The solution was shaken to ensure that all $\text{TiO}(\text{OH})_2$ was dissolved. The resulting solution (clear or partially cloudy) was transferred to a Teflon lined microwave autoclave or glass tube with crimp-on cap.

Two microwave reactors were used in this work. The first reactor provided a multi-mode microwave environment and was a standard domestic microwave oven, the make and model of which was: Panasonic NN- T552 W, 900 W, category D. Used at full power the manufacturer confirmed that the output was approximately 900 W. Irradiation time was an alterable parameter but all reactions in the multi-mode cavity were carried out at the same power. Results here describe samples prepared in a 1-4 min range. The second reactor was a single-mode CEM Discover®, CEM Corporation, Matthews, NC, USA, 300 W max. output, 2.45 GHz.

The post-treatment of samples from both reactors involved allowing the reaction vessel to cool to room temperature overnight. Following cooling, the sample was filtered, and the resulting powder was washed first with water then ethanol (approximately 3-5 mL each). Finally the powder was dried in an oven overnight at 80 °C. This process produced a very fine white powder, with an almost 100% yield. Samples were characterised using XRD, SEM, TEM, UV/Vis spectroscopy and BET surface analysis.

5.2 Results and discussion multi-mode cavity synthesis

Table 5-1 lists the prepared samples discussed in this work. All samples here were prepared using 2 M HCl concentration.

Table 5-1: Sample list, TiO₂, multi-mode reactor

Sample Identifier	Irradiation time / s
T1	30
T2	60
T3	60
T4	90
T5	90
T6	120
T7	150
T8	180
T9	240

Additional samples will be detailed in relevant sections.

5.2.1 Crystalline phase identification

All samples in Table 5-1 were identified as matching the rutile-phase of TiO₂ by XRD. All samples produced under ideal conditions (use of fresh reagents) produced single-phase TiO₂ in the rutile morphology. Shown below in Figure 5-1 is a standard pattern gathered by an overnight XRD scan.

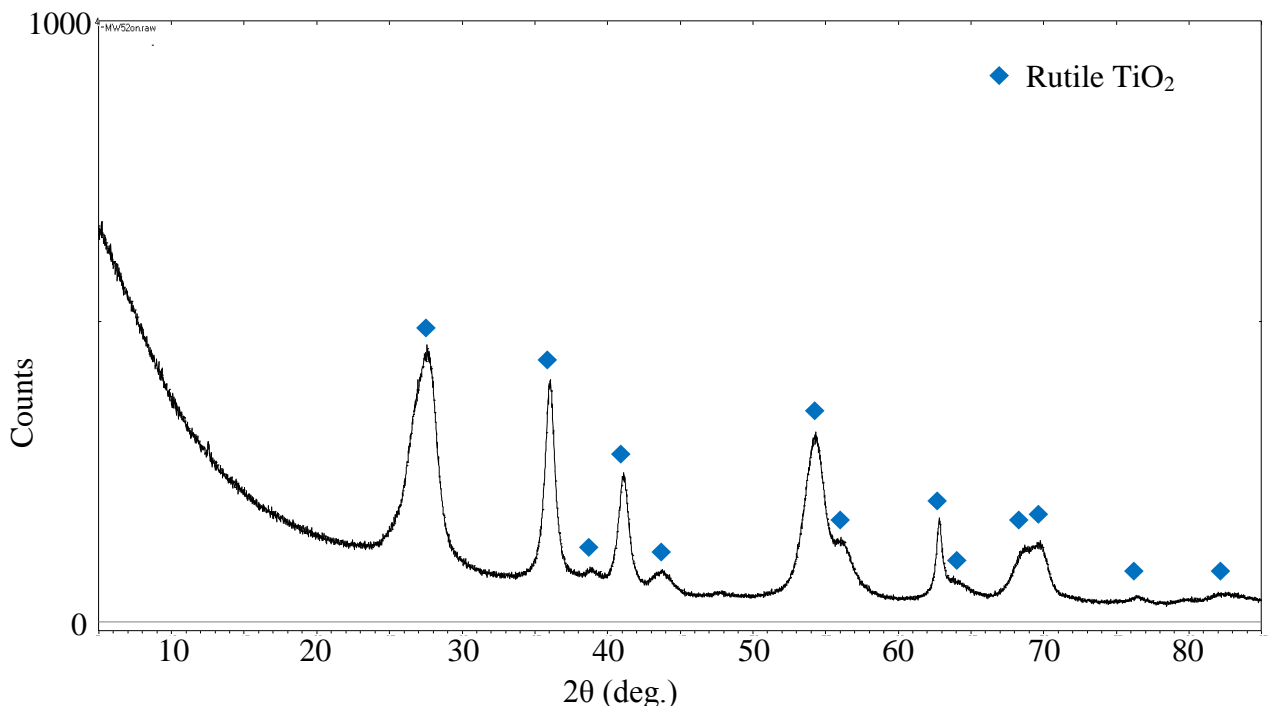


Figure 5-1: XRD pattern of multi-mode TiO₂ sample T4

The above sample (T4) was produced with an irradiation time of 90 s. All peaks present can be assigned to the rutile phase in tetragonal space group P4/mnm.

The irradiation time can be reduced and successful samples have been produced in 20 s. Reactions carried out with shorter irradiation times display a lower level of crystallinity. This can be observed in the reduction of X-ray diffraction peak intensity as shown in Figure 5-2 which shows sample T1 which was produced with only 30 s irradiation.

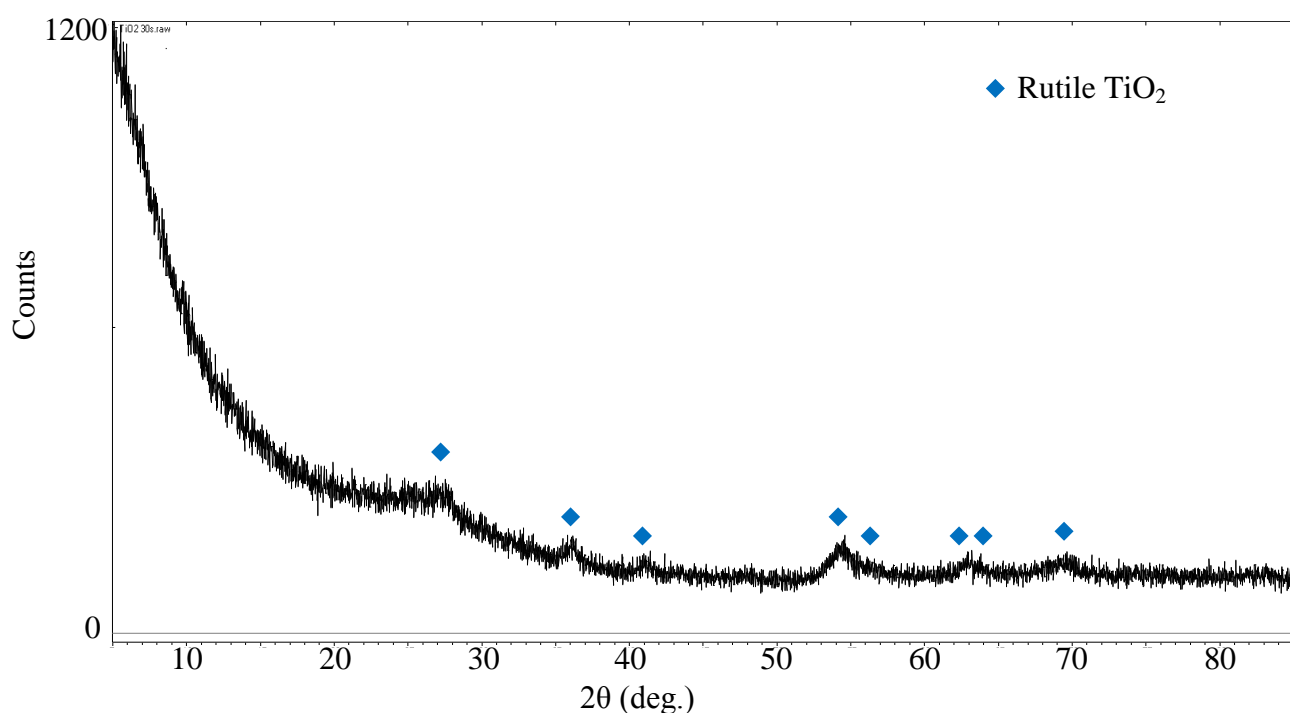


Figure 5-2: XRD pattern showing low crystallinity of sample T1

As can be seen from Figure 5-2 the peaks of T1 are of very low intensity. This was the case for samples produced with less than 60 s irradiation time. This is evidence of poor crystallinity of the sample. T1 therefore has a much higher content of amorphous material. The intensity of the reflections from a sample such as T1 (produced with short irradiation time) could be increased by sintering the samples in air. Morphology was retained and the intensities of the peaks were increased when heated at 200 °C in an open-ended tube furnace. XRD patterns of additional samples can be found in Appendix B (Figures 9-9 to 9-13). Samples T1-T9 all displayed the rutile structure.

5.2.2 Morphology

One of the most interesting aspects of this rapid synthesis is the reproducible production of a single morphology. Particles produced in this multi-mode microwave reaction were uniformly spherical and composed of nanorods that are orders of magnitude smaller in scale. Shown in Figure 5-3 are selected SEM micrographs from a range of samples and conditions which demonstrate the spherical morphology.

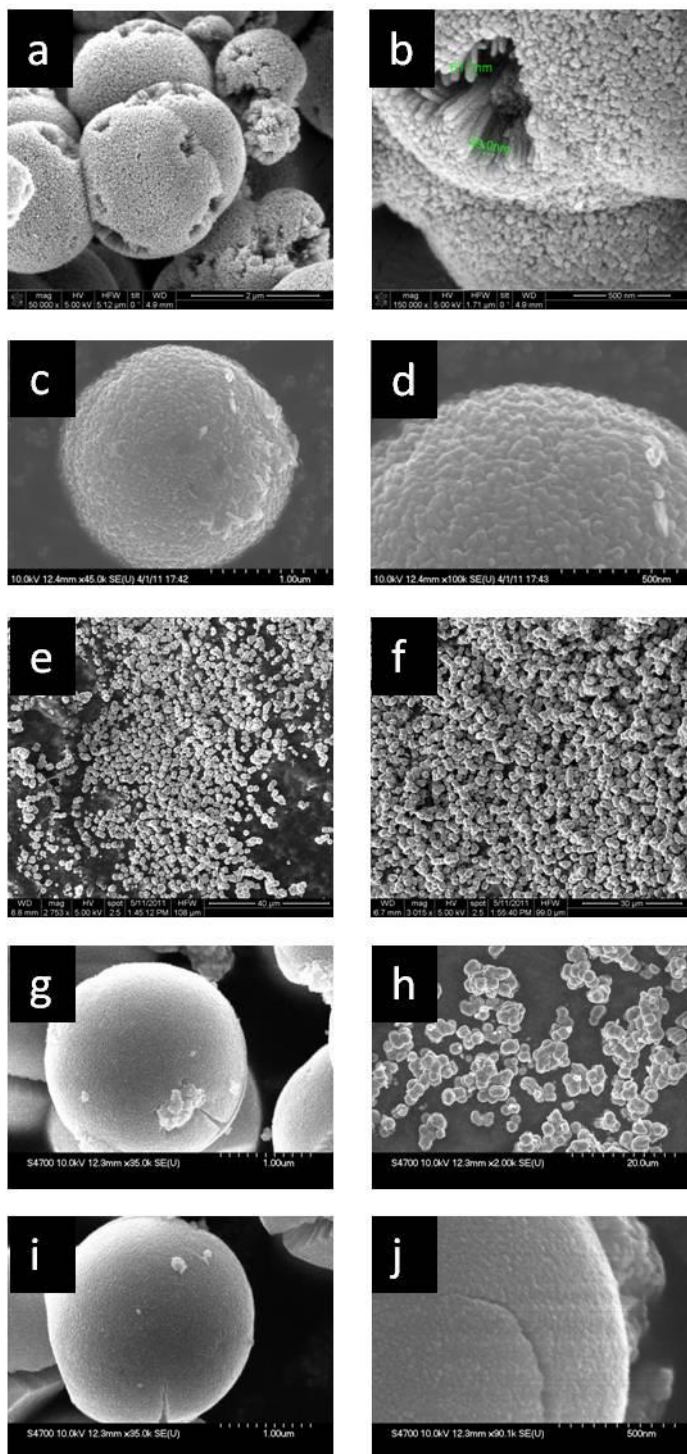


Figure 5-3: SEM micrographs showing particle morphology. (a and b) T8, (c and d) T3, (e) T6, (f) T5, (g-j) T7

The product had grown into spherical particles between 1 and 3 μm in diameter. On high magnification it can be seen that the spheres are composed of nanorods aligned radially. This can be most clearly seen on the damaged sites on sample T8 in Figure 5-3 b.

5.2.3 TEM analysis

5.2.3.1 Bright Field/ Dark Field images

Contrasting bright and dark field images highlights the radial growth and alignment of the rods. Excluding unscattered electrons and tilting the beam highlights similar crystal planes clearly show the rods aligned radially. In Figure 5-4 a segment of a sphere is shown. The centre of the sphere lies to the bottom left hand corner and the outer surface of the sphere runs from the top to the bottom right.

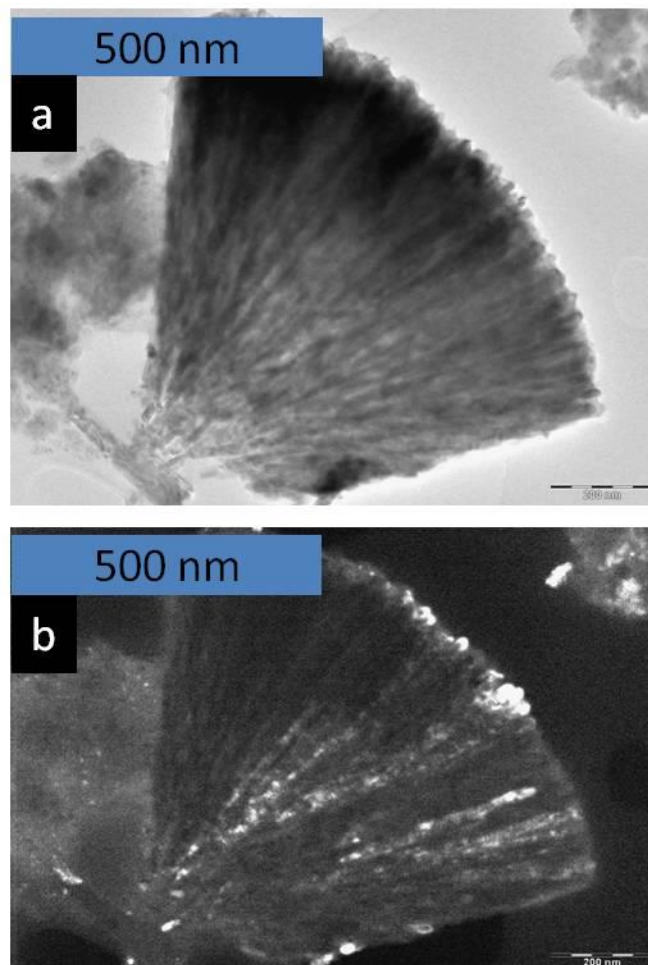


Figure 5-4: TEM micrograph showing (a) Bright field image and (b) Dark field image of sample T5

The dark field images highlight the similar crystal planes lying in the radial direction. As the beam is tilted, the rods visible in the dark field change showing the clear rod structure as the beam tilts and the ideal scattering condition is fulfilled for individual crystal planes.

5.2.3.2 Selected Area Electron Diffraction

A selected area used for electron diffraction is shown in Figure 5-5 along with the corresponding electron diffraction pattern.

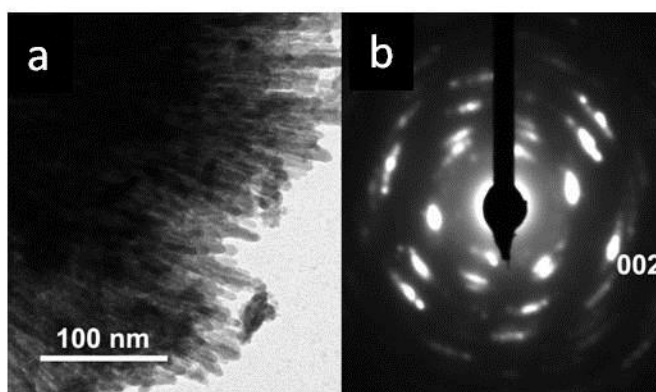


Figure 5-5: TEM micrographs of selected area diffraction of sample T5

Highlighted in the diffraction pattern are spots corresponding to the (002) direction in the reciprocal lattice. Therefore the nanorods are parallel to this and thereby parallel to the c -axis of the rutile structure with growth following the (001) plane.

5.2.3.3 High Resolution Transmission Electron Microscopy

High-resolution transmission electron microscopy (HRTEM) was performed by Dr Ian MacLaren of the School of Physics and Astronomy, University of Glasgow.

To visualise the growth more fully, HRTEM was employed to identify possible defects that could induce splitting of rods as they radiate towards the external surface of the TiO_2 spheres.

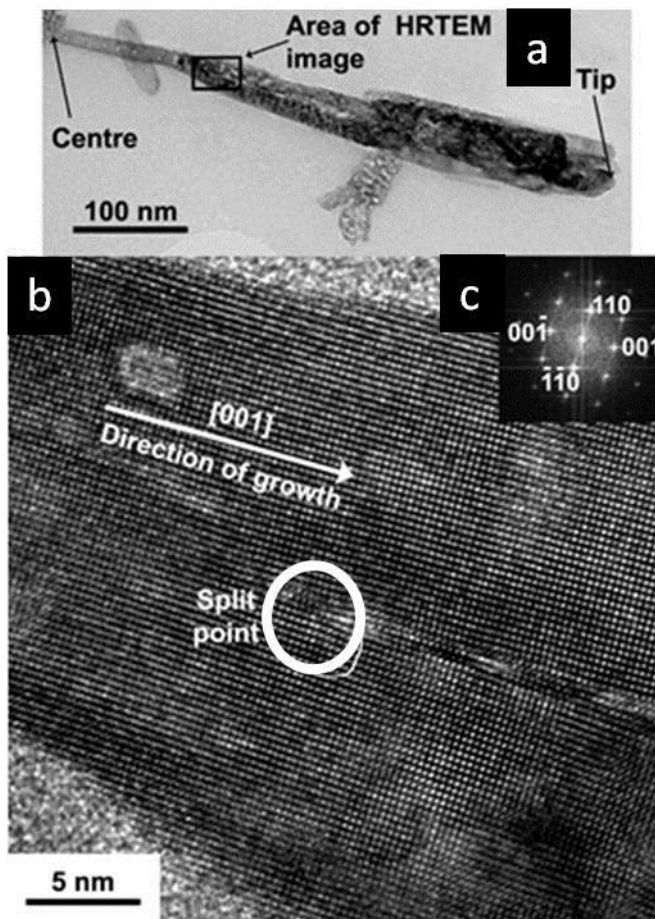


Figure 5-6: Sample T5. (a) TEM image of the rod structure, (b) HRTEM of area boxed in (a) illustrating the splitting point in rod growth, (c) fast Fourier transform electron diffraction pattern

From (c) in Figure 5-6 it can be seen that (b) was imaged along the (110) direction and the growth lies in the (001) direction.

One possible rationalisation for the rod-like structure is being a result of the preferential growth along the (001) direction. During growth the crystal encounters defects which create fractures splintering the crystal and giving rise to a rod-like appearance.

The growth along the (001) direction can be further rationalised with reference to existing literature. A number of articles identify (001) being the preferred direction for nanorod growth^{143, 146, 147}. Growth potential is dependent on the corners and edges available, and thus Mali *et al.* ordered the growth potential of the directions to be $(110) < (100) < (101) < (001)$ ¹⁴⁸. Additionally Cai *et al.* reported that when Cl^- ions are present in the reaction, they can selectively bind to the (110) plane resulting in anisotropic growth along the (001) direction¹⁴⁹.

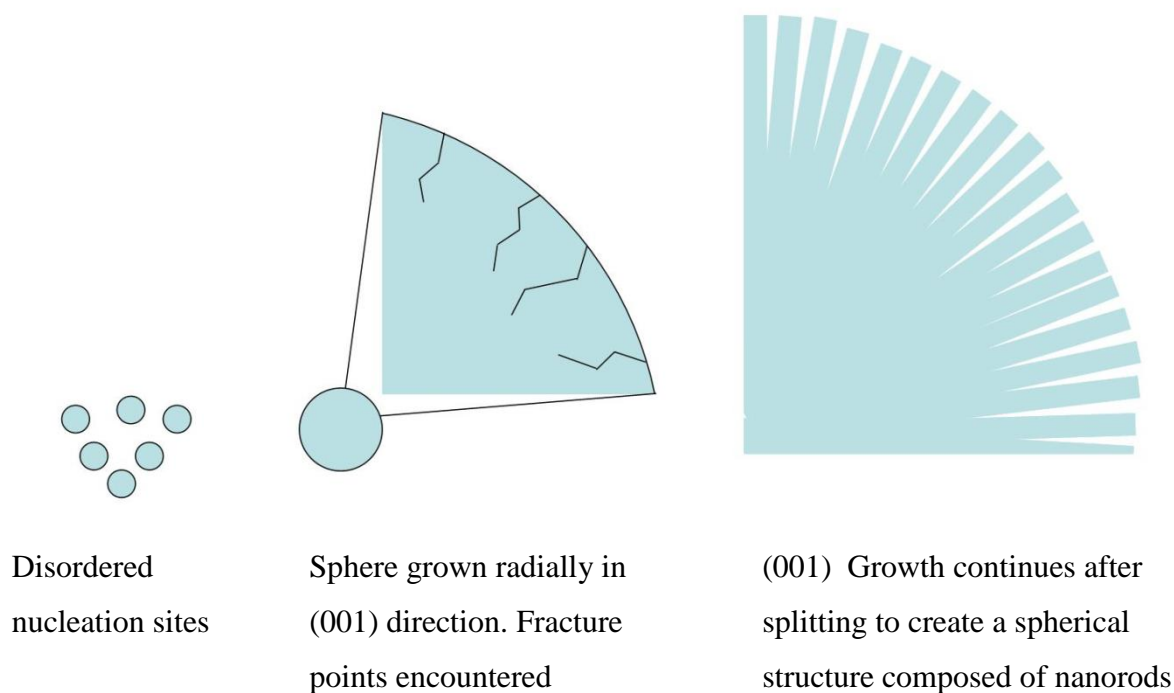


Figure 5-7: Defects leading to nanorods spherically aligned

This growth method was confirmed by TEM.

5.2.4 Phase characterisation

Raman spectroscopy was used as an additional characterisation technique to determine the phase of the product. Shown below in Figure 5-8 are Raman spectroscopy spectra from sample T6 and commercial rutile.

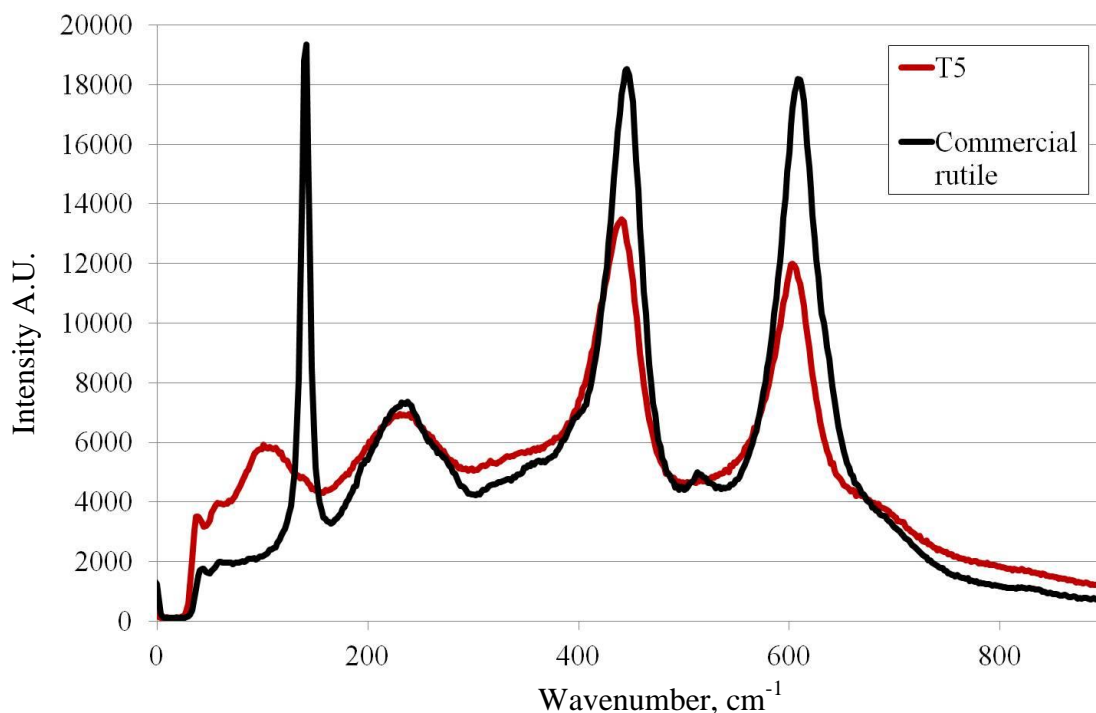


Figure 5-8: Raman spectroscopy spectra of commercial rutile and sample T6

Table 5-2: Raman peaks and assignment, TiO₂

	a	B _{1g}	b	E _g	A _{1g}
Commercial Rutile	-	141.4	237.6	446.0	608.3
Sample T6	105.0	-	235.7	440.8	603.2
Rutile ¹⁵⁰	105	143	237	447	612

The three characteristic bands are shown in the table above along with two second-order bands. The sharp B_{1g} band was not recorded in the microwaved sample. Two additional peaks were, however, assigned. In the commercial rutile sample, a peak was identified at 237.6 cm⁻¹ and sample T6 correspondingly showed a peak at 235.7 cm⁻¹. These peaks are attributed to second-order scattering features¹⁵⁰. Sample T6 showed a distinct peak at 105 cm⁻¹: this band was evidenced by Swamy and Muddle¹⁵⁰ when bulk rutile is reduced to a fine grain size, therefore this peak was attributed to the fine nanostructure of the rods.

5.3 Experimental parameters effect on morphology

Two control parameters, reaction time and titanium tetrachloride concentration, and their influence on particle radius were investigated. Additionally the effect of hydrochloric acid solution was investigated with regard to the particle morphology produced.

5.3.1 Effect of irradiation time

The diameter of the spheres were measured by eye using SEM software. Using the built-in measure function on the SEM software, a single point on the screen corresponding to the edge of a sphere is selected, followed by a second, diametrically opposite point; this gives a reading of the sphere diameter. Numerous spheres (upward of 20 across the sample) from a range of samples were recorded and the average diameter was estimated.

Holding the concentration of titanium tetrachloride at 0.5 M and input power at 900 W, a range of irradiation times was investigated between 30 and 180 s. Figure 5-9 shows the results of the irradiation time on the diameter.

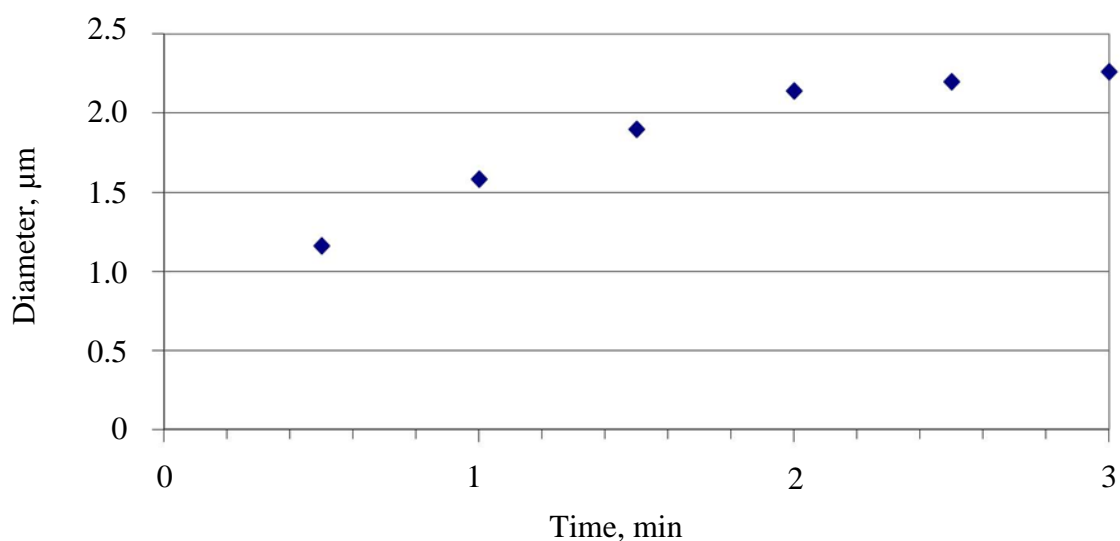


Figure 5-9: Effect of irradiation time on the mean diameter of the sphere

As error bars showing the standard error are obscured by the data points they can be found tabulated in Table 5-3. Errors were calculated on a minimum sample size of 15.

Table 5-3: Average TiO₂ sphere diameter over a range of irradiation times

Irradiation time/ s	Diameter/ μm
30	1.16 \pm 0.01
60	1.58 \pm 0.05
90	1.90 \pm 0.04
120	2.14 \pm 0.03
150	2.20 \pm 0.02
180	2.26 \pm 0.01

Plotting the range of diameters observed shows a clear relationship between the diameter of the spheres and MW irradiation time, and a longer irradiation time produces larger spheres. Reactions were not routinely carried out for over 180 s as the pressure could build to dangerous levels inside the sealed vessel. This was evident by the safety pressure release on the autoclave activating at high irradiation times. Additionally, on one occasion a 4 minute reaction caused irreparable deformation to the Teflon lining in the autoclave.

5.3.2 *Effect of titanium tetrachloride concentration*

The effect of concentration was also investigated using a series of reactions carried out with a constant irradiation time of 60 s, input power of 900 W and altering the titanium tetrachloride concentration between 0.1 and 0.6 M. The resulting graph of diameter verses TiCl₄ concentration from this investigation is shown in Figure 5-10.

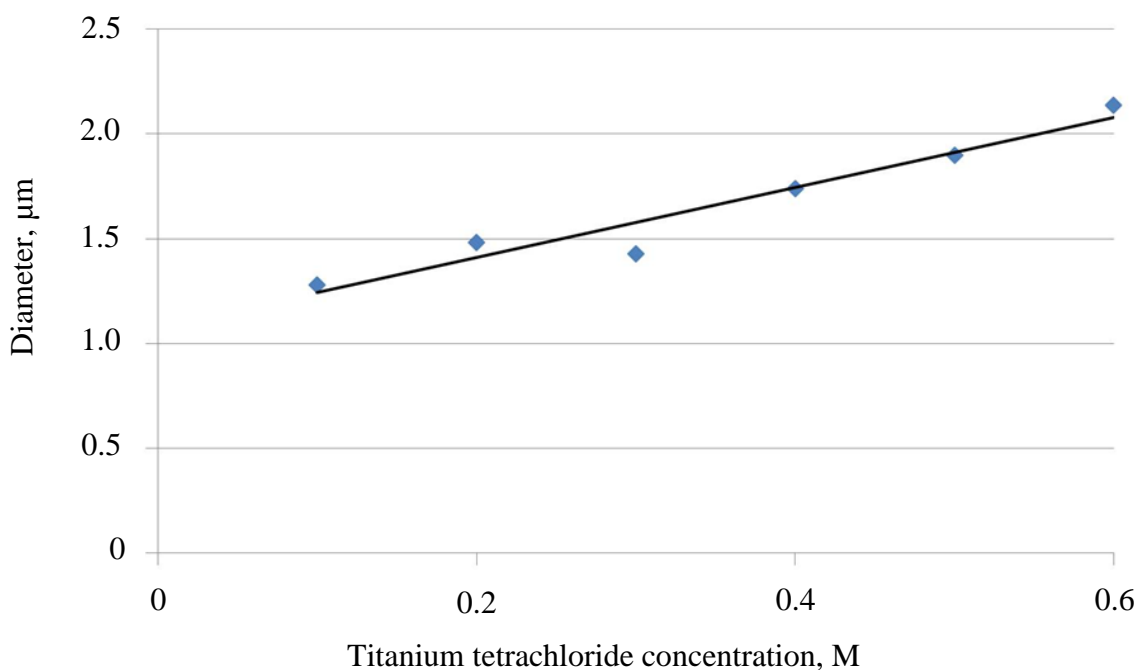


Figure 5-10: Concentration effect on sphere diameter

As the error bars are obscured by the data points the results with corresponding standard error are shown in Table 5-4, errors are based on a minimum of 15 measurements.

Table 5-4: Average TiO_2 sphere diameter over a range of TiCl_4 concentrations

TiCl_4 concentration/ M	Diameter/ μm
0.1	1.28 ± 0.01
0.2	1.48 ± 0.01
0.3	1.42 ± 0.02
0.4	1.74 ± 0.03
0.5	1.90 ± 0.01
0.6	2.14 ± 0.02

Figure 5-10 shows that there is a linear relationship observed between sphere diameter and TiCl_4 concentration. The sphere diameter lies within range of 1.28 - 2.14 μm . It does appear that there is a slight anomaly with the 0.3 M sample and it is worth further investigation why this does not fit with the trend. The 0.3 M reaction did prove to be a less successful reaction than the others. This has not been attributed to the effect of concentration as the success of the reaction can be influenced by factors such as the purity of the titanium tetrachloride (which will react quickly with oxygen) and the cleanliness of

the Teflon autoclave (previous reactants permanently embedded in the autoclave can seed growth influencing particle morphology).

5.3.2.1 Size distribution

As SEM measurements focus on selected areas of the sample and not the whole area, which introduces an error into the measurement of the average particle size, a disk centrifuge was employed to obtain clearer indication of particle size distribution. A typical size distribution is shown in Figure 5-11.

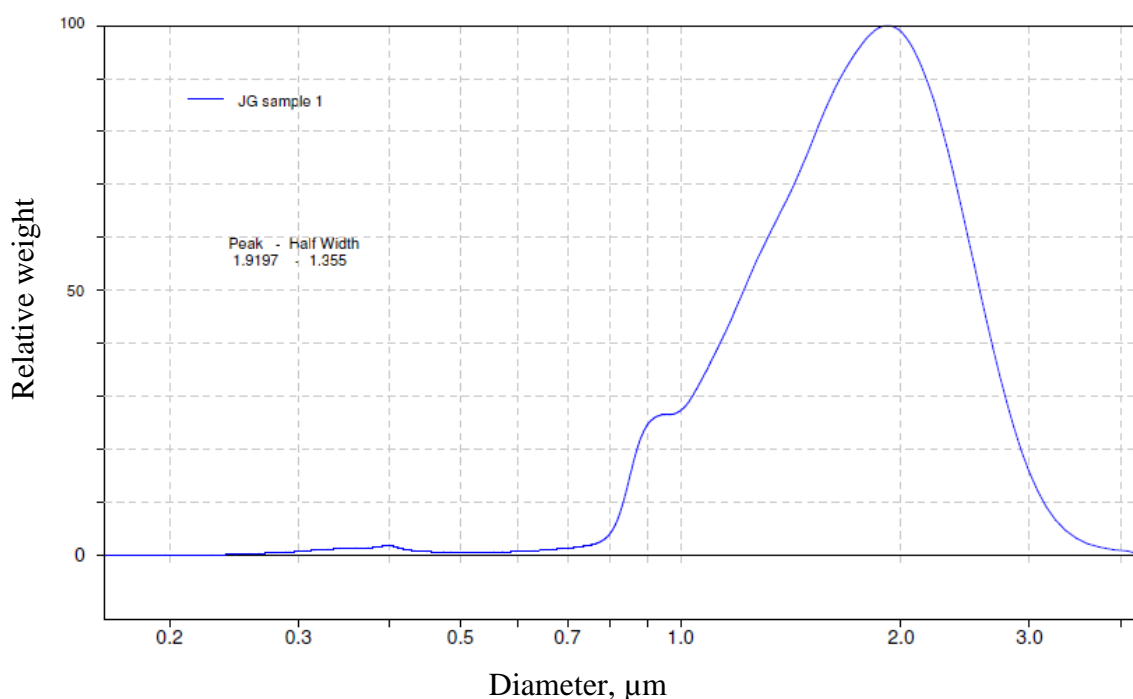


Figure 5-11: Size distribution for sample TD1 using disk centrifuge technique

The plot above shows a dominant peak, broadly resembling a Gaussian distribution, and it shows that almost all particles lie in the region of 1-3 μm with the median of 1.92 μm. These results were obtained at 3500 RPM and were calibrated using a TiO₂ standard of 1.4 μm diameter and a density of 1.385 g mL⁻¹.

The results of four samples are shown below in Table 5-5.

Table 5-5: Sample list, TiO₂, titanium tetrachloride concentration

	TiCl ₄ Concentration / M	Mean size / μm
TD1	0.1	1.78
TD2	0.2	1.88
TD3	0.4	2.11
TD4	0.5	2.41

The above samples were prepared using the standard method set out at the start of this chapter using 60 s reaction time and 2 M HCl solution. Samples were shown to match to rutile TiO₂ by XRD as evidenced in Appendix B (Figures 9-16 to 9-18). The results agree with the SEM results in showing a linear trend of increasing particle size with increasing titanium tetrachloride concentration.

The disk centrifuge was also used as a means to test the resilience of the particles to ultrasonic stress. Sample TD2 was analysed using the disk centrifuge, sonicated for 60 s in iso-propanol. It was assumed that this would result in severe sample degradation and the destruction of the spherical particles. However, the resulting size distribution for the sonicated sample showed no significant difference to the original sample, showing that the particles are stable enough to withstand extended sonication periods without structural damage.

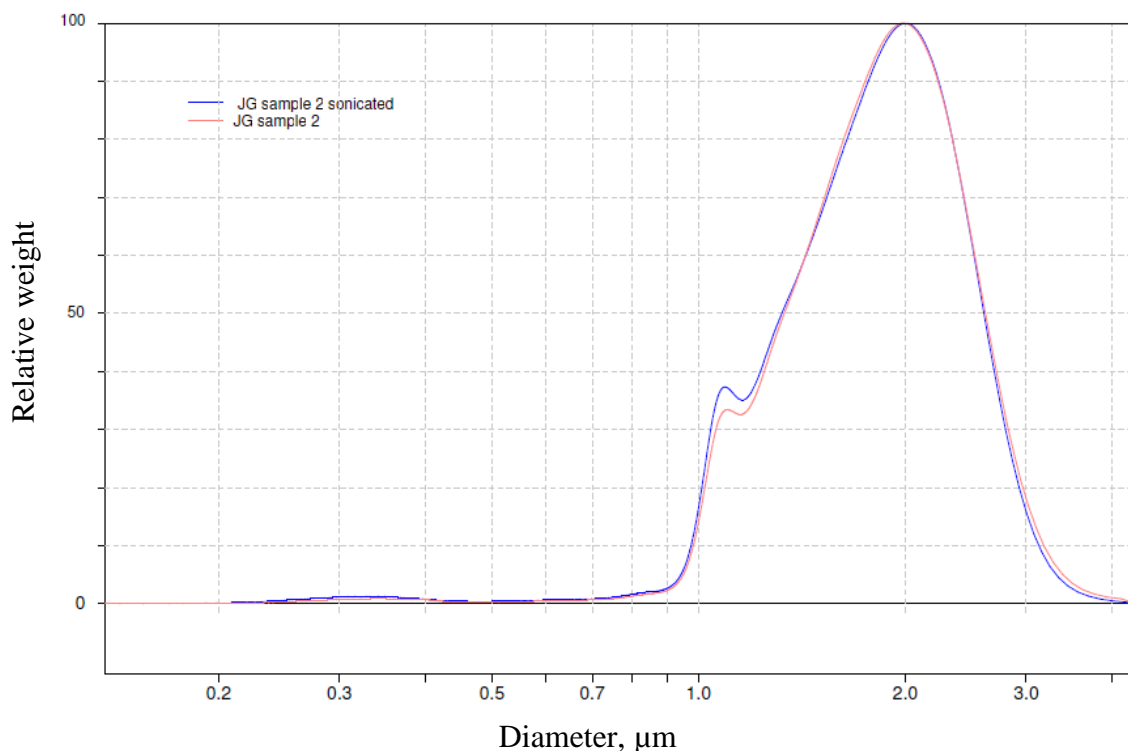


Figure 5-12: Size distribution of TD2 (red) overlaid with TD2 following sonication (blue)

5.3.3 Effect of hydrochloric acid concentration

Reactions were routinely carried out using a 2 M stock solution of hydrochloric acid. This retards the reaction of the titanium tetrachloride with oxygen allowing it to be suspended in solution until the microwave irradiation facilitates growth in the preferential (001) direction. Shown below in Figures 5-13 – 5-17 are a series of reactions, all using 60 s at 900 W with 0.5 M of TiCl_4 , while varying the concentration of the hydrochloric acid solution.

Table 5-6: Samples studied as a function of hydrochloric acid concentration

	HCl Concentration / M
TA1	0.5
TA2	1.0
TA3	2.0
TA4	3.0
TA5	4.0

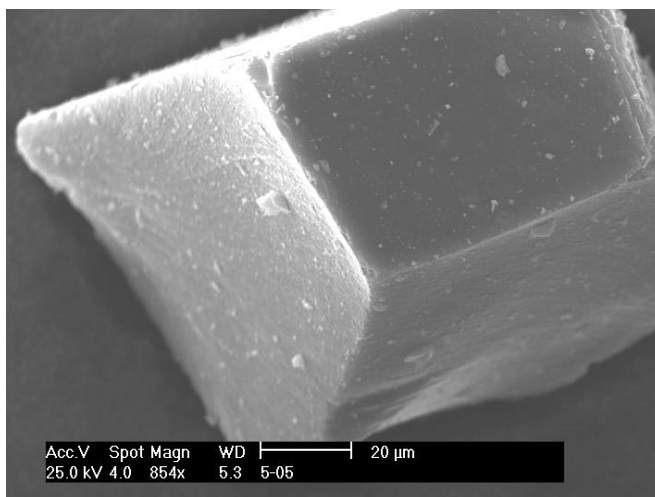


Figure 5-13: SEM micrograph of product from 0.5 M acid solution. Sample TA1

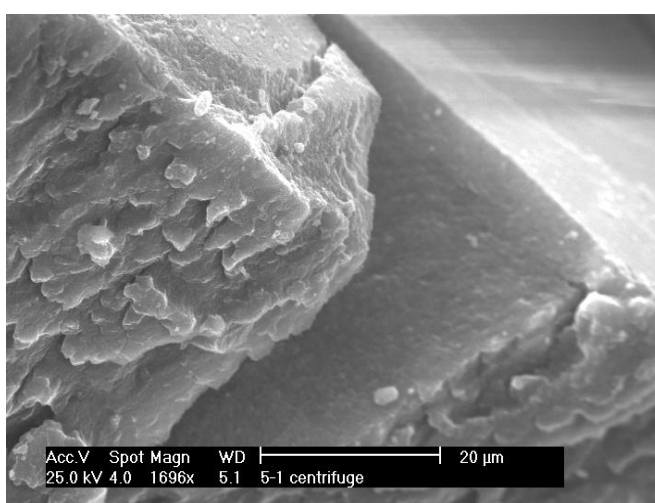


Figure 5-14: SEM micrograph of product from 1 M acid solution. Sample TA2

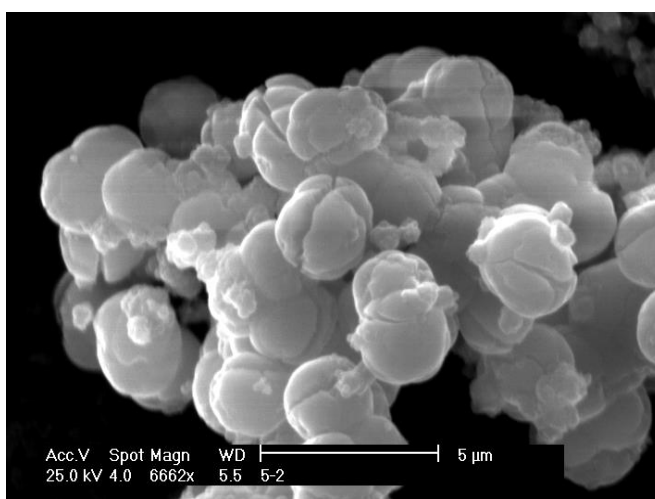


Figure 5-15: SEM micrograph of product from 2 M acid solution. Sample TA3



Figure 5-16: SEM micrograph of product from 3 M acid solution. Sample TA4

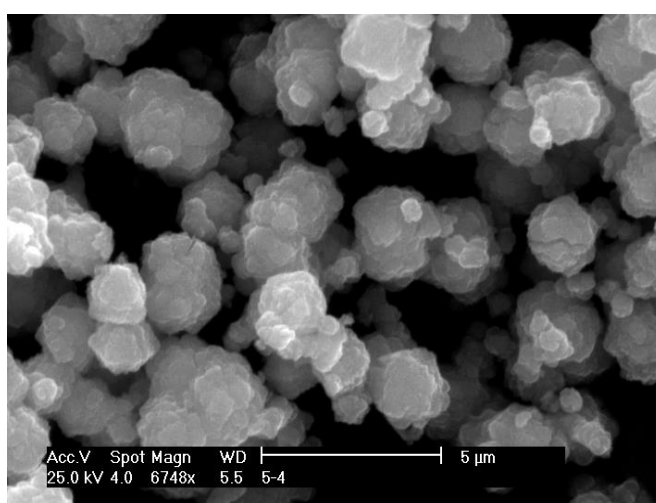


Figure 5-17: SEM micrograph of product from 4 M acid solution. Sample TA5

As evidenced by the SEM micrographs above, there is a striking influence on the particle morphology upon changing the concentration of the hydrochloric acid solution. Samples prepared using less concentrated HCl formed precipitates rapidly with the solution turning cloudy before irradiation. No spherical particles were observed following irradiation, and resulting materials formed large faceted particles. The XRD pattern of both TA1 and TA2 showed amorphous profiles with no discernible peaks. The structures of these samples showed no regular fine structure and appeared as large block particles. The particles were 100s of μm across. Particles showed signs of breaking caused by the stress of filtering, drying and storing of samples.

The sample prepared using 2 M HCl conformed well to other studies showing the spherical morphology and the rutile crystal structure. Increasing the acid concentration appeared to

retard the growth and also have an influence on the phase of the product. For TA4, spheres were still produced but they were not pure rutile. It was calculated by HighScore's quantification feature (using peak profile and intensities) that there was an 11.3% anatase component to the product. Sample TA5 with the highest acid concentration of 4 M showed irregular spheres. In samples prepared using 4 M HCl there was no evidence of the rod arrangement which was seen in all samples produced a 2 M acid concentration. The uniformity of the spheres seen in other samples was lost, and the 4 M reactions produced particles of various sizes with rough surfaces. While they were roughly spherical in shape, there was high agglomeration and little consistency across the sample. Again the product was not phase-pure showing an increase in the quantity of anatase. The XRD pattern shown below clearly shows the distinctive (101) reflection at 25.3 2θ (deg.), this appears as a shoulder peak to the (110) peak at 27.1 2θ (deg.) of rutile.

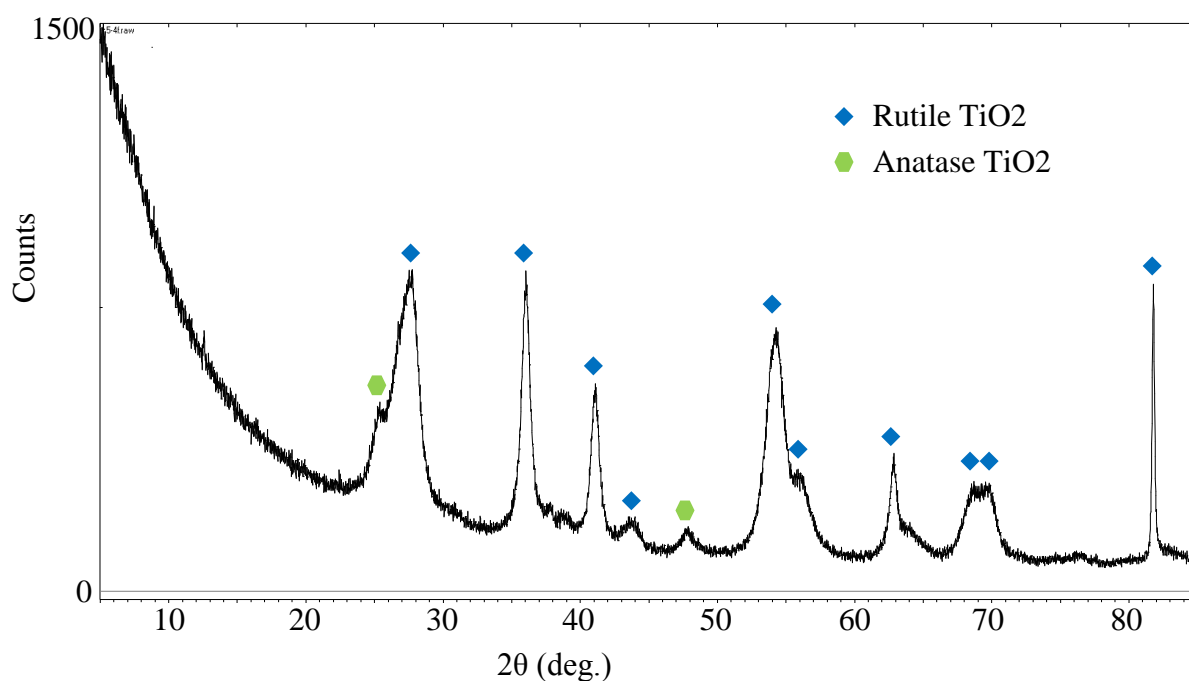


Figure 5-18: XRD pattern for sample TA4 showing a combination of anatase and rutile phases

Using the profile and peak intensities, it was calculated by the Panalytical Highscore computer programme that there was 17% anatase component– a further increase from the samples produced using a 3 M HCl concentration.

5.3.4 Conclusion of morphology control

The three parameters investigated– irradiation time, acid concentration and titanium tetrachloride concentration– all had significant effect on the particle morphology. Increasing the irradiation time or the titanium tetrachloride concentration produces particles of larger diameter. Controlling either of these parameters can lead to a tuneable growth for particles ranging from $<1.5\ \mu\text{m}$ to $\sim 2.5\ \mu\text{m}$.

The concentration of acid used played a vital role in the growth process. At low acid concentrations an amorphous product would spontaneously form with no distinct morphology or phase but with the familiar brilliant white colour of TiO_2 . Increasing the concentration to $>2\ \text{M}$ led to a mixed phase product. While rutile was still the dominant phase the quantity of anatase formed increased with increasing acidity. The highest concentration of acid attempted was $4\ \text{M}$ and this produced less symmetrical and only approximately spherical particles. These distorted spheres were noticeably smaller than the spherical particles produced at $2\ \text{M}$ suggesting that a higher acid concentration retards particle growth.

5.3.5 Band gap measurements

Titanium dioxide's primary applications are as photocatalyst or pigment and, as such, its optoelectronic properties are of great interest. UV/Visible light spectroscopy was employed to identify the optical band gap of samples produced. Sample T3 is shown (Figure 5-19) in comparison to commercially bought rutile and anatase.

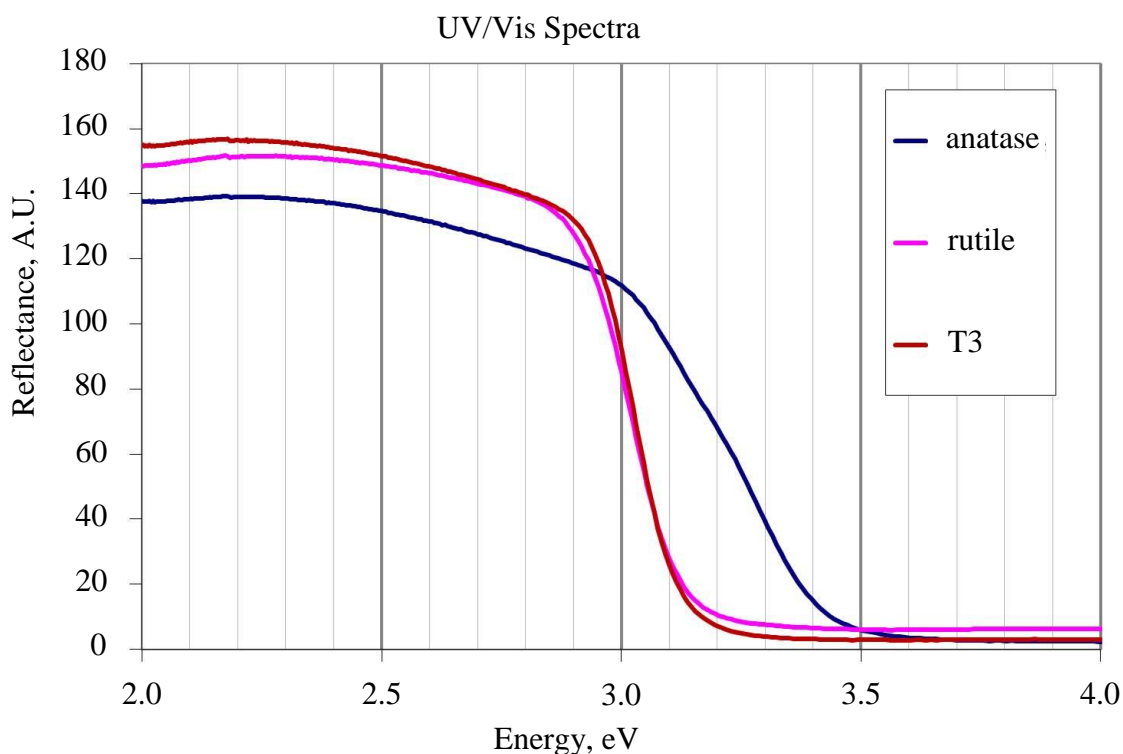


Figure 5-19: UV/Vis spectra showing standard rutile, anatase and sample T3

Low-energy radiation (in the visible region) is reflected from the white opaque solid. These wavelengths are below the band gap and do not have sufficient energy to promote an electron into the conduction band. The energy of the band gap corresponds to the energy at which the irradiation is absorbed providing energy for an electronic transition. The energy is sufficient to promote an electron from the valence to the conduction band and the radiation is absorbed in this energy-transfer process. The band-gap value is associated with the point of inflection at the bottom of the spectrum. To calculate the corresponding band-gap value, tangents to the lines either side of the point of inflection were plotted and the intercept value recorded (Figure 5-20).

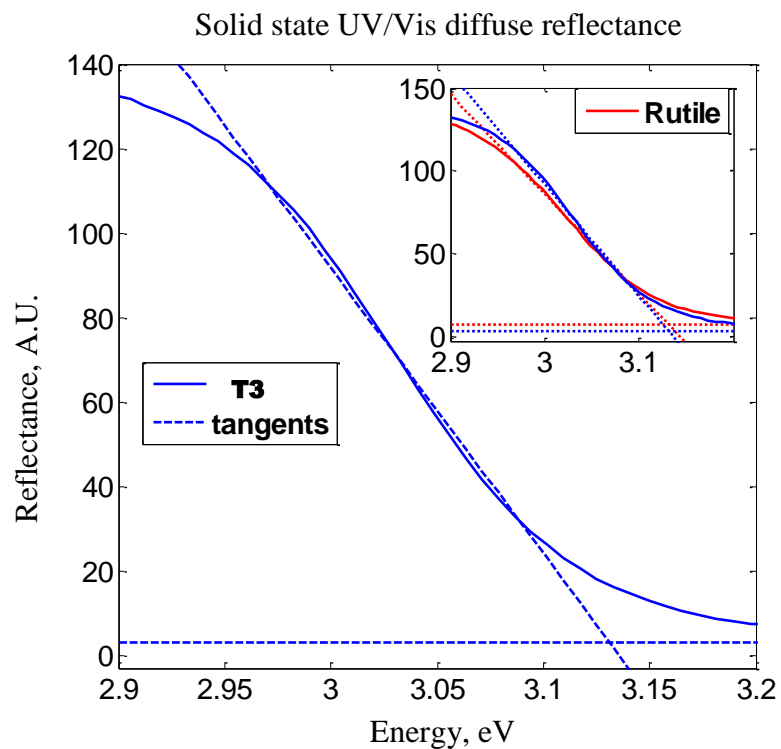


Figure 5-20: Tangents showing band gap. Inset shows comparison to rutile

Multiple samples were recorded by this method. The band gaps measured were close to the value for standard rutile and were recorded as 3.1 eV. UV/Vis spectra for additional samples can be seen in Appendix B (Figures 9-14 and 9-15). Samples T1-T9 all matched to a rutile TiO_2 profile.

5.3.6 Thermogravimetric analysis

Thermogravimetric analysis on sample T8 was performed over a temperature range of 30-1000 °C under an argon atmosphere. The results are shown in Figure 5-21 below.

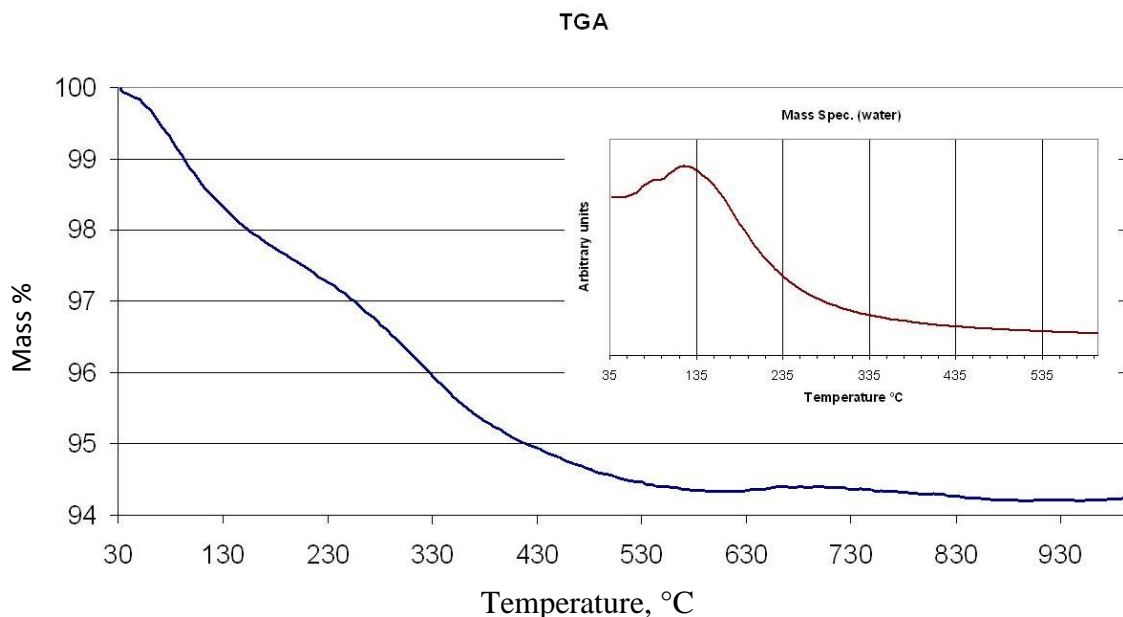


Figure 5-21: TGA plot of T8 under argon showing loss of water. Inset: Mass spectrum showing water evolution ($m/z=2$)

Over the temperature range used, the sample lost less than 6% of its original mass. This mass loss is attributed to water and occurs in two phases. The initial phase is the loss of surface water from the samples. This accounts for the first ca 2%. The continuing mass loss at higher temperatures is assigned to the loss of water from deep within the spherical structure and the liberation of oxygen creating a TiO_{2-x} phase.

There was a loss of the brilliant white colour of the original sample upon heating with samples becoming a dull grey colour. This suggests loss of oxygen at the high temperatures. As the only evolved gas detected was H_2O , the oxygen loss is likely to be minimal. Despite this indication the mass spectrometer was unable to discern any significant quantity of oxygen, chlorine or hydrogen released.

5.3.7 Surface area measurements

The hierarchical porous nanostructure observed already by SEM and TEM was expected to manifest in high surface area. To investigate the available surface area, samples were investigated by nitrogen sorption techniques and the data analysed using Brunauer–Emmett–Teller (BET) theory. The results and a comparison to a commercial TiO_2 are shown below. The commercial sample labelled P25 is was a sample of Degussa P25 the commercial photocatalyst.

Table 5-7: B.E.T. Results

	T3	T9	P25
BET Surface Area, m ² g ⁻¹	53	46	48
Single point Total V pore, cm ³ g ⁻¹	0.05	0.07	0.16
Average Pore diameter, Å	43	61	130

The surface area is directly comparable to that of a standard sample of commercial Degussa P25. Samples typically had a specific surface area between 40-60 m² g⁻¹ and an average pore diameter of 40-60 Å.

From these data, it is assumed that while the hierarchical nanorod structure does produce a high surface area, not all of the surface of the particle is readily accessible.

BET results for additional samples can be found in Appendix B (Table 9-1).

5.4 Single-mode microwave reactions

Thanks to Mr Yann Romani of University of Lille Nord de France for his assistance in this work during a summer studentship.

The use of a CEM microwave reactor provided a single-mode reaction chamber. The sample is placed in the centre of the cavity and irradiated (with controllable power). The reactor is also capable of monitoring temperature and pressure.



Figure 5-22: CEM microwave reactor

The samples were initially prepared using the same method described earlier with titanium tetrachloride added to aqueous hydrochloric acid. In each case, the resulting solutions were then decanted into the glass reaction vessels designed for the CEM reactor (Figure 5-23). Mixtures were subsequently irradiated for set periods of time.



Figure 5-23: CEM reaction vessel

The glass tube was sealed with a crimp-on cap that is fixed on using pliers and the cap was suitable for a single use only. There is a temperature sensor at the base of the CEM reactor which monitors the reaction temperature and provides an automatic cut off should the sample rise above 300 °C. Additionally the pressure sensor provides an automatic cut off should the 2 MPa pressure tolerance for the vessel be approached.

5.4.1 Results

Product was successfully obtained from a number of reaction conditions. Initial reactions were performed using the pressure cap, which monitors pressure evolution inside the vessel. This involves a needle gauge piercing the cap of the vessel to monitor pressure. After fewer than 10 seconds of irradiation the pressure reached 2 MPa and the power was automatically cut off. All further reactions were performed without pressure monitoring to avoid this cut-off.

Successful reactions produced a fine white suspension in the reaction vessel making the originally clear liquid turbid. The precipitate was filtered and dried overnight in an oven at 80 °C. The conditions for the sample preparation are set out in Table 5-8. A 2 M concentration of HCl was used and 0.5 M TiCl₄.

Table 5-8: List of samples prepared using the single-mode cavity reactor

	Power / W	Irradiation time / s
TS1	40	90
TS2	60	90
TS3	80	90
TS4	90	90
TS5	100	90
TS6	100	120
TS7	130	120

5.4.2 Crystalline phase identification

There was a stark difference in the composition of the product from the single-mode reactions when compared to those of the multi-mode cavity reactions. While all products had an XRD pattern matching to TiO_2 exclusively, they were not phase-pure. In these reactions anatase is demonstrated to be the most abundant phase whereas multi-mode reactions produced rutile. The single-mode reactions all matched to a mixed anatase/rutile composition with anatase accounting for 80- 90%.

Figure 5-24 shows the powder X-ray diffraction pattern produced from sample TS4.

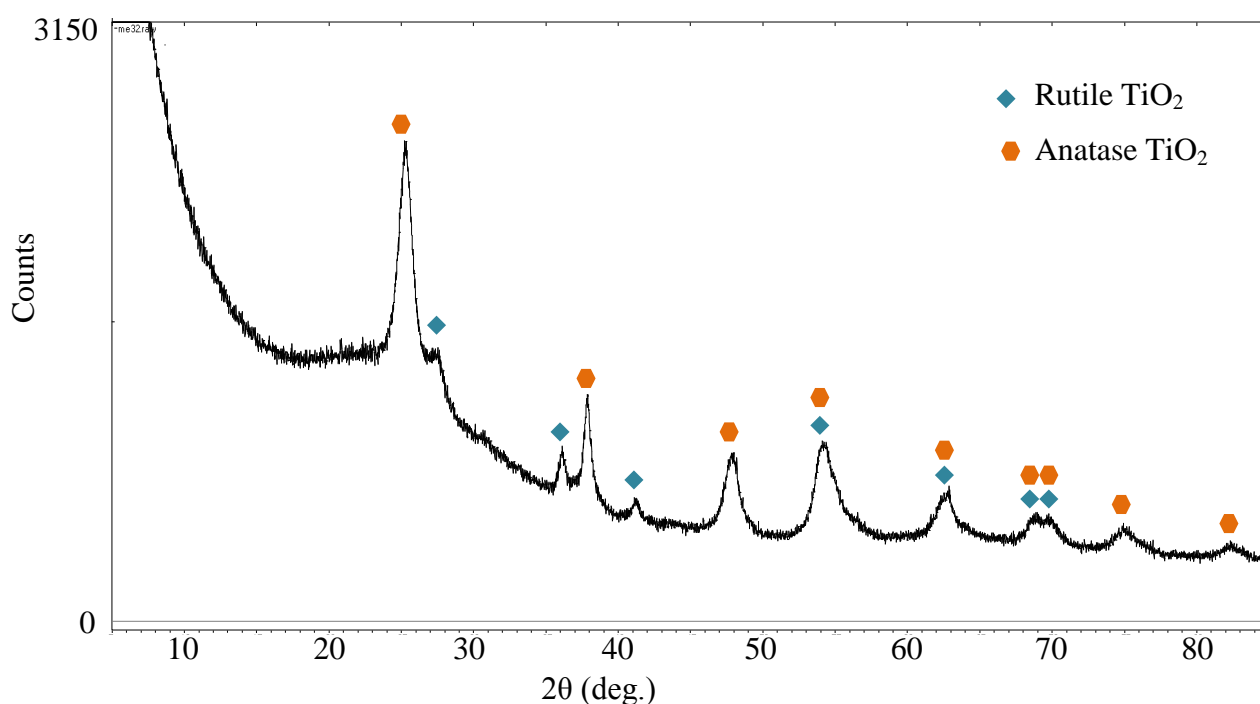


Figure 5-24: XRD pattern for sample TS4 showing mixed anatase and rutile phases of TiO_2

The above XRD pattern (Figure 5-24) clearly shows the characteristic (101) peak of anatase found at 25 2 θ (deg.) dwarfing the smaller (110) peak of rutile found at 27 2 θ (deg.). All samples showed this mixed phase composition. The above pattern was calculated to be 81.9% anatase and 18.1% rutile using the Panalytical HighScore programme. XRD patterns of additional samples can be found in Appendix B (Figures 9-20 to 9-23) and all samples show anatase as the dominant phase.

5.4.3 Phase characterisation

Raman spectroscopy was used as an additional characterisation technique to explore the phase of the product. Shown below in Figure 5-25 is the spectrum of sample TS7 compared to a commercial sample of anatase.

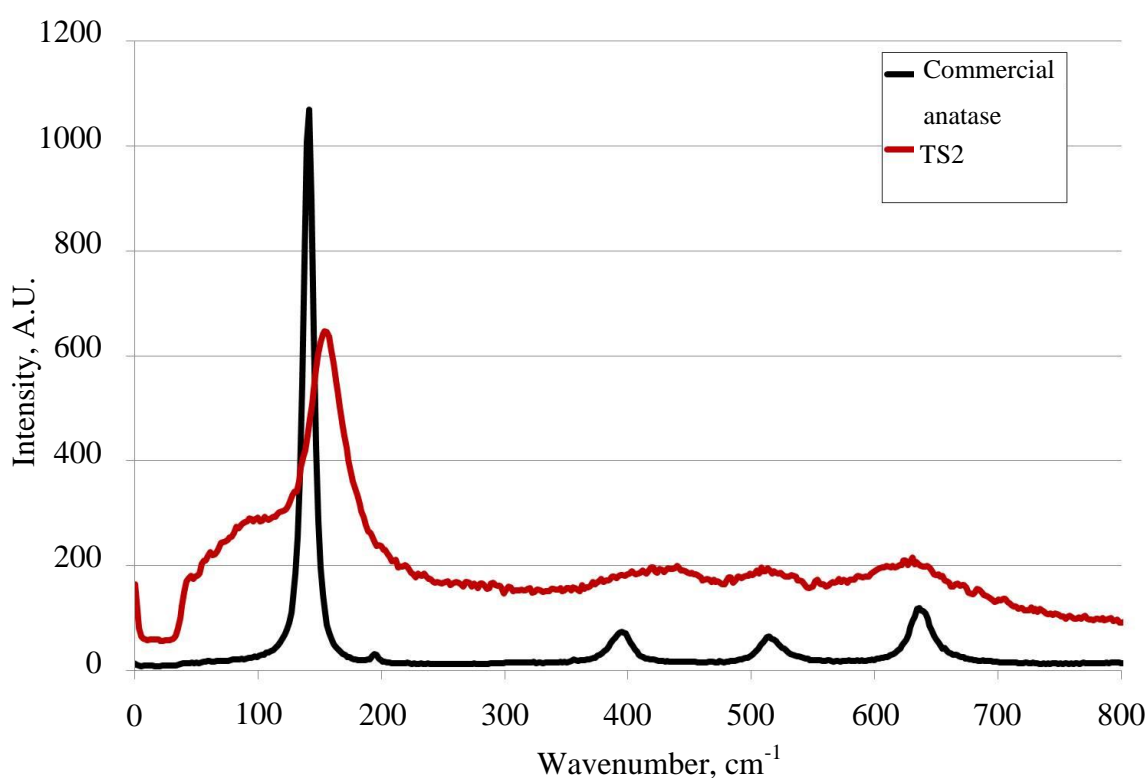


Figure 5-25: Raman spectra of commercial anatase and sample TS7

Table 5-9: Raman spectroscopy peaks and assignments, single-mode reactions

	E _g	E _g	B _{1g}	A _{1g}	E _g
Commercial	141	194	397	515	638
TS7	154		433	513	631
Anatase ¹⁵¹	144	197	390	523	637

The Raman spectrum for TS7 shown above shows a match to the anatase phase. All peaks identified in the spectrum have been assigned with reference to the literature¹⁵¹ and also shown to match with a commercial anatase sample. The small E_g peak could not be resolved in TS7.

5.4.4 Morphology

The morphologies of particles produced in the single-mode cavity proved to be less consistent and less symmetrical than those obtained from the multi-mode reactor. Samples were composed of approximately spherical agglomerated particles.

Particles were typically found to be between 0.8 and 1.2 μm across, smaller than the vast majority of the spheres produced by multi-mode methods.

Samples shown in Figure 5-26 are taken at a range of power settings with a constant irradiation time of 90 s.

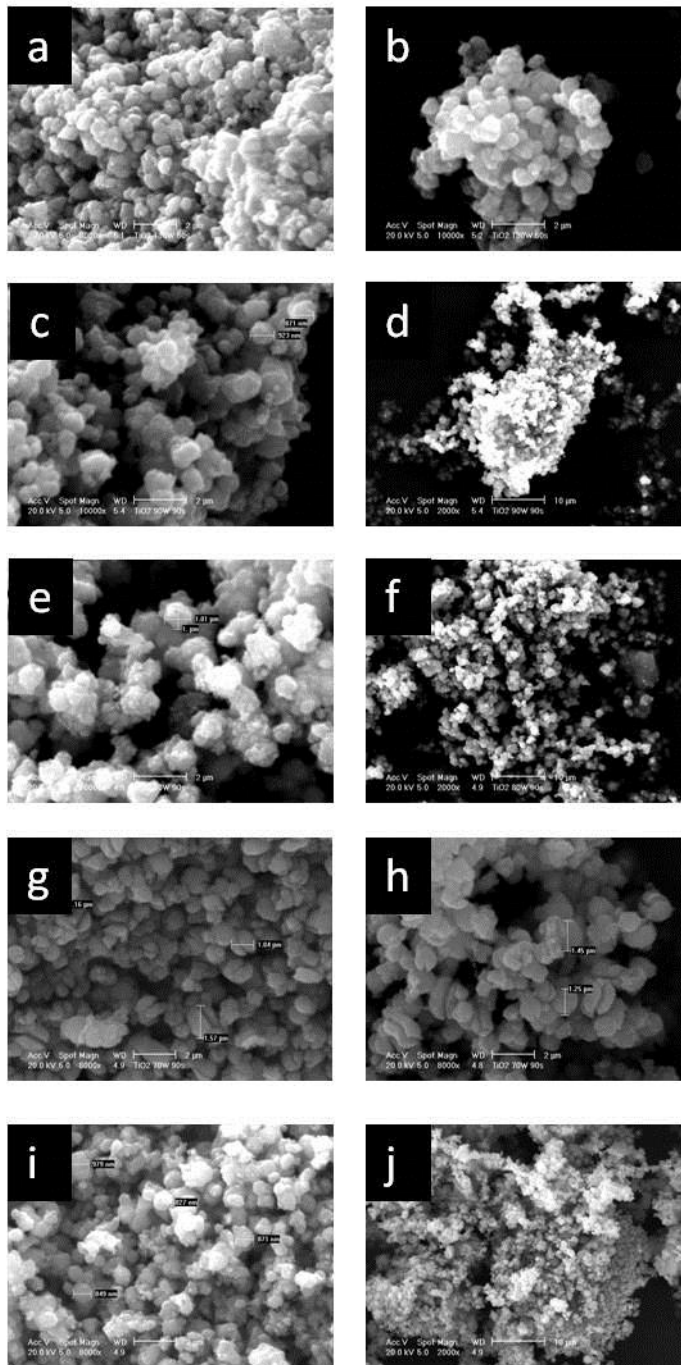


Figure 5-26: SEM micrographs showing particle morphology produced in single-mode reactions. (a-b) sample TS7, (c-d) sample TS4, (d-e) sample TS3, (e-f) sample TS2, (g-h) sample TS1, (i-j) sample TS5

The samples in Figure 5-26 show that the products from these reactions result in roughly spherical but agglomerated particles. The particle diameter bore no obvious relation to the power output of the microwave. The images are shown at a range of power settings from 40 to 130 W. All products displayed a wide range of particle sizes (as measured during SEM imaging).

The SEM micrographs shown in Figure 5-27 below show an example of constant power with variation in irradiation time.

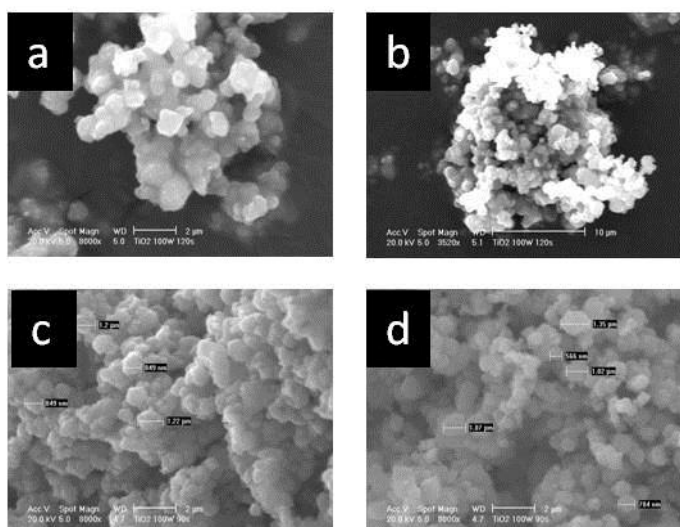


Figure 5-27: SEM micrographs showing reactions with 100 W power setting. (a-b) sample TS5, (c-d) sample TS6

Similarly no distinct pattern linking diameter to irradiation time was evident. Samples produced at various reaction times produced the familiar irregular spheres which displayed a range of particles sizes (where measurements were able to be clearly defined).

5.4.5 Band gap measurement

Samples were analysed using UV/visible spectroscopy. The spectra were compared to commercial samples.

Figure 5-28 shows a typical spectrum in comparison to commercial P25 from Degussa.

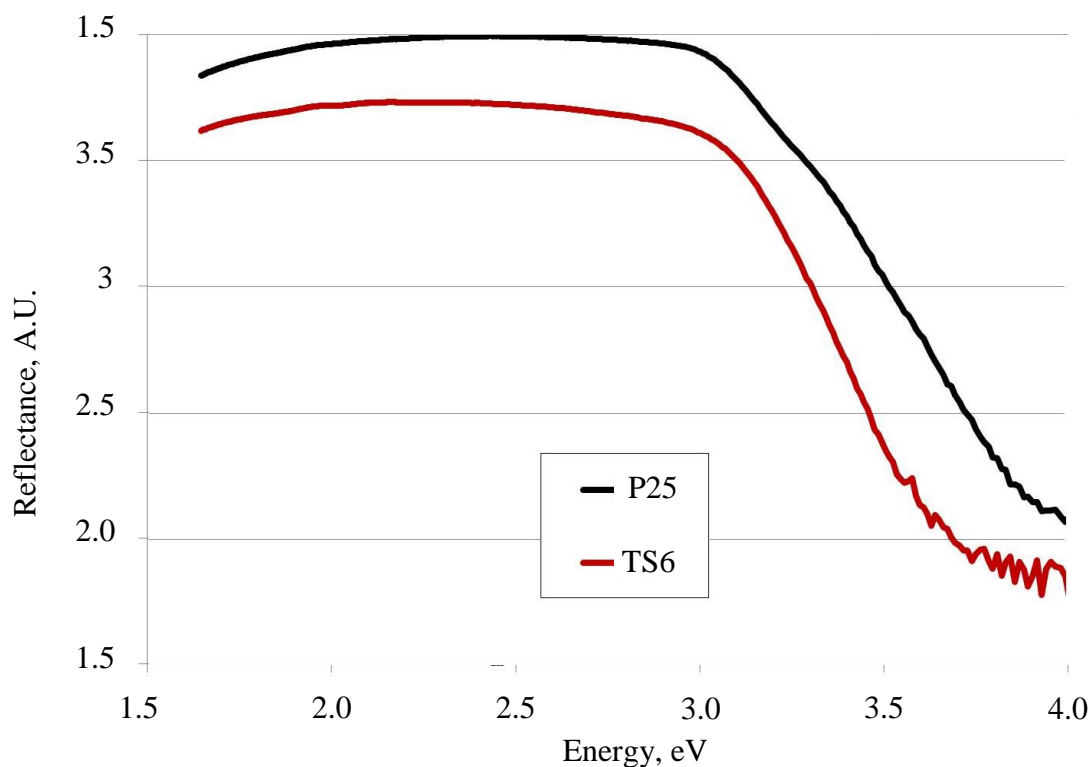


Figure 5-28: UV/Vis spectra of sample TS5 and P25

UV/Vis spectra resembled Degussa P25 (which is the leading photocatalyst and is, like the samples produced by single-mode reactions, mixed rutile and anatase phases). P25 has been regularly reported as being 70-80% anatase. It has also recently been reported that the remainder of the composition consist of both amorphous material and the rutile phase ($\approx 15\%$). As such, samples produced here from single-mode microwave reactions seem directly analogous to the P25 material. From the above plots their band gaps were calculated as being 3.05 eV for P25 and 3.10 eV for TS6. The band gap of P25 has been previously reported in the literature as 3.08 eV¹⁵².

5.4.6 Energy effect

From the work performed under a range of reaction conditions a trend linking both applied power and reaction time was apparent. The energy input to each reaction can therefore be approximated as the microwave power multiplied by the irradiation time.

It was noted that no product was synthesised when a total energy of less than 4.5 kJ was used. For example, a reaction using only 40 W could be successful if allowed to run for 120 s but would be unsuccessful at any time period below this value; a reaction of 80 W could be successful in half of this time.

Reactions which used an energy equal or greater to 8.4 kJ were liable to have input power to the reaction cut off due to the thermal sensor reaching the maximum of 300 °C.

An example of the above relation follows:

70 W for 60 s (4.2 kJ) = no reaction

70 W for 90 s (6.3 kJ) = reaction complete

70 W for 120 s (8.4 kJ) = early termination

Therefore the ideal reaction time lies in the range of 4.5-8.4 kJ. Keeping within the 60-120 s interval investigated in this work samples successfully produced product in a complete reaction at powers between 40 and 100 W.

5.5 Conclusions

Reported here is the rapid synthesis of TiO₂ through use of microwave heating. Initial investigation concentrated on the use of a multi-mode reactor, where titanium tetrachloride was added to dilute hydrochloric acid and sealed inside a teflon autoclave to react hydrothermally. The autoclave was then irradiated, which precipitated TiO₂.

Multi-mode microwave reactions produced spherical monodispersed spheres of 1-4 μm diameter. These spheres were rutile in phase and displayed the corresponding band gap. The spheres were discovered to be a hierarchical structure composed of nanorods radiating from the particle core. These were investigated further through use of TEM.

Phase was determined by use of powder XRD and Raman spectroscopy. The diameter of the rutile spheres was found to be controllable due to a strong correlation between the diameter of the sphere and the irradiation time. A second relationship between the sphere diameter and concentration of titanium tetrachloride was also identified. The effect of acid concentration was also investigated and it was discovered that a 2 M acid solution was ideal for producing spherical rutile particles.

Reactions were extremely quick. Successful reactions of single phase products occur after 30 s: a significant reduction over standard hydrothermal reactions¹³³.

The hierarchical spheres have a high surface area comparable to commercial TiO₂ samples. Additionally, the samples had a high capacity to store water. Water evolution was seen from thermogravimetric analysis at temperatures above 100 °C as water from the core of the spheres was liberated.

Following the success of the multi-mode microwave reactions, a single-mode investigation was carried out investigating the relationship between the power and irradiation time. The single-mode reactions produced roughly spherical particles of 1-2 μm in diameter. These particles were less uniform and showed a higher degree of agglomeration in comparison to the products from multi-mode reactions.

Reactions produced using a single-mode cavity produced a mixed-phase product. The dominant phase was anatase but all samples showed a 10-20% rutile component. The phase and composition was investigated by use of powder X-ray diffraction and Raman spectroscopy.

The single-mode microwave product composition is approximately analogous to Degussa P25, the widely used photocatalyst. The band gap of these materials closely resembles that of P25.

6 Doping of titanium dioxide spheres to nitride and oxynitride structures

An investigation into the possibility of pseudomorphic conversion of TiO₂ spheres was carried out. The TiO₂ for conversion were prepared in the multi-mode microwave reaction in a process set out in Chapter 5. These TiO₂ spheres were then exposed to an ammonia atmosphere at elevated temperatures to convert the structure to nitride and oxynitride structures. Following ammonolysis the products were characterised by XRD, SEM, TEM, BET analysis and UV/Vis spectroscopy.

The nanostructure of the TiO₂ sphere was hypothesised to lend suitability to a gas exchange mechanism due to large surface area. The nanorods provide access to the sphere's inner core and have a high surface area which is advantageous to gas exchange. The study described here aimed to investigate the possibility of nitrogen-oxygen exchange while preserving the monodisperse spherical morphology.

The importance of titanium nitride is outlined in Chapter 1. It is an attractive material owing to its good thermodynamic stability, extreme hardness and a high melting point. The main challenge to this process is the production of Magneli phases of TiO₂ in oxygen deficient environments at elevated temperatures¹⁵³. Magneli phases are represented by Ti_nO_{2n-1} (n=4-10)¹⁵⁴. According to Tang *et al.*¹⁵⁴ these phases may be avoided by keeping the reaction below 1050 °C.

There is a precedent for reacting TiN with O₂ to TiO₂. Although titanium nitride is thermodynamically stable it can be oxidised according to the following equation 6-1.



Equation 6-1 is favourable with a ΔG° of -582 kJmol^{-1} (at 25 °C)¹⁵⁵. It has been demonstrated that titanium nitride will preferentially oxidise into the rutile phase¹⁵⁶ making it suitable for a fully reversible ammonolysis process. Tompkins and co-workers also demonstrated the complete conversion of titanium nitride to an oxide in air¹⁵⁷.

Doping is also of interest to this work. The substitution of trace quantities of nitrogen into the oxide structure is shown to cause a shift in the TiO_2 band gap^{158, 159}. Presented here is a possible route to pseudomorphic doping of the spheres leading to the desired shift in band gap while the unique morphology is retained.

6.1 Full Conversion to TiN structure

6.1.1 Reaction set up

The samples described in this chapter used TiO_2 spheres as a precursor; these were produced *via* a microwave hydrothermal process outlined in Chapter 5. These spheres were single-phase TiO_2 conforming to the rutile crystal structure. The spheres were composed of nanorods aligned in a radial direction. Samples T8-T5 from Chapter 5 were selected for ammonolysis.

Titanium dioxide (150 mg) was placed inside a ceramic boat then inserted into a Vecstar tube furnace. The ends of the tube furnace were connected to a cylinder of ammonia. Samples were produced under an ammonia flow rate of 0.4 L min^{-1} . After the air had been purged the tube furnace was heated to $700 \text{ }^\circ\text{C}$. Ammonolysis was run over a time range of 12–40 h.

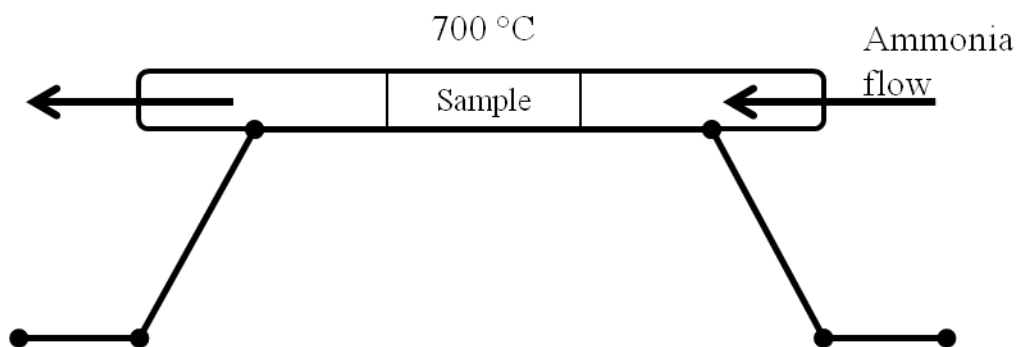


Figure 6-1: Reaction profile for ammonolysis

6.1.2 Results

The products from the ammonolysis procedure lost their brilliant white appearance and were a uniform black/blue colour.

6.1.2.1 Crystalline phase identification

Figure 6-2 shows an XRD pattern of sample T5 following ammonolysis for 40 h. Represented in red is the standard for TiN. No peaks associated with the TiO₂ rutile structure were present and there are the five characteristic peaks of cubic TiN. All product peaks are shifted significantly to the right. It is clear that all peaks are present and well defined and there is clearly no longer any rutile structure present. When all peaks of TiO₂ had been removed the reaction was labelled as a complete conversion.

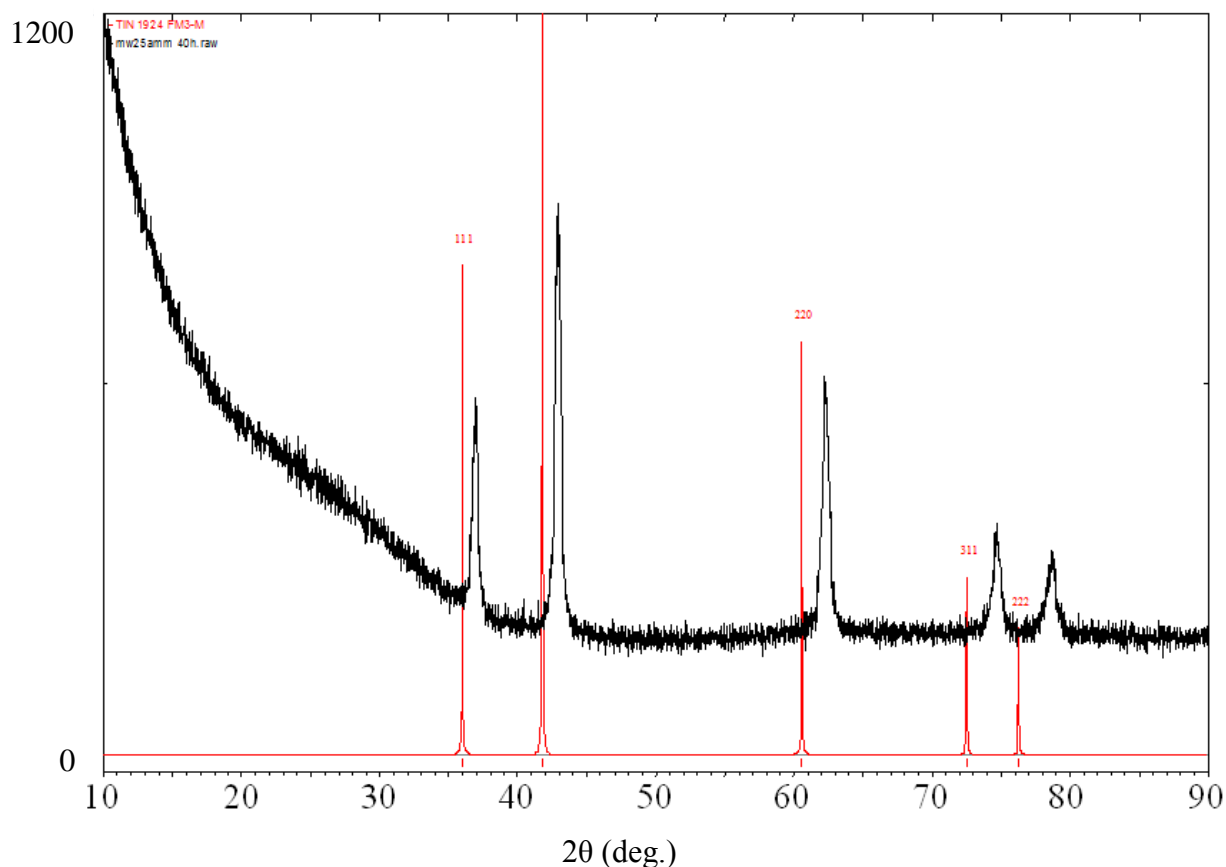


Figure 6-2: XRD pattern of T5 following ammonolysis showing shifted TiN structure

Using the pattern obtained in Figure 6-2 the cell volume was calculated to be 74.8 \AA^3 (using the CelRef programme refinement) this is lower than the expected value of 76.0 \AA^3 ¹⁶⁰ which can be explained by the lattice having a higher stoichiometric ratio of Ti to N and therefore smaller lattice parameters. This is consistent with samples run under ammonia for over 20 h.

When samples were run for less than 20 h a mixture of phases was evident. Figure 6-3 is the XRD pattern obtained for sample T7 following 12 h ammonolysis at 700 °C which

shows an incomplete conversion. XRD patterns for additional ammonolysis reactions can be seen in Appendix C (Figures 9-24 to 9-26).

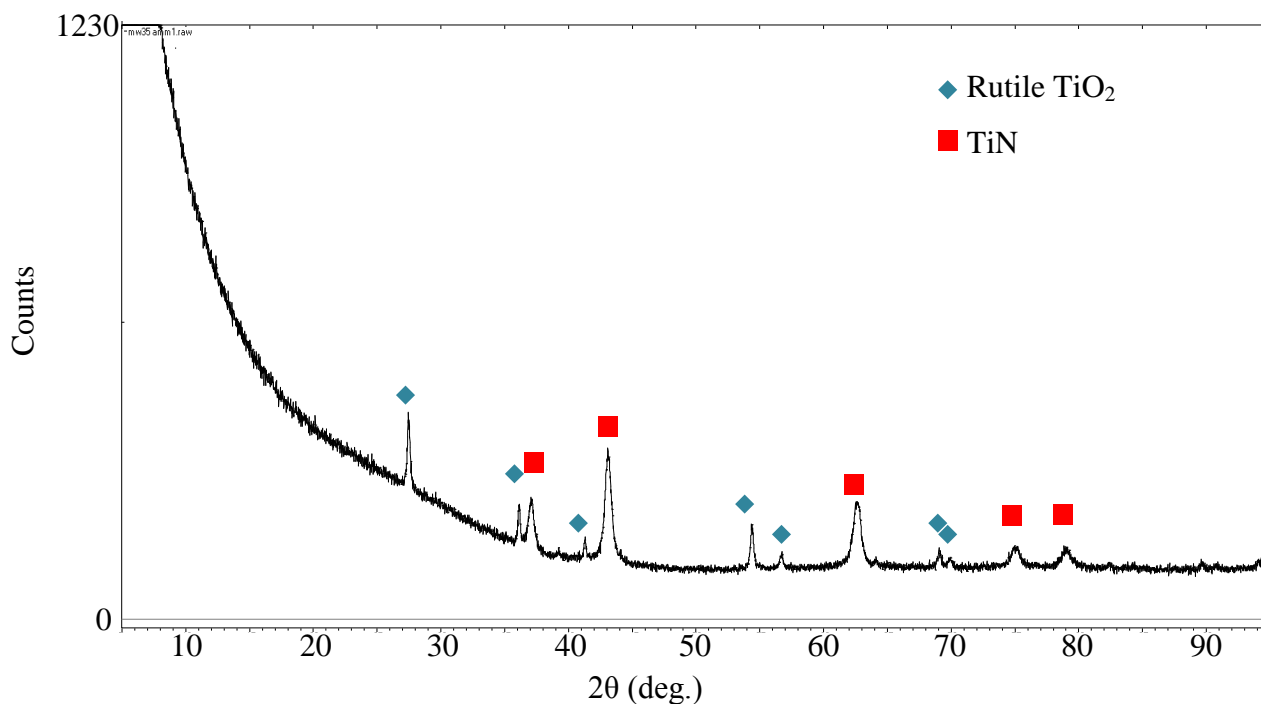


Figure 6-3: XRD pattern of T7 following 16 h ammonolysis showing both TiO₂ and TiN structures

Values for the volume of the unit cell were calculated using XRD patterns of fully converted samples and the CelRef program. Volumes were examined as a function of ammonolysis time. Figure 6-4 shows the cell volume increases in line with ammonolysis time.

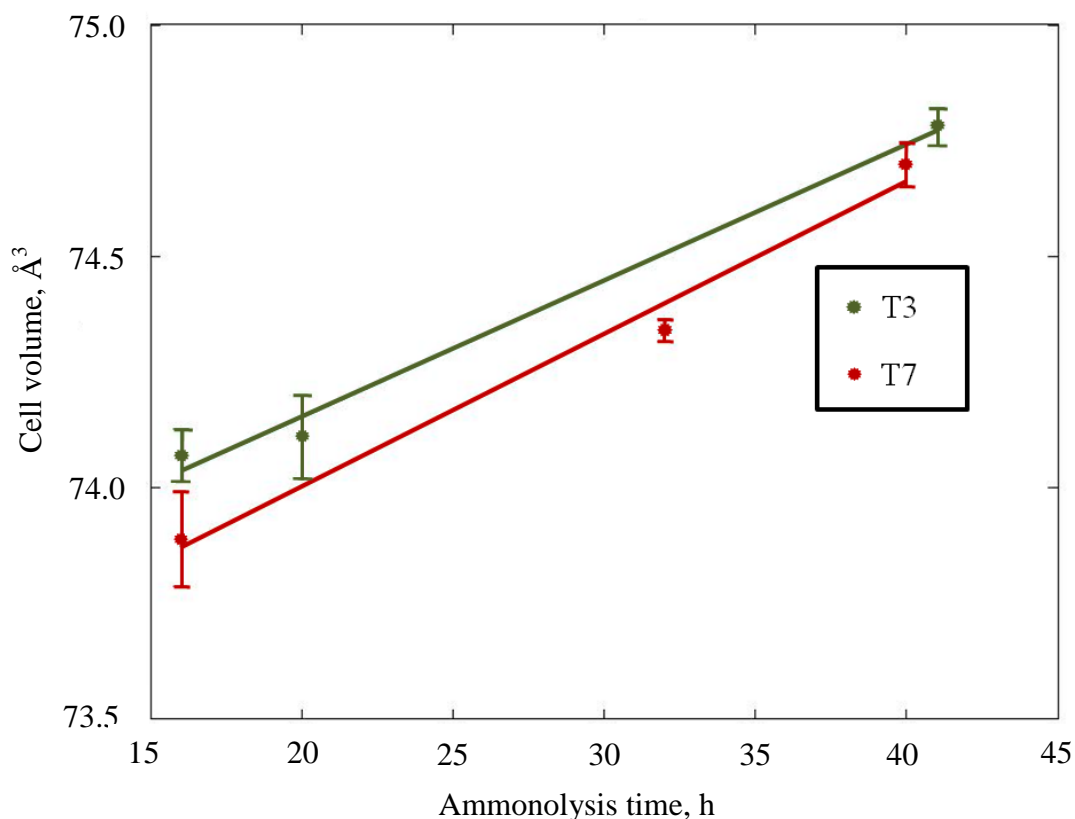


Figure 6-4: Cell volumes of T5 and T7 following ammonolysis

The trend shows an increasing cell volume with respect to ammonolysis time however even after 40 h samples still had a smaller cell volume than to be expected. The 40 h samples have a cell volume of $\approx 74.8 \text{ \AA}^3$ this is still slightly below the expected value of 75.2 \AA^3 ¹⁶⁰.

6.1.2.2 Morphology

At lower levels of SEM magnification the samples appear to be identical to the TiO_2 precursor, showing the spherical particles with no appreciable difference in appearance. At higher magnifications however this is not the case. Figure 6-5 shows a high magnification of a T8 sample prepared after 16 h under ammonolysis.

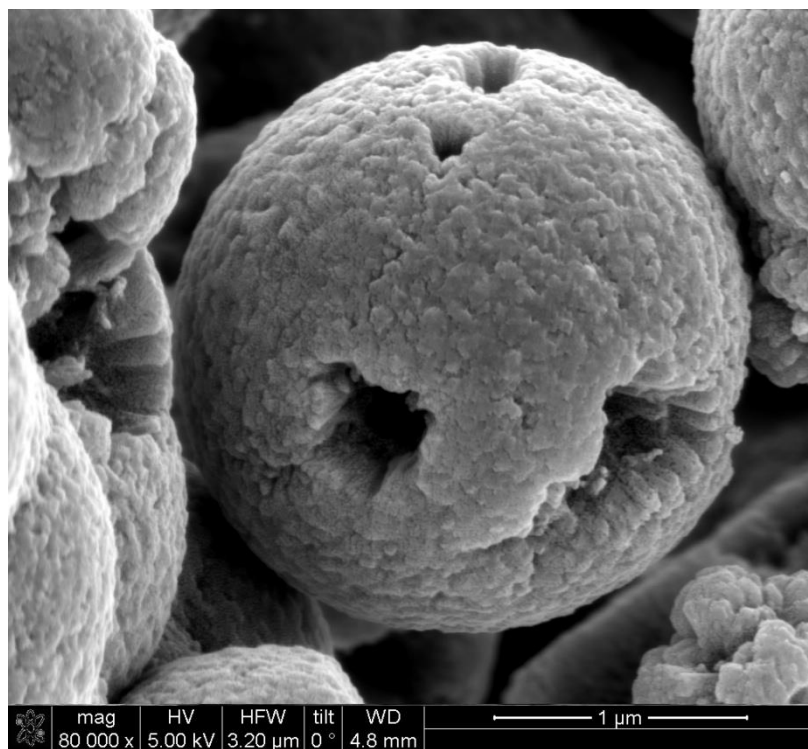


Figure 6-5: SEM micrograph of T8 following ammonolysis

From this image it can be seen that the spherical morphology has successfully been retained, despite reaction and heating. There is however a notable difference with the surface detail. Individual nanorod structure can no longer be seen, and the rods appear to have annealed together to form a smooth surface. The sample shown in Figure 6-5 can be directly compared to its appearance before ammonolysis in Figure 6-6.

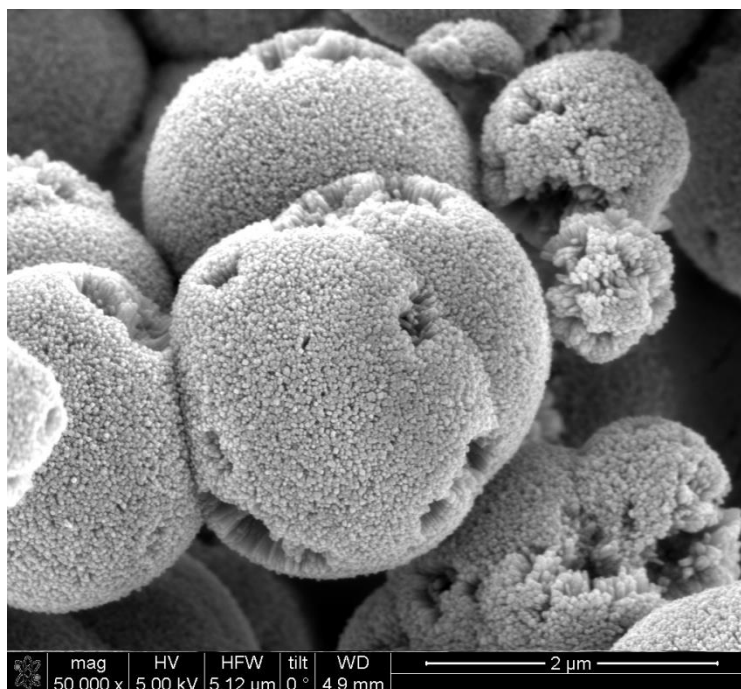


Figure 6-6: SEM micrograph of T8 before ammonolysis showing clear rod structure

6.1.2.3 TEM analysis

6.1.2.4 Imaging

A great deal can be understood about the particles following ammonolysis with TEM imaging. As the spheres are in the micron-scale regime they must be destroyed in order to be thin enough for TEM imaging to be of use. In preparation for TEM analysis the spheres were broken by grinding with mortar and pestle to ensure the samples were thin enough to be electron transparent. The most useful areas for analysis show particles where the derivation from the sphere can be clearly observed. These are described as fan segments; they are however in most cases of a roughly conical shape. The image in Figure 6-7 is one such fan segment:

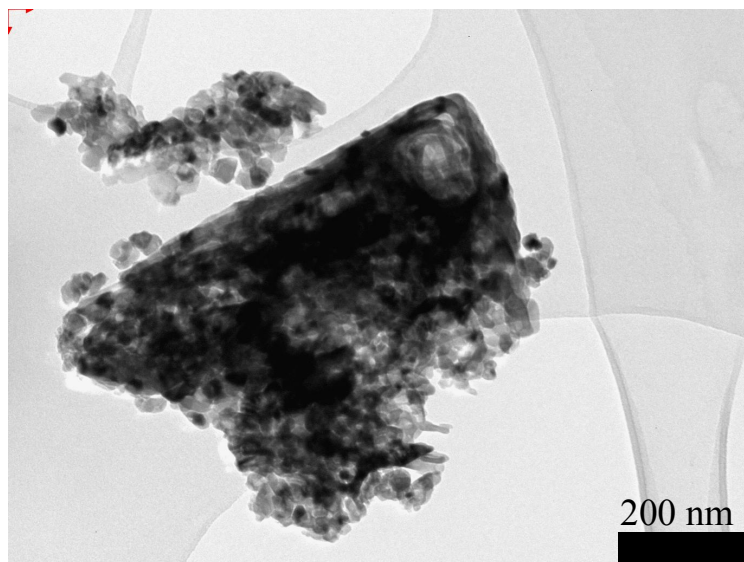


Figure 6-7: TEM image of sample T8 following complete ammonolysis

In Figure 6-7 above the outer surface of the sphere can be clearly seen to the top right of the particle in the centre. The straight edge sloping from the top right to the left is indicative of the rod like structure from which the TiO_2 was formed.

6.1.2.5 Bright field/dark field imaging

Bright field and dark field imaging was used to visualise the similar diffracting planes within the material.

The bright field and selected corresponding dark field images are shown below for sample T5 following 20 h ammonolysis.

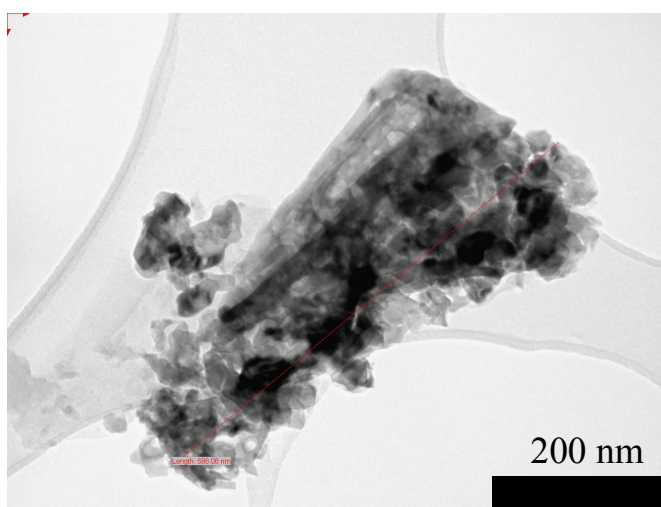


Figure 6-8: TEM bright field image of sample T8 after 20 hours ammonolysis

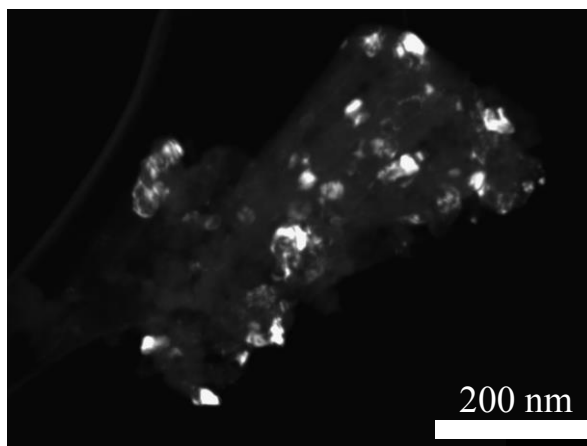


Figure 6-9: TEM dark field image of T5 following ammonolysis

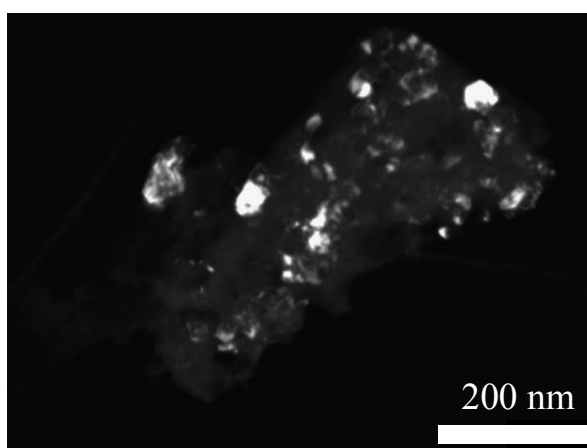


Figure 6-10: TEM dark field image of T5 following ammonolysis

From these images the degradation of the rods into smaller nanocrystals is apparent. Dark field imaging enhances this understanding. Figures 6-9 and 6-10 are dark field images of the particle represented in Figure 6-8. In the dark field imaging of the TiO_2 rods reported earlier in this work (Chapter 5) it can be seen that the rods are illuminated on tilting during imaging. This shows that along the length of the rods there are similarly oriented diffraction planes. This condition is not true following ammonolysis, rods are no longer illuminated and instead the smaller standalone areas are illuminated suggesting a polycrystalline nature. The long periods of ammonolysis broke the crystals into smaller fragments. The area to the right of the image in Figure 6-8 shows crystals that have separated during grinding and no longer appear as the long narrow rods. A great deal of the sample is composed of these nanocrystals. Once separated from the main sphere, the crystals (20-30 nm in dimension) adhere loosely together on the TEM grid.

6.1.2.6 Selected Area Electron Diffraction

Selected area electron diffraction (SAED) was used across TEM samples to determine the crystal structure. A typical example of the diffraction pattern is shown below; this was taken from T5 from the particles shown in Figure 6-8.

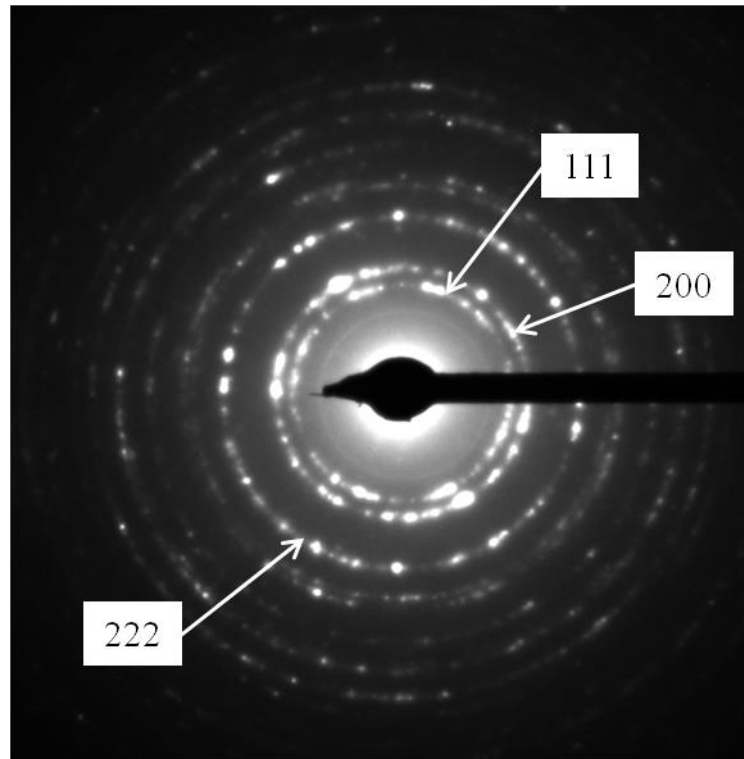


Figure 6-11: Selected area diffraction pattern from T8 following conversion matching to TiN structure

The selected area diffraction (SAD) pattern clearly indicates a polycrystalline structure, indicated by the ring like nature of the pattern. Superficially it can be seen to represent a cubic structure, having two rings close together, with a third at a greater distance. Images were measured in terms of pixels using Gatan Digital Micrograph. Measurements were calibrated against commercial anatase particles as a calibration standard.

The results are tabulated in Table 6-1.

Table 6-1: Selected area electron diffraction pattern, spacing and assignment

Ring number	Measured d/ Å	Expected d/ Å	Assignment
1	2.446	2.445	(111)
2	2.107	2.118	(200)
3	1.498	1.497	(220)
4	1.280	1.277	(311)
5	1.217	1.223	(222)
6	1.059	1.059	(004)

On average the measured d spacing varied from the expected distance by $\pm 0.2\%$. Using the relationship which relates the d spacing to lattice parameter it follows that the parameter also matched within the same error. Although only one diffraction pattern is displayed as labelled here, many were taken over a series of separate days and separate areas of sample and all conformed to the pattern shown above.

The diffraction patterns which were collected at different areas across the sample proved to be consistent with each other. The diffraction pattern from the crystals showed a cubic cell with a lattice parameter matching TiN. It does appear that there is some discrepancy with the XRD patterns which appear to show a shifted pattern and a smaller than expected lattice volume. This discrepancy should be further investigated but owing to the accuracy and selective nature of TEM it is assumed that the results from electron diffraction can be considered accurate.

6.1.2.7 Electron energy loss spectroscopy

During TEM analysis the particles were examined by EELS. Figure 6-12 shows an energy loss spectrum collected from areas on and around the large particle shown in Figure 6-8.

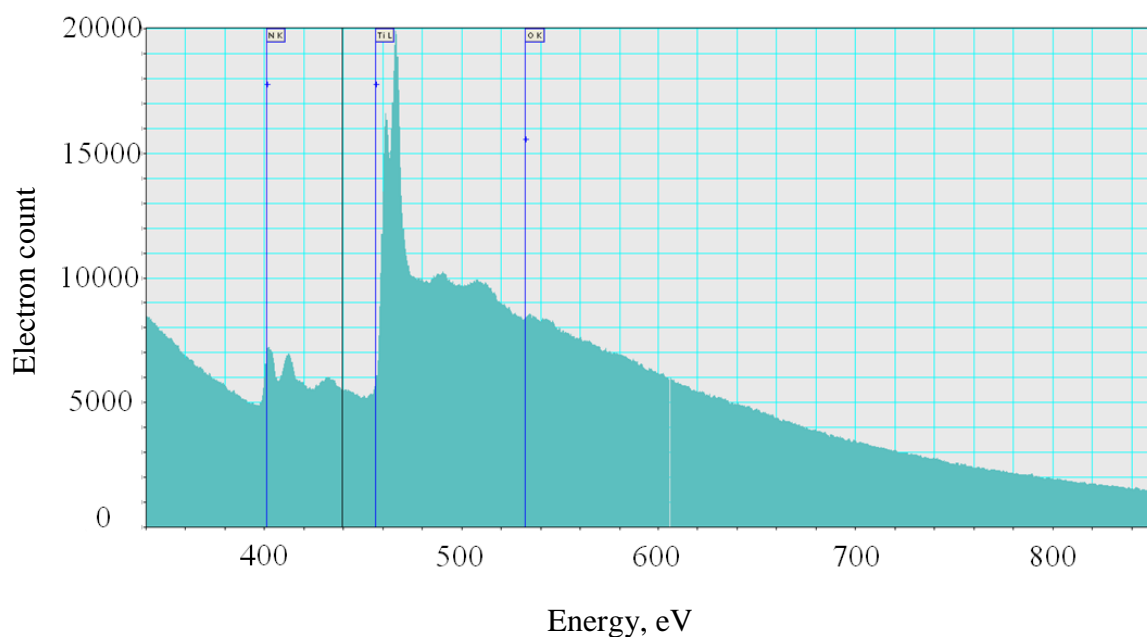


Figure 6-12: Electron energy loss spectra from T5 following ammonolysis

The spectrum shows the presence of the three elements that would be expected to be found in this sample. From left to right – the first peak is due to the nitrogen K edge (401 eV). The large double peak is caused by the Ti L₃ and L₂ edges (456 and 462 eV) and the oxygen K edge at 532 eV. The nitrogen content is too high to be regarded as interstitial or surface gas. The presence of oxygen does suggest that there may still remain oxygen incorporated into the lattice. Quantification of the spectra obtained has not been carried out- while this would be useful it is made non trivial by oxygen appearing within the Ti energy range.

6.1.3 UV/Vis spectroscopy

Spectra were recorded and compared with a standard TiN sample from Sigma-Aldrich. Spectra taken in the visible region would not be expected to fully correlate as the standard sample was not the same colour as the samples produced indicating different absorption in the visible region. After ammonolysis the sample was black with a small hint of blue, Sigma-Aldrich TiN is brown-gold.

Figure 6-13 shows T5 and T7 after 20 h ammonolysis along with a commercial sample of titanium nitride from Sigma-Aldrich. Superficially little about the structure of the compound can be derived from these spectra. Band gap determination is not trivial due to

the nature of the higher wavelength absorption. The samples had lost their distinctive TiO₂ UV/Vis reflectance spectra which can be seen in Chapter 5, Figure 5-19.

The reflectance spectra cannot be matched directly to that of commercial TiN and there appears to be a red shift of the maximum point of absorbance; the position at which there is minimum reflectance occurs is shifted to lower energy wavelengths. Commercial TiN also appears to have a much higher reflectance in the red end of the visible spectrum. The Sigma-Aldrich sample shows an almost 5-fold increase in intensity in the red end of the visible spectrum compared with the blue. No sample produced displayed an increase of this magnitude.

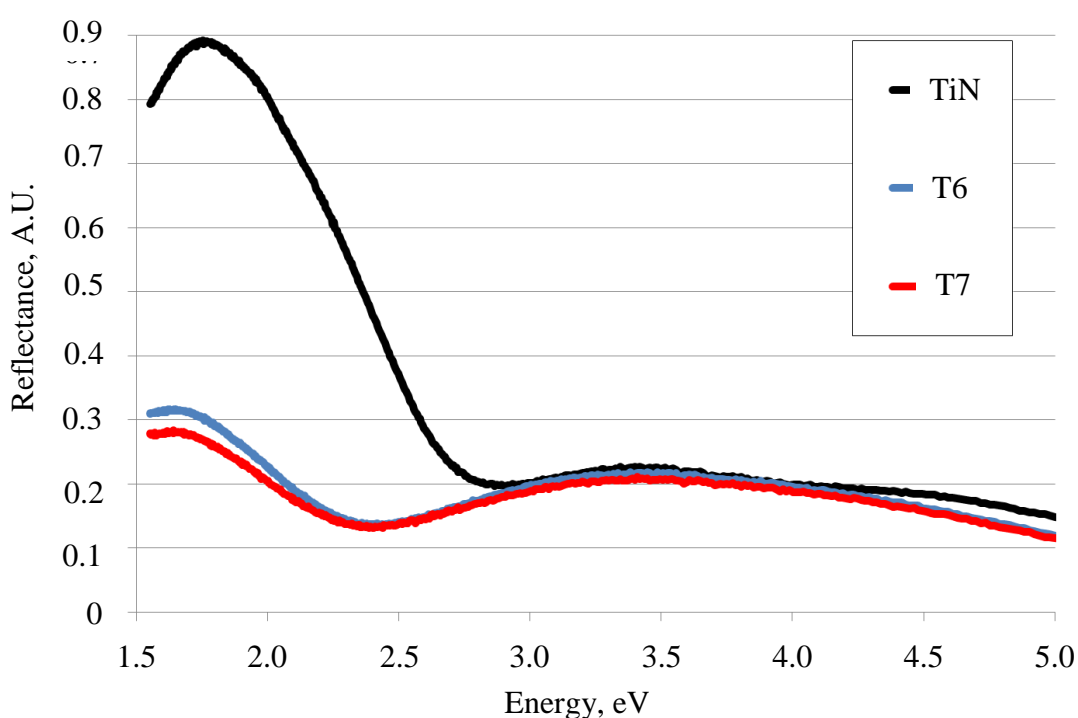


Figure 6-13: Diffuse reflectance spectra of TiN and T5 and T7, both following 20 h ammonolysis

6.1.3.1 Surface area analysis

The SEM results show that the particles which have undergone ammonolysis have a different fine structure to that of the TiO₂ particles. To investigate how this change in structure affected the surface area measurements using BET analysis were made. The results were compared with those already reported for the oxide synthesis described in Chapter 5, this comparison is shown in Table 6-2.

Table 6-2: BET surface area measurement following ammonolysis

	T9	T9 (20 h ammonolysis)
BET Surface Area, m ² /g	46	9
Average Pore diameter, Å	61	190

The results in Table 6-2 show that ammonolysis has caused a reduction in surface area. The original surface area is almost five times higher than that of the product following the ammonia reaction. This would agree with what is seen by SEM; that the rods appear to have agglomerated to form a smoother surface.

A further significant point from the BET analysis is the change in average pore diameter. This can be rationalised in terms of the gas exchange reactions during their preparation. It is possible that the process involved in the exchange of oxygen for nitrogen leads to the formation of larger channels into the particle. Additionally as the rods agglomerate and the space between the rods reduced, it may create channels as some rods become closer together others may become further apart.

6.1.4 Elemental analysis

Elemental analysis in the form of CHN combustion analysis was performed on selected samples to determine their nitrogen content by weight. An example of the results obtained are shown in Table 6-4.

Table 6-3: CHN analysis results showing nitrogen content, weight %

	T7-40 h	T8-20 h
Carbon	nil	nil
Hydrogen	0.1	0.2
Nitrogen	19.9	19.0

The values obtained for all samples showed nitrogen content to be approximately 20% by weight. Assuming complete conversion, a slightly higher value of nitrogen would be expected: 22.64%. As hydrogen was recorded at levels around 0.1% it can be attributed to “trace or nil” in this form of analysis.

T7-40 h was run in the furnace with flow of ammonia for twice the length of time as T8-20 h. Although this did increase the nitrogen content, considering the time was doubled it can be considered a relatively small change. Possibly if a TiO_2 was run for over 40 h (not carried out) the percentage could be increased to agree with the theoretical value. These results indicate the possible presence of TiO_xN_y .

6.1.5 Reconversion to TiO_2

Following the successful conversion to the nitride structure the reaction reversibility was investigated. This was carried out by reheating the previously converted samples at 700°C under oxygen. The reconversion to oxide based system were carried out in the same Vecstar tube furnace (with a new inner tube to avoid a contaminated atmosphere). Samples were run for 20 h. The samples reported in this section are described in Table 6-5. Samples described here (T3O and T7O) had both previously undergone conversion to TiN in a 16 h ammonolysis process. Following reconversion, samples had returned to the bright white colour of TiO_2 in contrast to the blue-black associated with the TiN samples.

6.1.6 Crystalline phase identification

X-ray diffraction was the primary technique for establishing the crystal phases present following ammonolysis. Before heating under a flow of oxygen the samples matched to a cubic structure.

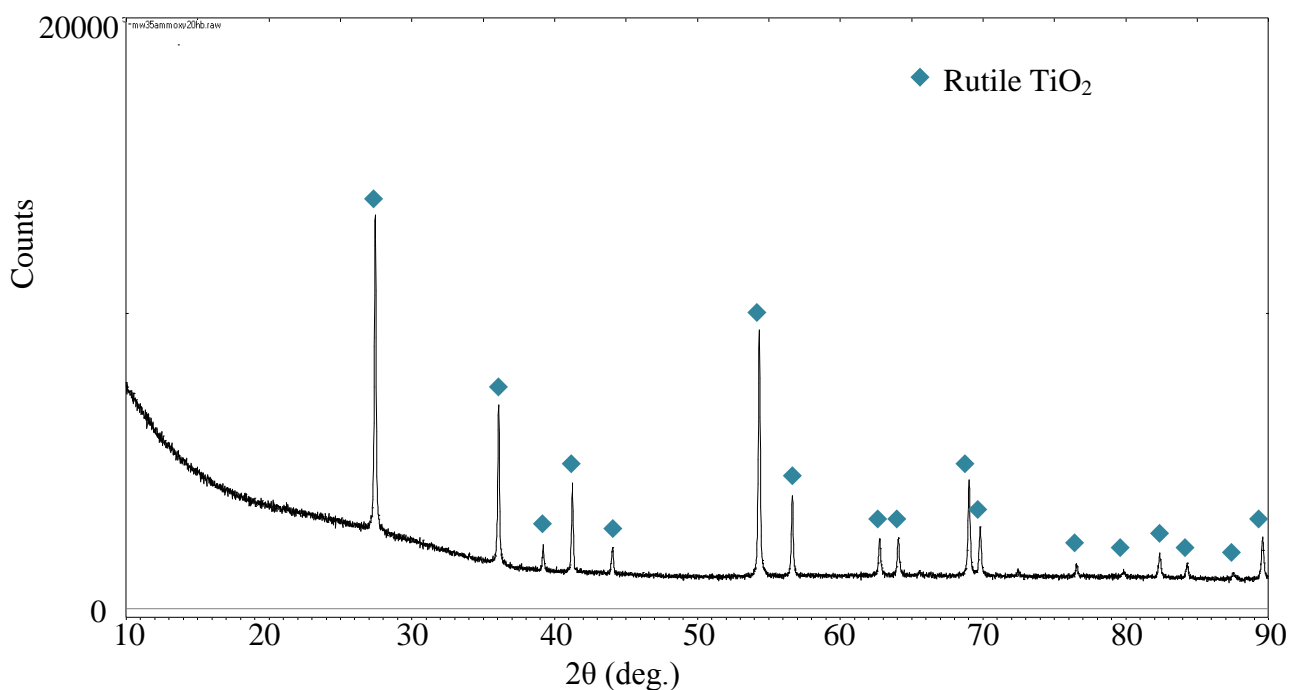


Figure 6-14: XRD pattern for sample T3O showing rutile TiO_2

The XRD pattern shown in Figure 6-14 is a clear match to the rutile phase of TiO_2 . All expected peaks are present in the investigated range. There are no residual peaks associated with the cubic titanium nitride structure. XRD patterns suggested a complete reverse conversion to the parent structure after 16 h. The XRD pattern of sample T7O can be seen in Appendix C (Figure 9-27), this also matches to rutile TiO_2 .

6.1.7 Morphology

SEM was used to obtain morphological information following reconversion reactions. One of the defining features of the microwave hydrothermally produced TiO_2 was the fine nanostructure of the spherical particles. This fine structure is lost on full conversion to the titanium nitride structure with the particles taking on a different surface structure (while still maintaining the spherical morphology). Figures 6-15 and 6-16 below show SEM micrographs of T3O.

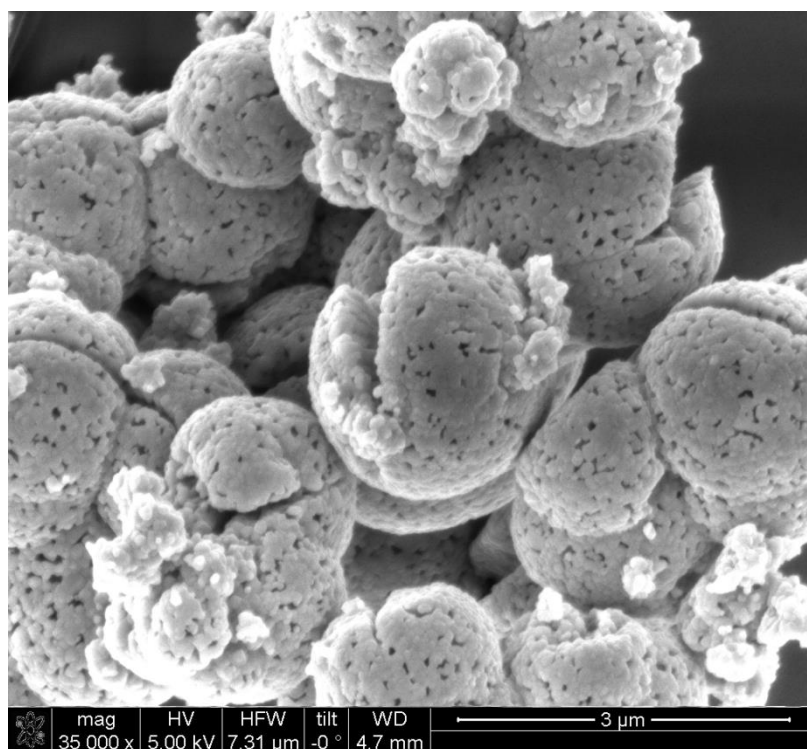


Figure 6-15: SEM micrograph showing particles following reaction with oxygen (sample T3O)

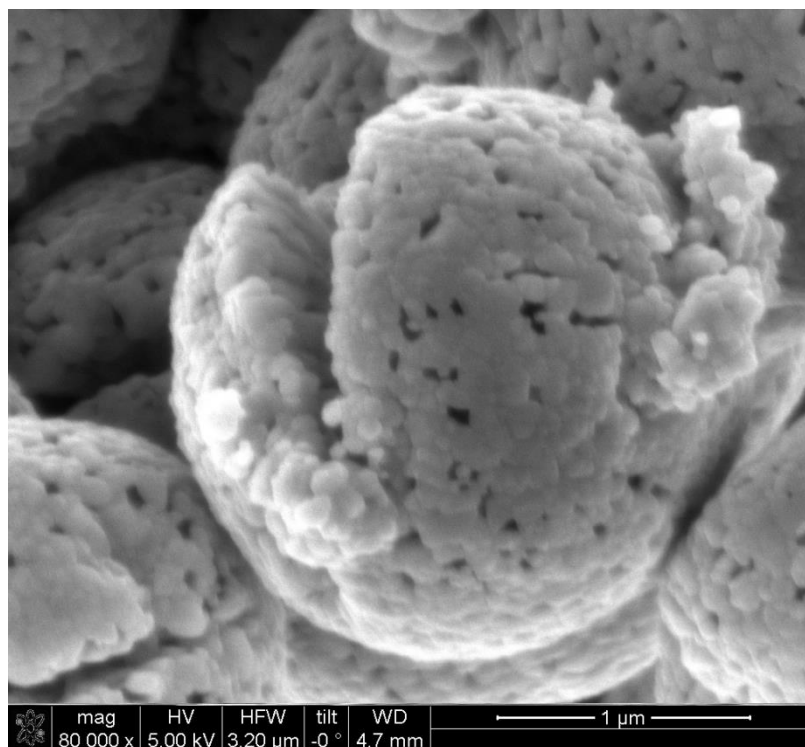


Figure 6-16: SEM micrograph showing spheres of T3O with a pore structure on the spheres

SEM showed the particles to have a distinct appearance in contrast to both the rod like parent structure and the more agglomerated surface of the ammonolysed samples. The spherical morphology of the particles remained but each particle was punctured by deep pores across the surface.

The deep pores can be attributed to the channels which would facilitate gas exchange while the particles are undergoing reaction with oxygen.

6.1.8 Surface area measurement

The reoxidised samples showed a higher surface area than to those converted to TiN. BET surface area measurements were performed on reoxidised samples. A standard result is show with comparisons in Table 6-5.

Table 6-4: BET surface area measurements results

	T9	T9- 40h	T3O
BET Surface Area, $\text{m}^2 \text{g}^{-1}$	41	9	33
Average Pore diameter, Å	52	200	110

It can be seen that the surface area is significantly increased upon reconversion. This can be attributed to the increased number of deep pores opposed to the smooth constant surface of the ammonolysed samples. The new surface area was not as high as the original TiO₂ particles; this can be understood as the nanorod structure was destroyed on the full conversion leading to a reduction in the area accessible for nitrogen adsorption.

6.1.9 Band gap measurement

UV/Vis spectroscopy was used as a means to further confirm phase and identify an optical band gap of the reoxidised material. An example spectrum produced from sample T7O with standard powdered rutile is shown in Figure 6-17.

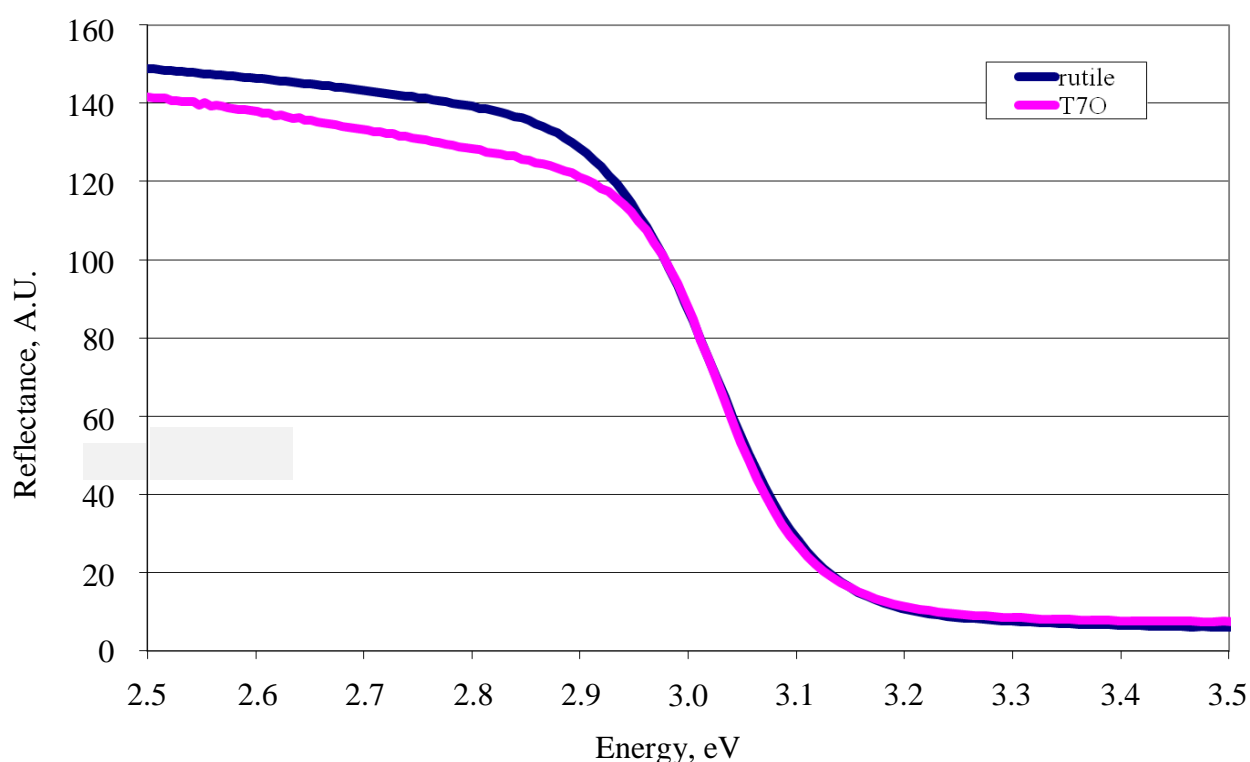


Figure 6-17: Diffuse reflectance spectra of T7O and standard rutile sample

The diffuse reflectance spectrum matches rutile TiO₂. It is clear from the above example that the distinctive band gap is once again present and is a good match to the standard rutile sample, indicating that the reoxidised particles return to a similar material following ammonolysis.

6.1.10 Conclusions

Reported here is the conversion of TiO₂ particles to a titanium nitride structure while retaining the particles original spherical morphology. The TiO₂ particles were synthesised by an ultra-rapid microwave hydrothermal process also reported in this work. These were fully characterised as spherical particles of rutile TiO₂ with a fine hierarchical nanorod structure. The reaction of these structures took place in a tube furnace at 700 °C under a constant flow of ammonia. The resulting products were characterised by XRD, SEM, TEM, BET surface area measurements and UV/Vis spectroscopy.

Following a reaction of 20 h no XRD peaks associated with TiO₂ could be detected and the pattern matched that of a cubic structure. The patterns were matched to a shifted TiN structure. It was found that the cell parameters were slightly reduced and that longer ammonolysis could improve this. It is believed that the structure is slightly nitrogen deficient leading to a reduction in cell parameters.

SEM confirmed that the spherical morphology had been retained but there had been a loss in the fine nanostructure of the particles. This was confirmed by BET which showed a significant reduction in surface area but a corresponding increase in average pore diameter believed to be caused by gas exchange during conversion.

TEM confirmed the structure as matching to TiN, and EEL spectroscopy showed the presence of nitrogen. The presence of oxygen remained unconfirmed due to the dominant titanium edge overlapping with expected distinctive energy loss associated with oxygen interaction. Dark field imaging also showed a distinct change in the rod-like structure, no longer showing similar diffraction conditions reached along the entire length of the rod but showing fragmented nanocrystals 20- 30 nm in diameter.

All evidence points to a slightly nitrogen deficient structure even following 40 h ammonolysis but all analysis clearly demonstrated that the structure now corresponds to a TiN structure opposed to one of TiO₂.

The ammonolysis reaction is shown to be reversible. Under a flow of oxygen at 700 °C the material was successfully reconverted to TiO₂, as was confirmed by XRD and UV/Vis spectroscopy. The spherical morphology was retained and was confirmed by SEM; once

again the gas exchange reaction had modified the surface structure of the particles. Following reaction with oxygen, the particles had the agglomerated surface structure seen with the ammonolysed samples with the addition of multiple deep pores across the surface which are believed to be caused by gas exchange during conversion. The new surface structure was reflected by a change in BET surface area measurements which showed an increase in comparison to ammonolysed samples but values did not return to the high values of original the TiO₂ particles described in Chapter 5. The increase compared to the TiN structure is attributed to the formation of deep pores exposing additional internal surfaces. It would not be expected for the particles to regain the high surface area seen in the nanostructured parent material as initial ammonolysis destroyed the fine structure which led to this initially high surface area.

6.2 Doping of TiO₂

Of high interest is the doping of TiO₂ with elements such as nitrogen. It is well established that nitrogen doping can lead to a shift in band gap resulting in visible light absorption¹⁶¹⁻¹⁶³. It has been reported that the shift in band gap is due to the p states of nitrogen mixing with the oxygen 2p states¹⁶³. The results in this section detail a process of removing some of the oxygen and replacing the atoms with nitrogen resulting in a lowering of the band gap into the visible region.

The experimental process was similar to that of the conversion process described above but with the temperature significantly reduced. In this work the spherical rutile particles with hierarchical nanorods structure were placed inside a Vectar tube furnace under flow of ammonia (0.4 L min⁻¹) the furnace was then heated to 450 °C for 12-16 h.

When samples were removed from the furnace they no longer retained their brilliant white colouration. Samples were fine green or yellow powders. The example system described in this section is labelled T9D and underwent 16 h ammonolysis at 450 °C.

6.2.1 Post-reaction appearance

Titanium dioxide is brilliant white as it reflects all visible wavelengths of light. An idealised material will be non-white indicating the absorption of visible wavelengths. Below Figure 6-18 shows the post-reaction appearance of T9D.



Figure 6-18: Image showing post-reaction appearance of T9D showing green colouration

6.2.2 Crystalline phase identification

Powder X-ray diffraction was used for crystal phase identification. For successful doping of the structure there should be no significant deviation from the parent structure. This was found to be the case, with each of the samples following low temperature ammonolysis showing a rutile TiO_2 structure. Shown below in Figure 6-19 is the XRD pattern obtained for T9D.

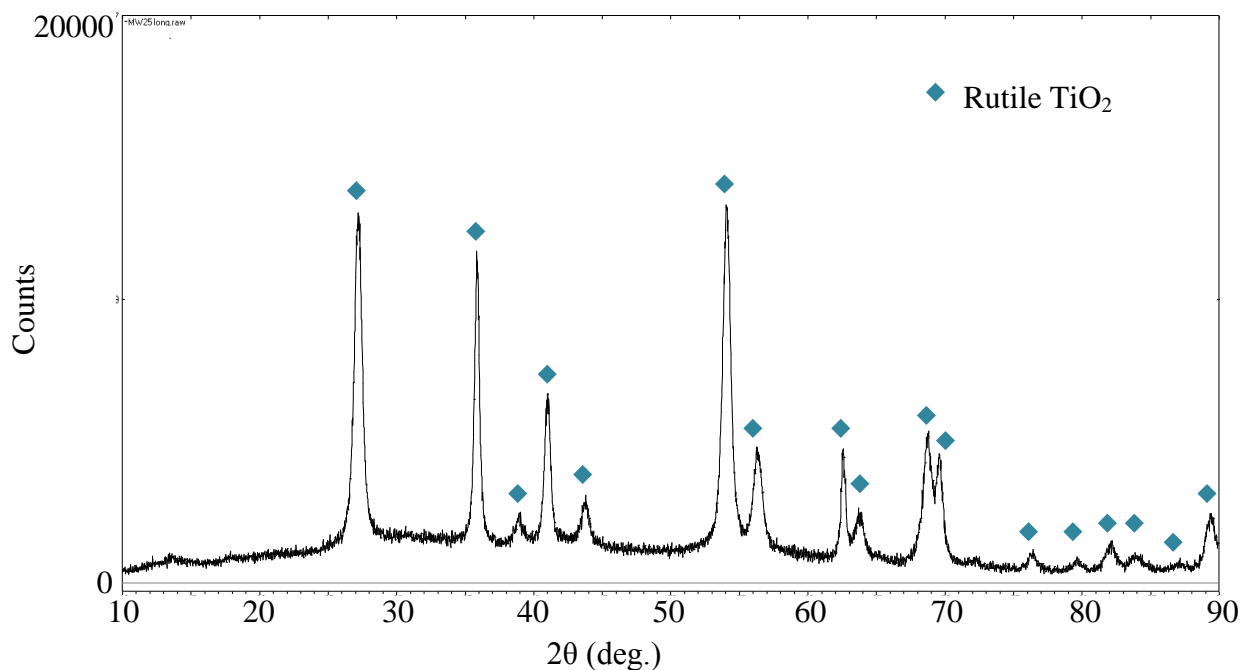


Figure 6-19: XRD pattern for sample T9D showing rutile structure

While reactions at 700 °C led to the formation of new peaks and the destruction of existing the reactions at 450 °C showed no new peaks. The post-reaction XRD pattern shows a clear match to the rutile structure with no significant change in pattern.

Using CelRef program to obtain lattice parameters the following was obtained:

Table 6-5: Cell parameters of doped structure

	a, Å	c, Å	V, Å ³
Literature	4.60	2.96	62.73
Calculated	4.59	2.96	62.36

Although values are slightly lower than those recorded in the literature they show no significant change in parameters.

6.2.3 Morphology

SEM was used to examine the surface morphology, this showed that the original morphology of the particles had remained intact.

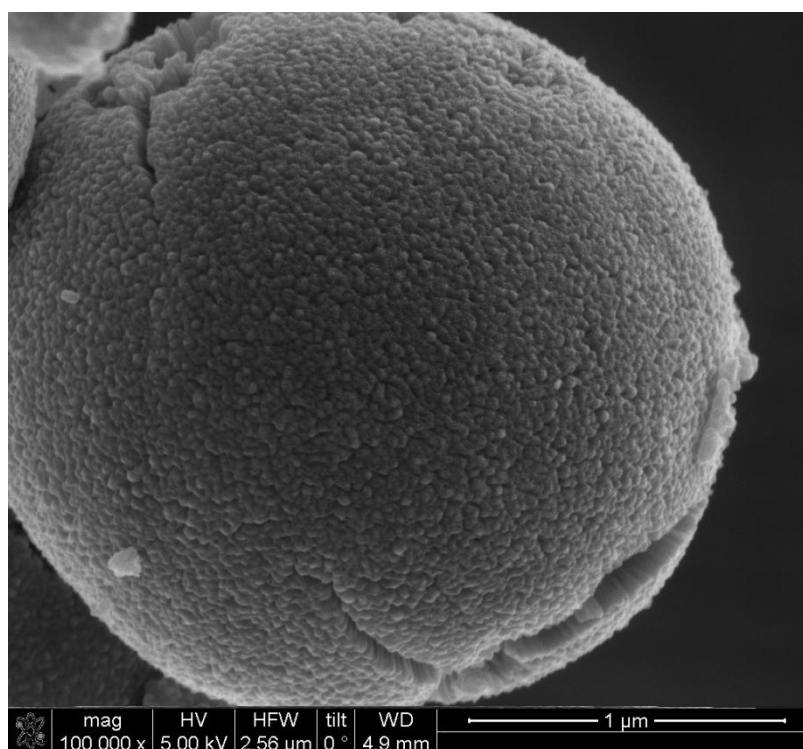


Figure 6-20: SEM micrograph of spherical particle in T9D

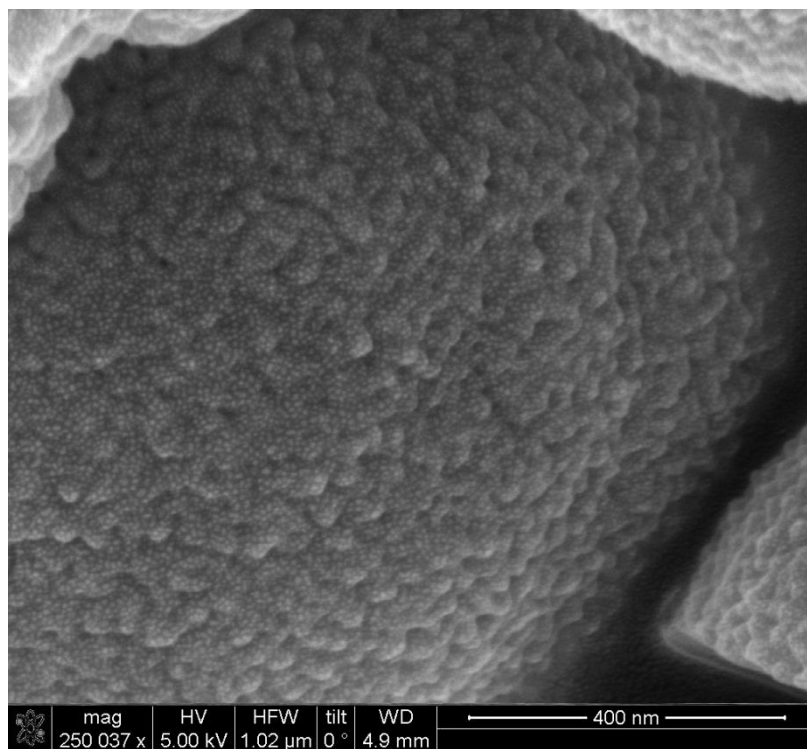


Figure 6-21: SEM micrograph showing high magnification of surface of T9D

The SEM of the particles following low temperature ammonolysis showed the rod structure more clearly than those of the higher temperature reactions. The rods however appear to be more closely packed than those seen in the starting materials. The rod tips appear to form a continuous surface. It is not clear from SEM whether there would be access to the inner surface of the rods following the doping process.

It should be noted that the speckling on the surface seen in Figure 6-21 is due the gold particles which were sputtered onto the sample before SEM analysis to reduce charging.

6.2.4 TEM

As with other samples described in this chapter, TEM was used to gain further understanding of the crystal structure and morphology. Below (Figures 6-23 to 6-27) are a series of images taken using dark field imaging which highlights the similar diffracting conditions as the sample is tilted in the beam.

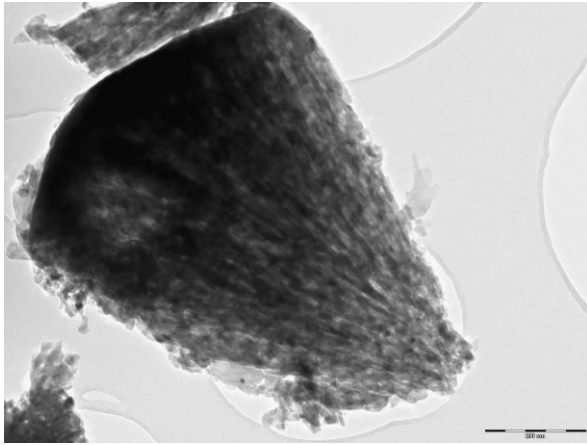


Figure 6-22: TEM bright field image of T9D showing rod structure

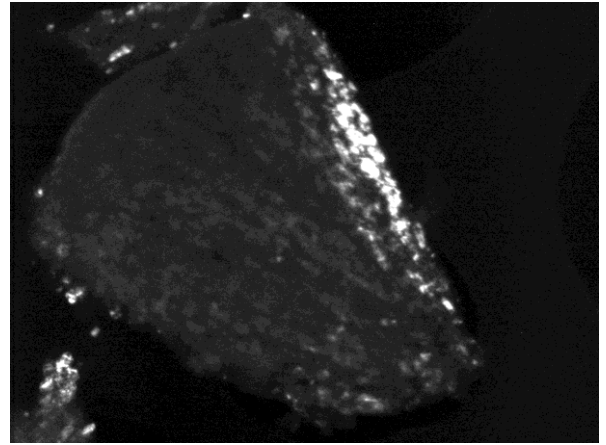


Figure 6-23: TEM dark field image of T9D

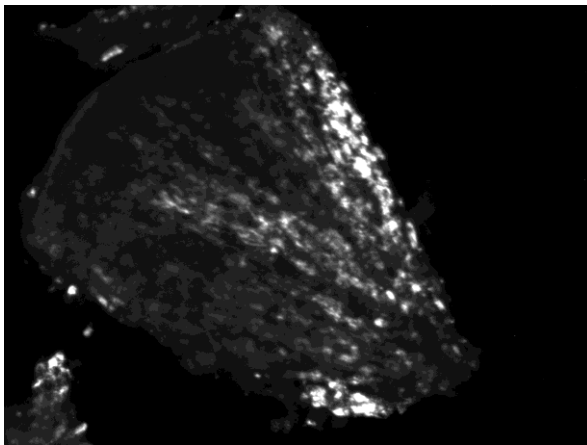


Figure 6-24: TEM dark field image of T9D

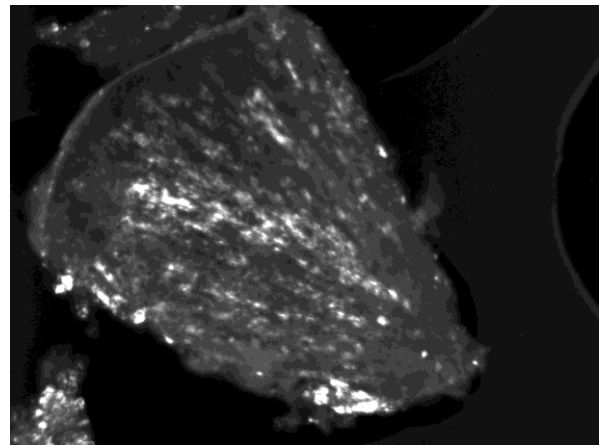


Figure 6-25: TEM dark field image of T9D

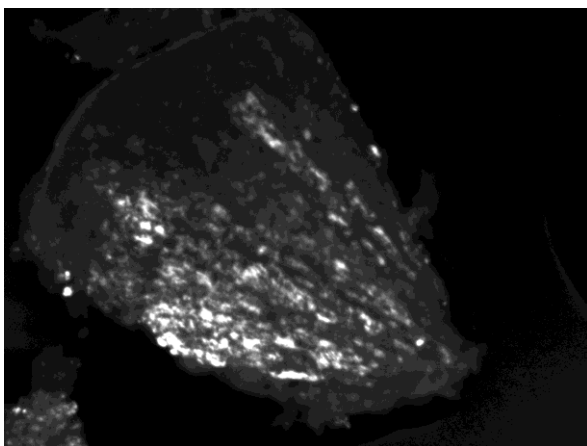


Figure 6-26: TEM dark field image of T9D

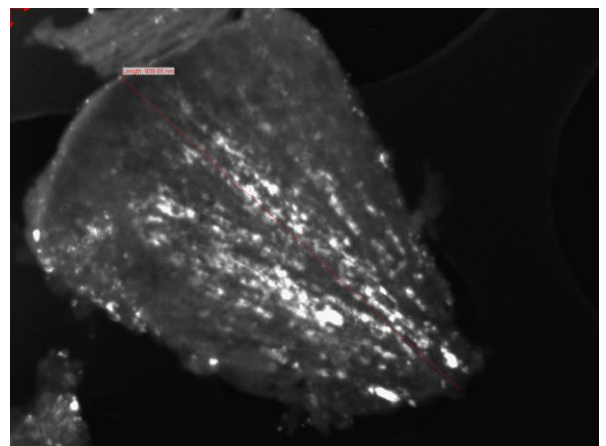


Figure 6-27: TEM dark field image of T9D

The series of images shown in Figures 6-22 to 6-27 shows firstly the bright field image of the fan like segment of T9D then 5 dark field images of the same particle. This image series highlight that the rod structure is still intact. It can be seen that as the sample is tilted individual areas are illuminated as similar Bragg diffraction conditions are met. In the higher temperature reactions there was no crystallographic association along the length of

the rods as the many smaller nanocrystals had formed each having a slightly different orientation from its neighbour.

6.2.4.1 Elemental analysis

The high resolution of EELS makes it suitable for detecting low concentration of dopants in a structure. Below (Figure 6-28) is a typical spectrum obtained from the T9D.

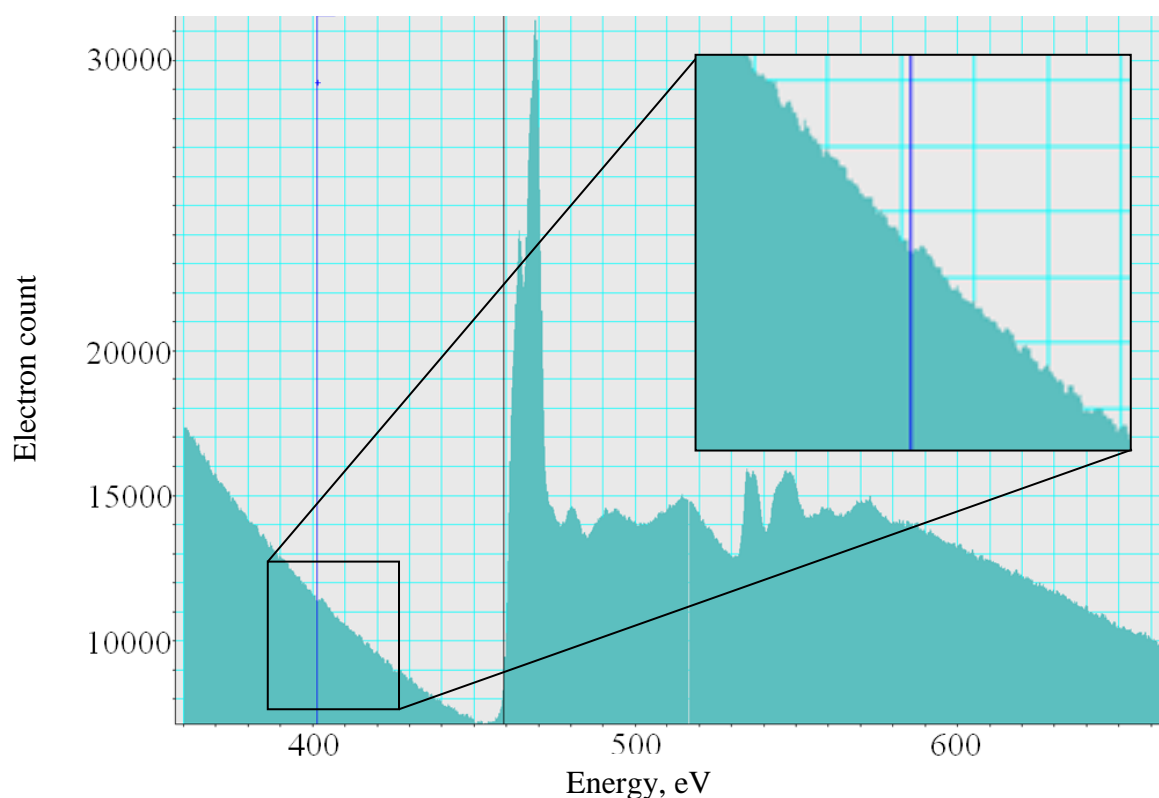


Figure 6-28: Electron energy loss spectrum from T9D. Inset shows zoomed in area highlighted

The EEL spectrum (Figure 6-28) shows a large double peak caused by the Ti L_3 and L_2 edges at 456 and 462 eV. The oxygen K edge at 532 eV is less prominent in this spectrum compared with that of the full conversion shown in Figure 6-12. The nitrogen K-edge is expected to be found at 401 eV and there is a small increase in the background count at this value which could be interpreted as nitrogen detection but the result is not conclusive. The small increase in count is not a substantially above the background reading and further work should be carried out to obtain a definitive elemental composition.

6.2.5 Surface area measurement

Ammonolysis of the oxide samples leads to a dramatically reduced surface area in the converted samples. This is attributed to the fusing of the nanostructure into a single surface. The doped samples were measured for nitrogen adsorption and the two structures were compared.

The results are shown in Table 6-6.

Table 6-6; BET surface area results for starting material, doped and converted structures

	T9	T9D	T9- 40h
BET Surface Area $\text{m}^2 \text{g}^{-1}$	41	4	10
Average Pore diameter, Å	52	94	200

The surface area identified by BET analysis shows a greatly reduced surface area compared with the starting materials. The doped structure of T9D shows a tenfold reduction. The surface area is even lower than that of the fully converted structure. There is however an increase in the average pore diameter.

The change in the surface area and pore diameter between the samples combined with SEM observations, is rationalised in the following manner:

1. The unreacted sphere shows fine rod like structure.
2. The lower temperature ammonolysis fuses these rods into a smooth surface.
3. Higher temperature reactions fuse the rods more completely and deep pores begin to form due to the high exchange of gas in the lattice

6.2.6 CHN elemental analysis

CHN microanalysis of doped samples returned “trace” or “nil” quantities of nitrogen in the structure.

6.2.7 Band gap measurement

The doping of TiO_2 is carried out in an attempt to lower the optical band gap of the material. The target was to shift the optical band gap into the visible region of the electromagnetic spectrum from the UV region (which the undoped material occupies). Figure 6-29 shows the UV/Vis spectrum for T8D with tangents plotted to calculate the band gap.

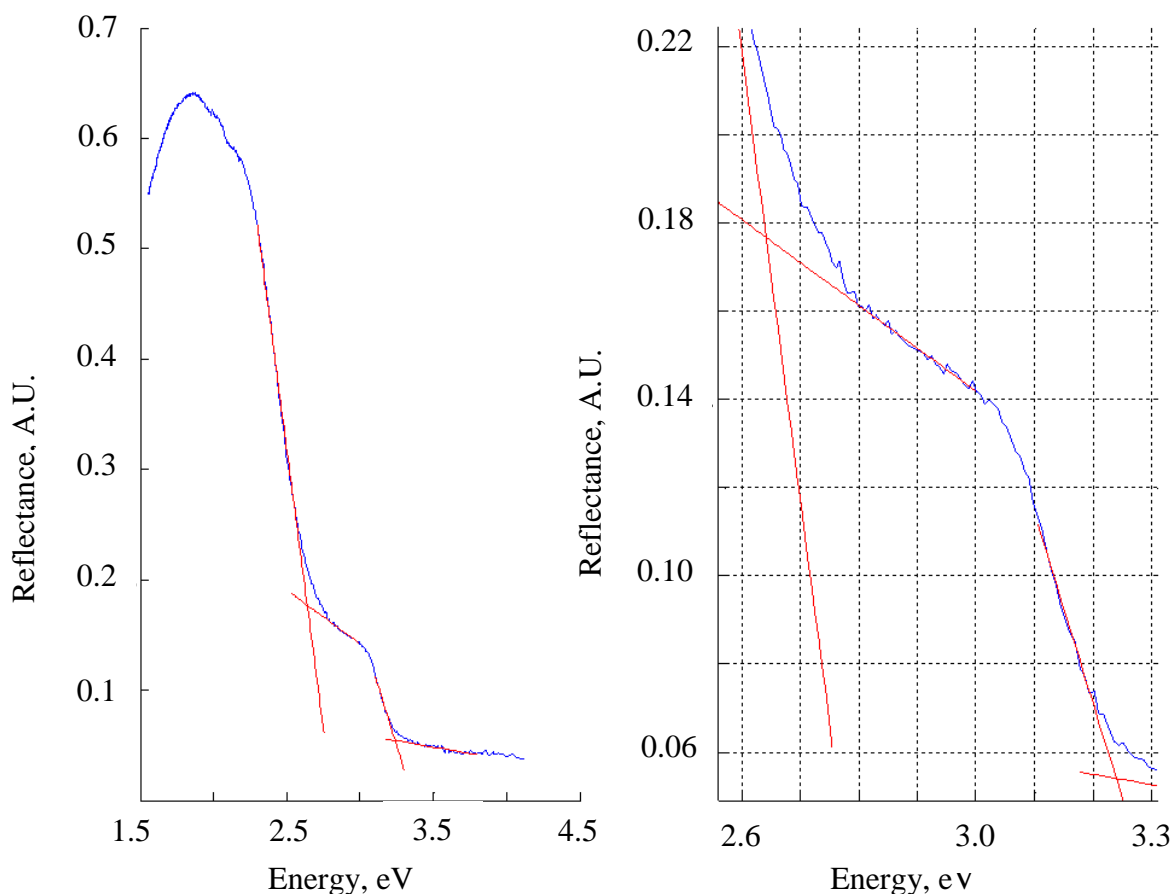


Figure 6-29: UV/Vis spectrum for T8D showing two band gaps

The spectra for doped samples are significantly different from the undoped samples. The undoped structure shows a single band gap corresponding to the rutile phase, while doped samples show two points of inflection. A second absorption region appears at lower energy than the first. Here the possible band gaps were calculated at 2.64 eV and 3.24 eV. The 3.24 eV band gap is attributed to the rutile structure but the 2.64 eV band gap is not seen in any stoichiometric rutile structures. The value of 2.64 eV corresponds to a wavelength of 470 nm which lies in the blue region of the visible spectrum.

6.2.8 Conclusions

Reported here is a possible route to the doping of spherical rutile particles to shift the band gap of the material into the visible region. The particles doped were hierarchical nanostructured spheres of TiO₂ grown by a microwave assisted hydrothermal process described in the previous chapter of this work.

The elemental composition of the particles was altered *via* heating to 450 °C under a flow of ammonia. The resulting material was characterised by XRD, SEM, TEM, EELS, BET surface area analysis and UV/Vis spectroscopy.

Doping of the structure led to a colour change as the entire visible spectrum was no longer being reflected. Samples emerged green or yellow depending on the duration of ammonolysis. The crystal phase however showed no deviation from that of the original rutile structure and the XRD pattern was shown to match the parent material.

SEM imaging showed that the particles as having a less porous appearance with the fusion of the surface into that of a continual smooth surface. This was confirmed by BET surface area analysis that exhibited a tenfold reduction in the surface area.

Dark field TEM showed that the crystals still displayed a common alignment along the rod lengths, highlighting similar rod areas simultaneously fulfilling Bragg diffraction conditions. TEM analysis EEL spectroscopy did not conclusively identify the presence of nitrogen and further examination will be required to confirm the low level doping of the structure or if the colour change and band gap augmentation is due to oxygen deficiency.

A significant difference from the starting material was the emergence of a second point of inflection in the UV/Vis spectrum which lay in the visible region of the spectrum. The doped structures were now capable of absorbing blue light and this has potentially exciting applications in photocatalysis.

Further work in this area should focus in quantifying the level of doping in each structure and the length of time requires for doping to further tailor the band gap of the material.

6.3 Conclusions

This chapter examines the doping and conversion of TiO₂ to TiO_{2-x}N_x and TiN structures. The TiO₂ was produced *via* the methods described in Chapter 5. In Section 6.1 full conversion to TiN is reported showing that after 20 h under flow of ammonia at 700 °C the spherical oxide particles have become TiN. This was evidenced by XRD, TEM, UV/Vis spectroscopy and elemental analysis. This process is of particular interest as the spherical

morphology of the particles was retained. The original oxide particles showed a fine nanorod structure which was shown by SEM to have annealed to a smooth surface and correspondingly the surface area had dropped by a factor of 10 as evidenced by BET analysis.

In Section 6.1.5 the ammonolysis process was demonstrated to be reversible as particles could be reconverted to TiO_2 by flowing oxygen over the TiN particles at 700 °C for 16 h. Once again the spherical morphology was retained. On reaction with oxygen there was an increase in surface area which is attributed to the large channels which open, likely caused by the gas exchange from the centre of the spheres. Following reaction with oxygen the samples once again conform to a rutile TiO_2 structure.

The final section of this work, Section 6.2, looks at potential doping of the oxide structure with nitrogen. Doping of TiO_2 is an excellent way of modifying the band gap of the material to lower it into the visible region. Reported here is the doping of spherical TiO_2 by using a flow of ammonia over the oxide particles at 450 °C. Samples emerged green having lost their characteristic white colour showing a narrowing of the reflected light into the centre of the visible spectrum. Samples showed two distinct regions of reflectance, one the familiar rutile 3.24 eV and the second in the visible region (2.64 eV). Samples were shown to retain both their spherical morphology and their rutile structure by SEM and XRD respectively. EELS was unable to resolve a clear nitrogen K-edge and further work should be carried out to identify nitrogen incorporation and oxygen stoichiometry.

7 Conclusions

This thesis looks at the growth and morphology of semiconducting materials which have potential applications in renewable energy generation. The first two results chapters detail low dimensional growth of materials with potential for use in the field of thermoelectrics and the second two results chapters describe growth and modification of materials with potential photocatalytic uses. This work demonstrates numerous routes by which particle morphology can be selected or controlled by the tuning of various reaction parameters.

One of the main focuses of materials science is the reduction in dimensions to the nanoscale as this brings inherent properties not associated with the bulk material. For thermoelectric applications low dimensional structures are particularly important due to the increases in efficiency attributed to quantum confinement effects and an increase in phonon scattering.

In Chapter 3 of this work the growth of Bi_2Te_3 on a silicon surface *via* CVD was examined. By altering reaction parameters different morphologies and phases are attainable. In a one-step CVD reaction, plates of Bi_2Te_3 are grown on a silicon surface with <2 nm of gold/palladium sputtered on the surface. The sputtering of metal before the reaction increases the number of potential nucleation sites to facilitate growth of particles. Silicon pieces with a minimal amount of gold/palladium were sealed in an evacuated ampoule along with elemental bismuth and tellurium. On heating to 700 °C for 48 h, the growth of Bi_2Te_3 occurred on all surfaces examined. The growth showed distinct hexagonal and triangular growth patterns. Plates were up to 40 μm in diameter but were <1 μm in thickness. This is not an uncommon structure for Bi_2Te_3 , as the plate structure is typical of its crystal structure forming layers along the *a* and *b* axes while having a potential to self terminate along the *c* axis with every series of quintuple layers held together with van der Waals forces. This synthesis route is advantageous over many syntheses found in the literature as it does not involve expensive precursors. MOCVD reactions are capable of producing similar structures but include the preparation of expensive precursors and also have potential to introduce contaminants in the form of the organic components. The plates reported here were characterised using SEM, EDX and XRD. Leading on from the platelets produced it was observed here that octahedra could be grown using a similar process with a modified silicon surface. Disruption of a flat silicon surface to introduce grooves and scratches onto the surface leads to the formation of the

bipyramids over the production of plates. As the plates grew parallel to the surface it can be understood that when the potential for smooth growth across the surface is interrupted then the growth self seeds into non-planar morphologies. The bipyramid structures were found on every reaction with a disrupted surface and no plates were found thereby demonstrating a route to morphology control by surface modification.

Not only was surface modification investigated but also the influence of reagents was examined. It was shown that removing tellurium from the reaction ampoule proved detrimental to the growth of structures on the silicon surface resulting in all closed spaced CVD reactions with bismuth as the sole reagent leading to no detectible growth. The introduction of a transport gas reagent proved equally detrimental to the reactions. Adding I_2 (a known CVD transport facilitator) hindered not only the tellurium and bismuth from transporting but also prevented them from reacting together. Following CVD reaction with I_2 , Bi and Te the Si substrate remained free from deposition and the powders remained in their elemental state. The only notable change in the reactions was I_2 had transported from one side of the reaction vessel to the other. Finally in Chapter 3, the growth of bismuth rich nanowires is reported. Using the same closed space CVD reactions as before but increasing the Bi/Te ratio to 1:1 the growth of bismuth rich wires with diameter <150 nm and up to 40 μm in length were produced. The wires were found to be seeded from larger areas of growth and were found with varying concentration across the surface from small groups of <20 to nanowires fully encasing large particles.

Chapter 4 employed similar closed space CVD reactions for the most part however alternatives to a silicon substrate were examined. Metal foils and commercial substrates were investigated. The most promising non-silicon surface for CVD growth of Bi_2Te_3 proved to be alumina. Growth of nanostructured spheres of Bi_2Te_3 was demonstrated using CVD at 700 $^\circ\text{C}$ for 48 h using elemental Bi and Te. The spheres were seen to be comprised of an agglomerated nanostructure resulting in spheres up to 20 μm in diameter composed of plates 50 - 850 nm wide. In contrast to the Si example above, bismuth did adhere well to the Al_2O_3 surface when used in a tellurium free environment. It was discovered that the growth patterns for Bi and Bi_2Te_3 were remarkably similar while Te growth in a Bi free environment was irregular and sparse. This suggests that the transport and growth of Bi is driving the morphology of the Bi_2Te_3 spheres. The other firm substrate investigated was GaAs. While GaAs is a useful substrate in the electrical industry it proved unsuitable with

respect to the high temperatures and reactive atmosphere produced in a CVD reaction. The substrates degraded during reaction and subsequent analysis on the substrate proved difficult and inconclusive. In addition, Cu and Co foils were investigated as potential substrates. While both proved ill-suited to Bi_2Te_3 growth they both exhibited interesting telluride growth. Both Cu and Co preferentially reacted with tellurium leading to the formation of copper and cobalt telluride structures. In copper CVD reactions at 700 °C the copper was entirely converted to dicopper telluride forming large triangular crystals. Lowering the temperature of the copper CVD reactions to 450 °C allowed the formation of arrays of vertically aligned plates across the surface. The plates were <500 nm in thickness but up to 25 μm in diameter. With the cobalt reactions the tellurium reacted with the cobalt but did not produce free standing surface structures and instead produced a smooth tellurium-rich surface. There were notable lattice-like features across the surface but due to high oxygen content these were attributed to contaminants from prior oxidation of the substrate. The final section in this chapter looks at a reproduction of a literature synthesis of Bi_2Te_3 which repeatedly produced a different morphology to that previously reported. The samples were produced following the method described by Zhang *et al.*¹³¹ and a comparative study was carried out. Additionally this method produced sufficient bulk quantities of Bi_2Te_3 to be examined by Raman spectroscopy.

The third results chapter presented here looks at the growth of TiO_2 from a TiCl_4 precursor using an aqueous acid microwave hydrothermal approach. Single phase rutile TiO_2 is produced in a multi-mode microwave reactor with the particles in the form of 1-3 μm spheres comprised of radially aligned nanorods. The spheres are characterised by TEM as well as SEM and XRD to show a single phase product. TEM gives insight into the growth mechanism showing preferential growth along the (001) axis. Furthermore systematic study demonstrates the link between microwave irradiation time and sphere diameter as well as the influence of TiCl_4 concentration on particle size. This study showed that increasing either irradiation time or TiCl_4 concentration leads the production of spheres with a larger diameter. The chapter also demonstrates the influence of the microwave reactor showing that multi-mode reactors will preferentially grow rutile TiO_2 while a single-mode reactor will produce a mixed phase product showing the presence of anatase.

The final results chapter of this work (Chapter 6) explores the pseudomorphic doping and conversion of the structures produced in Chapter 5. Using ammonolysis, TiO_2 spheres were fully converted to TiN. Investigation by TEM revealed the rod structure of the spheres to no longer be intact but SEM showed that the overall spherical morphology was retained. Full conversion was achieved by flowing ammonia over the TiO_2 at 700 °C for 20 h. Lowering the temperature of ammonolysis to dope nitrogen into the structure proved capable of lowering the optical band gap of TiO_2 into the visible region. The presence of doped levels of nitrogen was unable to be confirmed by EELS but a very slight increase in the background reading was observed where the nitrogen K-edge is to be expected, further work must be carried out to identify the stoichiometry of the final product. The presence of an optical band gap at 2.64 eV (along with rutile's 3.24 eV) was evidenced by UV/Vis spectroscopy. Finally in this chapter the reversibility of the conversion and doping reactions was demonstrated by reconvertng TiN to its former single phase rutile structure with corresponding band gap demonstrated by UV/Vis spectroscopy. This chapter also demonstrates that during conversion as the rods anneal there is a loss in surface area (shown by BET analysis and SEM) while on the final reconversion back to the TiO_2 structure there is once again an increase in surface area as compared to the TiN.

8 References

1. L. M. Goncalves, C. Couto, P. Alpuim and J. H. Correia, *Journal of Micromechanics and Microengineering*, 2008, **18** (6), 064008
2. F. R. Stabler, Proceedings of Materials Research Society Symposium, Boston, 2005, **88** (F), doi: <http://dx.doi.org/10.1557/PROC-0886-F01-04>
3. A. W. V. Herwaarden and P. M. Sarro, *Sensors and Actuators*, 1986, **10**, 321
4. M. Niffenegger, K. Reichlin and D. Kalkhof, *Nuclear Engineering and Design*, 2005, **235** (17-19), 1777
5. T. J. Seebeck, *Annalen der Physik*, 1826, **18** (2), 133
6. D. Gonzalez-Mendizabal, P. Bortot and A. L. Lopez de Ramos, *International Journal of Thermophysics*, 1998, **19** (4), 1229
7. J. Martin, T. Tritt and C. Uher, *Journal of Applied Physics*, 2010, **108** (12), 121101
8. G. J. Snyder, M. Christensen, E. Nishibori, T. Caillat and B. B. Iversen, *Nature Materials*, 2004, **3** (7), 458
9. R. Venkatasubramanian, E. Siivola, T. Colpitts and B. O'Quinn, *Nature*, 2001, **413**, 597
10. R. Venkatasubramanian, T. Colpitts, B. O'Quinn, S. Liu, N. El-Masry and M. Lamvik, *Applied Physics Letters*, 1999, **75** (8), 1104
11. G. Chen, B. Yang, W. L. Liu, T. Borca-Tasciuc, D. Song, D. Achimov, M. S. Dresselhaus, J. L. Liu, K. Wang, Proceedings of the 20th International Conference on Thermoelectronics, Beijing, 2001, 30
12. T. C. Harman, M. P. Walsh, B. E. LaForge and G. W. Turner, *Journal of Electronic Materials*, 2005, **34** (5), 19
13. M. S. Dresselhaus, G. Chen, M. Y. Tang, R. G. Yang, H. Lee, D. Z. Wang, Z. F. Ren, J. P. Fleurial and P. Gogna, Proceedings of Materials Research Society Symposium, Boston, 2005, 88 (f), doi: <http://dx.doi.org/10.1557/PROC-0886-F01-01>
14. Z. F. Ren, B. Poudel, Y. Ma, H. Q. Y. C. Lan, A. Minnich, A. Muto, J. Yang, B. Yu, X. Yan, D. Z. Wang, J.M. Liu, M. S. Dresselhaus and G. Chen, Proceedings of the Materials Research Society, San Francisco, 2009, **1166**(N), doi: <http://dx.doi.org/10.1557/PROC-1166-N04-03>
15. X. B. Zhao, X. H. Ji, Y. H. Zhang, T. J. Zhu, J. P. Tu and X. B. Zhang, *Applied Physics Letters*, 2005, **86** (6), 062111
16. B. C. Sales, B. C. Chakomakos and D. Mandrus, *Science*, 1996, **272**, 1325
17. B. C. Sales, B. C. Chakoumakos and D. Mandrus, *Physical Review B*, 2000, **61** (4), 2475
18. L. Hicks and M. Dresselhaus, *Physical Review B*, 1993, **47** (24), 16631
19. C. J. Vineis, A. Shakouri, A. Majumdar and M. G. Kanatzidis, *Advanced Materials*, 2010, **22** (36), 3970
20. N. Gothard, J. E. Spowart and T. M. Tritt, *Physica Status Solidi(a)*, 2012, **207** (1), 157
21. J. Y. Yang, X. A. Fan, R. G. Chen, W. Zhu, S. Q. Bao and X. K. Duan, *Journal of Alloys and Compounds*, 2006, **416** (1-2), 270
22. M. M. Nassary, H. T. Shaban and M. S. El-Sadek, *Materials Chemistry and Physics*, 2009, **113** (1), 385
23. A. Boulouz, A. Giani, F. Pascal-Delannoy, M. Boulouz, A. Foucaran and A. Boyer, *Journal of Crystal Growth*, 1998, **194**, 336
24. Y. C. Jung, J. H. Kim, S. H. Suh, B. K. Ju and J. S. Kim, *Journal of Crystal Growth*, 2006, **290** (2), 441

25. S. D. Kwon, B. k. Ju, S. J. Yoon and J. S. Kim, *Journal of Electronic Materials*, 2009 **38** (7), 920
26. R. Venkatasubramanian, T. Colpitts, E. Watko, M. Lamvik and N. El-Masry, *Journal of Crystal Growth*, 1997, **170**, 817
27. Y. Zhang, C. L. Hapenciuc, E. E. Castillo, T. Borca-Tasciuc, R. J. Mehta, C. Karthik and G. Ramanath, *Applied Physics Letters*, 2010, **96** (6), 062107
28. G. S. Nolas, J. L. Cohn, G. A. Slack and S. B. Schujman, *Applied Physics Letters*, 1998, **73** (2), 178
29. A. Saramat, G. Svensson, A. E. C. Palmqvist, C. Stiewe, E. Mueller, D. Platzek, S. G. K. Williams, D. M. Rowe, J. D. Bryan and G. D. Stucky, *Journal of Applied Physics*, 2006, **99**, 023708
30. P. Rogl in *Thermoelectrics Handbook: Macro to Nano*, ed. D. M. Rowe, Taylor and Francis, United States of America, 2006, Section 3, ch 32 pp 32-2
31. H. Kleinke, *Chemistry of Materials*, 2010, **22** (3), 604
32. V. L. Kuznetsov, L. A. Kuznetsova, A. E. Kaliazin and D. M. Rowe, *Journal of Applied Physics*, 2000, **87** (11), 7871
33. J. R. Salvador, J. Y. Cho, Z. Ye, J. E. Moczygemba, A. J. Thompson, J. W. Sharp, J. D. König, R. Maloney, T. Thompson, J. Sakamoto, H. Wang, A. A. Wereszczak and G. P. Meisner, *Journal of Electronic Materials*, 2012, **42** (7), 1389
34. C. Uher in *Thermoelectrics Handbook: Macro to Nano*, ed. D. M. Rowe, Taylor and Francis, United States of America, 2006, Section 3, ch 34 pp 34-4
35. X. Shi, H. Kong, C. P. Li, C. Uher, J. Yang, J. R. Salvador, H. Wang, L. Chen and W. Zhang, *Applied Physics Letters*, 2008, **92** (18), 182101
36. R. M. Thompson, *American Mineralogist*, 1949, **34**, 341
37. M. Weller in *Inorganic Chemistry*, Oxford University Press, Oxford, sixth edition, 2014, Ch. 1 p 85
38. N. Gothard, B. Zhang, J. He and T. M. Tritt, *Proceedings of the Materials Research Society*, Boston, 2005, **886(F)**, 05-04
39. D. Teweldebrhan, V. Goyal and A. A. Balandin, *Nano Letters*, 2010, **10** (4), 1209
40. H. Scherrer and S. Scherrer in *Thermoelectrics Handbook: Macro to Nano*, ed. D. M. Rowe, Taylor and Francis, United States of America, 2006, Section 3, ch 27 pp 27-4
41. S. Li, H. M. A. Soliman, J. Zhou, M. S. Toprak, M. Muhammed, D. Platzek, P. Ziolkowski and E. Muller, *Chemistry of Materials*, 2008, **20**, 4403
42. O. Yamashita, S. Tomiyoshi and K. Makita, *Journal of Applied Physics*, 2003, **93** (1), 368
43. L. Francioso, C. De Pascali, I. Farella, C. Martucci, P. Cretì, P. Siciliano and A. Perrone, *Journal of Power Sources*, 2011, **196** (6), 3239
44. Z. Wang, V. Leonov, P. Fiorini and C. Van Hoof, *Sensors and Actuators A: Physical*, 2009, **156** (1), 95
45. NASA, Voyager power reports, <http://voyager.jpl.nasa.gov/mission/weekly-reports/index.htm> (accessed 07/01/14)
46. NASA, Spacecraft Lifetime, <http://voyager.jpl.nasa.gov/spacecraft/spacecraftlife.html> (accessed 07/01/14)
47. D. A. Gurnett, W. S. Kurth, L. F. Burlaga and N. F. Ness, *Science*, 2013, **341**, 1489
48. NASA, NASA spacecraft embarks on historic journey into interstellar space, http://www.nasa.gov/mission_pages/voyager/voyager20130912.html (accessed 07/01/14)
49. D. J. Yang, Z. F. Yuan, P. H. Lee and H. M. Yin, *International Journal of Heat and Mass Transfer*, 2012, **55** (4), 1076

50. S. Su, T. Liu, Y. Wang, X. Chen, J. Wang and J. Chen, *Applied Energy*, 2014, **120**, 16
51. T. Chen, G. H. Guai, C. Gong, W. Hu, J. Zhu, H. Yang, Q. Yan and C. M. Li, *Energy & Environmental Science*, 2012, **5 (4)**, 6294
52. A. R. Khataee and M. B. Kasiri, *Journal of Molecular Catalysis A*, 2010, **328**, 8
53. A. Mills and S. Le Hunte, *Journal of Photochemistry and Photobiology A: Chemistry*, 1997, **108**, 1
54. M. Annunziata, L. Guida, L. Perillo, R. Aversa, I. Passaro and A. Olivia, *Journal of Materials Science: Materials in Medicine*, 2008, **19**, 3585
55. O. Carp, *Progress in Solid State Chemistry*, 2004, **32 (1-2)**, 33
56. A. Fujishima and K. Honda, *Nature*, 1972, **238**, 37
57. K. S. Raja, M. Misra, V. K. Mahajan, T. Gandhi, P. Pillai and S. K. Mohapatra, *Journal of Power Sources*, 2006, **161 (2)**, 1450
58. C. Xu, R. Killmeyer, M. L. Gray and S. U. M. Khan, *Electrochemistry Communications*, 2006, **8 (10)**, 1650
59. E. Y. Kim, J. H. Park and G. Y. Han, *Journal of Power Sources*, 2008, **184 (1)**, 284
60. C.C. Tsai and H. Teng, *Applied Surface Science*, 2008, **254 (15)**, 4912
61. S. K. Mohapatra, V. K. Mahajan and M. Misra, *Nanotechnology*, 2007, **18 (44)**, 445705
62. T. L. Hathway, Ph.D Thesis, *Titanium dioxide photocatalysis: studies of the degradation of organic molecules and characterization of photocatalysts using mechanistic organic chemistry*, Iowa State University, 2009
63. K. Lv, H. Zuo, J. Sun, K. Deng, S. Liu, X. Li and D. Wang, *Journal of Hazardous materials*, 2009, **161 (1)**, 396
64. X. W. Lou, L. A. Archer and Z. Yang, *Advanced Materials*, 2008, **20 (21)**, 3987
65. M. Mattesini, J. de Almeida, L. Dubrovinsky, N. Dubrovinskaia, B. Johansson and R. Ahuja, *Physical Review B*, 2004, **70 (21)**, 212101
66. R. Chu, J. Yan, S. Lian, Y. Wang, F. Yan and D. Chen, *Solid State Communications*, 2004, **130 (12)**, 789
67. P. C. Ricci, C. M. Carbonaro, L. Stagi, M. Salis, A. Casu, S. Enzo and F. Delogu, *The Journal of Physical Chemistry C*, 2013, **117**, 7850
68. A. L. Linsebigler, G. Lu and J. John T. Yates, *Chemical Reviews*, 1995, **95 (3)**, 735
69. J. K. Burdett, *Inorganic Chemistry*, 1985, **24**, 2244
70. M. Weller in *Inorganic Chemistry*, Oxford University Press, Oxford, sixth edition, 2014, Ch. 1 p 85
71. R. D. Shannon, *Solid State Communications*, 1967, **2**, 139
72. Y. Liu, C. Zheng, W. Wang, C. Yin and G. Wang, *Advanced Materials*, 2001, **13 (24)**, 1883
73. F. Jiao and P. G. Bruce, *Advanced Materials*, 2007, **19**, 657
74. B. White, F. Dachille and R. Roy, *Journal of the American Ceramic Society*, 1961, **44 (4)**, 170
75. T. Berger, T. Lana-Villarreal, D. Monllor-Satoca and R. Gómez, *Chemical Physics Letters*, 2007, **447 (1-3)**, 91
76. J. H. Park, S. Kim and A. J. Bard, *Nano letters*, 2006, **6 (1)**, 24
77. J. Jitputti, Y. Suzuki and S. Yoshikawa, *Catalysis Communications*, 2008, **9 (6)**, 1265
78. L. Francioso, A. Taurino, A. Forleo and P. Siciliano, *Sensors and Actuators B: Chemical*, 2008, **130 (1)**, 70
79. S. Daothong, N. Songmee, S. Thongtem and P. Singjai, *Scripta Materialia*, **57 (7)**, 567

80. S. Pavasupree, S. Ngamsinlapasathian, Y. Suzuki and S. Yoshikawa, *Materials Letters*, 2007, **61 (14-15)**, 2973
81. K. Madhusudan Reddy, C. V. Gopal Reddy and S. V. Manorama, *Journal of Solid State Chemistry*, 2001, **158 (2)**, 180
82. M. Anpo, *Journal of Catalysis*, 2003, **216 (1-2)**, 505
83. G. Schmid, M. Bäuml, M. Geerkens, I. Heim, C. Osemann and T. Sawitowski, *Chemical Society Reviews*, 1999, **28**, 179
84. Z. Ambrus, N. Balázs, T. Alapi, G. Wittmann, P. Sipos, A. Dombi and K. Mogyorósi, *Applied Catalysis B: Environmental*, 2008, **81 (1-2)**, 27
85. Z. Wu, F. Dong, W. Zhao and S. Guo, *Journal of Hazardous Materials*, 2008, **157 (1)**, 57
86. T. Umebayashi, T. Yamaki, H. Itoh and K. Asai, *Applied Physics Letters*, 2002, **81 (3)**, 454
87. T. Graziani, *Journal of Materials Science Letters*, 1995, **14**, 1078
88. S. V. Didziulis, J. R. Lince and T. B. Stewart, *Inorganic Chemistry*, 1993, **33**, 1979
89. J. F. Creemer, D. Briand, H. W. Zandbergen, W. van der Vlist, C. R. de Boer, N. F. de Rooij and P. M. Sarro, *Sensors and Actuators A: Physical*, 2008, **148 (2)**, 416
90. N. Kumar, *Journal of Vacuum Science & Technology A: Vacuum, Surfaces, and Films*, 1987, **5 (4)**, 1778
91. Y. S. Wu, Y.-H. Lee and Y.-L. Tsai, *Journal of Materials Processing Technology*, 2008, **208 (1-3)**, 35
92. G. Demazeau, *Research on Chemical Intermediates*, 2011, **37**, 107
93. O. Palchik, S. Avivi, D. Pinkert and A. Gedanken, *Nanostructured Materials*, 1999, **11 (3)**, 415
94. M. Knoll, *Technical Physics*, 1935, **11**, 467
95. R. D. Leapman, *Journal of Microscopy*, 2003, **210 (1)**, 5
96. R. Venkatasubramanian, T. Colpitts, E. Watko, M. Lamvik and N. El-Masry, *Journal of Crystal Growth*, 1997, **170**, 817
97. H. You, S. Hyub Baek, K. C. Kim, O. J. Kwon, J. S. Kim and C. Park, *Journal of Crystal Growth*, 2012, **346 (1)**, 17
98. A. Giani, A. Boulouz, F. Pascal-Delannoy, A. Foucaran, E. Charles and A. Boyer, *Materials Science and Engineering B*, 1999, **B64**, 19
99. A. G. Kunjomana and E. Mathai, *Crystal Research and Technology*, 1992, **27 (3)**, 329
100. N. W. Gothard, Ph.D. Thesis, *The effects of nanoparticle inclusions upon the microstructure and thermoelectric transport properties of bismuth telluride-based composites*, Clemson University, 2008
101. K. Jacob John, Ph.D. Thesis, *An investigation on the preparation and properties of reactively evaporated SnSe and Bi₂Te₃ thin films and bismuth selenide crystals*, Cochin University of Science and Technology, 1996
102. S. L. Benjamina, C. H. de Grootb, C. Gurnania, A. L. Hectors, R. Huangb, E. Koukharenkob, W. Levason and A. G. Reid, *Journal of Materials Chemistry A*, 2014, **2**, 4865
103. T. Mårtensson, M. Borgstrom, L. Samuelson, W. Seifert and B. J. Ohlsson, *Nanotechnology*, 2003, **14**, 1255
104. D. E. Perea, E. R. Hemesath, E. J. Schwalbach, J. L. Lensch-Falk, P. W. Voorhees and L. J. Lauhon, *Nature Nanotechnology*, 2009, **4 (5)**, 315
105. J. J. Fu, Y. N. Lu, H. Xu, K. F. Huo, X. Z. Wang, L. Li, Z. Hu and Y. Chen, *Nanotechnology*, 2004, **15 (7)**, 727

106. Y. Zhao, R. W. Hughes, Z. Su, W. Zhou and D. H. Gregory, *Angewandte Chemie International Edition*, 2011, **50**, 10397
107. G. Hao, X. Qi, L. Yang, Y. Liu, J. Li, L. Ren, F. Sun and J. Zhong, *AIP Advances*, 2012, **2** (1), 012114
108. M. H. Francombe, *Philosophical Magazine*, 1964, **10** (108), 989
109. M. J. Kim and Y. D. Huh, *Materials Letters*, 2011, **65** (4), 650
110. A. Purkayastha, A. Jain, C. Hapenciuc, R. Buckley, B. Singh, C. Karthik, R. J. Mehta, T. Borca-Tasciuc and G. Ramanath, *Chemistry of Materials*, 2011, **23** (12), 3029
111. D. Kong, W. Dang, J. J. Cha, H. Li, S. Meister, H. Peng, Z. Liu and Y. Cui, *Nano Letters*, 2010, **10** (6), 2245
112. V. Goyal, D. Teweldebrhan and A. A. Balandin, *Applied Physics Letters*, 2010, **97** (13), 133117
113. K. M. F. Shahil, M. Z. Hossain, D. Teweldebrhan and A. A. Balandin, *Applied Physics Letters*, 2010, **96** (15), 153103
114. D. Teweldebrhan, V. Goyal, M. Rahman and A. A. Balandin, *Applied Physics Letters*, 2010, **96** (5), 053107
115. R. Vaidya, M. Dave, S. S. Patel, S. G. Patel and A. R. Jani, *Pramana Journal of Physics*, 2004, **63** (3), 611
116. R. Hillel, C. Bec, J. Bouix, A. Michaelides, Y. Monteil, A. Tranquard and C. Bernard, *Journal of The Electrochemical Society*, 1982, **129** (6), 1343
117. Y. Feutelais, B. Legendre, N. Rodier and V. Agafonov, *Materials Research Bulletin*, 1992, **28**, 591
118. A. Hiraki, M-A. Nicolet, and J. W. Mayer, *Applied Physics Letters*, 1971, **18** (5), 178
119. L. Huang, Y. Yu, C. Li and L. Cao, *The Journal of Physical Chemistry C*, 2013, **117** (12), 6469
120. J. H. Kim, D. Y. Jeong, B. K. Ju, S. J. Yoon, J. S. Kim, Proceedings of the 25th International Conference on Thermoelectrics, Vienna, 2006, 411
121. A. L. Prieto, M. S. Sander, M. S. Martin-Gonzalez, R. Gronsky, T. Sands, and A. M. Stacy, *Journal of the American Chemical Society*, 2001, **123**, 7160
122. S. A. Sapp, B. B. Lakshmi and C. R. Martin, *Advanced Materials*, 1999, **11** (5), 402
123. J. H. Dycus, R. M. White, J. M. Pierce, R. Venkatasubramanian and J. M. LeBeau, *Applied Physics Letters*, 2013, **102** (8), 081601
124. A. Koma, *Thin Solid Film*, 1992, **216**, 72
125. R. P. Gupta, O. D. Iyore, K. Xiong, J. B. White, K. Cho, H. N. Alshareef and B. E. Gnade, *Electrochemical and Solid-State Letters*, 2009, **12** (10), H395
126. H. Pathan, *Applied Surface Science*, 2003, **218** (1-4), 291
127. H. Li, R. Brescia, M. Povia, M. Prato, G. Bertoni, L. Manna and I. Moreels, *Journal of the American Chemical Society*, 2013, **135** (33), 12270
128. B. S. Farag and S. A. Khodier, *Electronics and Optics*, 1991, **201**, 231
129. J. Zhou, X. Wu, A. Duda, G. Teeter and S. H. Demtsu, *Thin Solid Films*, 2007, **515** (18), 7364
130. F. de Moure-Flores, J. G. Quiñones-Galván, A. Guillén-Cervantes, A. Hernández-Hernández, M. D. L. L. Olvera, J. Santoyo-Salazar, G. Contreras-Puente, M. Zapata-Torres and M. Meléndez-Lira, *Surface and Coatings Technology*, 2013, **217**, 181
131. G. Zhang, B. Kirk, L. A. Jauregui, H. Yang, X. Xu, Y. P. Chen and Y. Wu, *Nano letters*, 2012, **12** (1), 56

132. E. Hazifejzovic, J. Gallagher, I. MacLaren and D. H. Gregory, Unpublished work, 2014
133. J. Jean and T. Ring, *Langmuir*, 1985, **2**, 251
134. J. Y. G. Shu Juan Liu, Bo Hu, and Shu Hong Yu, *Crystal Growth & Design*, 2009, **9** (1), 203
135. S. Komarneni, R. Roy and Q. H. Li, *Materials Research Bulletin*, 1992, **27** (12), 1393
136. P. Chen, J. D. Peng, C. H. Liao, P. S. Shen and P. L. Kuo, *Journal of Nanoparticle Research*, 2013, **15**, 1465
137. K. F. Moura, J. Maul, A. R. Albuquerque, G. P. Casali, E. Longo, D. Keyson, A. G. Souza, J. R. Sambrano and I. M. G. Santos, *Journal of Solid State Chemistry*, 2014, **210** (1), 171
138. J. Du, W. Chen, C. Zhang, Y. Liu, C. Zhao and Y. Dai, *Chemical Engineering Journal*, 2011, **170** (1), 53
139. F. Dufour, S. Cassaignon, O. Durupthy, C. Colbeau-Justin and C. Chanéac, *European Journal of Inorganic Chemistry*, 2012, **16**, 2707
140. M. I. Dar, A. K. Chandiran, M. Grätzel, M. K. Nazeeruddin and S. A. Shivashankar, *Journal of Materials Chemistry A*, 2014, **2** (6), 1662
141. R. V. Anirudha Jena, S. A. Shivashankar, and G. Madras, *Industrial & Engineering Chemistry Research*, 2010, **49**, 9636
142. S. Baldassari, S. Komarneni, E. Mariani and C. Villa, *Materials Research Bulletin*, 2005, **40** (11), 2014
143. X. Z. Guobin Ma, J. Zhu, *International Journal of Modern Physics B*, 2004, **19**, 2763
144. S. Yoon, E. S. Lee and A. Manthiram, *Inorganic Chemistry*, 2012, **51** (6), 3505
145. Y. Li, H. Li, T. Li, G. Li and R. Cao, *Microporous and Mesoporous Materials*, 2009, **117** (1-2), 444
146. S. F. E. Hosono, K. Kakiuchi and H. Imai, *Journal of the American Ceramic Society*, 2004, **126**, 7790
147. X. Wu, Z. Chen, G. Q. M. Lu and L. Wang, *Advanced Functional Materials*, 2011, **21** (21), 4167
148. S. S. Mali, H. Kim, C. S. Shim, P. S. Patil, J. H. Kim and C. K. Hong, *Scientific Reports*, 2013, **3**, 3004
149. J. Cai, J. Ye, S. Chen, X. Zhao, D. Zhang, S. Chen, Y. Ma, S. Jin and L. Qi, *Energy & Environmental Science*, 2012, **5** (6), 7575
150. B. C. M. Varghese Swamy, *Journal of the Australian Ceramic Society*, 2008, **44** (2), 1
151. G. Rangel-Porras, E. Ramos-Ramírez and L. M. Torres-Guerra, *Journal of Porous Materials*, 2009, **17** (1), 69
152. D. Sojic, V. Despotovic, B. Abramovic, N. Todorova, T. Giannakopoulou and C. Trapalis, *Molecules*, 2010, **15** (5), 2994
153. R. D. Peelamedu, M. Fleming, D. K. Agrawal and R. Roy, *Journal of the American Ceramic Society*, 2002, **85**, 117
154. C. Tang, D. Zhou and Q. Zhang, *Materials Letters*, 2012, **79**, 42
155. N. C. Saha and H. G. Tompkins, *Journal of Applied Physics*, 1992, **72** (7), 3072
156. M. Wittmer, *Journal of Applied Physics*, 1981, **52** (11), 6659
157. H. G. Tompkins, *Journal of Applied Physics*, 1991, **70** (7), 3876
158. R. Asahi, T. Morikawa, T. Ohwaki, K. Aoki and Y. Taga, *Science*, 2001, **293** (5528), 269
159. Y. Nosaka, M. Matsushita, J. Nishino and A. Y. Nosaka, *Science and Technology of Advanced Materials*, 2005, **6** (2), 143

160. D. S. Rickerby, *Journal of Vacuum Science & Technology A: Vacuum, Surfaces, and Films*, 1986, **4 (6)**, 2809
161. G. Yang, Z. Jiang, H. Shi, T. Xiao and Z. Yan, *Journal of Materials Chemistry*, 2010, **20**, 5301
162. O. Diwald, T. L. Thompson, T. Zubkov, E. G. Goralski, S. D. Walck, and J. T. Yates, Jr, *The Journal of Physical Chemistry B*, 2004, **108**, 6004
163. R. Asahi, T. Morikawa, T. Ohwaki, K. Aoki and Y. Taga, *Science*, 2001, **293**, 269

9 Appendix

9.1 Appendix A

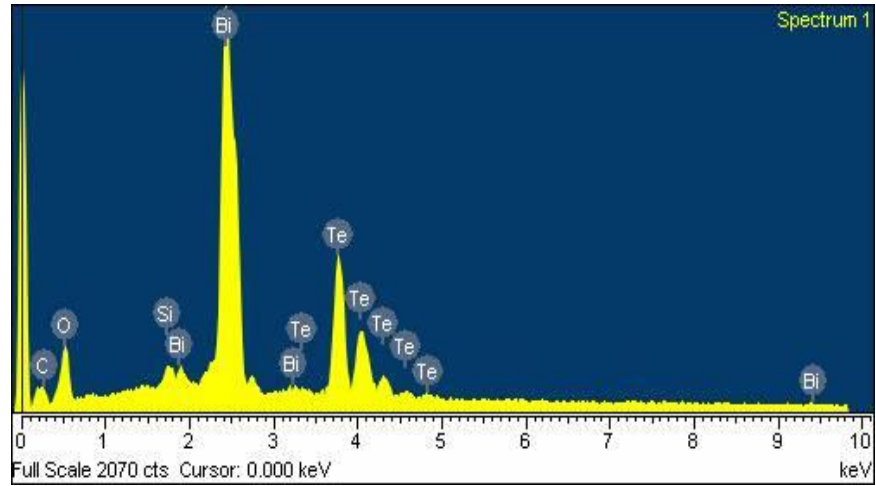


Figure 9-1: EDX pattern from G1 showing Bi_2Te_3

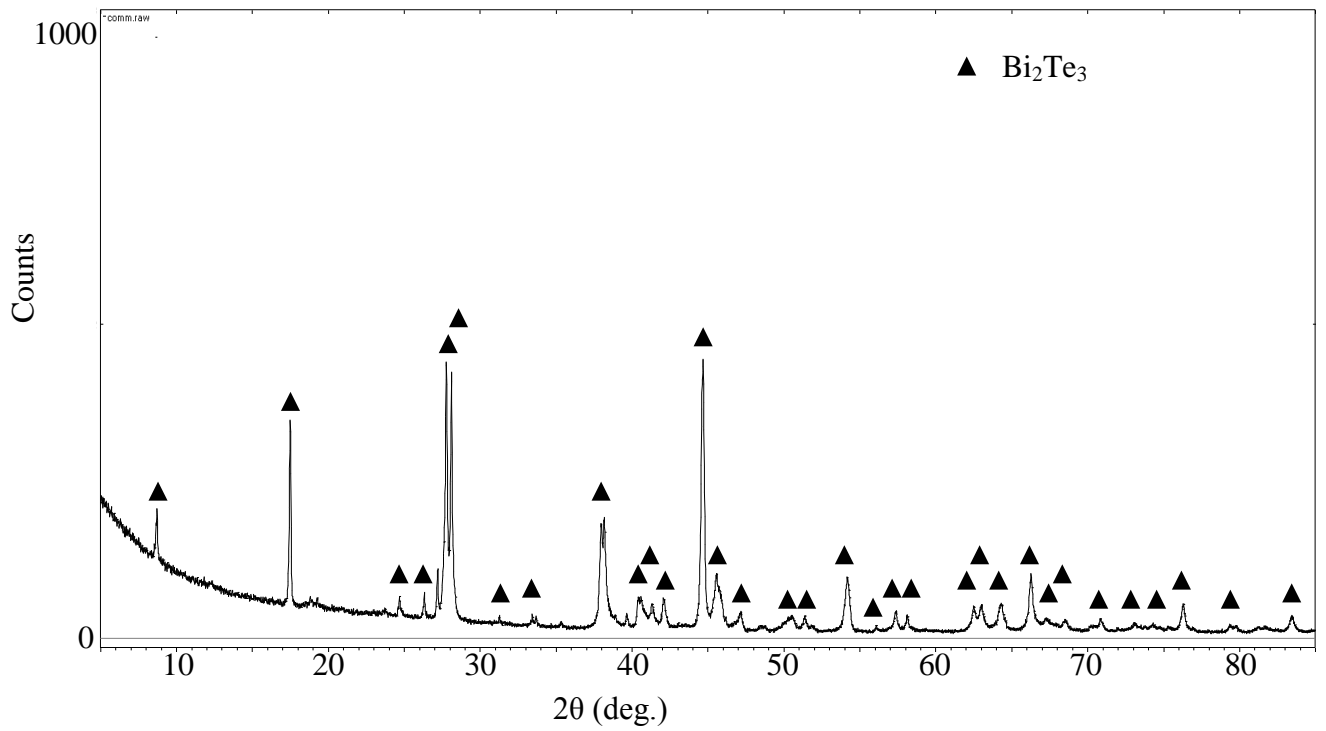


Figure 9-2: XRD pattern of commercial Bi_2Te_3

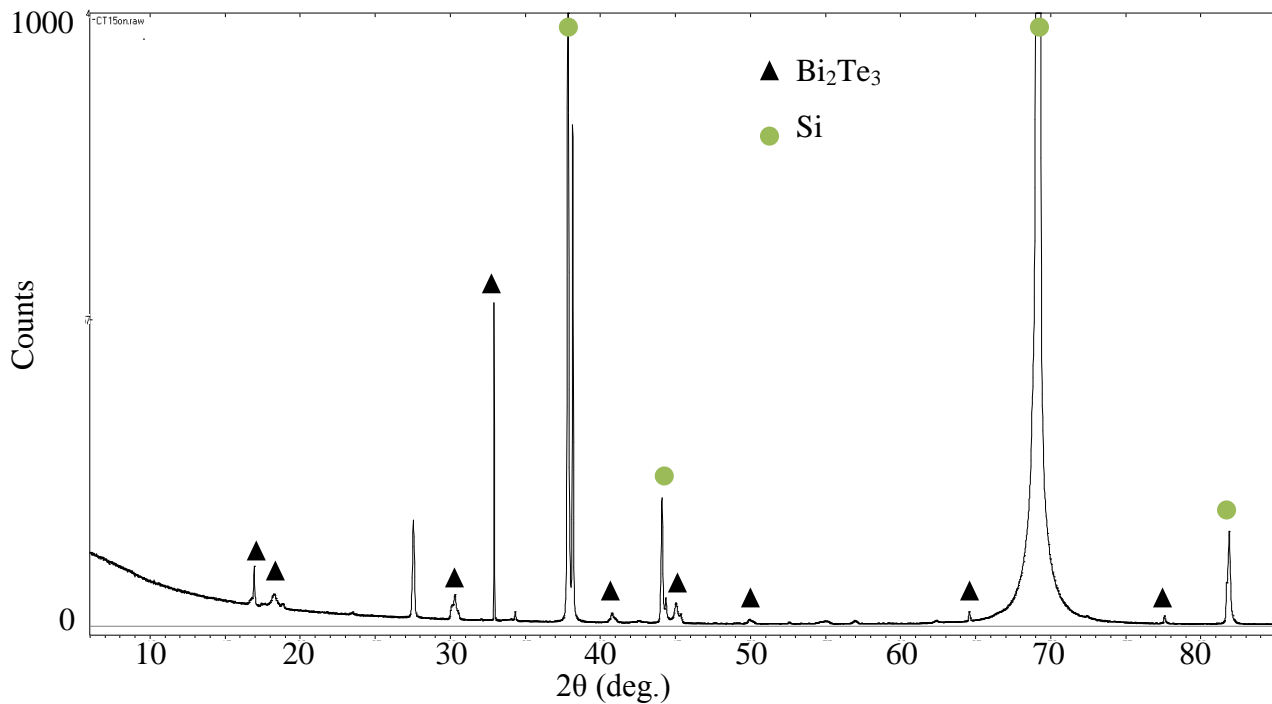


Figure 9-3: XRD pattern of sample G1 showing Bi_2Te_3 on Si surface

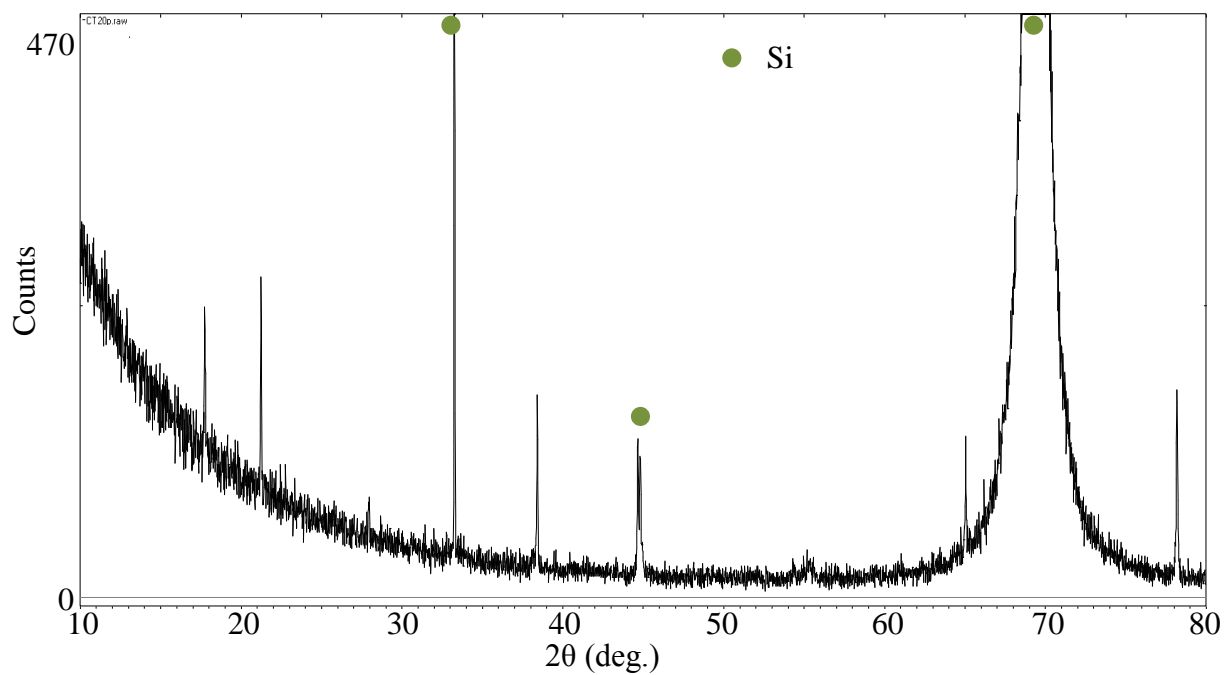


Figure 9-4: XRD of G3 showing low intensity unassigned peaks

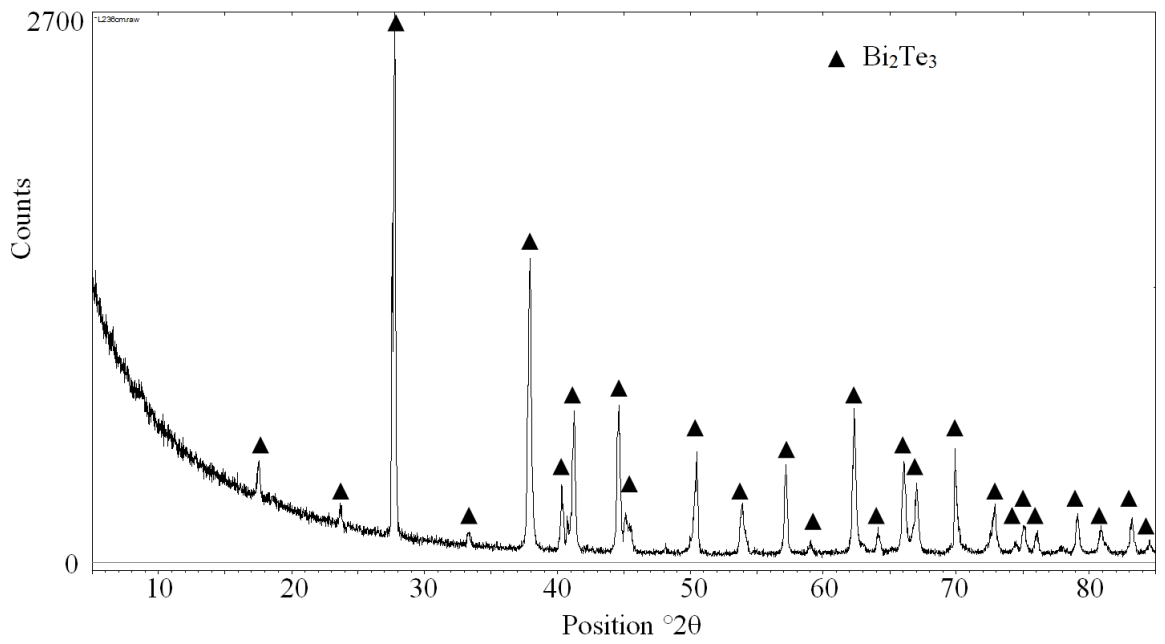


Figure 9-5: XRD pattern of L2 showing Bi_2Te_3

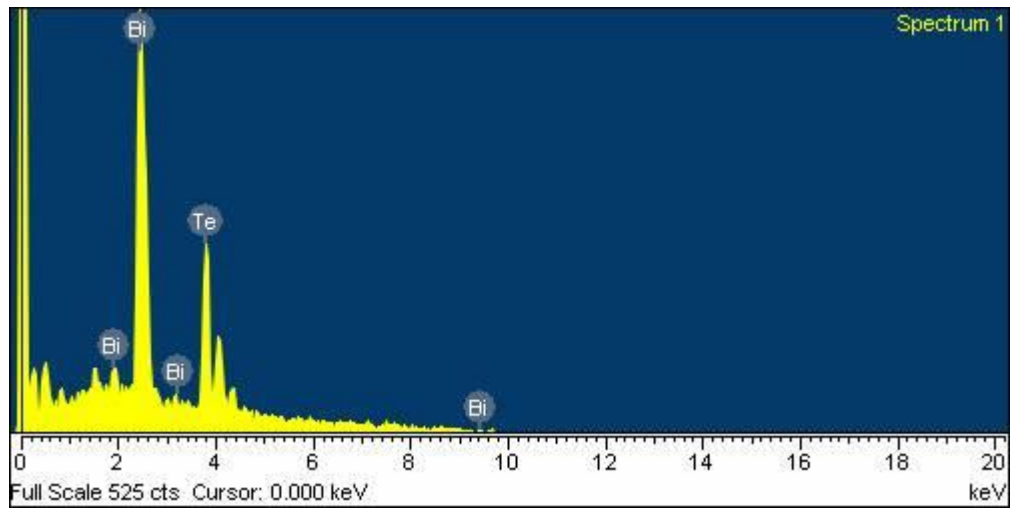


Figure 9-6: EDX from sample L1(repeat) from hotter deposition zone showing Bi_2Te_3

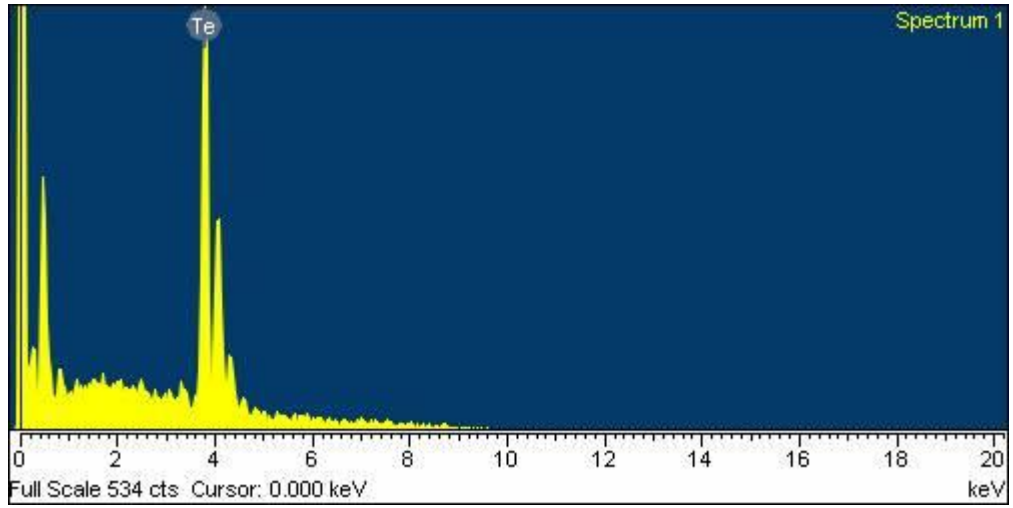


Figure 9-7: EDX of sample L1(repeat) from cooler deposition zone showing Te

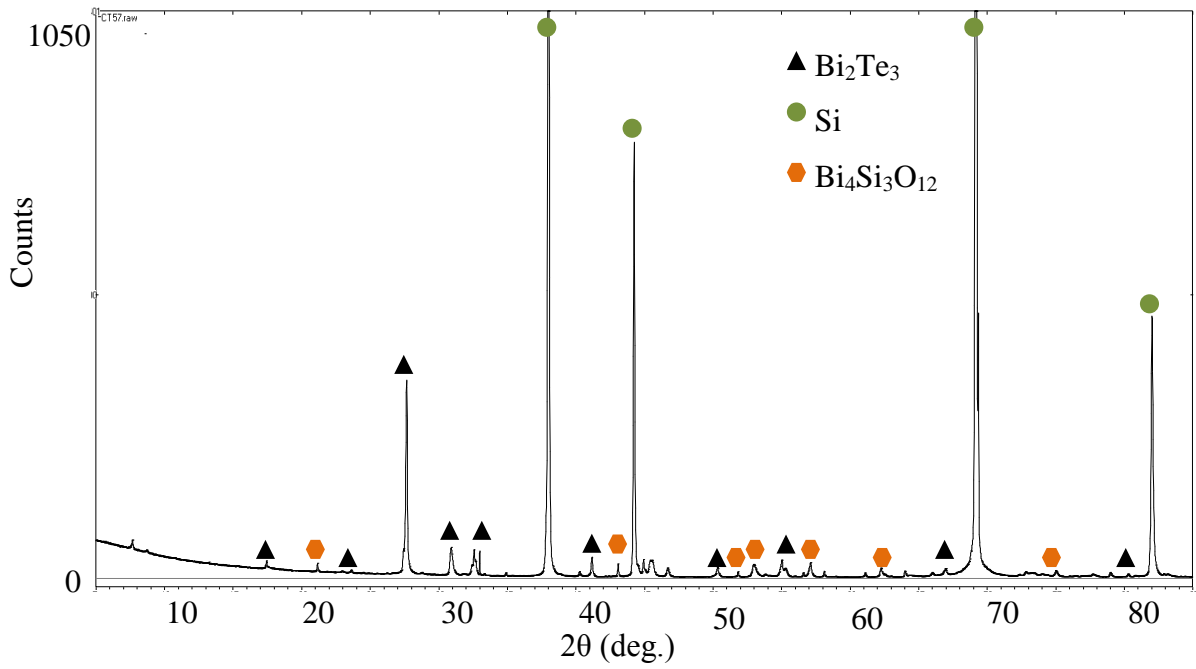


Figure 9-8: XRD pattern of EB1(repeat) showing Bi_2Te_3 and oxide phases

9.2 Appendix B

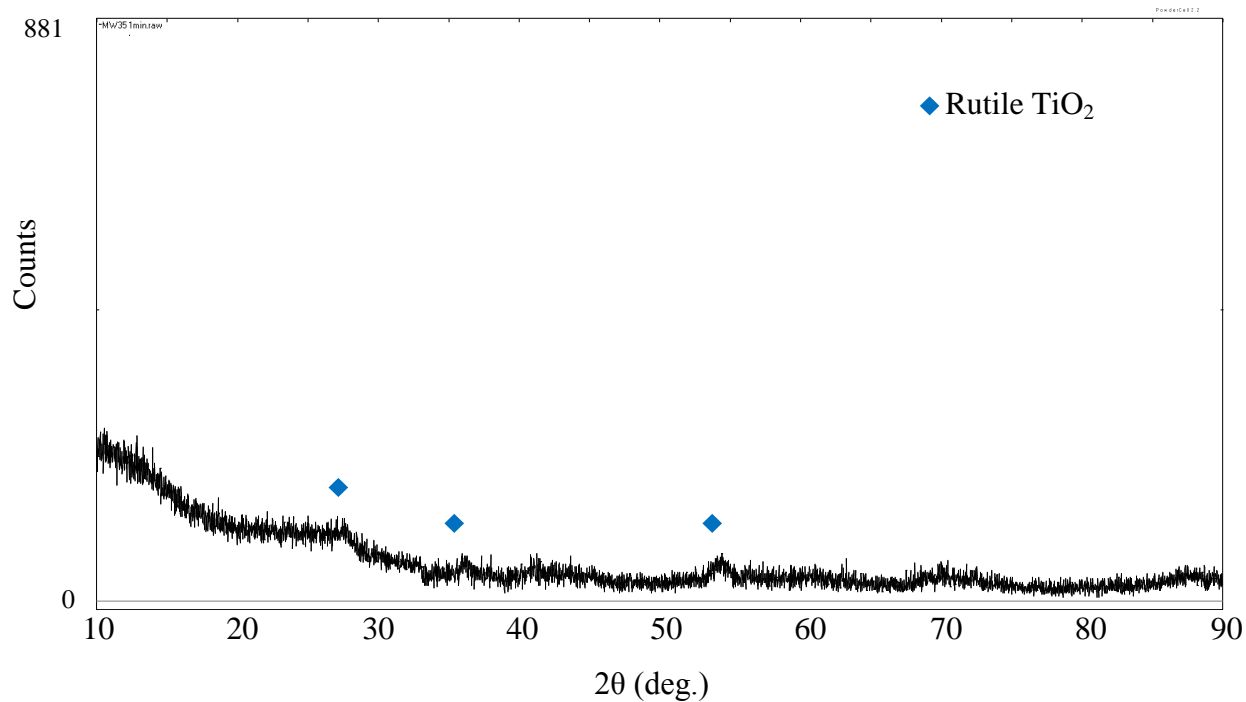


Figure 9-9: XRD pattern of T2 showing rutile TiO₂

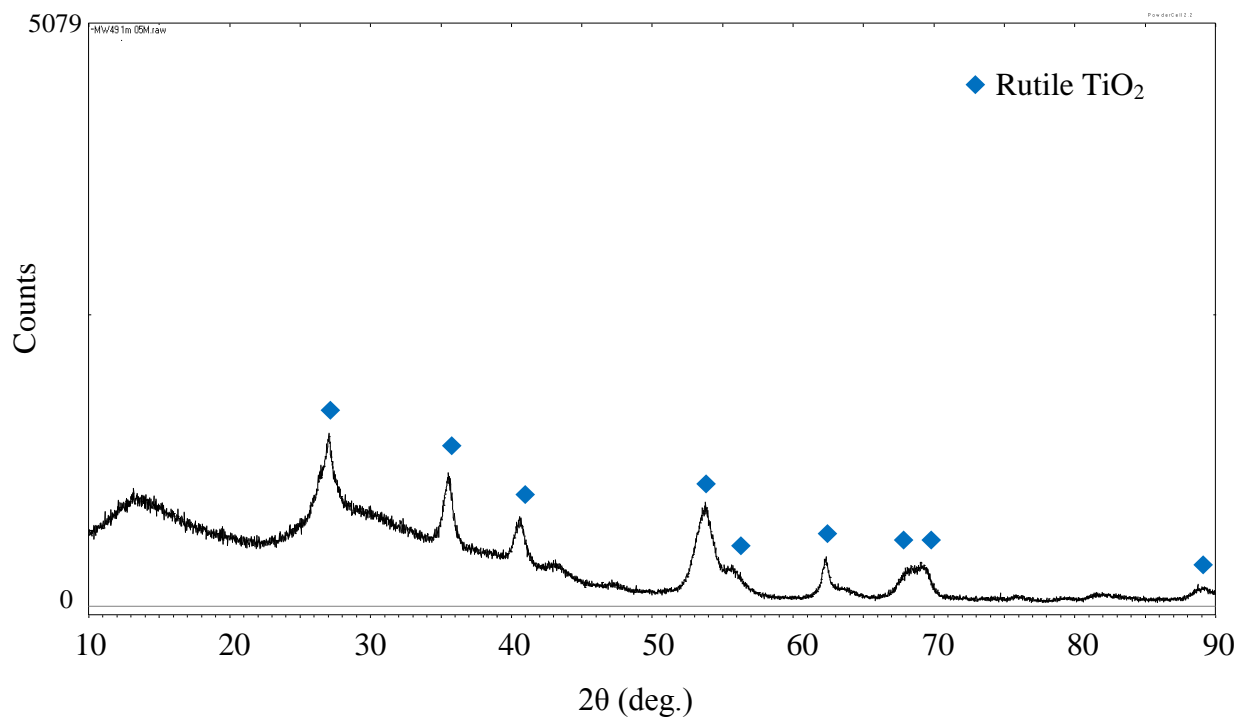


Figure 9-10: XRD pattern of T3 showing rutile TiO₂

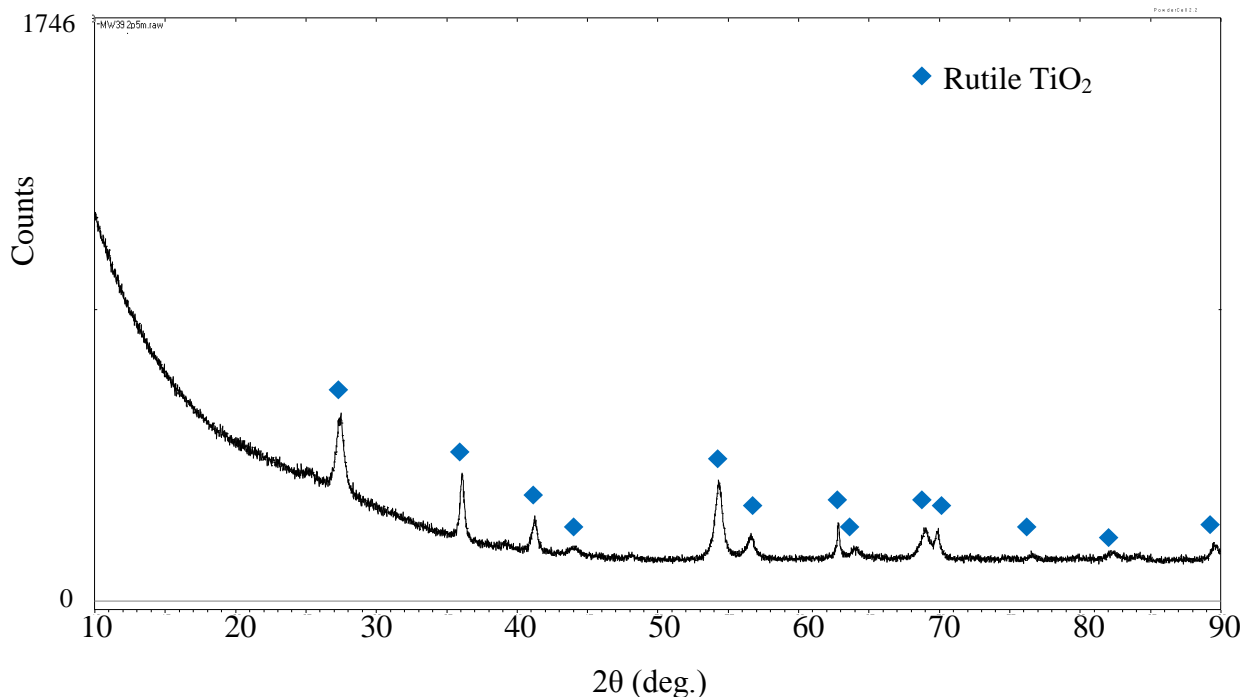


Figure 9-11: XRD pattern of T5 showing rutile TiO₂

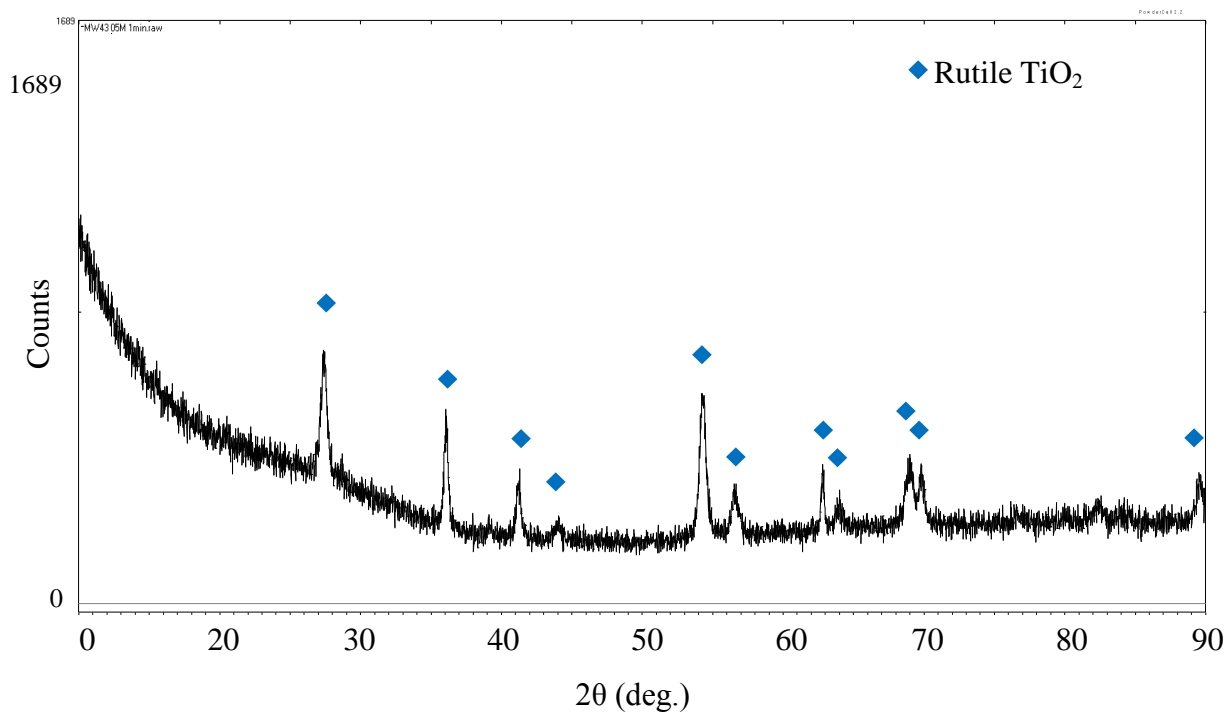


Figure 9-12: XRD pattern of T8 showing rutile TiO₂

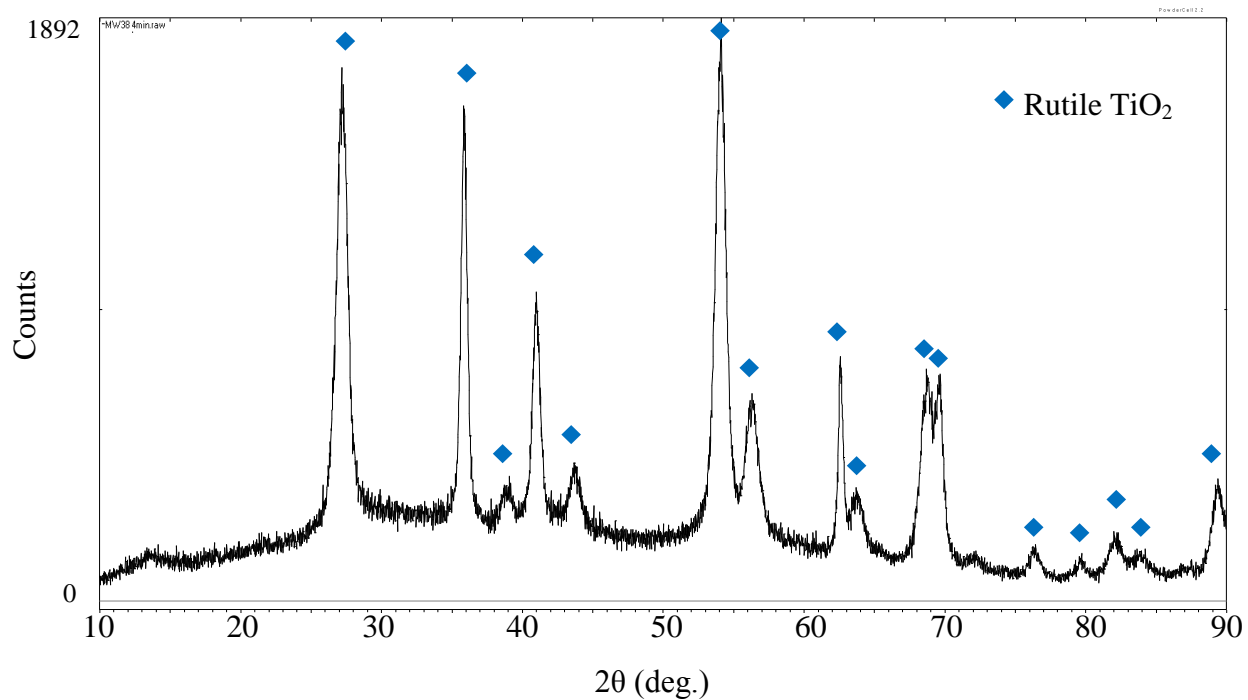


Figure 9-13: XRD pattern of T9 showing rutile TiO₂

Table 9-1: BET results samples T4, T8 and T7

	T4	T8	T7
BET Surface Area m ² /g	41	47	72

UV/Vis profile of T1

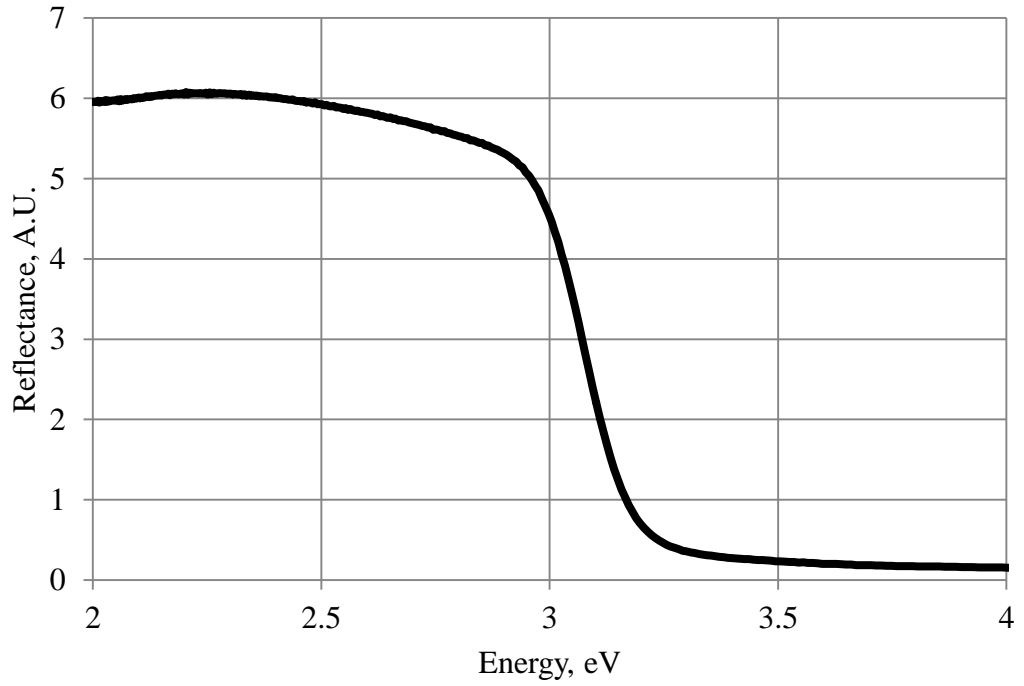


Figure 9-14: UV/Vis profile of T1

UV/Vis profile of T4

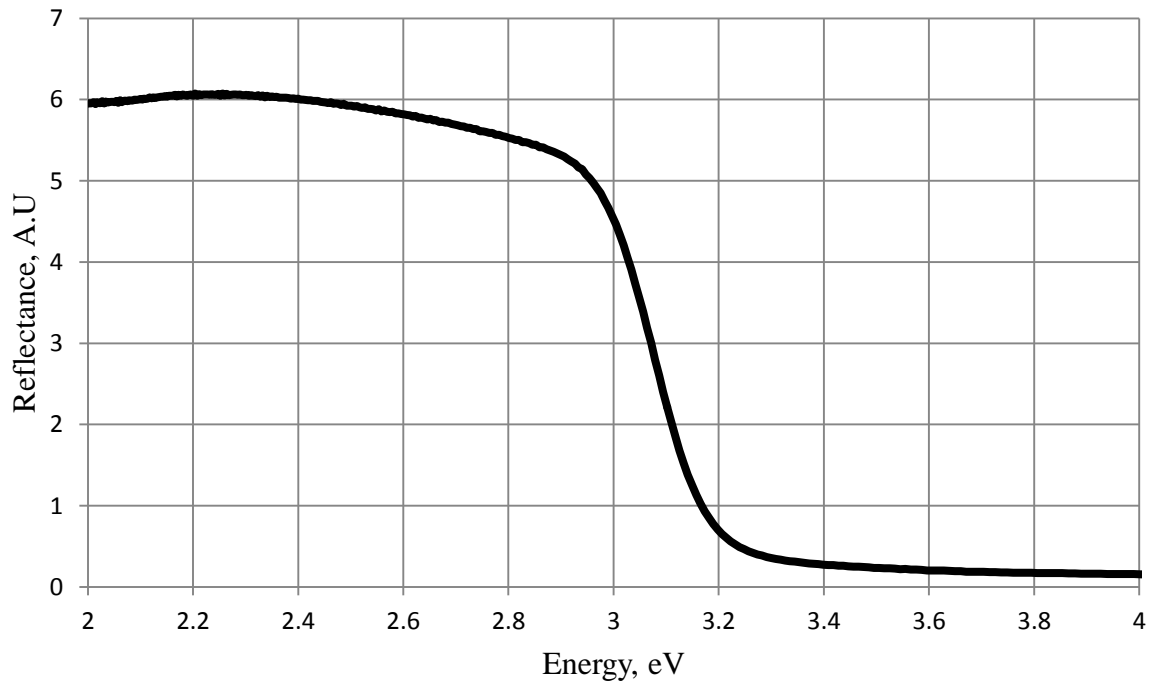


Figure 9-15: UV/Vis profile of T4

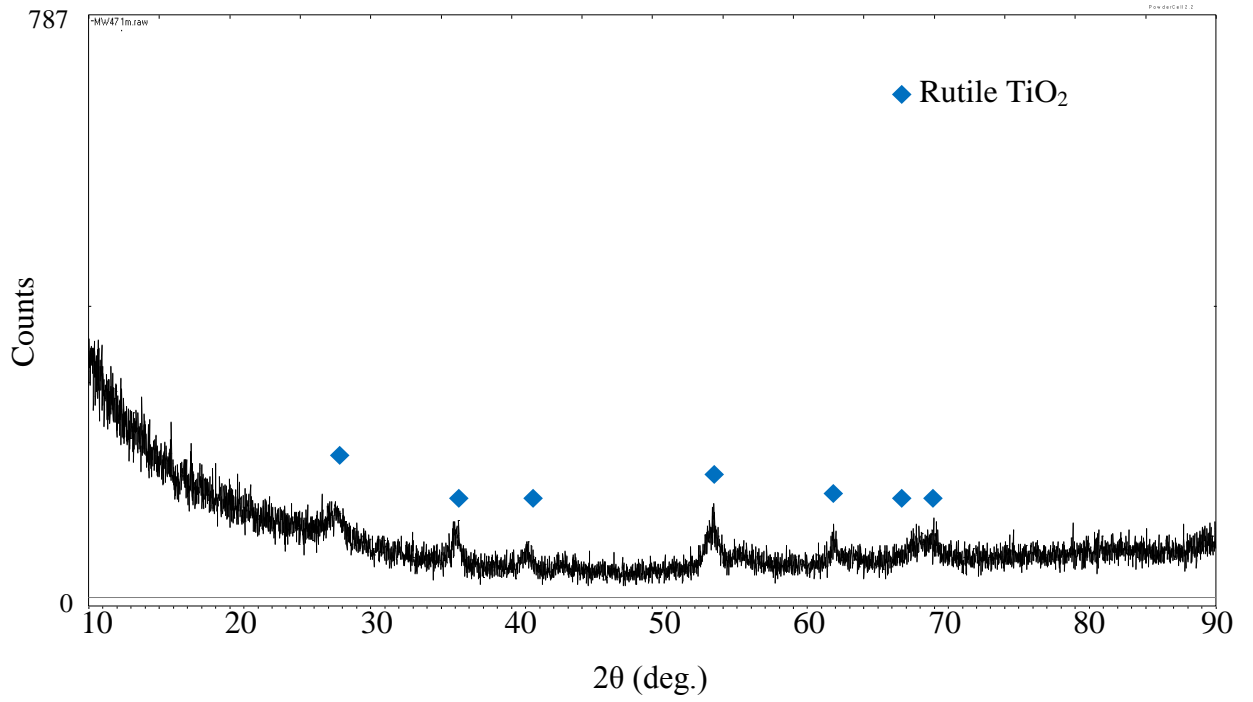


Figure 9-16: XRD pattern of TD1 showing rutile TiO₂

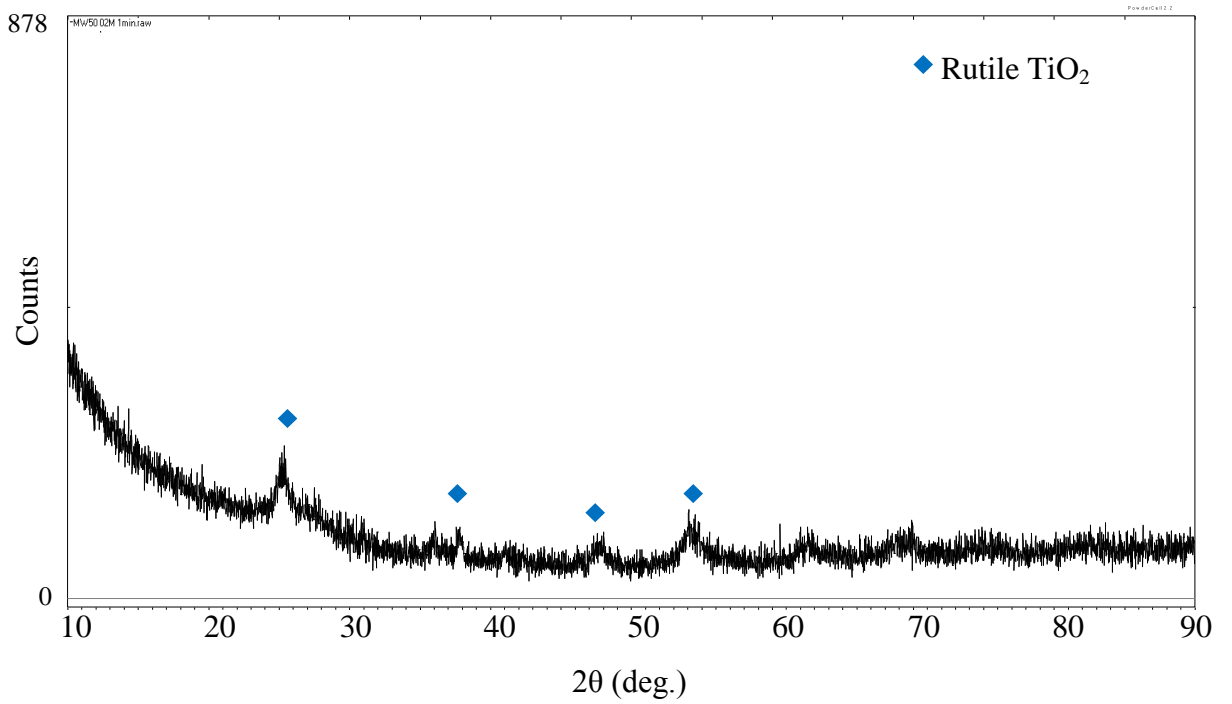


Figure 9-17: XRD pattern of TD2 showing rutile TiO₂

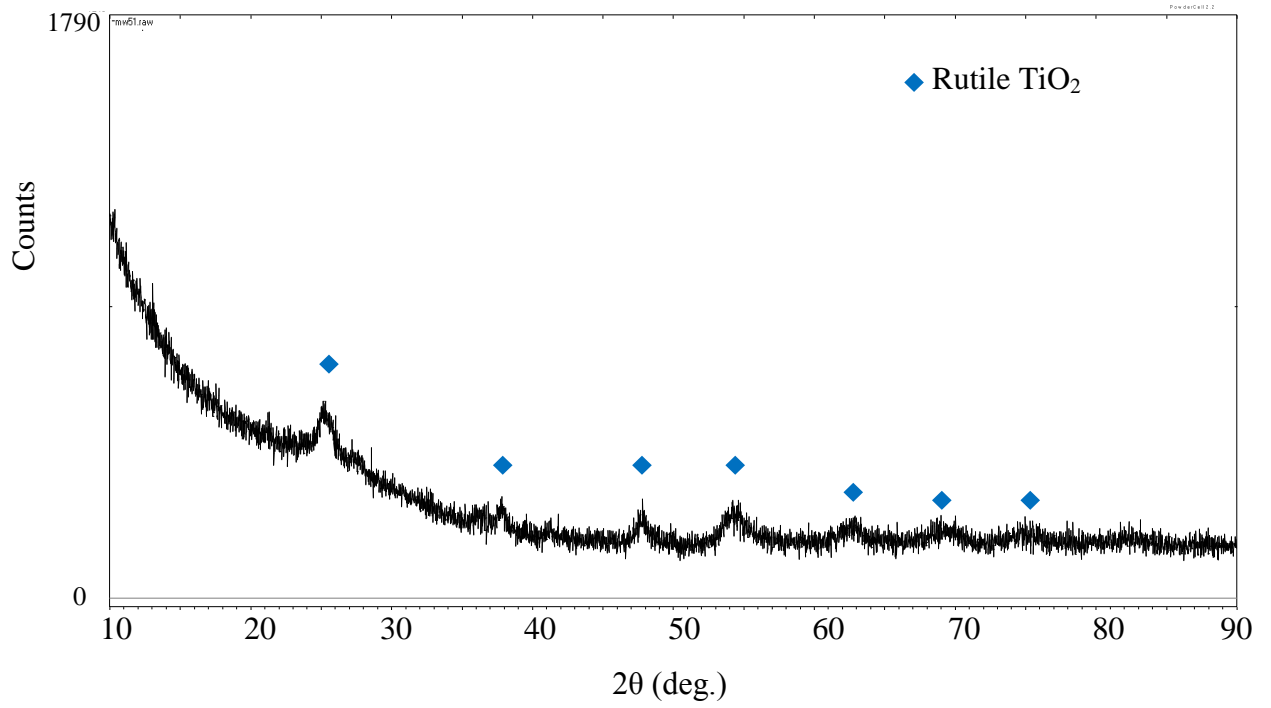


Figure 9-18: XRD pattern of TD3 showing rutile TiO₂

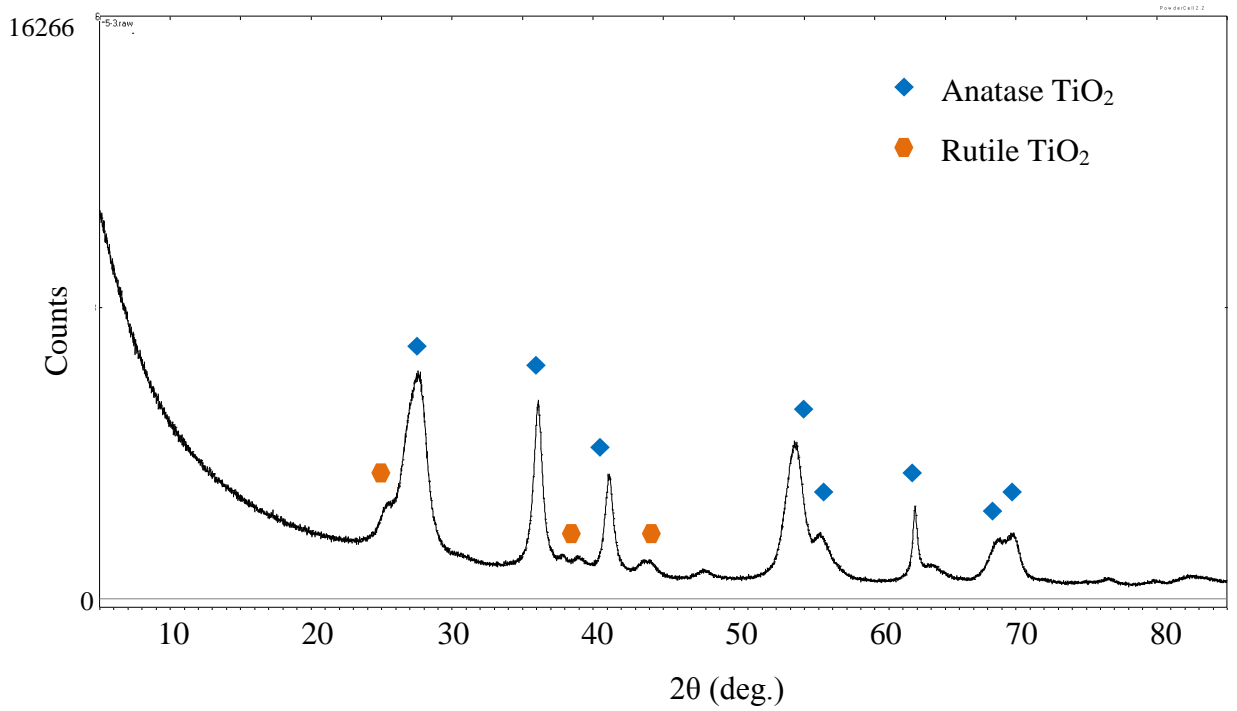


Figure 9-19: XRD pattern of TA3 showing mixed rutile and anatase TiO₂ phases

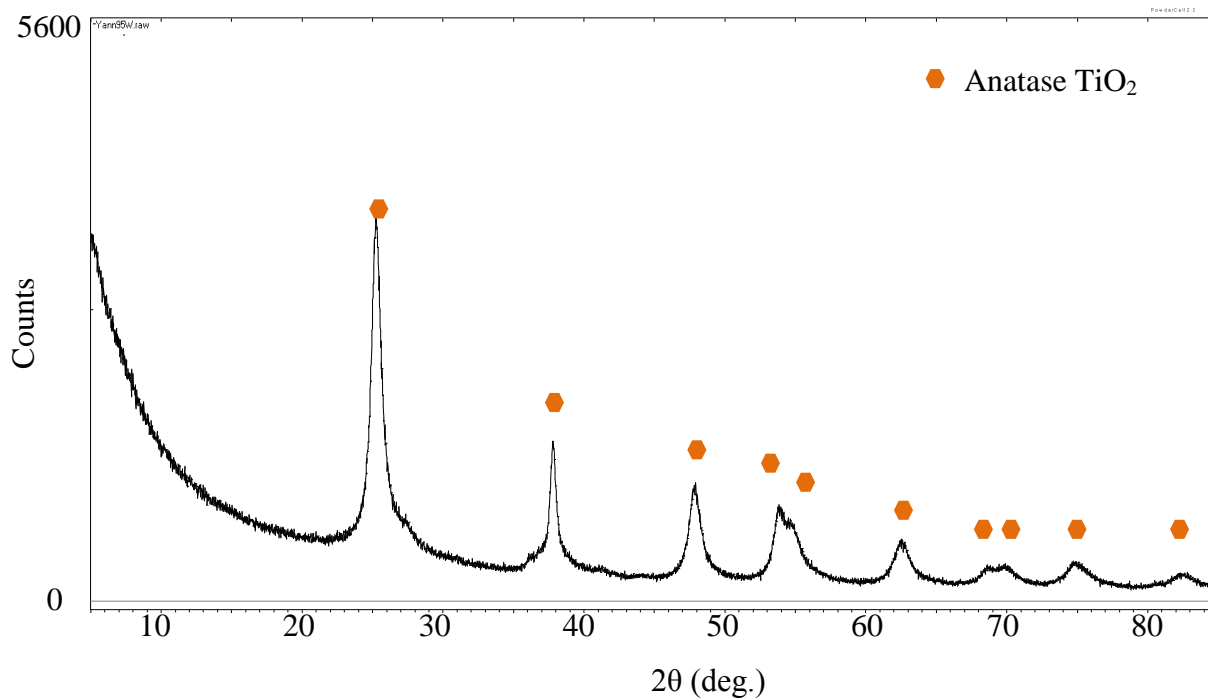


Figure 9-20: XRD of TS7 showing anatase TiO_2

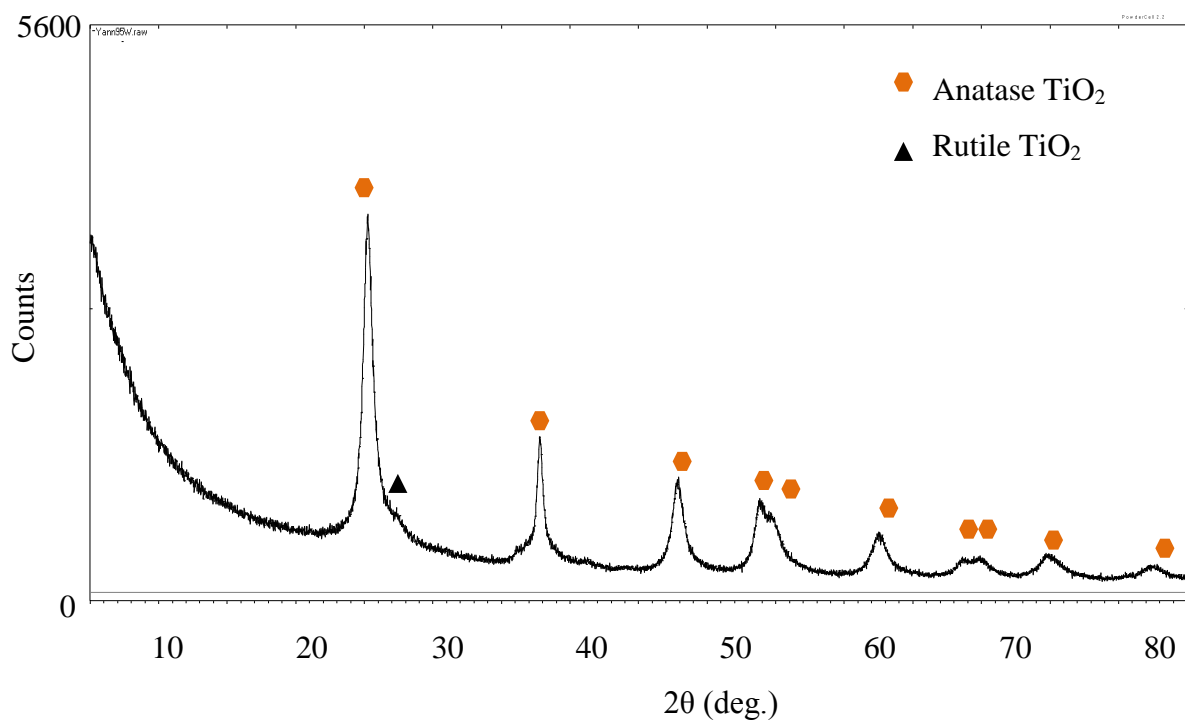


Figure 9-21: XRD profile of TS2 showing anatase TiO_2 with single low intensity rutile TiO_2 peak

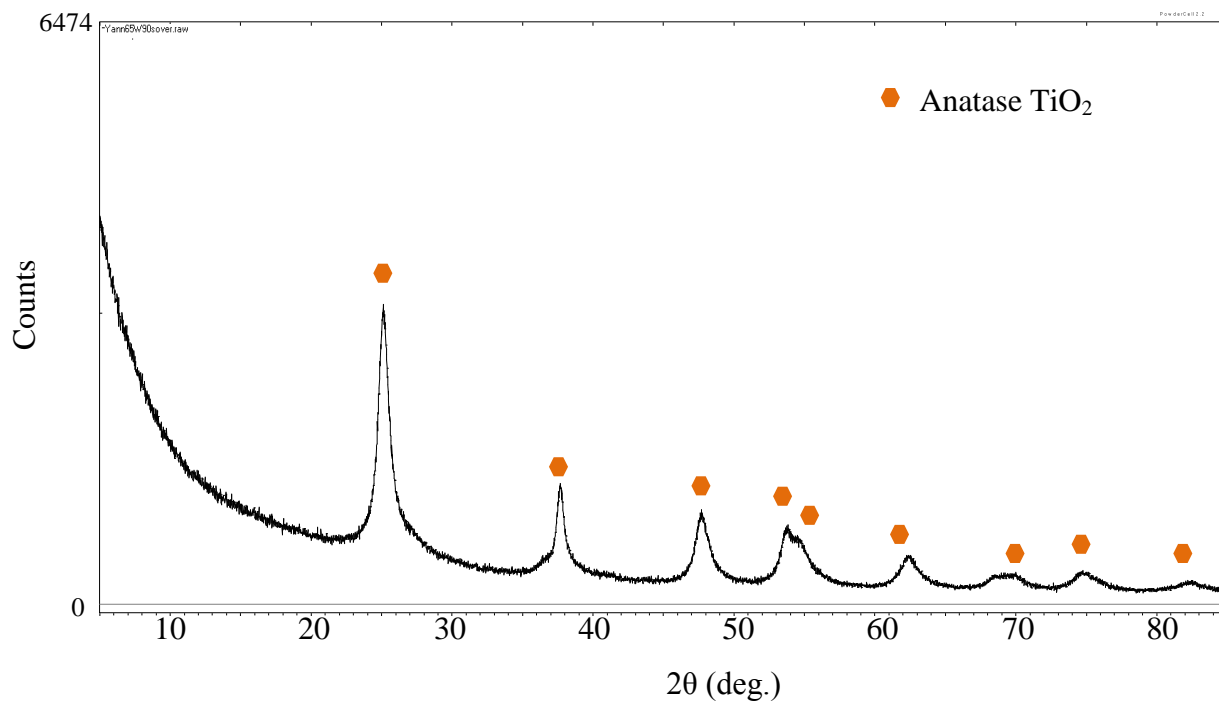


Figure 9-22: XRD profile of TS1 showing anatase TiO₂

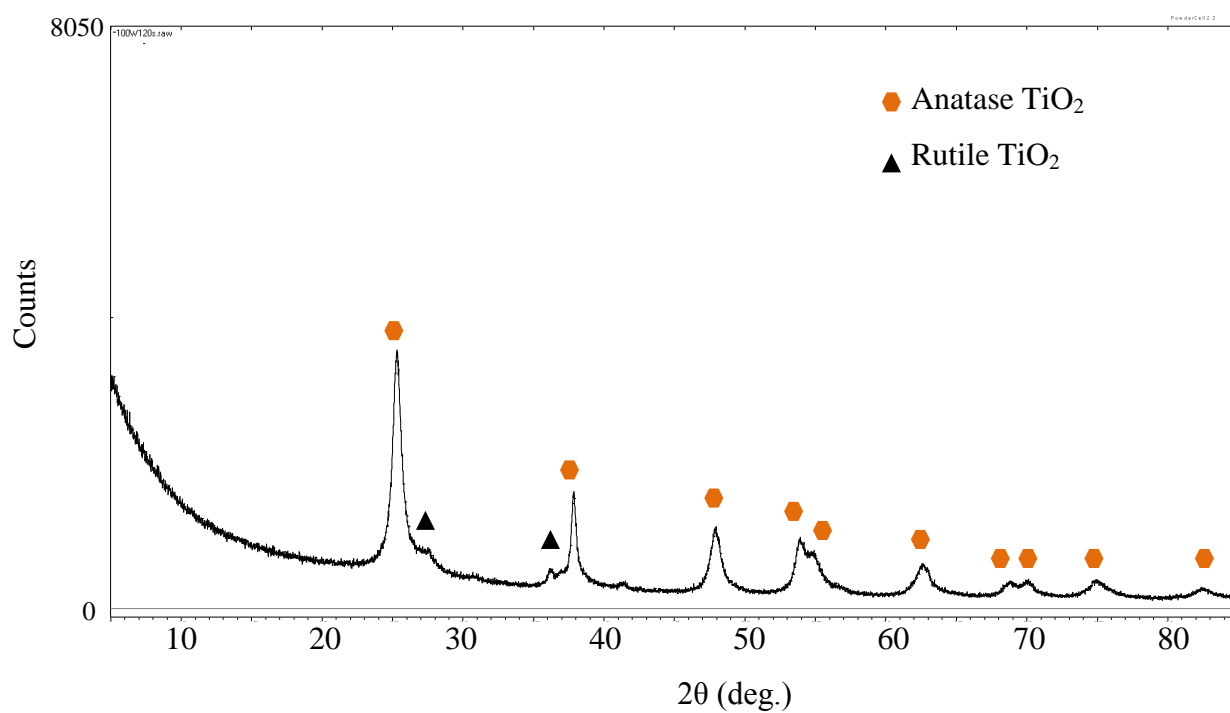


Figure 9-23: XRD profile of TS6 showing anatase and rutile TiO₂

9.3 Appendix C

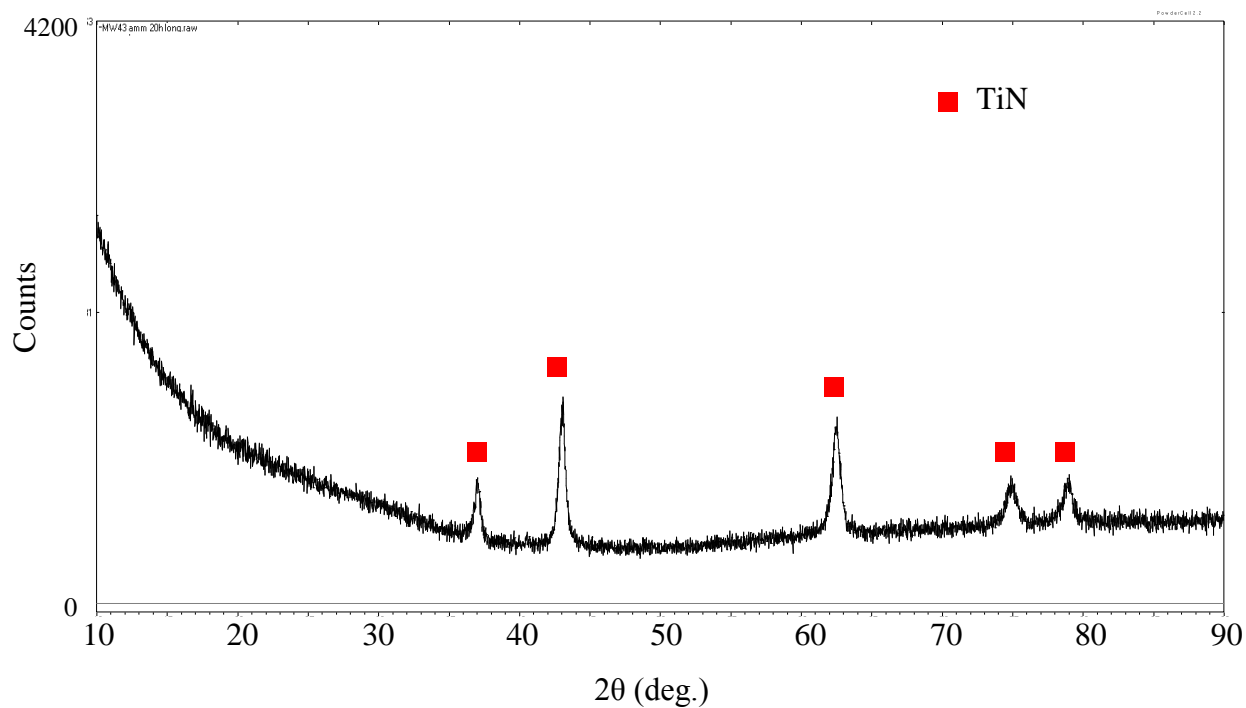


Figure 9-24: XRD pattern of T8 following 20 h ammonolysis showing a cubic structure

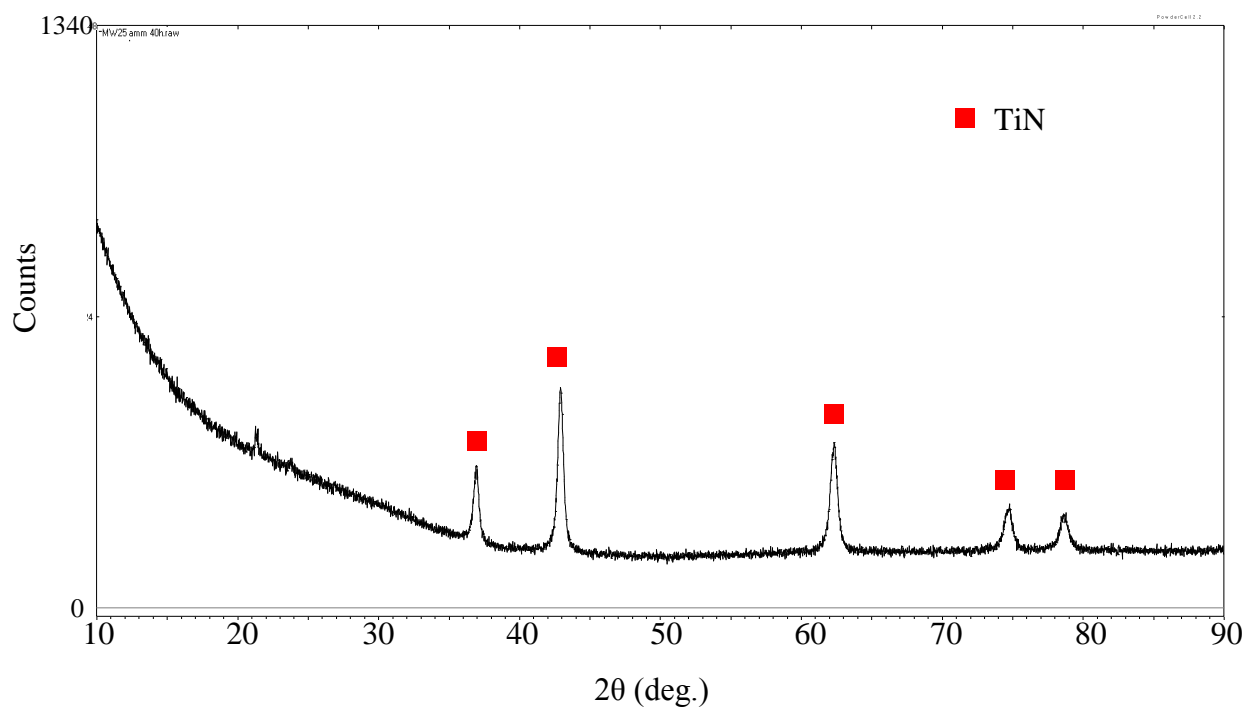


Figure 9-25: XRD pattern of T3 following 16 h ammonolysis showing a cubic structure

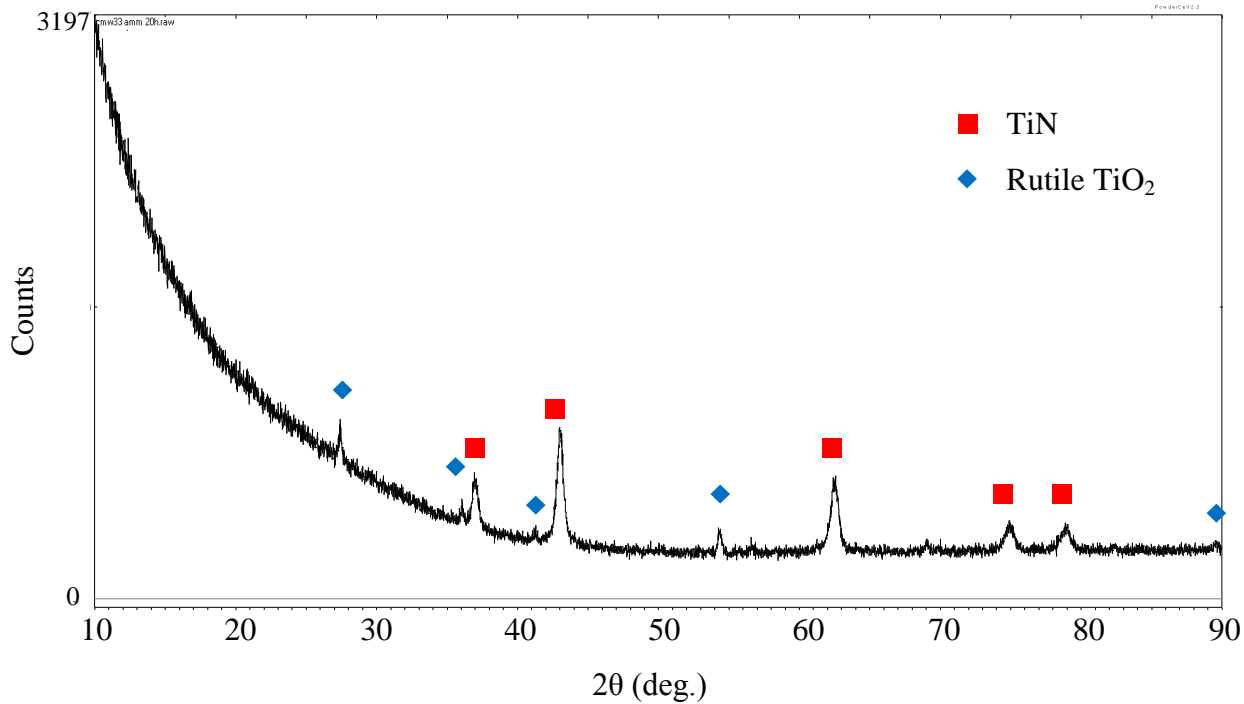


Figure 9-26: XRD pattern of T5 following 12 h ammonolysis showing a mixture cubic and rutile TiO₂ structures

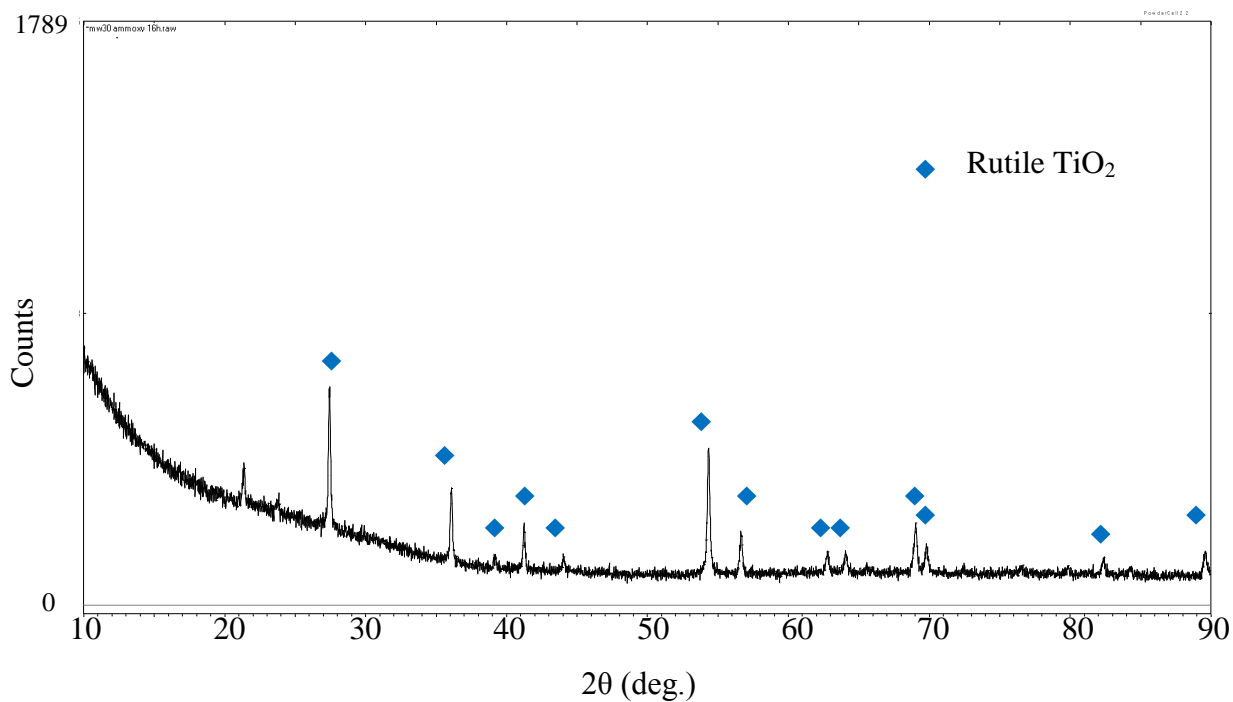


Figure 9-27: XRD pattern of T7O following reaction with oxygen to return to TiO₂ showing a match to rutile